Synthesis and characterization of rare earth doped fluorotellurite glasses, glass-ceramics, and thin film glasses for active photonic applications

Síntesis y caracterización de vidrios, vitrocerámicos, y vidrios en lámina delgadas de fluoroteluritos dopados con tierras raras para aplicaciones fotónicas activas

Memoria presentada para optar al grado de Doctor en Físicas por

Roberta Morea

Dirigida por

Dr. José Gonzalo de los Reyes

Con la tutoría de

Dr. Eugenio Cantelar Alcaide

Presentada en el

Departamento de Física de Materiales,
Facultad de Ciencias de la Universidad Autónoma de Madrid

CSIC
Consejo Superior de Investigaciones Científicas

IO LPG

UAM
Universidad Autonoma de Madrid

Madrid, Mayo de 2015

Agradecimientos

El trabajo que está reflejado en esta memoria de tesis no hubiera sido posible sin la contribución de las personas que quiero aquí mencionar.

En primer lugar me gustaría dar las gracias a mi director de tesis, el Dr. José Gonzalo, por haberme dado la oportunidad de llevar a cabo este trabajo en el Grupo de Procesado por Láser del Instituto de Óptica. Le agradezco mucho haber estado siempre disponible para ayudarme tanto en el trabajo experimental como en la interpretación de los resultados obtenidos. También le agradezco el haberme animado a participar en conferencias, cursos, y estancias en otros centros de investigación para completar mi formación.

En segundo lugar agradezco todos los componentes del grupo por su paciencia, ayuda y disponibilidad en el día a día en el laboratorio y por su simpatía dentro y fuera del laboratorio. En particular, me gustaría expresar mi sincero agradecimiento al Prof. José María Fernández Navarro por haberme ayudado en la fabricación de los vidrios y por haberme enseñado los trucos del oficio. Su pasión por el mundo de los vidrios y su dedicación al trabajo han sido para mí un gran ejemplo. También quiero dar especialmente las gracias a Giorgio, Miguel, y Johann por su desinteresada ayuda cada vez que la he necesitado; a Toney por estar siempre disponible a entablar largas discusiones científicas; y, por último, a Javi e Iván por hacer que me sintiera a gusto en nuestro despacho.

Agradezco también al personal administrativo y a todos los compañeros del Instituto de Óptica tanto su amabilidad y profesionalidad como su agradable compañía.

Fuera del Instituto de Óptica, me gustaría agradecer a todos los que han contribuido a la caracterización de los vidrios fluoroteluritos. En particular, quiero agradecer al departamento de Física Aplicada I de la Universidad del País Vasco de Bilbao, y entre ellos especialmente a Adrián Miguel y a la Prof.ª Rolindes Balda, por su colaboración en la caracterización de la respuesta fotoluminiscente de los vidrios.

Quiero también agradecer a Marga Hernández y la Prof.ª Concha Domingo del Instituto de Estructura de la Materia por su disponibilidad y ayuda con las medidas de espectroscopía Raman.

Finalmente, quiero dar las gracias a mi familia, que me ha apoyado siempre a pesar de haber sufrido por la distancia que nos separa y las largas temporadas sin vernos. Y por último, agradezco a mi novio que fue quién más me animó en su día para que hiciera el doctorado y que me ha seguido apoyando a lo largo de estos años.

Fuentes de financiación

Este trabajo se ha desarrollado en el marco de los proyectos de investigación MAT2009-14282-C02-01 y TEC2012-38901-C02-01. Asimismo agradezco a la Secretaría de Estado de Investigación del Ministerio de Economía y Competitividad la concesión de una ayuda FPI (BES-2010-038084).

Table of contents

1

Introduction

1.1 Context

In the year that has been declared by the United Nations as the *International Year of Light*, we stress the importance of **photonics** as the leading light-based technology of the 21st century. Actually, this word derives from the Greek word *φωτός* (phōtos), which means light, and appeared at the end of the 1960s, in analogy with electronics, to describe a field of research based on the use of photons for practical purposes, as electronics is based on electrons [1]. In particular, the term photonics refers to the generation, transmission, amplification, processing, and detection of light from the ultraviolet to infrared spectral regions [1].

Undoubtedly, research in the field of photonics was devoted in the past decades mainly to the development of **optical communication systems** to replace the old electronic communication systems, which were based on coaxial cables to transmit the information between two distant points. Even if high frequency signals can be transmitted in these conductive cables, they present many drawbacks such as a low capacity, large attenuation losses (0.5-1 dB/m), heavy weight, low flexibility, and moreover, they are affected by electromagnetic interference [2]. These drawbacks stem from the characteristics of electrical signals and they can be eliminated when using optical signals to carry the information.

With the invention of the laser [3] and the laser diode [4] in the 1960s, high-coherent and collimated monochromatic light beams became available. However, a low loss medium able to transmit information in the form of light signals was missing. Kao and Hockman were the first who, in 1966, proposed that **glass** was an adequate material to develop low loss dielectric waveguides able to propagate light signals [5], due to the

low scattering and absorption losses of glass. Glass absorption losses in the infrared region are related to the presence of impurities, such as metal and hydroxyl ions, and they can be strongly reduced by using high purity starting chemicals and adequate fabrication procedures [5]. Thus, only few years later, in 1970, low loss optical fibres with intrinsic losses of 7 dB/km, close to Kao's theoretical limit, were demonstrated [6]. However, the fabrication of ultra low loss fibres, having an attenuation of 0.2 dB/km at 1.55 µm, from a P_2O_5-doped SiO_2 glass [7] showed in 1979 that Kao's theoretical limit was conservative. Nowadays, we know that attenuation losses of 0.2 dB/km are close to the real theoretical minimum losses of silica fibres (0.125 dB/km at 1.55 µm). These intrinsic losses stem from Rayleigh scattering and infrared absorption. In addition, residual OH^- impurities generate an extrinsic absorption band at ~1.4 µm as it is illustrated in Fig. 1.1.

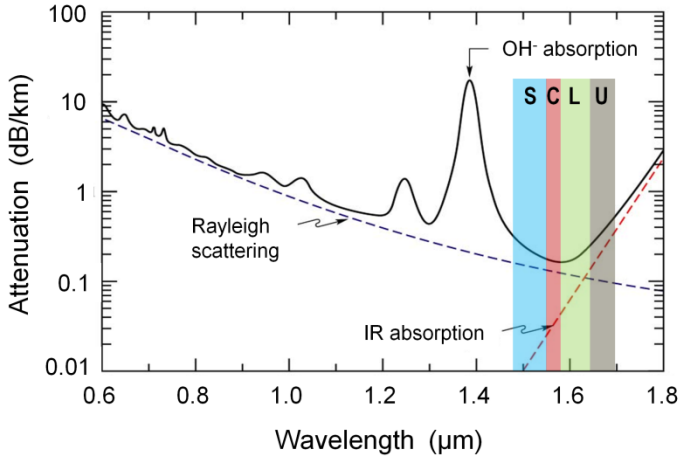

Figure 1.1: Attenuation of a conventional silica fibre as a function of wavelength, adapted from [8]. The spectral regions corresponding to the short (S), conventional (C), long (L), and ultralong (U) wavelengths of the current optical transmission window are indicated in the figure.

With the fabrication of ultra low loss silica fibres, the transmission of optical signals over large distances (up to 50 km) became possible without the need of amplification, but optical-electrical-optical (OEO) repeaters were needed if larger distances wanted to be covered [2]. However, the high cost of OEO repeaters and their low efficiency, *i.e.* each OEO could amplify only the signal at one wavelength, needed to be overcame by replacing them with all-optical amplifiers in order to make optical communications feasible [2]. In 1987, an efficient optical amplifier at 1.54 µm was achieved at last by doping silica fibres with Er^{3+} ions [9]. This was possible thanks to the matching

between the minimum loss region of silica fibres and the main Er^{3+} photoluminescent emission around 1.5 μm. The popular **erbium doped fibre amplifiers** (EDFA) was born. With the use of EDFAs, a transoceanic transmission of 2.4 Gbit/s data over 21000 km was demonstrated in 1995 [10]. A major advantage of EDFAs is that they amplify many wavelengths at the time, thus, they allowed implementing wavelength division multiplexing (WDM) systems to increase the data capacity of optical fibres by dividing the transmission window in several bands, each of them transmitting independent signals [11]. The early WDM systems used the spectral region where the fibre attenuation losses are minimum and the EDFA amplification is maximum (1.53-1.56 μm) for long-haul transmission systems. This was named the conventional band (C-band) [12]. With the development of broadband EDFAs or Raman amplifiers, WDM systems could exploit larger bandwidths around 1.5 μm to increase the data capacity of optical fibres, such as the short (S), long (L) and ultralong (U) transmission bands (Fig. 1.1) [12]. However, the spread of Internet along with the demand for more transmission capacity have boosted an increase of fibre capacity of a factor of ~10 every 4 years, as it is shown in Fig. 1.2, requiring additional systems to WDM ones [13]. Nowadays, optical fibres transmit signals that have been multiplexed in time, wavelength, polarization, and phase (*High spectral efficiency coding*) to send more information than ever before. However, the maximum capacity of 100 Tbit/s per fibre cannot be overcome with the current technology. Thus, new types of fibres and new technologies have to be addressed, such as space division multiplexing (SPD), which is based on optical fibres able of supporting hundreds of spatial modes that can be exploited as parallel channels for transmitting independent signals [13].

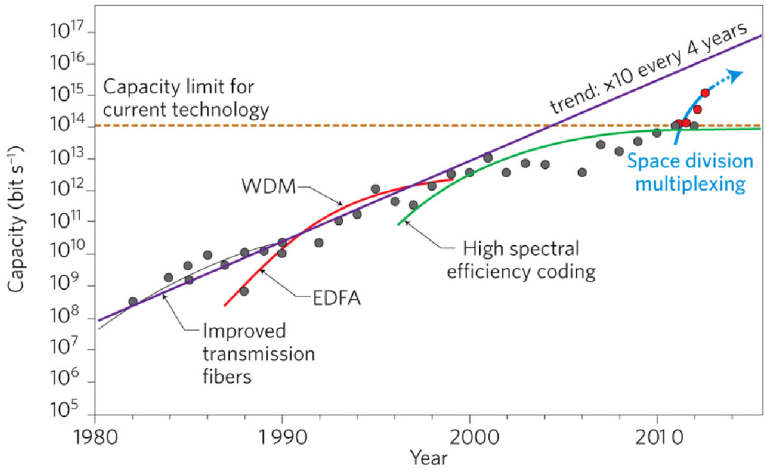

Figure 1.2: Evolution of transmission capacity of optical fibres as evidenced by laboratory demonstrations, from Ref. [13].

Even if optical fibres ensure the transmission of large amounts of data with low losses, the performance of current data networks is limited by the electronics necessary to distribute the data to the final user through the routing, storing and queuing of data packets [14]. The elimination of this bottleneck implies necessarily the replacement of electronic components with optical components that will allow the future development of high-capacity all-optical networks [14]. Moreover, the successful migration from electronic to optical devices is strictly related to the capability of fabrication and integration of multiple optical components such as waveguides, beam splitters, gratings, couplers, polarisers, interferometers, sources, and detectors on a common planar substrate (***integrated photonics***) since this implies size reduction, production costs savings, low power consumption and compatibility with the current fibre technology [15]. For example, the success of EDFA and the advantages of integrated photonics led to strong research efforts to develop Er doped waveguide amplifiers (EDWA) and lasers (EDWL) over the last 20 years [16]. Today, EDWA can enhance light signals on a robust, low-cost, miniature chip, as it is schematically represented in Fig. 1.3.

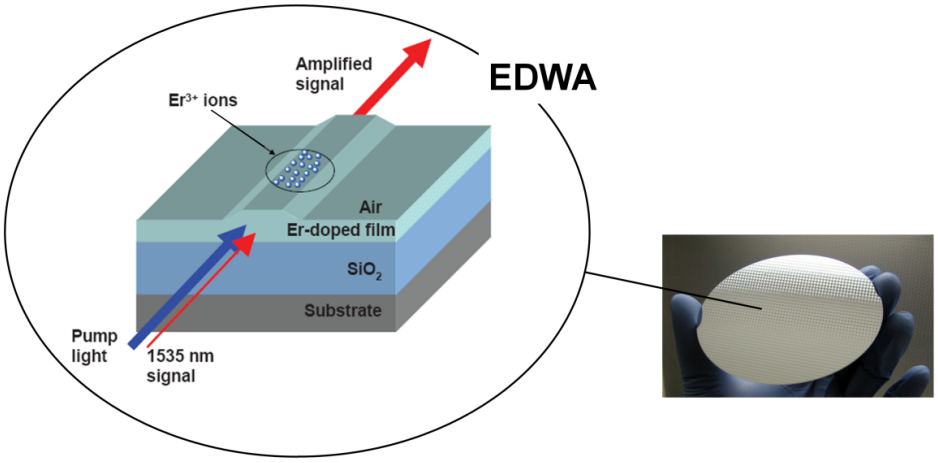

Figure 1.3: Schematic representation of an Er doped waveguide amplifier (EDWA) for integrated applications, adapted from Ref. [16].

With the development of integrated photonic devices, new and ubiquitous applications have emerged in many different fields apart from optical communications, as illumination, information processing, metrology, spectroscopy, holography, bio-medicine, defence, material processing and manufacturing, green-energy, agriculture, robotics, etc. [17]. In this regard, Figure 1.4 illustrates how the European funding dedicated to photonics during 2007-2012 (Framework Programme 7) has been assigned

to many different research areas, health care and biology being the most funded ones [18].

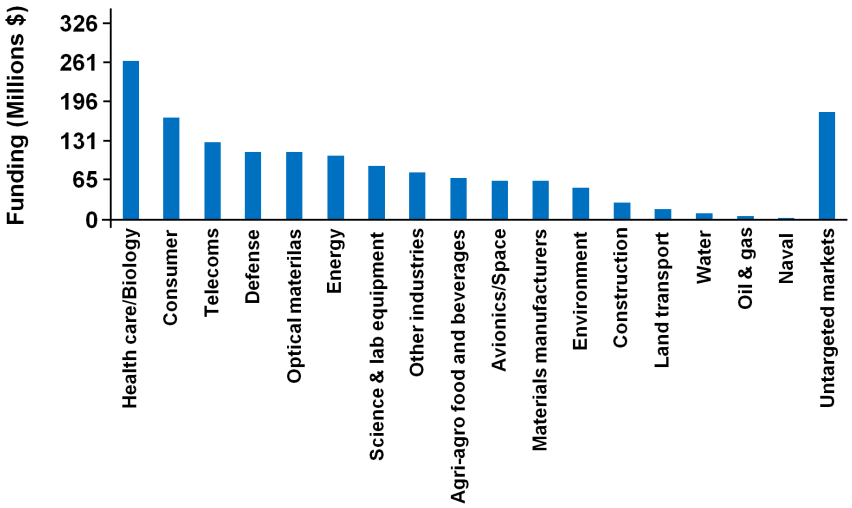

Figure 1.4: Distribution of photonics-related funding in the EU under Framework Programme 7 (2007-2012) [18].

Due to the diversification of photonic applications, new devices are designed for spectral regions that are beyond the near-infrared (0.7-2.0 µm) and comprise the visible (0.4-0.7 µm) and mid-infrared (2.0-15 µm) regions [17]. Applications in the visible include lasers for consumer equipments such as barcode scanners, laser printers, DVD/Blu-ray devices, as well as phosphors for illumination and displays [17]. On the other hand, laser sources in the mid-infrared are of tremendous scientific and technological interest for applications in spectroscopy, bio-medicine, materials processing, and chemical or bio molecular sensing since the strong characteristic vibrations of many important molecules (H_2O, CO_2, CH_4, NO_2, etc.) lie in this spectral region [19]. For instance, mid-infrared laser sources at the fundamental stretching vibration of O-H (2.95 µm) have significant benefits in soft-tissue surgery due to the absence of carbonization and fast ablation rates [20]. Moreover, LIDAR (light detection and ranging) systems employing mid-infrared lasers may be used to detect greenhouse gases (CO_2, CH_4) and pollutants (NO_2) through their characteristic absorption 'fingerprints' [20]. Finally, the two atmospheric transmission windows (3-5 and 8-13 µm) in which the Earth's atmosphere is relatively transparent, can be used for atmospheric, security, and industrial applications such as remote explosive detection, countermeasures against heat-seeking missiles, and covert communication systems [19].

However, the development of integrated photonic devices is a complex task since there is not a unique optical material, as it is silicon for microelectronics, that is suitable for the design and fabrication of different optical components on a single chip [15]. Moreover, adequate materials should not only present the proper optical properties to implement a given function in the desired spectral range, but they should also be compatible with the existing fabrication techniques and integration on microelectronic chips [15]. Therefore, a large number of organic and inorganic materials have been studied to develop integrated photonic devices [21, 22, 23]. Undoubtedly, silicon has been the most researched material to develop integrated photonic devices since it allows using standard semiconductor fabrication techniques and it can be easily integrated with microelectronic chips [24, 25]. However, the principal drawback of Si resides in its indirect bandgap which strongly limits efficient light emission and therefore the achievement of a Si laser at room temperature [25]. Photonic materials based on silicon are out of the scope of this thesis and more information can be found in the review by Pavesi [25] and in the paper by Liang and Bowers on Si lasers [26].

Apart from silicon, glass is obviously among the most promising materials for the development of integrated photonic devices due to its very good optical properties, the ease of preparation and possibility of shaping it in a variety of forms (bulk, fibre, thin film) with a relatively low-cost production [27, 28]. In addition, glass is a very versatile material since its properties[1] can be easily tuned by adjusting its composition and processing parameters in order to meet the requirements for a specific application [27]. In the particular case of optical and photonic glasses, such as these considered in the present thesis, they are required to have good chemical stability, homogeneity, thermo-mechanical properties together with a low absorption and adequate linear and nonlinear refractive indices in the desired wavelength range [28].

Photonic glasses are usually divided in two types: active photoluminescent glasses, and nonlinear glasses [27, 28]. While the nonlinearity is an intrinsic property of glass [29], photoluminescence is obtained by doping glasses with rare earth ions [30]. In this thesis we focus only on **photoluminescent glasses**. The peculiarity of rare earth ions resides in their electronic configuration[2] which presents multiple excited levels that can decay either radiatively or nonraditively. Radiative transitions of rare earth ions cover a broad

[1] Glass properties are described in chapter 2.

[2] The electronic configuration and spectroscopic properties of rare earth ions in solids are presented in chapter 2.

spectral range from the visible to infrared, thus rare earth doped glasses have been employed as optical amplifiers, solid-state lasers, phosphors, etc. [27, 30]. For instance, optical amplifiers for telecommunication have been obtained at 1.5 μm from Er^{3+} doped glasses, as described above, while many solid state lasers at 1.0 μm have been achieved from Nd^{3+} doped glasses thanks to the high efficiency of their emission [30]. Moreover, Er^{3+} presents many excited levels that may decay radiatively in glasses, emitting in the visible and mid-infrared regions [30]. However, the probability of radiative or nonradiative transitions depends mainly on the glass composition and structure, since they determine two important parameters such as the solubility of rare earth ions and the maximum phonon energy of the glass matrix [30]. In particular, glasses with a high rare earth solubility, large linear refractive index and low phonon energy are suitable hosts for rare earth ions since maximize their probability of radiative transitions [30].

Therefore, during the last decades, the research on glass as host for rare earth ions has been focused on the study of novel glass compositions in order to obtain improved rare earth emissions [27]. In this context, **tellurite glasses** have been indicated as promising candidates for developing high-performance integrated active devices [31, 32] and broadband amplifiers or lasers [33, 34], since they present:

i. Wide transparency region in the visible and infrared wavelength range (typically 0.4-6 μm), compared to silicate glasses (0.2-3 μm) [35].
ii. Good thermal stability and corrosion resistance, which are important in glass manufacture [35].
iii. The lowest phonon energy (~800 cm^{-1} vs. ~1100 cm^{-1} of silica glasses) among oxide glasses, which reduces the probability of nonradiative decay through multiphonon relaxation [33, 35].
iv. High linear refractive index and rare earth solubility, which enhances the electromagnetic field at rare earth sites and reduces concentration quenching effects, respectively [35].

As we show in this thesis, the addition of fluoride compounds to the composition of tellurite glasses improves further the efficiency of their photoluminescent emissions. Fluorotellurite glasses present an increased mid-infrared transparency and low OH^- content due to the presence of fluorine that acts as a drying agent [36, 37]. Thus, nonradiative rare earth transitions induced by the high energy vibrations of OH^- groups

are reduced in theses glasses. Finally, fluorotellurite glasses offer a more ionic environment to rare earth ions than tellurite glasses, with the consequent reduction of the probability of their multiphonon relaxation [38].

In addition to the fabrication of novel rare earth doped glasses with improved photoluminescence emissions, another way to enhance rare earth emissions goes through the production of **transparent rare earth doped glass-ceramic** hosts [39, 40]. They can be synthesized through controlled crystallisation[3] [41, 42] of glass, which allows reducing light scattering and producing highly transparent glass-ceramics [43]. These materials show enhanced properties (*e.g.* large absorption and emission cross-sections, high energy transfer rates), compared to their glassy counterparts, when a crystalline phase of the desired nature and structure is generated around rare earth ions [39, 40]. In particular, oxyfluoride glass-ceramics have been indicated as the most promising host for rare earth ions since to achieve high-efficient emissions, since they combine the properties of an oxide glass matrix with those of a fluoride crystalline phase [42, 44]. In such a way, when rare earth ions are segregated in the fluoride crystalline phase, they are found in an ionic environment characterized by a low phonon energy that leads to a strong reduction of nonradiative decay of excited rare earth levels [42, 44]. In this regard, fluorotellurite glasses, which belong to the family of oxyfluoride glasses, are adequate candidate to produce rare earth doped glass-ceramic with improved emissions, as we demonstrate in this thesis.

1.2 Aim and methodology

The Laser Processing Group (LPG) of the *Instituto de Óptica* (CSIC, Madrid) has a well established experience in the production of bulk and thin film glasses for optical applications. In particular, the wide expertise of the group about pulsed laser deposition for fabricating dielectric films with good optical properties [45, 46, 47, 48], has been successfully applied to the synthesis of multicomponent film glasses [49, 50, 51]. Rare earth doped glass films were considered for application as waveguide amplifiers in integrated optical devices [49] while lead-niobium-germanate [52] and

[3] The controlled crystallisation process to obtain glass-ceramics is described in chapters 2 and 5.

tellurite [53] glass films showed a large optical nonlinear susceptibility which make them promising to implement integrated ultrafast optical switches. Moreover, the LPG has been devoted to the study of optical properties of glasses [52, 54], femtosecond laser writing of waveguides in glasses [55, 56] and the study of the photoluminescence response of rare earth doped glasses [50, 57, 58].

The know-how of the LPG on glass fabrication and characterization techniques, together with its knowledge on the relation between the structure and composition of glass with its optical properties, is applied in this thesis in the case of rare earth doped TeO_2–ZnO–ZnF_2 glasses and glass-ceramics.

The starting point of this thesis has been the synthesis and characterization of two different TeO_2–ZnO–ZnF_2 glasses doped with Er^{3+}. The structure, linear optical properties, thermal properties, and visible upconverted and near infrared photoluminescence emissions of these glasses have been studied in order to find the glass composition having the best properties for active applications. Moreover, the glasses have been doped with increasing Er^{3+} content (0.5-3 wt%) to study how this affects their photoluminescence response. The most promising TeO_2–ZnO–ZnF_2 glass host was finally codoped with Er-Yb or Er-Tm with the aim of improving the pumping efficiency of Er^{3+} ions and generating an ultra broad near infrared emission, respectively.

The characterization of rare earth doped TeO_2–ZnO–ZnF_2 glasses settled the basis for the main objective of this thesis, that was the production of transparent rare earth doped TeO_2–ZnO–ZnF_2 glass-ceramics. This was performed by the controlled crystallisation of precursor glass samples in a temperature range indicated by the experimental nucleation and crystal growth curves. Then, the microstructure, optical properties, and photoluminescence response of the transparent Er^{3+} doped TeO_2–ZnO–ZnF_2 glass-ceramics have been studied and compared to those of the precursor glass sample. From these analyses, we have confirmed that large part of Er^{3+} ions are segregated in a fluoride crystalline phase in glass-ceramics. This affects strongly the photoluminescence response of Er^{3+} ions, and in particular the upcoverted red emission.

Finally, the last objective of the thesis has been the fabrication of Er doped TeO_2–ZnO–ZnF_2 thin film glasses. The experience of the LPG on the fabrication of transparent tellurite film glasses by pulsed laser deposition [53] served as starting point to determine the appropriate parameters, such as oxygen pressure and laser fluence, for

successful fabrication of transparent fluorotellurite glass films with good optical quality. Both as-grown and annealed films have been studied and compared to the bulk glass. In particular, the annealed films showed an improver near infrared emission at 1.5 μm while maintaining similar structure and optical properties to those of as-grown films and bulk glass.

1.3 Thesis structure

The work developed in this thesis is structured in seven chapters, whose content is summarized in the following:

- **Chapter 1** corresponds to the present introduction, where the context, the aim, and the methodology of the thesis are described.

- **Chapter 2** focuses on the main properties of glass and rare earth ions in solids. At the end of the chapter some relevant applications of rare earth doped glasses and glass-ceramics are presented.

- **Chapter 3** describes the experimental techniques used in this thesis for the synthesis of bulk and film glasses and for the compositional, structural and optical characterization.

- **Chapter 4** is dedicated to the characterization of rare earth doped TeO_2–ZnO–ZnF_2 fluorotellurite glasses with different Zn/Te and F/O ratios and rare earth (Er^{3+}, Er^{3+}-Yb^{3+}, Er^{3+}-Tm^{3+}) concentration. In particular, the thermal and optical properties along with their photoluminescence response are related to the glass composition and structure.

- **Chapter 5** presents the production and characterization of Er^{3+} doped TeO_2–ZnO–ZnF_2 glass-ceramics. Initially, the chapter focuses on the thermodynamic behaviour of Er doped fluorotellurite glasses in order to design appropriate thermal treatments that lead to transparent glass-ceramic samples. Once this goal is achieved, the structure, optical properties, and photoluminescence response of the produced glass-ceramics are studied.

- **Chapter 6** reports the fabrication of Er doped TeO_2–ZnO–ZnF_2 film glasses by pulsed laser deposition in a dynamic oxygen atmosphere at room temperature. The composition, structure, optical properties, photoluminescence response, and OH^- content of as-grown and annealed films are compared to those of the bulk glass used as target in the pulsed laser deposition.

- **Chapter 7** summarizes the main conclusions of the thesis.

Introducción

El **vidrio** es un material que la humanidad ha utilizado desde hace siglos. Entre sus características destacan su baja absorción y su muy pequeña dispersión de la luz visible. Sin embargo, solo fue a partir del los años 60 del pasado siglo, con el nacimiento de la fotónica [1], cuando se impulsó la investigación de este material con el objetivo de poder propagar la luz con muy bajas perdidas [5]. El desarrollo y fabricación de fibras ópticas con pérdidas de tan solo 0.2 dB/km (a 1,55 μm) [7], y posteriormente, de amplificadores en fibra dopados con erbio (EDFA) [9], basados en la coincidencia entre la región espectral de mínimas perdidas de las fibras de sílice vítrea y la emisión principal de los iones Er^{3+} (a 1,54 μm), hizo posible el empleo de señales ópticas para transmitir la información en los sistemas de telecomunicación.

Actualmente, la investigación en materiales fotónicos está dirigida principalmente a la integración de múltiples componentes ópticos en un único dispositivo para reducir el tamaño y los costes de producción de los mismos [17]. Además, el campo de aplicación de estos dispositivos se ha ampliado desde las comunicaciones ópticas hacia otras áreas como biomedicina, iluminación, defensa, agricultura, energía, etc. [17]. Esto implica que la región espectral para la cual los dispositivos fotónicos deben estén diseñados se haya ampliado desde el infrarrojo cercano (0,7-2,0 μm) al visible (0,4-0,7 μm) y al infrarrojo medio (2,0-15 μm) [17]. Por ejemplo, equipos de consumo tan habituales como impresoras, reproductores DVD, lectores de códigos de barras, etc., emplean láseres visibles mientras que los materiales luminiscentes se utilizan en la fabricación de pantallas y dispositivos de iluminación [17]. Por otro lado, láseres operando en el infrarrojo medio podrían ser empleados en biomedicina, como por ejemplo en cirugía mínimamente invasiva; en el procesado de materiales; en la detección de gases responsables del efecto invernadero, entre otras aplicaciones, ya que en esta región espectral se encuentran las bandas de absorción de moléculas químicas y biológicas tan importantes como las de H_2O, CO_2, CH_4, entre otras. [19]. Además, en el infrarrojo

medio se encuentran dos ventanas de transmisión (3-5 y 8-13 μm) en las cuales la atmosfera de la tierra es poco absorbente, que pueden permitir el desarrollo de sistemas de defensa y de comunicación [19].

Para desarrollar nuevos dispositivos fotónicos o mejorar los que ya existen se han considerado tanto materiales orgánicos como inorgánicos [21, 22, 23]. Entre estos últimos, el **vidrio** presenta algunas ventajas importantes, con respecto a otros materiales, como la facilidad de producción en multíplices formas, con un coste relativamente bajo, además de ser extremadamente versátil ya que muchas de sus propiedades[1] (ópticas, térmicas, mecánicas, etc.) pueden ser ajustadas a la aplicación de interés modificando su composición y su procesado [27, 28]. Si nos centramos en los vidrios ópticos, estos deben poseer: buena estabilidad química, buena homogeneidad, elevada resistencia termo-mecánica y, además, deben presentar una baja absorción y un índice de refracción, lineal y no lineal, con el valor deseado en el intervalo espectral de interés [28]. Por último, según la configuración que presente el vidrio (masivo, fibra, lámina delgada), este podrá ser empleado en dispositivos diferentes. Así, vidrios en láminas delgada, con un espesor de pocas micras, y que se hayan depositado sobre un sustrato plano, son aptos para el desarrollo de dispositivos integrados [15].

Entre las principales aplicaciones de los vidrios en óptica y fotónica destacan las no lineales y las luminiscentes [27]. Mientras la no linealidad es una propiedad intrínseca del vidrio [29], los vidrios fotoluminiscentes se obtienen mediante el dopado con iones activos, como las **tierras raras** [30]. Estos iones se caracterizan por una configuración electrónica[2] con numerosos niveles excitados que al decaer pueden emitir luz en un intervalo espectral que va desde el ultravioleta al infrarrojo medio en función de la tierra rara. La probabilidad de transiciones radiativas o no radiativas[2] de las tierras raras depende principalmente de la composición y estructura del vidrio, que determinan a la vez la solubilidad de estos iones y la máxima energía de fonón de la matriz vítrea [30]. Una alta solubilidad y una baja energía de fonón minimizan la probabilidad de transiciones no radiativas de los iones de tierras raras y en consecuencia maximizan la eficiencia de las transiciones radiativas [27, 28]. Por ello, es fundamental tener en cuenta la composición del vidrio en relación a su dopado con los iones de tierras raras.

[1] Las propiedades del vidrio se describen en el capítulo 2.
[2] La configuración electrónica y las transiciones radiativas y no radiativas de los iones de tierras raras en los sólidos se presentan en el capítulo 2.

Entre los vidrios de óxidos, los **teluritos** poseen la menor energía de fonón (~800 cm^{-1}), así como una alta solubilidad para los iones de tierras raras, un elevado índice de refracción lineal y no lineal, un amplio intervalo de transparencia (0.4-6 μm), además de una buena estabilidad térmica y una elevada resistencia a la corrosión [33, 35]. Por ello, estos vidrios son muy atractivos como matrices para las tierras raras [31]. Además, la introducción del flúor en la composición de los teluritos mejora las propiedades de dichos vidrios, especialmente en lo que se refiere a su dopado con iones de tierras raras. Por un lado, el entorno de los iones de tierras raras se vuelve más iónico, con lo que disminuye el acoplo electrón-fonón que causa el decaimiento no radiativo de los iones de tierras raras [38]. Por otro lado, el flúor actúa como un agente "desecante" durante la fabricación de los vidrios, disminuyendo la concentración de grupos hidroxilos y así la absorción del vidrio en el infrarrojo medio [36, 37]. La reducción de los grupos hidroxilos es también beneficiosa para los iones de tierras raras ya que estos grupos, con su vibración, inducen el decaimiento no radiativo de las tierras raras [30].
Por último, pero no menos importante, los vidrios de fluoroteluritos pertenecen a la gran familia de vidrios de oxifluoruros que es de las más prometedoras para la síntesis de vitrocerámicos dopados con iones de tierras raras altamente eficientes, que combinen una matriz vítrea con las propiedades de los vidrios de óxidos, con una fase cristalina de fluoruros [42, 44]. De este modo, los iones de tierras raras que se encuentran en la fase cristalina "perciben" una máxima energía de fonón muy reducida con respecto a la de la matriz vítrea, aumentando así la eficiencia de sus emisiones rediativas [42, 44].

En esta tesis se estudian los vidrios y vitrocerámicos de fluoroteluritos del sistema TeO_2–ZnO–ZnF_2 como matrices para iones de tierras raras. Además, los vidrios de teluritos han sido previamente estudiados por el Grupo de Procesado por Láser (GPL), demostrando ser candidatos prometedores tanto para aplicaciones lineales como no lineales [52, 54].

El punto de partida del trabajo presentado en esta tesis ha sido la síntesis y la caracterización de vidrios de TeO_2–ZnO–ZnF_2 dopados con Er^{3+} (**Capítulo 4**). Se ha estudiado la estructura, las propiedades ópticas, y la respuesta fotoluminiscente de dichos vidrios en el visible y en el infrarrojo cercano para determinar cuál de ellos era el más prometedor para eventuales aplicaciones activas. Además, se ha estudiado el efecto del aumento de concentración de Er^{3+} (0,5-3,0 % en peso) en la respuesta fotoluminiscente. El vidrio que se ha considerado más prometedor se ha codopado con

Er-Yb u Er-Tm con el objetivo de mejorar la eficiencia de bombeo de los iones Er^{3+} y de generar una emisión de banda ultra ancha en el infrarrojo cercano, respectivamente.

A partir de dicho estudio se abordó el que era uno de los objetivos principales de esta tesis: la producción de vitro-cerámicos transparentes de TeO_2–ZnO–ZnF_2 dopados con iones de tierras raras (**Capítulo 5**). Esta se llevó a cabo mediante cristalización controlada de muestras de vidrio en el intervalo de temperaturas determinado a través del estudio de los procesos de nucleación y crecimiento cristalino. Posteriormente, se estudió la microestructura, propiedades ópticas, y respuesta fotoluminiscente de los vitro-cerámicos transparentes de TeO_2–ZnO–ZnF_2 dopado con Er^{3+} y se comparó con las del vidrio. A partir de estos análisis, se confirmó que gran parte de los iones de Er^{3+} se encuentran en un entorno cristalino de fluoruro en los vitro-cerámicos sintetizados. Este hecho afecta principalmente la emisión visible (a 650 nm) por conversión de energía (*upconversion*) de los iones de Er^{3+}.

El último objetivo de esta tesis ha sido la fabricación de láminas delgadas de vidrios de TeO_2–ZnO–ZnF_2 dopados con Er^{3+} (**Capítulo 6**). La experiencia del GPL en la fabricación de láminas delgada de vidrios de teluritos mediante la técnica del depósito por láser pulsado, ha sido utilizada para determinar los parámetros experimentales para la fabricación de láminas de fluoroteluritos con una muy buena calidad óptica. Sucesivamente, se estudiaron las propiedades y la respuesta fotoluminiscente (a 1,5 micras) de láminas crecidas a temperatura ambiente y de láminas tratadas térmicamente y se compararon con las del vidrio masivo. Los tratamientos térmicos mejoraron notablemente la respuesta fotoluminiscente de las láminas delgadas, sin alterar sus propiedades ópticas y estructurales lo que se ha relacionado con la reducción del contenido de iones hidroxilos en las láminas recocidas.

2

Properties of glass and rare earth ions

2.1 Introduction

A key figure and one of the forefathers of modern glass research was the German scientist Dr. Friedrich Otto Schott (1851-1935). He was one of the first researchers who used scientific methods to study the effects of different chemical elements on the optical and thermal properties of glass. In 1884, Schott established in association with Dr. Ernst Abbe and Carl Zeiss, the *Glastechnische Laboratorium Schott & Genossen* (Schott & Associates Glass Technology Laboratory) in Jena, which manufactured specialized glasses with precisely defined and reproducible properties. This made possible the mass production of powerful microscopes and other optical devices giving to glass the status of relevant optical material. A few decades later, the research in the field of glass acquired an increasing importance as it is witnessed by the establishment of the *International Commission on Glass* by W.E.S. Turner in 1933 *"to promote international collaboration and to spread information throughout the glass community"* [59].

Nowadays the research on glass covers many fields in modern technology. In optics, glass has been and will continue to be the material of choice in *imaging systems* [60]. In this area, the research on high quality imaging system for aircraft and space applications is focused on the development of glasses with low mass density in order to reduce the weight of the optical system [60]. Moreover, microlenses and radial gradient index (planar) lenses have been made possible the production of integrated optical systems [27, 60]. Optical glasses with improved chemical resistance and low thermal expansion coefficient represent another important field of research for optical applications in extreme conditions [60].

Besides to imaging systems, glasses are also the material of choice in ***optoelectronic*** and ***photonic systems*** [21, 27, 28, 60]. For example, in microelectronics, the wavelength of the radiation source used in lithography processes has decreased accordingly with the dimensions of integrated circuits increasing the demand of glass substrates with an improved ultraviolet transmission in order to increase the diffraction limit of the system [60]. Glass substrates are also replacing traditional aluminium substrates for developing magnetic discs with high density storage capacity due to their very high surface smoothness [60]; while glasses with a large nonlinear refractive index have been proposed as ultrafast light modulators or switches in optical circuits [27, 28].
Finally, active photoluminescent glasses, that are obtained by doping glasses with rare earth ions, have played and still play a major role to produce optical amplifiers, solid-state lasers, phosphors, etc. [27, 30]. Moreover, the spectroscopic properties of rare earth ions are strongly related to the structure and optical properties of the glass.

Since this thesis is devoted to the study of rare earth doped glasses, we will first describe the principal properties of glasses, to stress their uniqueness as optical material. Then, we will focus on rare earth ions in solids, with special emphasis on the relation between the properties of the host material (*e.g.* crystalline/amorphous, refractive index, phonon energy, *etc.*) and the spectroscopic properties of rare earth ions. Finally, we will briefly illustrate how the choice of the glass composition and the modification of its structure, *i.e.* glass-ceramics, have been employed to achieve improved rare earth ions emissions.

2.2 Structure and properties of glass

The most relevant properties of glass are undoubtedly its optical properties, quantified by means of its refractive index, dispersion and transmission. However, these properties are largely determined by the chemical composition of glass and, to a lesser degree, by the fabrication method employed (*e.g.* melt-quenching, chemical vapour deposition, *etc.*) since they affect the structure of glass and determine how this interacts with light. Therefore, we first describe how glass is produced from a fast cooling melt and then we focus on the glass structure and how it affects the optical properties of glass.

2.2.1 Thermodynamic properties

Glass can be defined as a ***super-cooled liquid***, which is in a thermodynamically metastable state and it has a viscosity larger than 10^{14} dPa [59]. This definition is strictly related to the most common way to produce glass, that is through a fast cooling of a homogeneous melt. This thermodynamic process can be described by considering the volume-temperature curve shown in Fig. 2.1.

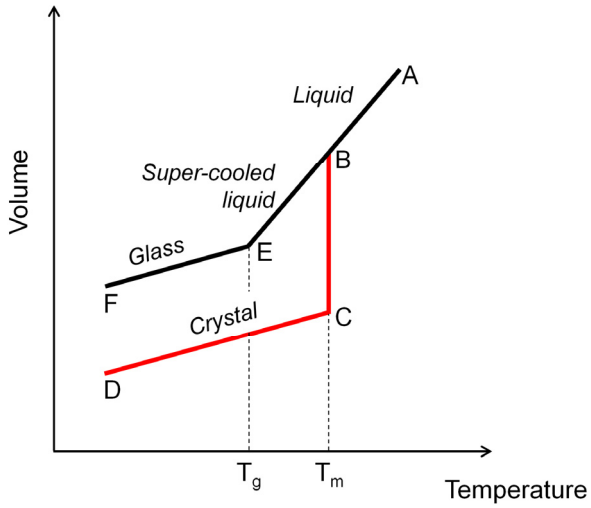

Figure 2.1: Volume-temperature curves for the formation of glass and crystal from a melt.

When a melt is cooled from a high temperature, its volume diminishes in a continuous way until it reaches the **melting temperature** T_m (line A-B in Fig. 2.1). At this temperature, if the cooling rate is slower than the crystal growth rate, the melt goes

through the region B-C in Fig. 2.1 and undergoes a contraction. Then further cooling of the melt can generate a solid crystalline material (line C-D in Fig. 2.1). But, if the cooling rate is faster than the crystal growth rate, the melt passes T_m without crystallising and becomes a super-cooled liquid (line B-E in Fig. 2.1). The transition between a super-cooled liquid to a solid glass (point E in Fig. 2.1), which corresponds to a high value of viscosity (~10^{14} dPa), occurs at a temperature that is called the **glass transition temperature** $\boldsymbol{T_g}$. This temperature is not constant for a given glass but it depends on its cooling rate. In fact, a rapid cooling will produce a glass with a higher T_g and therefore, it will present a higher volume and a more open structure than a slowly cooled melt. Typically, optical glasses are reheated at a temperature close to T_g to reduce strains formed by non-uniform volume changes during the fast cooling of the melt. At this temperature, the atomic arrangement of glass is modified and strains are reduced through a process known as *structural relaxation* [59].

The transformation from a glass to a viscous liquid is reversible and it occurs when the glass is heated at a temperature higher than T_g. Moreover, in the temperature range between T_g and T_m, the glass can crystallise if the duration and temperature of the annealing are adequate. The crystallisation of glass is an exothermic process, *i.e.* it releases energy. The optimal temperature for glass crystallisation, known as **crystallisation temperature** $\boldsymbol{T_c}$, is the one for which the crystal growth rate is maximum. However, the crystallisation of glass is a process that usually occurs in two steps. First, when the glass is reheated, submicroscopic clusters of atoms, arranged in a periodic manner, are formed (nuclei); then, nuclei become crystals once they reach a critical size. Nuclei formation is named **nucleation** while their growth is the **crystal growth**. Figure 2.2 illustrates the temperature dependence of nucleation and crystal growth rates in glasses [41].

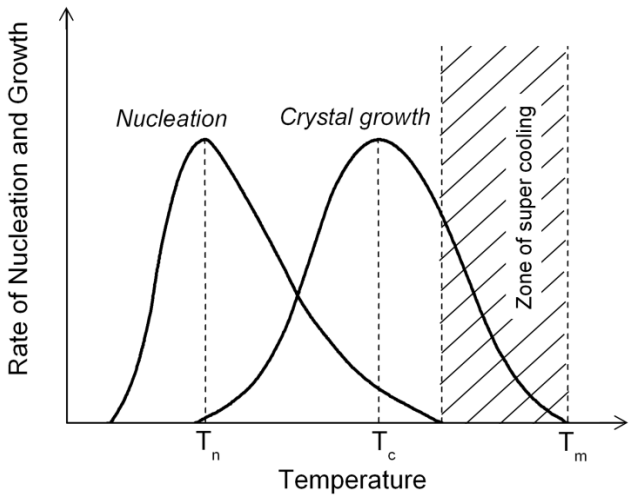

Figure 2.2: Schematic representation of nucleation and crystal growth rates in glasses as a function of temperature. The dashed region represents the zone of super cooling of the melt.

The nucleation rate is limited by viscosity at low temperatures, close to T_g, while the crystal growth rate is limited by the lack of thermodynamic driving forces close to T_m. Moreover, the two curves may overlap in a temperature range where the nucleation and crystal growth processes occur at the same time. The maximum nucleation rate is reached at the optimal temperature of nucleation (T_n in Fig. 2.2) while the temperature at which the nucleation curve reaches zero defines the start of the *zone of super cooling* (Fig. 2.2).

The knowledge of nucleation and crystal growth rates as a function of temperature is fundamental both to avoid the crystallisation of glass during its manufacture and to design thermal treatments able to induce a controlled devitrification of glass. In the last case, **glass-ceramic** materials can be produced, which consist of a glass matrix in which a crystalline phase is dispersed. The interest in these materials arises from their unique properties, such as high thermal resistance and mechanical strength or improved electrical and optical response, with respect to both crystalline ceramics and glasses [43, 61]. At the end of the chapter we will focus on the properties of active glass-ceramics, with special emphasis on rare earth doped oxyfluoride glass-ceramics.

The properties of glass-ceramics depend mainly on their microstructure: the type of crystals and their morphology, as well as the chemical composition and physical properties of the residual glass. Nucleation plays the major role in determining the microstructure of glass-ceramics and, therefore, it has been the focus of extensive

research for decades [62]. Nucleation can be classified as *homogeneous* or *heterogeneous*. In homogeneous nucleation, nuclei form in the absence of any phase inhomogeneity, surface borders or interfacial boundaries. On the contrary, heterogeneous nucleation starts at interface boundaries and surfaces and is catalyzed by the presence of foreign impurities and nucleating agents, as introduced by Stookey during the 1950s [63]. Another classification of nucleation is related to where the crystals are nucleated first. In *bulk or volume nucleation*, crystals are first nucleated in the glass volume while in *surface nucleation* they are first nucleated on the glass surface. Fundamental studies on nucleation and crystal growth in glass melts are often restricted to *isochemical* systems, where the crystal phase which is formed has the same chemical composition of the amorphous phase [64]. Thus, little is known on the nucleation and crystal growth mechanisms in multi-component glasses, which are usually *non-isochemical* systems [41].

Finally, there are two important parameters that are commonly used to characterize the thermodynamic behaviour of glass. They are: the ***glass-forming ability*** and the ***glass stability***. The glass-forming ability relates to the ease of forming a glass by cooling a melt while avoiding its crystallisation. A quantitative measure of glass-forming ability is based on the critical cooling rate, that is the slowest cooling rate (R_C) at which a glass can be produced [65]. For example, pure tellurite glasses are difficult to obtain due to their high critical cooling rate [66]. In fact, while most glasses are formed by cooling a melt at a rate between 1-5 ºC/min., pure tellurite glasses could be formed only at a minimum cooling rate of 20 ºC/min [67].

The glass stability is defined as the resistance of glass towards devitrification during reheating, especially above the glass transition temperature T_g. A quantitative measure of glass stability is given by ($T_c - T_g$), where T_c and T_g are the crystallisation and the glass transition temperature, respectively. T_c and T_g can be determined by differential scanning calorimetry (DSC) or differential thermal analysis (DTA) measurements, which will be described in the next chapter. It must be noted that T_c depends on the heating rate in DSC/DTA measurements as well as on the particle size of glass sample used in the case that glass nucleates from the surface. Therefore, the glass stability is not an unambiguous value [41, 65].

The glass-forming ability and the glass stability are relevant properties in technological applications which involve glass manufacture. For example, they have to be taken into

account when producing optical fibres by heating preforms. In fact, if devitrification occurs during glassmaking, then the preforms will be flawed and unusable; whereas if the glass stability ($T_c - T_g$) is too small, then fibre drawing will not be possible without glass crystallisation.

2.2.2 The *vitreous* state

Another definition of glass refers to its structure and is that of a noncrystalline solid that shows a glass transition [27]. In fact, the atomic arrangement of glass lacks of a long range order as liquids; but, contrary to them, it is solid at room temperature. Besides, contrary to crystalline materials, there is neither crystal lattice nor lattice point in the structure of glass and thus, its X-ray diffraction (XRD) pattern presents a broad halo instead of the characteristic diffraction peaks of crystalline materials.

Early theories on the glass structure considered that glass was an aggregate of very small crystals embedded in amorphous regions [59]. However, structural analysis of vitreous SiO_2 and GeO_2 by XRD made by Warren in 1930 [68], showed that the structure of glass was typical of a noncrystalline solid. In such a way, Warren established the fundaments of the glassy state which was later generalized by Zachariasen, who introduced the ***random network theory*** on the atomic arrangement of glass. This theory considers that the structural units of glass and crystal are the same, but they are connected in different ways [69]. In his own words:

> *"The atoms in glass are linked together by forces essentially the same as in crystals. Over large ranges of temperature the atoms are oscillating about definite equilibrium positions. As in crystals extended three-dimensional networks are formed. The principal difference between a crystal network and a glass network is the presence of symmetry and periodicity in the former and the absence of periodicity and symmetry in the latter."*

We can illustrate this model with the case of silica glass. The structural units that form the structure of amorphous silica (fused silica) and crystalline silica (quartz) are the same SiO_4 tetrahedra. But, they are randomly connected in fused silica, whereas they possess a periodic arrangement in quartz, as shown in the schematic representation of Figure 2.3. However, the structure of glass exhibits a ***short range order*** (up to few Å), due to the chemical bonding constraints in local atomic polyhedra. For example, in

silica glass every silicon atom is coordinated to 4 oxygen atoms in each SiO_4 tetrahedral unit and the Si-O bond length shows only small variations in the entire structure, as shown by X-ray scattering and neutron scattering analysis [68, 70]. Moreover, besides the short range order in the glass network, some authors have also addressed a *medium range order* (extending up to ~20 Å) in some glasses, that is represented by how the neighbouring structural units, *i.e.* cation-centred tetrahedra or pyramids, are positioned and oriented [71, 72, 73].

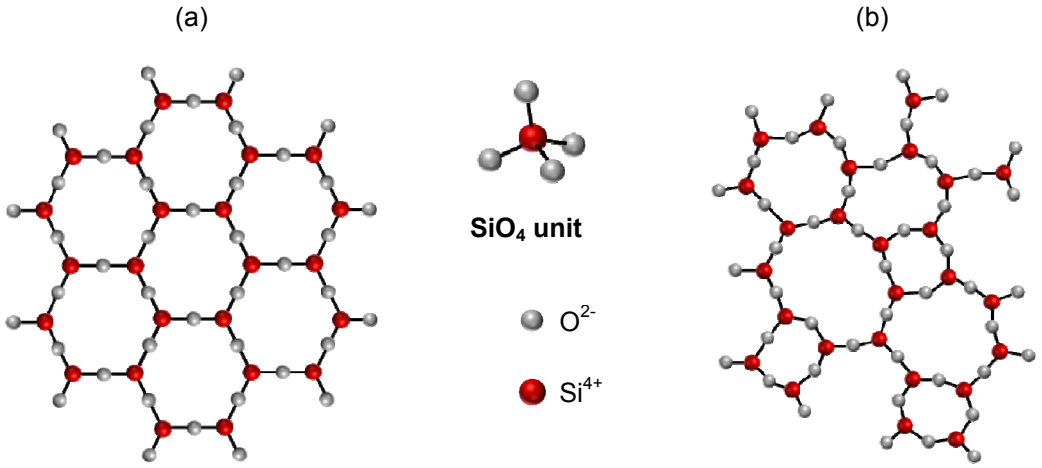

Figure 2.3: Two-dimensional schematic representation of the atomic arrangement of: (a) crystalline SiO_2; (b) glassy SiO_2. A fourth oxygen atom, here omitted for clarity, is bonded to each silicon atom either under or above the plane.

A variety of inorganic compounds such as oxides, halides and chalcogenides are able to form glass. The principal component of a glass is the ***network former*** which constitutes the backbone of the glass structure. In principle, a glass can be formed by only one chemical compound, *e.g.* SiO_2 in fused silica (Fig. 2.3). In this case, oxygen ions act as bridges between the structural units, *e.g.* SiO_4 tetrahedra, and thus, they are called *bridging oxygens* (BO). However, in multi-component glasses, other compounds are added in a small percentage to modify the properties of the glass. They are called ***network modifiers***. They participate in the glass network by occupying thermodynamic stable sites or by replacing some of the network formers. The introduction of network modifiers breaks the glass network and leads to the creation of *non-bridging oxygens* (NBO): contrary to BO, they are negatively charged and are connected to the glass network only at one end. As an example, Figure 2.4 represents a scheme of the binary sodium silicate glass where Na_2O is the network modifier [74]. The braking of Si-O-Si bonds leads to the creation of NBO ions.

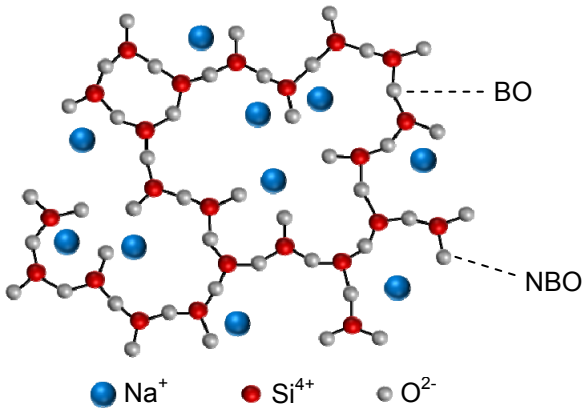

Figure 2.4: Schematic representation of the atomic arrangement of a sodium silicate glass [74]. SiO_2 is the network former while Na_2O is the network modifier. The introduction of Na_2O generates NBO (non-bridging oxygens) while BO (bridging oxygens) connect two Si^{4+} ions in the network. In the sketch are represented only the bonds between the SiO_4 units.

The introduction of network modifiers and the formation of NBO decrease the connectivity of the glass network which becomes more flexible and less strong [27]. Therefore, the short range order in the glass network is altered by the introduction of network modifiers. The structural modifications induced by the compositional changes affect the macroscopic properties of glass such as its chemical resistance, transmittance, and ability to fiberisation, among others [27]. The correlation between the chemical composition of glasses, their structure, and their macroscopic properties is on the basis of modern glass science. In particular, we will focus in this thesis on zinc tellurite (TeO_2–ZnO) glasses with partial substitution of ZnO with ZnF_2. In this glass system TeO_2 is the glass former and ZnO and ZnF_2 are the glass modifiers. In chapter 4 we will discuss how the relative content of glass modifiers affects the optical properties of TeO_2–ZnO–ZnF_2 glasses.

2.2.3 Optical properties

Glass has been extensively used for various optical components for many centuries due to its very high transparency in the visible region of the electromagnetic spectrum. In this regard, Galileo built a telescope at the beginning of the XVII century, using only 38 mm lenses and a 1 m long wooden tube (Figure 2.5).

This simple instrument made possible the observation of the Moon, the closest planets, and the Sun, thus providing evidences on the role of the Earth in the Solar system.

Figure 2.5: Galileo's first telescope (*Museo Galileo*, Florence).

The origin of the optical properties of glass is found in its microstructure. Actually, when the glass is free from defects, it has very low intrinsic scattering losses since there are not grain boundaries or interfaces within its volume. However, a small contribution to Rayleigh scattering is always present in glass due to local variations in its density and composition [27]. The **transparency region**, or low absorption loss region, of glass is determined by its two *intrinsic absorption edges* in the ultraviolet and infrared regions [75]. Electronic transitions from the valence band to the conduction band happen when the electromagnetic energy matches the band-gap energy of glass. This high energy (short wavelength) defines the absorption edge of glass in the ultraviolet. On the other extreme of the transparency region, the lowest energy (high wavelength) that generates atomic and molecular vibrations in glass corresponds to the glass absorption edge in the infrared region. Apart from ultraviolet and infrared intrinsic absorption losses (α_{in}), which depend on the composition and structure of glasses, *extrinsic absorption losses* (α_{ex}) may also be present due to the presence of impurities such as transition metal ions and water (OH^-) [75]. Thus, optical glasses are produced from the purest chemical reagents to minimize the value of α_{ex} [27].

As an example of the importance of the composition and structure of glass on its optical properties, Figure 2.6 compares the transparency region of silica and tellurite glasses.

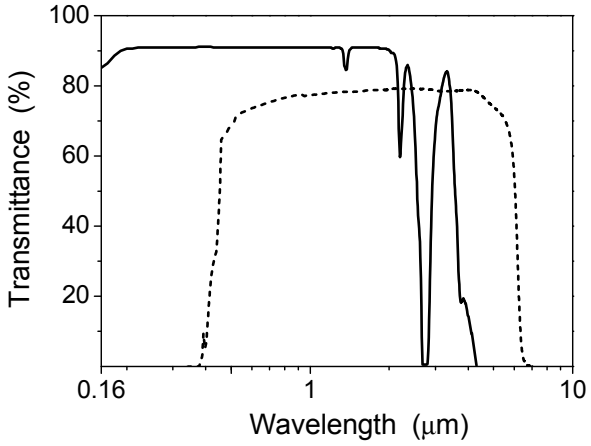

Figure 2.6: Transmittance (%) of silica (—) and tellurite (---) glasses. Intrinsic absorption edges are observed for the tellurite glass while the absorption band due to the presence of OH^- is observed in the spectrum of the silica glass in the 2-3 μm range.

Silica glass shows a higher transmittance than tellurite glass in the ultraviolet and visible spectral regions; but its transparency in the infrared region ($\lambda > 2$ μm) is strongly limited by intrinsic and extrinsic losses. On the contrary, the tellurite glass shows a red shifted UV absorption edge (~400 nm) but its transparency region extends in the infrared up to 5 μm.

In addition to transparency, another fundamental optical property of glass is the **refractive index** which, at the macroscopic scale, accounts for the velocity and bending of light, *i.e.* refraction, when it passes from one medium to another. At the microscopic scale, the refractive index is correlated with the electric dipole moment (p) generated by the interaction between the electromagnetic field (E) of the incident beam and the glass atoms. The two major factors which contribute to the refractive index value (n) are the glass density (ρ) and the glass polarizability ($\alpha = p/E$), which are connected one to the other by the Lorentz-Lorenz formula [76]:

$$\frac{n^2 - 1}{n^2 + 2} = \frac{4\pi}{3}\frac{N_A \rho}{M}\alpha \qquad (2.1)$$

where M is the molar weight and N_A is the Avogadro number. This relation holds when the macroscopic polarization induced in the medium (P) is proportional to the electric field by the linear electric susceptibility tensor ($\chi^{(1)}$): $P = \chi^{(1)}E$. However, when the intensity of the electric field E is very high, for example in the case of laser beams, higher order terms have to been take into account in the relation between P and E. Then, P is expressed as a power series of the field strength E as [77]:

$$P = \chi^{(1)}E + \chi^{(2)}E^2 + \chi^{(3)}E^3 + \cdots \quad (2.2)$$

For simplicity, *P*, *E*, and the n-order susceptibility $\chi^{(n)}$ are scalar quantities in eq. 2.2. However, in a more general notation $\chi^{(n)}$ are tensors and *P* and *E* vectorial fields [77]. The coefficients $\chi^{(2)}$ and $\chi^{(3)}$ in eq. 2.2 are the second-order and the third-order nonlinear susceptibilities, related to second and third order nonlinear effects, respectively; while other components of the nonlinear susceptibility with order higher than three are negligible [76]. However, in *centrosymmetric* isotropic materials, such as glasses, which possess inversion symmetry, $\chi^{(2)}$ is equal to zero since polarization changes in opposite directions compensate each other [27]. On the contrary, third-order nonlinear optical interactions can occur both in centrosymmetric and noncentrosymmetric media. The principal third-order nonlinear effect is the **Kerr effect**, that is the dependence of the refractive index on the intensity of the applied light (*I*) or, in other words, the anisotropic refractive index induced in a transparent medium by a strong electric field [78]:

$$n = n_0 + n_2 I \quad (2.3)$$

In eq. 2.3 n_0 is the linear refractive index and $\boldsymbol{n_2}$ the **nonlinear refractive index** (in m^2/W or *esu*, depending on the system of units used). The third-order nonlinearity is present in all glasses and it is a non-resonant intrinsic effect when the wavelength of excitation is larger than the band-gap wavelength. The nonlinear refractive index is mostly due to electronic contribution, *i.e.* anharmonic terms of the polarization of bound electrons [78]. The response time of the nonlinear optical effect is ultrafast (~fs) and, for this reason, optical glasses having high nonlinear optical susceptibility have been proposed as ultrafast photonic switches [79]. Usually, optical glasses with a large linear refractive index and high dispersion are good candidates as nonlinear optical materials [80]. On the other side, glasses with a low nonlinear refractive index are needed in high power laser applications in order to avoid self-focusing effects and the damage that these induce [27].

In summary, glass is an optically isotropic material that is usually also chemically and thermally stable. In addition, the optical and structural properties of glass may show large variations depending on its composition and fabrication process. Thus, it is possible to tune the glass properties in order to meet the requirements for the desired

application. In particular, for active applications of rare earth doped glasses, it is important to take into account the glass structure, which determines the maximum phonon energy of the glass network and the environment of rare earth ions.
In the next sections, we recall the basic fundamentals on the electronic and spectroscopic properties of rare earth ions in solids. We will focus on the relation between the probability of radiative and nonradiative transitions of rare earth ions and the structure of their host material.

2.3 Electronic and spectroscopic properties of rare earth ions in solids

Traditionally, the term **rare earth** (RE) **ions** refers to trivalent lanthanide ions (**Ln^{3+}**) with partially filled 4*f* orbitals, whose electronic *f-f* transitions are of interest in optical applications: from cerium (Ce, Z= 58) to ytterbium (Yb, Z= 70). Even if "rare earth" is a misnomer because lanthanides, except promethium (Pm), actually are not rare elements, this term is widely employed in the optics community and so it will be used in this thesis.

The study of RE ions began at the end of the 19th century when lanthanide optical spectroscopy was employed by chemists such as Sir Crookes, Lecoq de Boisbaudran, and Demarçay to test the purity of their crystallisations [81]. The characteristic luminescence spectra of lanthanide ions allowed Lecoq de Boisbaudran to discover gallium, samarium and dysprosium. Some years later, Demarçay isolated europium from a contaminated samarium sample. The interest in the absorption and emission transitions of Ln^{3+} ions in crystalline solids led Van Vleck in 1937 to analyze the physical mechanisms involved in order to explain the experimental results [82].The principal characteristic of Ln^{3+} ions is that they absorb and emit light in a broad range of wavelengths: from ultraviolet (Gd^{3+}) to visible (e.g. Pr^{3+}, Sm^{3+}, Eu^{3+}, Tb^{3+}, Dy^{3+}, Tm^{3+}, Er^{3+}, *etc.*) and infrared (*e.g.* Er^{3+}, Yb^{3+}, Ho^{3+}, Nd^{3+}, *etc.*) wavelength range [81]. Moreover, the characteristics of their emissions depend strongly on the material where they are found [21].

The optical absorption and emission spectra of Ln^{3+} ions originate from intrashell 4*f* electronic transitions between different energy levels related to the 4*f* orbitals. Therefore, the understanding of photoluminescence emissions of Ln^{3+} ions requires a deeper analysis of the electronic configuration of these ions. The neutral electronic configuration of lanthanides is, with minor exceptions, $[Xe]4f^{(n+1)}6s^2$. Upon their incorporation in a host, they are normally found in the trivalent oxidation state (Ln^{3+}) after losing their weakly bounded $6s^2$ and usually one 4*f* electron. The usual electronic configuration of Ln^{3+} ions is therefore: $[Xe]4f^n$, being *n* the number of 4*f* electrons (from 1 to 13). Depending on the number of 4*f* electrons, these can be distributed in different energy levels, which basically arise from electron-electron and electron-host interactions [81].

In this thesis we adopt the **Russell-Saunders**, or ***LS***, coupling scheme [83] to label these energy levels. Following the notation of this coupling scheme, each energy level that can be occupied by 4*f* electrons in Ln^{3+} ions is denoted as $^{2S+1}L_J$, where:

- ***S*** is the total spin angular momentum;
- ***L*** is the total orbital angular momentum;
- ***J*= *S*+*L*** is the total angular momentum.

L and ***S*** are the vector sums of the orbital and spin quantum numbers for all the 4*f* electrons of a given Ln^{3+} ion, respectively. The splitting into several energy levels of a single 4*f* level, representing the central field approximation[1], stems from electron-electron and electron-host interactions. As an example, Fig. 2.7 shows the energy diagram of Eu^{3+} which illustrates the interactions leading to the splitting of electronic energy levels.

[1] In this approximation each electron is assumed to move independently in a spherical and symmetric potential due to the contribution of the nucleus and all other electrons. The quantum numbers L, S, and J are degenerated in the central field approximation.

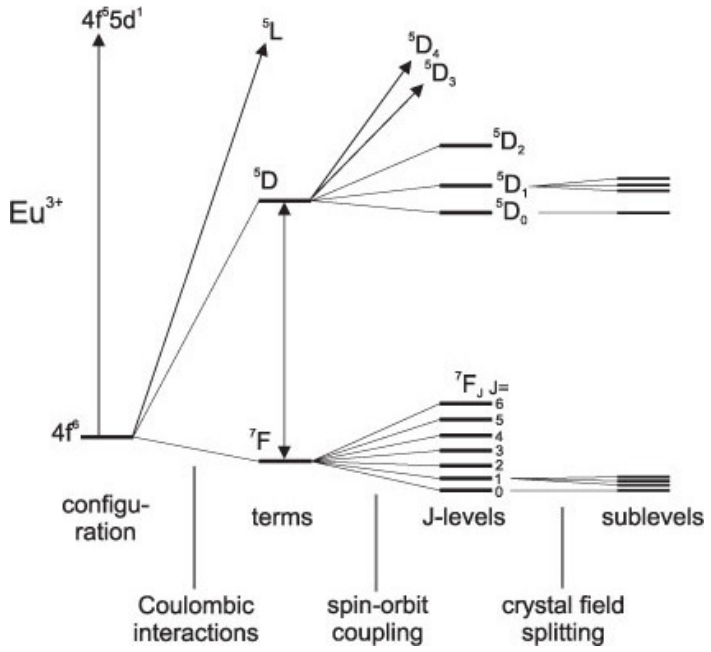

Figure 2.7: Energy level diagram of Eu^{3+} with the interactions leading to the splitting of electronic energy levels.

First, Coulomb, or electrostatic, interactions between 4*f* electrons lift the angular degeneracy and produce the ^{2S+1}L energy levels (LS terms), separated by an energy of ~10^4 cm^{-1}. Then, the spin-orbit coupling, the strongest of magnetic interactions, lifts the degeneracy in the total angular momentum (J) and splits the LS terms into J levels ($^{2S+1}L_J$), separated by ~10^3 cm^{-1}. The J levels represent the energy levels of a Ln^{3+} free ion. However, when the ion is in a host, electron-host interactions further split the J levels into Stark sublevels, due to the effect of the electric field of the matrix (crystal field effect) [30]. This effect is quite small, compared to the previous ones, and shifts the J levels only few ~100s cm^{-1} since the 4*f* orbitals are shielded from the environment by the filled 5*s* and 5*p* sub-shells. This is an important characteristic in the spectroscopy properties of rare earth ions, since they maintain an atomic-like energy level structure even when they are incorporated in a host material [30].

Nevertheless, the crystal field induced by the host is what determines the shape of the absorption and emission spectra of Ln^{3+} ions [30]. The most relevant spectroscopic difference is observed when comparing the spectra of RE ions in crystals and glasses. In the first case, the absorption and emission bands have a very narrow bandwidth, even at room temperature. On the contrary, the spectra of RE ions in glasses show a broad bandwidth at room temperature. Two processes are responsible for the spectral broadening of Ln^{3+} ions in noncrystalline solids [30]. The first is caused by lifetime

broadening due to phonon-induced transitions among Stark components of the same J level. Since this process is the same for each Ln^{3+} ion in the host, it is referred as *homogeneous* broadening. Instead, the second process stems from the differences in the sites occupied by Ln^{3+} ions in the host, and thus, each Ln^{3+} experiences a different crystal field. In this case the process is termed *inhomogeneous* and the spectral broadening is the result of the energy distribution of each Stark sublevel.

To conclude, Fig. 2.8 shows the energy levels of the thirteen trivalent lanthanide ions in a silicate glass [84].

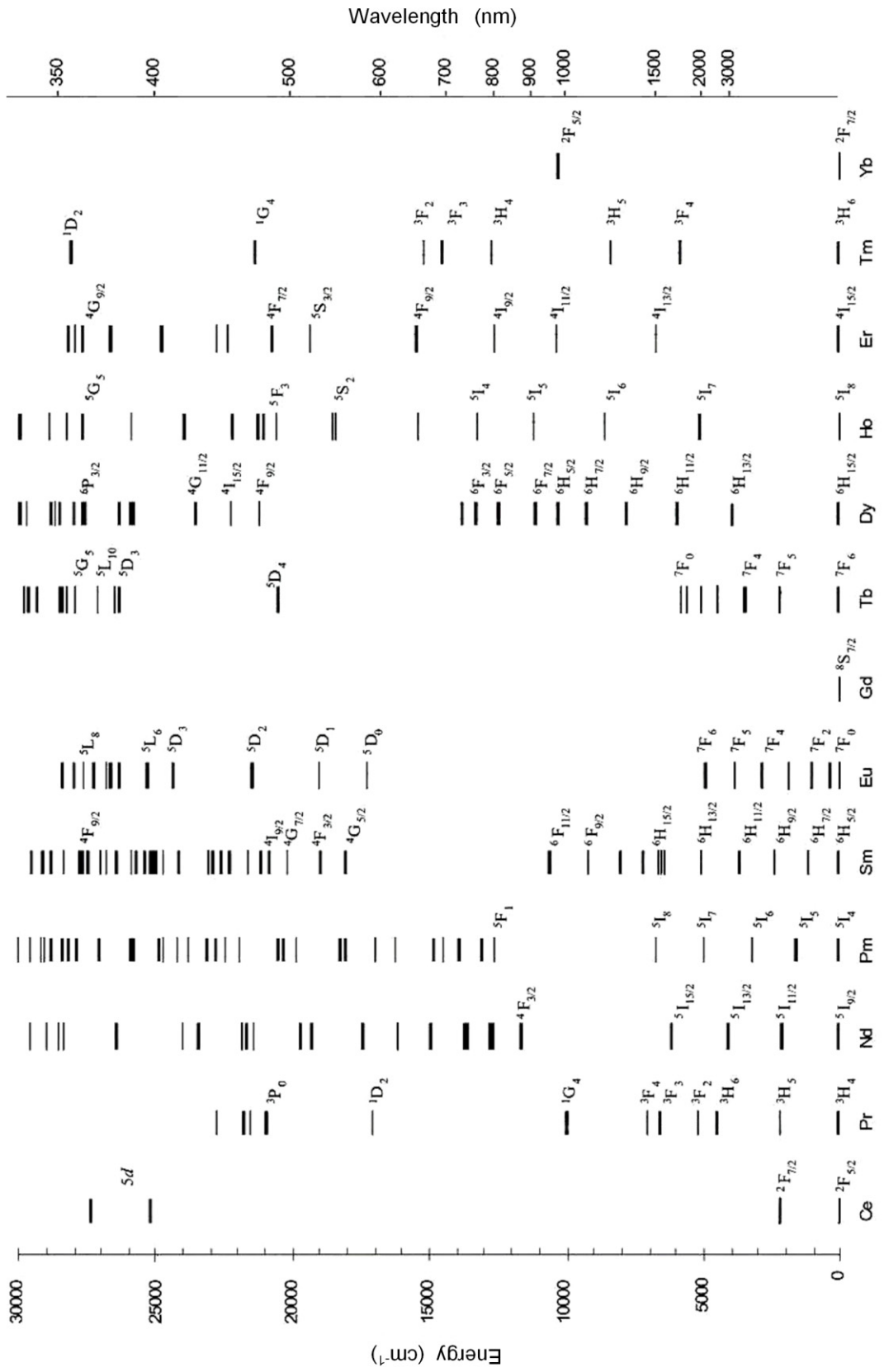

Figure 2.8: Energy level diagram of trivalent RE ions in a silicate glass. Adapted from Ref. [84].

2.3.1 Radiative transitions

Absorption of photons with an adequate energy promotes 4*f* electrons of Ln^{3+} ions from the ground level to a higher energy level. Then, the decay of excited 4*f* electrons from the high energy level to a lower energy one can generate emission of photons. In this case, the intrashell 4*f* transition is called *radiative*. On the contrary, when the deexcitation is not accompanied by light emission, the transition is called *nonradiative*. We have seen in the previous sections that the electronic configuration of Ln^{3+} ions is little affected by their host; but the probability of radiative and nonradiative 4*f* transitions is strongly affected by their environment. Thus, the choice of an adequate host material is very important in relation with the photoluminescence response of rare earth ions.

In this section we recall the parameters commonly used to characterise the radiative transition of rare earth ions and that will be employed in the next chapters.

According to Laporte's parity selection rule, ***electric dipole*** (ED) *f-f* transitions should be forbidden in Ln^{3+} ions since they are between states with the same parity [85]. However, they become partially allowed when the Ln^{3+} ion is under the influence of a ligand field. This last generates non-centrosymmetric interactions which mix electronic states of opposite parity into the 4*f* wavefunctions, thus relaxing Laporte's selection rule [85]. The partially allowed ED transitions are therefore called *forced* or induced. Apart from *forced ED transitions*, other types of *f-f* transitions are possible in Ln^{3+} ions. They are: *magnetic dipole* (MD) and *electric quadrupole* (EQ) transitions, that are parity allowed. However, the low symmetry of sites occupied by Ln^{3+} ions in glasses makes MD and EQ transitions weaker than forced ED transitions [27, 30, 85].

If we define $A_{r,ab}$ ($A_{nr,ab}$) as the probability of a spontaneous radiative (nonradiative) transition between two energy levels *a* and *b* of a given Ln^{3+} ion, each of them characterized by their *L*, *S*, and *J* quantum numbers; then, the fraction of excited Ln^{3+} ions at time t ($N(t)$) can be estimated through the equation [27]:

$$\frac{dN(t)}{dt} = -\left(A_{r,ab} + A_{nr,ab}\right)N(t) \tag{2.4}$$

The solution to eq. 2.4 is:

$$N(t) = N(0)e^{-\left(A_{r,ab} + A_{nr,ab}\right)t} = N(0)e^{-\frac{t}{\tau_{obs}}} \tag{2.5}$$

With:

$$\tau_{obs} = \frac{1}{A_{r,ab} + A_{nr,ab}} \tag{2.6}$$

where τ_{obs} is the observed, or experimental, **lifetime** of the spontaneous emission $a \rightarrow b$ that describes the decay of electrons from the excited level a to the lower energy level b. The inverse of the lifetime is commonly called the *decay rate*. In the absence of nonradiative decay processes ($A_{nr,ab}$ = 0), the **radiative lifetime** is defined as: τ_{rad} = $1/A_{r,ab}$. An important parameter used to characterise the efficiency of radiative transitions is the **quantum yield** (Q) that is related to the ratio between the number of emitted photons to the number of absorbed photons per unit time [27, 86]:

$$Q = \frac{\tau_{obs}}{\tau_{rad}} \tag{2.7}$$

The maximum quantum yield for a radiative transition is equal to 1, when τ_{obs} = τ_{rad} ($A_{nr,ab}$ = 0).

The **cross-section** is a commonly used parameter to quantify the likelihood of optically induced transition events, either absorption or emission, of Ln^{3+} ions in glasses [30]. It is expressed as a function of the wavelength, or photon frequency (ν), of light. In particular, considerable efforts have been devoted to determine the cross-section of the fundamental Er^{3+} transition ($^4I_{13/2} \rightarrow {}^4I_{15/2}$) due to its importance in lasers and optical amplifiers. In this regard, the McCumber's relation allows calculating the emission cross-section (σ_e) of the $^4I_{13/2} \rightarrow {}^4I_{15/2}$ Er^{3+} transition from the absorption cross-section (σ_a) of the $^4I_{15/2} \rightarrow {}^4I_{13/2}$ transition [87]:

$$\sigma_e(\nu) = \sigma_a(\nu)\, e^{\left(\frac{\varepsilon - h\nu}{kT}\right)} \tag{2.8}$$

where h is the Planck constant, k is the Boltzmann constant, and ε is the net free energy required to excite one Er^{3+} ion from the $^4I_{15/2}$ to the $^4I_{13/2}$ level at temperature T. σ_a is easily calculated from the absorption spectrum of bulk glasses through the Beer-Lambert law (chapter 3): $\sigma_a(\nu) = A(\nu)/NL$, where A is the absorbance, N is the rare earth ion concetration per unit volume, and L is the thickness of the sample. The exact calculation of ε requires the knowledge of the position of all Stark levels for both the $^4I_{15/2}$ and $^4I_{13/2}$ manifolds, which is obtained through detailed measurements of the

electronic structure of Er^{3+} ions in the host. However, usually an approximate procedure is used to determine ε without the need of knowing the Er^{3+} electronic structure [88].

The probability of a spontaneous radiative transition $a \rightarrow b$ ($A_{r,ab}$) can be calculated theoretically in terms of a dimensionless quantity, that is its *oscillator strength* (f_{ab}), in the case of an induced ED transition [85]:

$$A_{r,ab} = \frac{8\pi^2 e^2 \nu^2}{mc^3} \chi_{ED}\, f_{ab} \tag{2.9}$$

where m is the mass and e the charge of the electron; c is the speed of light in vacuum; ν is the frequency of the transition $a \rightarrow b$ (in 1/s); $\chi_{ED} = n(n^2+2)^2/9$ is the local field correction for ED transitions and represents the enhancement of the electric field in the proximity of Ln^{3+} ions, due to the polarizability of the medium (n is the linear refractive index).

In addition, the oscillator strength of the transition $a \rightarrow b$ is proportional to the spectral integral of the corresponding absorption cross-section (σ_a). Thus, f_{ab} can be calculated from the experimental absorption spectrum, through [85]:

$$f_{ab}^{exp} = \frac{mcn^2}{\pi e^2} \frac{1}{\chi_{ED}} \int \sigma_a(\nu)\, d\nu \tag{2.10}$$

In the framework of the **Judd-Ofelt theory** [89, 90], the theoretical oscillator strength of the radiative ED transition $a \rightarrow b$ is expressed through the Judd-Ofelt intensity parameters, Ω_t (t= 2, 4, 6), and the matrix element of the tensor operator, $\| U^{(t)} \|$, in the form:

$$f_{ab} = \frac{8\pi^2 m\nu}{3h(2J_a+1)} \sum_{t=2,4,6} \Omega_t \, | < a \| U^{(t)} \| b > |^2 \tag{2.11}$$

where J_a is the total angular momentum of the initial state a. While the Ω_t parameters depend on the characteristics of the sites occupied by rare earth ions (*i.e.* the crystal field effect), the matrix elements of the tensor operator are considered independent from the host. Thus, the values calculated by Morrison for the matrix elements are widely employed [91] and the Judd-Ofelt intensity parameters Ω_t (t= 2, 4, 6) can be determined by a least-square fitting procedure between the theoretical and experimental oscillator strengths of ED transitions [92]. Once the Ω_t parameters are known for a given Ln^{3+}-host, the probability of any radiative transition is easily obtained through eq. 2.9.

2.3.2 Nonraditive transitions

In the previous section we have introduced the probability of the nonradiative transition $a \rightarrow b$ ($A_{nr,ab}$) but we have not described the processes that contribute to it. The principal nonradiative decay process of excited 4*f* electrons in RE ions occurs by energy transfer to the host through the emission of phonons, which conserve the energy of the transition. This decay mechanism is called ***multiphonon deexcitation*** or relaxation. The theory of multiphonon relaxation was first formulated for RE ions in crystals [93] and then extended to glasses [94].

Multiphonon relaxation of RE ions in glasses arises from the same general physical processes as in crystals. It is caused by the interaction of rare earth ions with the fluctuating crystal field due to lattice and molecular vibrations (called *oscillators*) [94]. Therefore, multiphonon deexcitation is extremely host dependent and the dominant contribution stems from the maximum phonon energy of the host. In glasses, these vibrations are the higher energy stretching modes of the polyhedra forming the glass network. Thus, the maximum phonon energy of glasses can be determined from their Raman spectra. Table 2.1 reports the maximum phonon energy of some glass hosts used in optical applications [27, 86].

Table 2.1: Maximum phonon energy of glass hosts commonly used in optical applications.

Glass host	Phonon energy (cm^{-1})
Borate	1400
Phosphate	1200
Silicate	1100
Germanate	900
Tellurite	800
Fluorozirconate	500
Chalcogenide	350

The order of the multiphonon de-excitation is the number of phonons required to bridge the energy gap between two consecutive levels. The probability of multiphonon relaxation decreases exponentially with the order of the process and with the energy gap between the two levels [94]. For example, multiphonon relaxation between the $^4I_{13/2}$ and $^4I_{15/2}$ Er^{3+} levels ($\Delta E \approx 6500$ cm^{-1}) is significant only for borate glasses at room

temperature while for other glasses the order of the process is larger than five (see Table 2.1) and therefore the probability of multiphonon relaxation is very small.

The other relevant nonradiative mechanism is due to **interionic processes [**95, 96**]**. These are electric dipole-dipole interactions, which cause energy transfer between neighbouring rare earth ions. The two main processes causing nonradiative decay of excited states between two adjacent RE ions are **cross-relaxation** and **energy transfer upconversion** (ETU). They become important when the distance (d) between RE ions is small, *e.g.* in case of a high concentration or clustering of ions, since their probability scales as $1/d^6$ [96].

In cross relaxation an excited Ln^{3+} ion gives half its energy to an adjacent ion in the ground state so, at the end, both Ln^{3+} ions are in an intermediate energy level [27, 30]. From this level the two ions relaxes to the ground state through multiphonon de-excitation. Thus, all the excitation energy is lost nonradiatively. For example, this mechanism is considered the responsible for the concentration quenching of Nd^{3+} [30].

On the contrary, ETU happens between two neighbouring Ln^{3+} ions, which are both in an excited state [27, 30, 96]. One of them transfers its energy to a close ion, which is promoted to a higher energy level, while the first relaxes to the ground state. From this higher level, the ion can relax either by emitting a photon with higher energy than the exciting photon (*i.e.* upconverted emission) or via phonons and a lower-energy photon. In any case, at least one exciting photon is lost in the ETU process.

Besides to energy transfer between adjacent RE ions, nonradiative decay is also caused by interactions between excited RE ions and impurities or defects in the host material [95]. Among the most important impurities that causes nonradiative decay of excited RE ions in glasses there are **OH^- groups** (hydroxyl ions) [30]. In a similar way to what happens with phonon vibrations, the fluctuations in the crystal field by experienced by rare earth ions due to vibrations of hydroxyl ions, may induce their nonradiative deexcitation. Moreover, due to the high-energy O-H stretching vibrations (~3000 cm^{-1}), OH^- groups are more important luminescence quenchers than phonons for the majority of rare earth ions [30]. As mentioned above, the probability of multiphonon relaxation of the $^4I_{13/2}$ level is very small for Er^{3+} ions in glass hosts, but energy transfer to hydroxyl ions play a major role in the nonradiative decay of this level [95, 97, 98]. Since the energy gap between the $^4I_{13/2}$ and $^4I_{15/2}$ Er^{3+} levels is ~6500 cm^{-1} the vibration of two OH^- groups (~6000 cm^{-1}) is enough to bridge the gap, thus nonradiative de-

excitation of the $^4I_{13/2}$ level by OH^- vibrations is similar to a two-phonons quenching mechanism [95, 97].

Finally, Yan and co-authors [97] have proposed two possible energy-transfer mechanisms between Er^{3+} and OH^- groups since the $^4I_{13/2} \rightarrow {}^4I_{15/2}$ emission has shown a reduction with the increase of both the Er^{3+} and OH^- concentrations. In the first, a small fraction of excited Er^{3+} ions, very close to OH^- groups, are quenched by transferring their energy to OH^- groups; while in the second, excited Er^{3+} ions may transfer their energy to neighbouring non-excited Er^{3+} ions until an OH^- is found in the transfer route and the energy is lost. The latter mechanism is considered dominant because usually most of excited Er^{3+} ions are not close to OH^- groups.

2.4 Applications of rare earth doped glasses and glass-ceramics

Glass hosts offer several advantages over crystalline and ceramic hosts. The principal one is that glass can be fabricated easily in a broad variety of forms from very small (films of 10s nm, fibres of 100s μm) to very large dimensions (rods up to 1m in length and over 10 cm in diameter) with good optical quality [99]. Moreover RE ions in glasses show broad absorption and emission spectra that are advantageous to increase the wavelength tolerance for the pump source and to obtain tuneable sources and ultrashort pulses, respectively [99].

In the last decades, many remarkable results have been obtained from rare earth doped glasses in the development of solid-state lasers and optical amplifiers [30, 86]. Traditionally, silicate-based glasses have been the most employed hosts for RE ions because of their excellent properties such as high stability and chemical durability, together with good fluorescence performance. In fact, the first glass laser reported, in 1961, was a Nd^{3+} doped barium-silicate glass by Snitzer [100]. Few years later, the first glass fibre laser was demonstrated in the same system [101]. The first erbium-doped fibre amplifier (EDFA) was developed in a silicate fibre too in 1987, thanks to the matching between the Er^{3+} transition ($^4I_{13/2} \rightarrow {}^4I_{15/2}$), around 1.5 μm, and the low loss window of silica glass [9]. Since then, EDFAs have been and still are widely used in

long-haul optical telecommunication fibres to amplify optically the high speed light signals travelling along the fibre in a wavelength division multiplexing (WDM) configuration [102]. Light from an external source (usually at 980 or 1450 nm) is used to excite Er^{3+} ions which then amplify the signal by generating stimulated emission of photons at the signal wavelength [30]. The same principle is used in erbium doped waveguide amplifiers (EDWAs) and lasers, that are also based on Er doped glasses as gain media; but, contrary to EDFAs, they are conceived for integration on a photonic circuit board. However, the manufacture requirements are much more stringent for EDWAs than for EDFAs. Fundamental issues are about the glass composition and the technique to pattern the waveguide, as this should possess adequate dimensions and low losses. The doping technique plays an important role too, since a much higher concentration of RE ions is required in devices of small dimensions, and often homogenous doping is not the best option. The review of Bradley and Pollnau provides an exhaustive description of the background and the state of the art about Er doped waveguide amplifiers and lasers [16].

The attainment of best performances by EDFAs has driven the search of glass hosts for rare earth ions different than silica, since this last present important drawbacks such as a low refractive index, high phonon energy and OH^- content [103]. Alternative glass hosts should have a low phonon energy, high refractive index, and large solubility of rare earth ions in order to improve the efficiency of rare earth ions emissions [27]. In this regard, the demonstration in 1994 of a broadband emission at 1.5 μm in Er doped **tellurite glasses,** together with their excellent rare earth solubility, triggered the interest in these hosts [33]. Soon after, a single-mode Nd^{3+} doped tellurite fibre laser was successfully achieved together with a broadband Er^{3+} doped tellurite fibre amplifier that almost doubles the bandwidth of silica-based EDFA [104, 105].

Moreover, tellurite glasses show other attractive properties such as: a wide transparency region in the visible and infrared wavelength range (typically 0.4-6 μm); a higher non-linear refractive index, lower phonon energy, lower processing temperatures (relative to silica glass) and a large number of compositions leading to stable glasses [33, 66].

Rare earth doped oxide glasses have been employed successfully as lasers and amplifiers devices in the near infrared spectral region, but the development of active devices in the visible and mid-infrared regions is not possible with such glass hosts due to their high phonon energy, which reduces the efficiency of their emissions in these

regions. Thus, novel glass compositions such as fluorides, and chalcogenides, characterised by a low phonon energy, have been considered to develop active devices in the visible and mid-infrared [106]. For example, strong green, blue, and ultraviolet emissions have been observed in Eu^{3+} doped fluoride glasses [107]; a three-color, solid-state, volumetric display has been demonstrated based on upconversion emissions of rare earth-doped heavy metal fluoride glasses [108]; rare earth doped chalcogenide and fluoride glasses have been proposed to develop mid- and long- infrared fibre lasers [20, 109]. However, the poor stability and troublesome fabrication of non-oxide glasses are still unsolved issues [20].

An attractive alternative to fluoride and chalcogenide glasses is represented by **transparent glass-ceramics** as hosts for rare earth ions [110]. As described in the previous sections, glass-ceramics are composite materials, consisting in a glass matrix and a crystalline phase dispersed in it. Transparent glass-ceramics can be achieved when the crystals are large (~μm) but with low birefringence and similar refractive index to the glass matrix, or when the crystals are much smaller than the wavelength of visible light (~10s nm) [43]. The most interesting glass-ceramics as host for rare earth ions are **oxyfluoride glass-ceramics** that combine the high chemical resistance and refractive index of the oxide glass matrix with the low phonon energy and high rare earth solubility of the fluoride crystal phase [42]. Wang and Ohwaki reported for the first time, in 1993, a transparent oxyfluoride glass-ceramic co-doped with Er^{3+} and Yb^{3+}, containing fluoride nanocrystals dispersed throughout the aluminosilicate base glass [111]. This glass-ceramic showed an upconverted visible emission 100 times stronger than the precursor oxyfluoride glass due to the segregation of rare earth ions into the fluoride nanocrystals (Fig. 2.9).

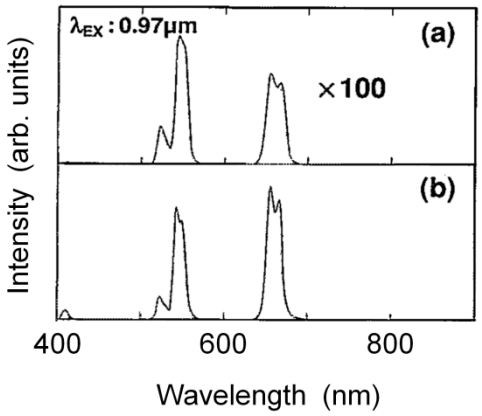

Figure 2.9: Room temperature fluorescence spectra of (a) oxyfluoride glass before the thermal treatment; (b) oxyfluoride glass after the thermal treatment excited at 0.97 μm (From Fig. 3 of Ref. [111]).

Then, Dejneka demonstrated improved visible emissions from Eu^{3+} in aluminosilicate glass-ceramics with LaF_3 nanocrystals [112]. LaF_3 is one of the most studied crystalline phases for doping with Ln^{3+} ions since there is a small crystallographic mismatch between LaF_3 and LnF_3 crystals, which eases the incorporation of Ln^{3+} ions into the LaF_3 crystalline phase [113, 114].

Later on, many rare earth doped oxyfluoride glass-ceramics based on silicate glass matrices and a fluoride crystal phase, such as LaF_3, CaF_2, PbF_2, *etc*. have been proposed as active media for solid state lasers, optical amplifiers, phosphors or to enhance the efficiency of photovoltaic cells [115, 116, 117, 118, 119, 120]; while little information is found in the literature on other rare earth doped oxyfluoride glass-ceramics, different from oxyfluoride silicate glasses [42, 110].

In chapter 5 we show how we have successfully produce transparent glass-ceramics with Er^{3+} ions segregated in fluoride nanocrystals through controlled crystallisation of Er doped TeO_2–ZnO–ZnF_2 glasses. To our knowledge, it is the first time that such glass-ceramics have been obtained. They present an improved visible upconverted emission with respect to the precursor glass.

3

Experimental techniques

3.1 Introduction

In this chapter we introduce the experimental techniques employed. First, we describe the techniques used to synthesize the glass samples: bulk glasses were produced by melt-quenching while pulsed laser deposition was considered in the case of thin film glasses.

The composition, thermal, structural and optical properties of glass samples were determined using different methods. Ion beam analysis techniques: Rutherford backscattering spectrometry (RBS) and proton induced gamma-ray emission (PIGE) were employed to determine the atomic composition of bulk and film glasses. The thermal properties of bulk glasses were studied using differential scanning calorimetry (DSC). The glass structure of both bulk and film samples was determined by Raman spectroscopy. Moreover, the microstructure of glass ceramics was studied through transmission electron microscopy (TEM) and energy dispersive X-ray spectrometry (EDX), while the surface of film glasses was analyzed by scanning electron microscopy (SEM). Finally, we describe the techniques involved in the optical characterization of the samples. Linear optical properties of bulk and film glasses were studied by spectroscopic ellipsometry and spectrophotometry. The first allowed measuring the linear refractive index of bulk and film glasses and the thickness of the latter. The second provided information about the transparency range and the absorption coefficient of glasses. The chapter ends with the description of the techniques employed to study the photoluminescence response of rare earth ions in bulk glasses and glass-ceramics, and in thin film glasses: steady-state and time-resolved photoluminescence spectroscopy techniques.

3.2 Glass fabrication

The glass samples studied in this thesis have been produced by melt quenching (bulk glasses) and pulsed laser deposition (thin film glasses).

3.2.1 Melt-quenching

Bulk glass fabrication process is commonly referred to as melt-quenching technique. Although it is a simple technique from the conceptual point of view, there are many chemical and physical transformations that take place at high temperature during the transformation of a batch of powders into a molten glass. The dissociation of chemical reagents, their recombination as well as the existence of phase transformations, make the process of glass formation a very complex field of study [59]. In this section we restrict ourselves to a general description of the experimental procedure employed to prepare the fluorotellurite glasses studied in this work.

First, a batch of the desired glass composition was prepared from commercial high-purity (> 99.99% in weight) powder reagents (TeO_2, ZnO, ZnF_2, LnF_3 where Ln= Er, Nd, Yb, Tm). We chose to use rare earth fluorides instead of rare earth oxide reagents because the first are well known to act as nucleation agents in glasses and thus, they could favour the attainment of glass-ceramic samples [44].

Prior to the glass melting, the batch was mechanically mixed in an agate ball mill during 10 minutes at 320 rpm. Then, the batch was placed in a covered platinum crucible and introduced in an electrical vertical furnace at a temperature in the range 750-850 ºC, depending on glass composition, for 30 minutes. Only platinum crucibles were used since platinum does not react with the fluorine present in the batch. Furthermore, the crucible was covered in order to reduce the fluorine evaporation from the melt when forming volatile compounds such as HF (see Section 4.2.1). Before pouring the melt, this was homogenized by using an electrical platinum stirrer. Finally, the melt was poured on a preheated brass mould having the desired shape and introduced immediately into an annealing furnace to minimize thermal stress and strains. Glass samples were kept in the annealing furnace for 15 minutes at temperatures ranging from 300 to 320 ºC and then cooled down to room temperature at a controlled cooling rate of 1 ºC/min.

3.2.2 Pulsed laser deposition

Pulsed Laser Deposition (PLD) is a thin film deposition technique based on the use of a laser to ablate material from a target to be deposited in a thin film. Therefore, its origin is strongly connected to that of the laser. Soon after the fabrication of the first optical laser, the ruby laser in 1960 [3]; the interest on the interaction of a laser beam with a solid began to be an important a subject of research. Only two years later, Breech and Cross studied the emission spectrum of a solid material vaporized by a ruby pulsed laser [121] and in 1965 the first demonstration of PLD took place [122]. However, the technique did not arise significant interest since the deposited films showed inferior optical quality than those obtained via other deposition techniques, such as chemical vapor deposition (CVD) or molecular beam epitaxy (MBE). Nevertheless, in 1987 the situation completely changed with the deposition of superconductive ceramic materials ($YBa_2Cu_3O_7$) with very good quality [123]. This triggered the interest in the technique and favoured its spreading. At the same time the development of new laser technologies, such as lasers with high repetition rate, short pulse durations, and short wavelength made PLD a very competitive and reliable tool for the growth of thin films with complex stoichiometry [124].

As in the case of melt-quenching, PLD seems a simple technique. However, the physical processes involved from the ablation of the target material to the nucleation and growth of the thin film are very complex. They exceed the aim of this thesis, since we only used PLD as a deposition technique to synthesize thin films from bulk glasses produced by melt-quenching. Thus, in this section, we describe briefly PLD basics and we mainly focus on the experimental set-up employed. A detailed description of the fundamentals of PLD and of the state of the art of the technique can be found in the book by Eason [125].

Pulsed laser deposition is based on a high power ($>10^8$ $W \cdot cm^{-2}$) pulsed laser, typically in the ultraviolet range, which is focused on the surface of a target material that is placed inside a vacuum chamber [126, 127]. When the laser pulse hits the target, and its energy is higher than a threshold, the material is ablated from the surface before the end of the pulse. The ejected material expands in the direction perpendicular to the target surface while the absorption of the laser pulse tail by the ablated material generates a plasma plume. This contains a significant fraction of ionized species (electrons and ions) and atoms with a high kinetic energy (10-100 eV) [126]. The expansion of the ejected

material can occur either in vacuum (~10^{-4} Pa) or in the presence of a background gas (up to 10s Pa) such as argon (inert atmosphere) or oxygen (reactive atmosphere). In particular, an oxygen atmosphere is usually used to ensure the stoichiometry of oxide films, as we will see next in the case of thin film glasses. By placing a substrate in the path of the expanding plasma, it is possible to collect a fraction of the ablated material, which thus leads to the nucleation and growth of a thin film. The film can be either amorphous or crystalline depending on the type of substrate and its temperature.

There are many advantages in the use of PLD for the growth of thin films. Without any doubt, the most relevant one is its capability for **stoichiometric transfer** of material from target to substrate. This is due to the congruent vaporization of the target surface by the laser pulse, which is a consequence of the removal of material at a faster rate than those of the segregation of individual target components [127]. Moreover, if PLD takes place in the presence of a background atmosphere it is possible to modify the plasma dynamic through multiple collisions that reduce the kinetic energy of the plasma species. In addition, a reactive atmosphere can compensate for the loss of target components such as oxygen or nitrogen [127, 128, 129]. This is one of the key features of PLD, which enables the deposition of thin film with a complex composition, such as glasses and semiconductors [125]. Almost any material which absorb the laser beam can be deposited at relatively high deposition rates (~10s nm/min) with a very precise control of the amount of material deposited, due to the pulsed nature of PLD [125]. Besides, the high kinetic energy of the ablated species (10-100 eV) promotes their surface mobility which improve the adherence of the material to the substrate and lead to dense films without the need of annealing [128]. Another advantage of PLD, compared to other film deposition techniques, is that it allows the growth of multilayer films in an efficient and easy way by sequentially changing the target material during deposition. This technique is often called ***alternate* PLD** (a-PLD).

Of course PLD presents technical and fundamental drawbacks as well. First of all, due to the high energy of the laser pulse, the ablated material may contain molten droplets of up to ~10 μm in size [126, 127]. This phenomenon is negligible in dielectric materials but becomes important in metals with high thermal conductivity and low melting temperature, which leads to films with poor properties [129]. This drawback can be controlled by reducing the laser fluence. Second, the plasma plume created during the laser ablation process is highly forward directed, therefore the area of deposited material

is typically limited to few cm^2. Another consequence of the high directionality of the plasma plume is that the thickness of the deposited film may be non-uniform and the film composition may vary across the deposited surface as well, due to the different angular distribution of the species in the plume [127]. However, uniform films, in thickness and composition, can be produced by rastering the laser spot across the target surface and rotating the substrate during the deposition.

In particular, the characteristics of PLD make the technique adequate to synthesize thin films of the fluorotellurite glasses considered in this thesis, which have a complex stochiometry (TeO_2–ZnO–ZnF_2–ErF_3). The fluorine present in the plasma plume does not represent a problem, since PLD works well in presence of reactive gases and films containing fluorine have been previously deposited by PLD [130]. Moreover, in order to produce transparent films with a similar stoichiometry to the bulk target glass, they were deposited in an oxygen atmosphere. Figure 3.1 shows a scheme of the PLD set-up used to deposit fluorotellurite thin films. It comprises an excimer laser source, a vacuum chamber where the substrate and multi-target stages are placed, and an ***in-situ*** **reflectometry system** to monitor the film deposition process. Two motors ensure the rotation of the target and the substrate stages during the deposition. The objective is to reduce the cumulative damage on the target surface due to the laser ablation process and, as described above, to homogenize the distribution of the material deposited on the substrate. The laser, the multi-target stage, and the reflectometry system are connected to a PC which enables the automatic control of the deposition process with the capability of changing the ablation target in order to grow multilayered films.

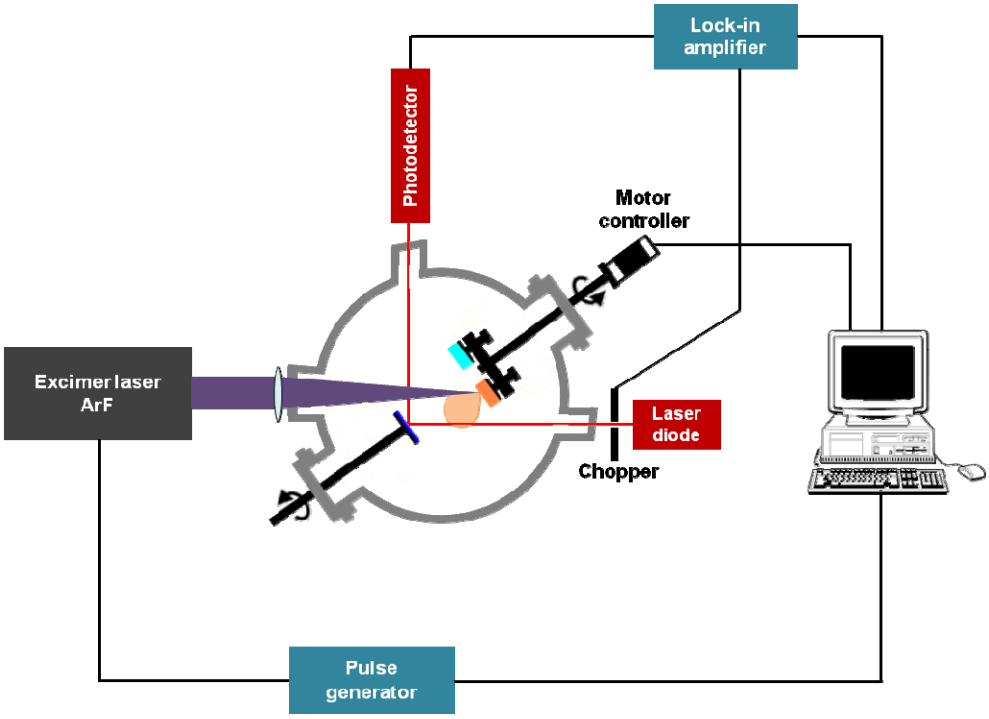

Figure 3.1: Scheme of the pulsed laser deposition system used.

The ArF excimer laser generates laser pulses at 193 nm with a duration of ≈ 20 ns (full width at half maximum). The laser beam is focused using a fused silica lens on the surface of the target at an angle of incidence of 45º, which lead to a spot size of ≈ 1.5 mm^2. The substrate is placed parallel to the target at a distance of 4 cm. We have employed a moderate fluence of 2 J/cm^2 and a repetition rate of 10 Hz to ablate the glass target. The deposition took place at room temperature in a dynamic oxygen pressure of 10 Pa to compensate for the oxygen losses in the films. Film glasses were deposited on silicon and fused silica substrates that were previously ultrasonically cleaned with acetone and ethanol. These substrates are well suited to the different structural and optical characterization techniques employed. Si substrates were used for compositional analysis and linear optical characterization, whereas fused silica substrates were used to measure the transmission and the Raman spectra as well as infrared absorption spectra of the produced thin films.

The *in-situ* reflectometry system (in red in Fig. 3.1) is composed by a laser diode (λ = 670 nm) incident on the substrate and a Si photodetector, connected to a lock-in amplifier, to detect the reflected beam. The interference between the beams reflected on the air-film and film-substrate interfaces leads to a periodic variation of the reflected signal as the film is being deposited, whose amplitude and number of periods are related

to the optical constants (*n* and *k*) of both the film and the substrate and to the film thickness [76]. The experimental reflectivity can be fitted using the Fresnel reflection coefficients, which allow us to extract film thickness and the linear refractive index at the diode wavelength.

As an example, Figure 3.2 shows the evolution of the reflectivity during the deposition of transparent and absorbing glass films on silicon and fused silica substrates, respectively.

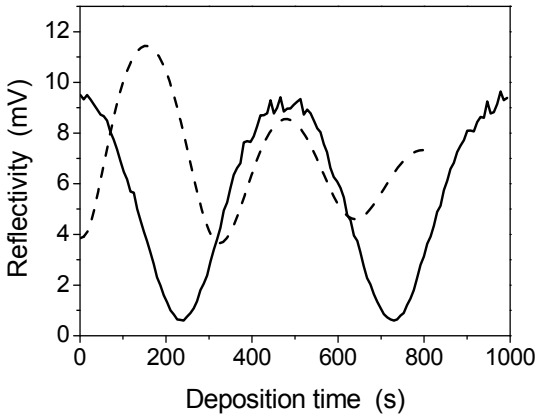

Figure 3.2: Reflectivity signal from (—) a transparent glass film on Si substrate and from (---) an absorbing glass film on fused silica substrate.

In the case of the transparent film the period and the intensity of the reflectivity are constant with the deposition time, since the signal is not attenuated (*k* is negligible) as the film is becoming thicker. On the contrary, the reflectivity signal of the absorbing film presents a decreasing intensity and period as the deposition time increases (and so the film thickness), which indicates that *k* is large. Therefore, the *in-situ* measurement of reflectivity allows checking simultaneously the thickness of the film being deposited, related to the number of periods; and the film optical properties, related to the intensity of oscillations.

3.3 Compositional, thermal, and structural characterization

The techniques used in this thesis to characterize the TeO_2–ZnO–ZnF_2 glass samples were: *i*) Rutherford backscattering spectrometry and proton-induced gamma-ray emission to determine their composition; *ii*) differential scanning calorimetry to

analyse their thermodynamic behaviour; and *iii*) Raman spectroscopy to study their structural units. Finally, we introduce transmission electron microscopy and scanning electron microscopy which have been used to analyse the microstructure of glass-ceramics and thin films glasses, respectively.

3.3.1 Ion beam analysis techniques

The composition of the fabricated bulk and thin film glass samples has been determined using ion beam analysis techniques: **Rutherford Backscattering Spectrometry** (RBS) and **Proton-Induced Gamma-ray Emission** (PIGE). They are based on the use of an ion beam with high energy, typically in the range 0.5-4 MeV, which impinges on the sample surface and interact with the atomic nuclei of the sample. Both RBS and PIGE measure the concentration and in-depth distribution of elements (up to few micrometers) in the sample in a non-destructive way, but the physical processes involved in each technique are different [131].

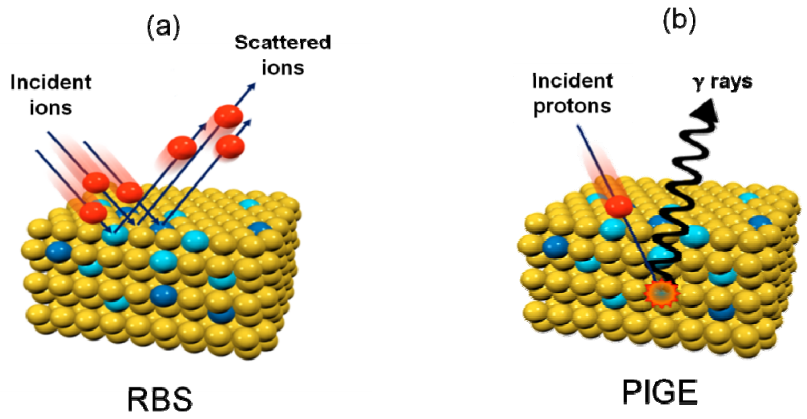

Figure 3.3: Sketch of the ion beam analysis techniques used in this work. (a) Rutherford Backscattering Spectrometry (RBS); (b) Proton-Induced Gamma-ray Emission (PIGE).

Figure 3.3 illustrates the two techniques. RBS (Fig. 3.3a) is an elastic ion scattering process which relies on Coulomb interactions between the incoming ions and the target nucleus. It is a non-destructive quantitative technique which does not need reference samples. For these characteristics, it is widely used for the near surface layer analysis of solids and thin films. As illustrated in Fig. 3.3a, after bombarding the sample with high energy light ions such as protons or He^{2+}, these are elastically scattered with different

energy and directions by the atoms constituting the target. RBS records the energy of the backscattered ions by means of an energy sensitive detector, typically a solid state detector, positioned at an appropriate backscattered solid angle with respect to the incident ion beam. The energy of the backscattered ions is dictated by conservation of energy and momentum between the incident ion and the scattering atom and thus can be related to the depth and mass of the atoms in the sample [132]. Moreover, the amount of backscattered ions from any given element is proportional to its concentration [132]. Therefore, RBS can be used as a tool to measure the depth profile of individual elements in a solid. However, a spectrum simulator is needed to determine the atomic concentration of the elements present in the sample by fitting the experimental RBS spectrum with a calculated one. Finally, since the Rutherford cross-section, *i.e.* the number of scattered ions per unit time, is proportional to the atomic numbers (Z) of the incident ion and the target nucleus, the sensitivity of the technique is low for light elements. This is an important drawback of RBS which requires its combination with other nuclear based methods such as nuclear reaction analysis (NRA) or PIGE for the analysis of light elements [131].

Contrary to RBS, which involves electrostatic interactions, PIGE is based on low-energy nuclear forces. Basically, in PIGE, the ion beam impinging on the sample should have an energy high enough to penetrate the Coulomb barrier of atomic nuclei to induce various nuclear reactions, resulting in excited nuclei. Then, these nuclei emit γ-rays during their de-excitation process (Fig. 3.3b). The energy of the emitted γ-rays is a fingerprint of the nuclei (isotopes). Moreover, the concentration of the isotope in the sample can be determined by measuring the yield of γ photons collected by the detector, which has to be previously calibrated with a well known sample [133]. Since PIGE cross-sections drastically drop when increasing Z of the target element, due to increased Coulomb repulsion, the best sensitivity is obtained for low-Z elements ($3 < Z < 20$). Besides, contrary to RBS, PIGE does not show continuous sensitivity but it depends strongly on the element to measure and on the possibility that their nuclear reactions with the incident beam emit γ-rays. The most common reaction in PIGE is the nuclear reaction by Coulomb excitation (inelastic Coulomb scattering). The projectile (proton: p) exchanges energy with the target through the Coulomb interaction, thus, the target is driven to an excited state which decay through emission of γ-rays and protons of lower energy (p') [133].

Ion beam analysis experiments were performed at the *Centro Nacional de Aceleradores* (Sevilla) in collaboration with F.J. Ferrer. For the RBS measurements a proton beam at 1.5 MeV was used to irradiate the samples and the backscattered protons were collected through a solid state detector at a dispersion angle of 160º. Then, the experimental RBS spectra were simulated with the SIMNRA code [134] to obtain the atomic percentage of Te, Zn, Er, and O. As an example, Figure 3.4a shows an experimental RBS spectrum and the corresponding simulation of a bulk TeO_2–ZnO–ZnF_2 glass.

The edges belonging to (Te + Er) at ~1520 keV, Zn at ~1480 keV, and O at ~1200 keV are marked in Fig. 3.4a. By enlarging the region close to 1500 keV, it is possible to distinguish the small edge of Er from that of Te (inset of Fig. 3.4a). The intensity of each edge is proportional to the atomic percentage of the corresponding element. The experimental error in the atomic percentage is ± 10 % for the elements with well defined edges (O, Zn, Te in Fig. 3.4a) while is larger, ± 30 %, in the case of elements having overlapping edges and/or small atomic percentages, as in the case of Er.

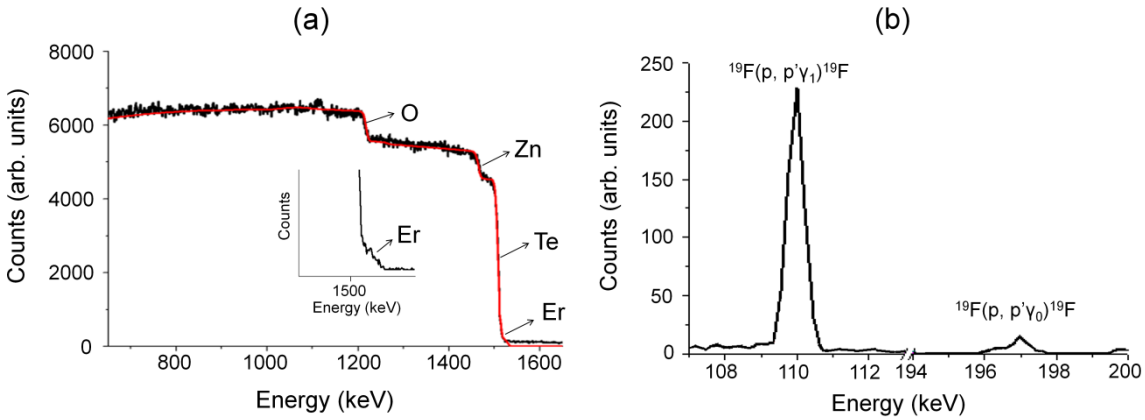

Figure 3.4: RBS and PIGE spectra of a TeO_2–ZnO–ZnF_2: ErF_3 bulk glass. (a) RBS spectrum (black line) along with its fitting using the SIMNRA code (red line); (b) PIGE spectrum showing the peaks corresponding to the nuclear reaction $^{19}F(p,p'\gamma)^{19}F$. The edges corresponding to Er, Te, Zn and O are indicated in (a). The inset in (a) zooms in the region corresponding to the Er edge at ~1520 keV.

PIGE analysis was employed to quantify the fluorine concentration of TeO_2–ZnO–ZnF_2 glasses. A proton beam at 2.3 MeV and a detection angle of 145º were used. Figure 3.4b presents an experimental PIGE spectrum from a fluorotellurite bulk glass. It shows two peaks at 110 and 197 keV that correspond to the γ photons emitted by the nuclear reaction $^{19}F(p, p'\gamma)^{19}F$ [135]. The fluorine concentration in the samples was determined

by comparing the area of the peak at 110 keV with that of a reference sample, having a known fluorine concentration [136].

3.3.2 Differential scanning calorimetry

Differential scanning calorimetry (DSC) monitors heat effects associated with phase transitions and chemical reactions in a material as a function of temperature. It is a very important technique for the thermodynamic characterisation of materials, particularly glasses. A DSC trace records the difference in the heat flow to the sample and a reference as a function of temperature, which are held in a gas flow at the same temperature. The sample is placed in a container (*e.g.* in an alumina pan), while a second empty container is used as reference. Both containers have individual heating elements as well as temperature sensors associated with them. The sample and the reference are heated equally at a constant rate until a transformation occurs in the sample. At this point, the sample temperature deviates from that of the reference, thus, the DSC adjusts the heat input to each container in order to maintain a zero temperature difference ($\Delta T = 0$) between them [137]. Since the DSC operates at a constant pressure, the quantity of electrical energy per unit time (*i.e.* heat flow: dE/dt) applied to the heating elements in order to maintain $\Delta T = 0$ between the sample and the reference is assumed to be proportional to the enthalpy change per unit time ($d(\Delta H)/dt$), [137]:

$$\left(\frac{\mathrm{d}E}{\mathrm{d}t}\right) \propto \frac{\mathrm{d}(\Delta H)}{\mathrm{d}t} \tag{3.1}$$

Moreover, the heat flow difference between the sample and the reference can be either positive or negative, indicating the type of transformation which is occurring in the sample. In fact, in an **endothermic process**, heat is absorbed by the sample and, therefore, heat flow to the sample is higher than to the reference ($dE/dt > 0$). For example, glass transition and melting are endothermic processes. On the contrary, in an **exothermic process**, such as crystallisation, heat is released by the sample and then the heat flow to the sample is lower than to the reference ($dE/dt < 0$).

We have used a commercial DSC (TA Instruments, SDT-Q600), to study the thermodynamic properties of glass samples. The DSC provided simultaneous measurements of weight changes and differential heat flow. It was calibrated before

each measurement using the melting point of zinc (T_m= 419.5 ºC). We have measured both glass chips and grinded glass samples of 10s mg, by placing them in high purity alumina pans and heating them at a constant rate (5-20 ºC·min^{-1}) in a N_2 gas flow (100 ml/min). An empty alumina pan was used as reference and a baseline taken with empty pans was subtracted from each DSC run. DSC heat flow data were dynamically normalized using the instantaneous sample weight at any given temperature. Finally, the convention for the sign of the heat flow is changed in the DSC traces shown in this thesis: the heat flow is positive for exothermic reactions and negative for the endothermic ones. Figure 3.5 shows a characteristic DSC trace obtained for a TeO_2–ZnO–ZnF_2 glass sample studied in this thesis.

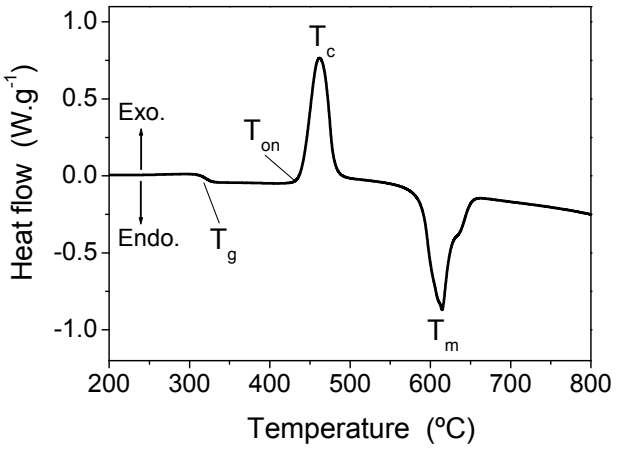

Figure 3.5: DSC trace of a TeO_2–ZnO–ZnF_2 glass. The glass transition (T_g), onset of crystallisation (T_{on}), crystallisation (T_c) and melting (T_m) temperatures are indicated in the figure.

From the DSC trace shown in Fig. 3.5 it is possible to determine the characteristic temperatures of glass. We have determined the glass transition temperature (T_g) as the inflection point of the first endothermic variation in the heath flow (Fig. 3.5); the onset of crystallisation temperature (T_{on}) as the point where the exothermic peak begins, the crystallisation (T_c) and melting (T_m) temperatures as those corresponding to the exothermic and endothermic peaks, respectively [137]. These temperatures were found to be reproducible within ± 3 ºC for different DSC runs of the same sample.

3.3.3 Raman spectroscopy

Raman spectroscopy has been employed to determine the structural units that compose the glass network of the produced bulk and thin films glasses. It relies on the **inelastic scattering of light**, which was first described by Sir C.V. Raman, awarded with the Nobel Prize for Physics in 1930 for his discovery [138]. He observed that, when a monochromatic light goes throughout a transparent solid, some of the scattered light changes its colour. This phenomenon is due to the energy variation, *i.e.* wavelength, of the photons that are scattered by the atoms and molecules of the solid [139]. When photons interact with matter, they are usually absorbed or elastically scattered (Rayleigh scattering) while only a small fraction of them is inelastically scattered (Raman scattering). Figure 3.6 summarizes these processes.

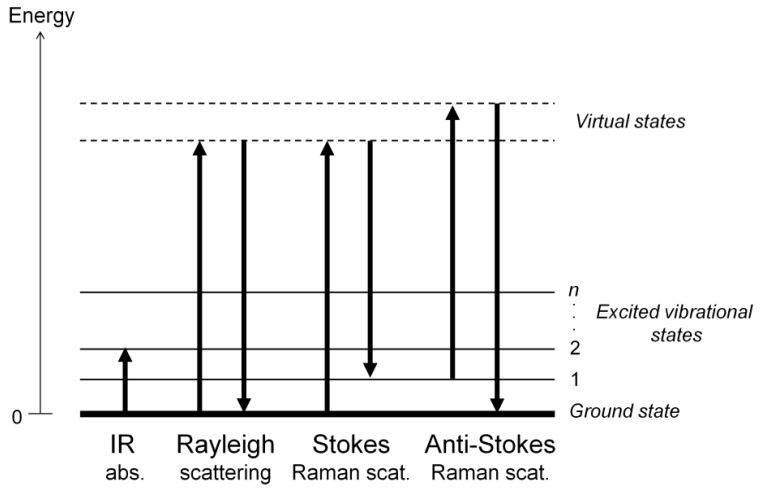

Figure 3.6: Diagram representing the energy transitions involved in infrared absorption, Rayleigh scattering and Raman scattering processes. Up arrows indicate absorption of photons while down arrows the emission of photons.

Photons are absorbed (IR abs. in Fig. 3.6) when their energy matches the difference between two energy levels of the system; then, the system is promoted to an excited state. Instead, in the case of Rayleigh and Raman scattering, the energy of photons does not match with any excited state of the system, so photons are not absorbed. However, the photon-matter interaction distorts the electron cloud around the nuclei and therefore the molecule is promoted to a high energy short-lived state, called virtual state, that relaxes immediately by re-emitting the photon (Fig. 3.6). The difference between elastic and inelastic scattering lies in the energy of incident and scattered photons. In the first case, there is no variation in the energy of the incident and scattered photons, and the

system is found in the ground state before and after the interaction with photons (Rayleigh scattering). On the contrary, the energy of the incident and scattered photons is different in the inelastic scattering and it depends on the initial state of the system. If the system is found in the ground state when photons hit it, then the energy of the scattered photons will be lower than that of the incident photons (Stokes Raman scattering) since part of their energy is lost in the excitation of vibrational states. In contrast, if the system is in an excited vibrational state when photons hit it, the scattered photons will have a higher energy than the incident ones (anti-Stokes Raman scattering). The relative intensities of Stokes and anti-Stokes Raman scattering are related to the thermal population of the different vibrational states of the system and, therefore, the intensity of Stokes scattering is usually much higher than that of anti-Stokes scattering.

The number and the energy shift of inelastically scattered photons give important information about the vibrational states of the system under investigation. In this regard, in 1970, Shuker and Gammon presented a calculation which allowed relating the intensity of Raman scattering to the vibrational density of states in amorphous materials [140]. Thus, it is possible to determine the type of structure of a given system and the relative amount of structural units which compose the system through its Raman spectrum.

In Raman spectroscopy, a laser beam is used to excite the sample under investigation. Then, the more intense Rayleigh scatting, which has the same wavelength of the laser, is filtered out and the intensity of the Raman scattering is measured using a monochromator and a detector. Raman spectra are often represented as a function of the energy difference (Raman shift) between the laser energy and the scattered signal.

Raman spectra from bulk and film fluorotellurite glasses of this thesis were recorded in collaboration with C. Domingo and M. Hernandez from the *Instituto de Estructura de la Materia* (CSIC, Madrid). Two different systems were used: a Fourier Transform (FT)-Raman (Bruker MultiRAM) equipped with a laser line at 1064 nm and a confocal Raman microscope (Renishaw inVia) equipped with different laser lines. In particular, we used a laser diode emitting at 785 nm and a He-Cd laser emitting at 442 nm. In addition, in the case of the Raman microscope, the laser beam was focused on the samples using 50x (bulk glasses) and 100x (film glasses) magnification objectives with a spectral resolution of 2 cm^{-1}. The output laser power was ~30 mW in both cases.

Rayleigh and anti-Stokes scattering were removed using an edge filter and the signal was detected by means of an electrically refrigerated CCD camera. Acquisition time was 5-10 minutes for each spectrum.

All the Raman spectra shown in this thesis were corrected by using the ***reduced spectrum correction***, to eliminate spurious effects due to thermal population and frequency effects [141]. These appear mainly in the low-frequency range of the Raman spectrum and are due to the scattering by thermally-excited low-energy phonons and to the Rayleigh scattering, respectively. Once they are eliminated by applying the correction for the reduced Raman spectrum, it is possible to compare spectra recorded at different temperatures as well as the intensity of low frequency Raman bands with that of high frequency bands in the same spectrum.
The intensity of the reduced (Stokes) Raman spectrum was obtained by applying the relation [141]:

$$I_{red}(\omega) \propto I_{exp}(\omega)\,\frac{1}{(\omega_L - \omega)^4}\,\frac{\omega}{n(\omega,T)+1} \qquad (3.2)$$

where $I_{red}(\omega)$ and $I_{exp}(\omega)$ are the intensity of the reduced and the experimental Raman spectrum, respectively; ω is the value of the Raman frequency shift; ω_L is the frequency of the laser excitation line (in cm^{-1}); and $n(\omega,T) = [\exp(-\hbar\omega/k_BT) - 1]^{-1}$ is the Bose-Einstein distribution function for phonons at Stokes frequency.

Raman spectra of the studied glass samples were reduced and normalized to their maximum intensity to ease their comparison. Moreover, in the case of thin film glasses, the contribution to the Raman spectra from the substrate was carefully subtracted.

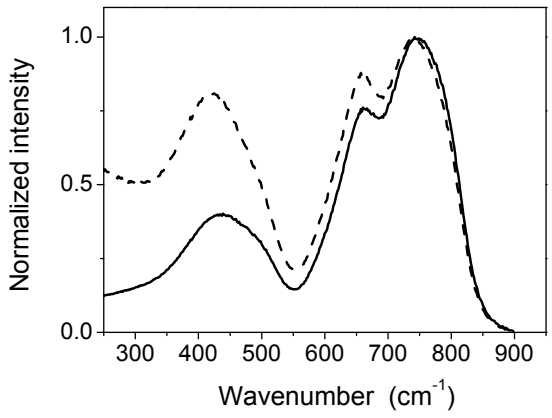

Figure 3.7: (---) Experimental and (—) reduced Raman spectra of a bulk TeO_2–ZnO–ZnF_2 glass of this thesis.

Figure 3.7 compares an experimental and the corresponding reduced Raman spectra of a bulk TeO_2–ZnO–ZnF_2 glass, where we can observe the three characteristic bands of tellurite glasses at 400-550, 600-700, and 700-850 cm^{-1}. As it will be shown in chapter 4, these bands correspond to the vibrational modes of Te-O bonds in the different structural units that comprise the vitreous network of tellurite glasses. Finally, we note that the intensity of the low frequency Raman bands decreases in the reduced Raman spectrum with respect to the experimental spectrum, whereas the Raman band at high frequency is little affected by the correction.

Finally, we have performed what is known as Raman micro-spectroscopy, that is based on *hyperspectral imaging*, in the case of glass-ceramic samples. In this case, Raman spectra are taken at different points across a portion of the sample surface. Then, a map of the sample composition and structure at a microscale can be obtained by analyzing all the collected spectra, which shows the location and amount of different components. Confocal Raman microscopes have a very high spatial resolution; therefore they allow hyperspectral imaging of the sample without the need of any sample preparation. We have used this technique to look for evidence of micro-crystallisation at the surface of glass-ceramic samples, as it can induce phase separation with the consequent degradation of the optical quality of the samples (see chapter 5). Hyperspectral images of glass-ceramics samples were obtained by means of a 2D spatial scanning, with a step of 2 μm, on a 20x20 μm^2 sample surface. Each Raman spectrum, corresponding to a point of the hyperspectral image, was acquired by exciting at 442 nm and focusing the laser beam with a 50x objective.

3.3.4 Electron microscopy techniques

Electron microscopy techniques were used to study the microstructure of fluorotellurite glass-ceramics and thin films. In the first case, we employed **transmission electron microscopy** (TEM), which are among the most versatile and powerful tools for microstructural characterization, whereas **scanning electron microscopy** (SEM) was used to study the surface morphology of thin film glasses.

Both TEM and SEM employ a source of electrons, such as a heated tungsten filament, maintained at a high voltage in order to accelerate the electron beam. Typically, the

applied voltage is of ~100s kV in TEM while in SEM is only 10s kV [142]. Since the high energy electron beam has a limited path length in air, the whole electron microscope column is kept under vacuum (~10^{-5} Pa) [142]. Figure 3.8 compares TEM and SEM techniques highlighting the similarities and differences between them.

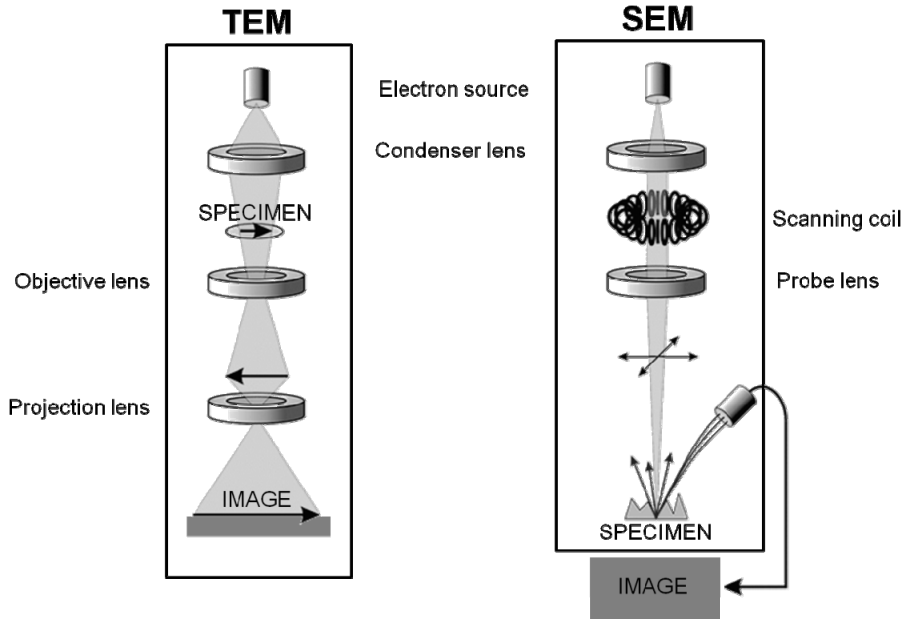

Figure 3.8: Schematic representation of transmission electron microscopy (TEM) and scanning electron microscopy (SEM) techniques.

Both microscopes use electromagnetic condenser lens systems to focus the electron beam, but the process to acquire an image of the specimen is different in each case.

In TEM, the electron beam impinges on the specimen. In order to allow most of the high energy electrons to pass through the specimen, its thickness should be less than 100 nm. Elastically scattered electrons, which emerge from the specimen, carry information about its structure. The objective, composed by electromagnetic lenses, magnifies the collected electron image of the specimen. An important feature of TEM is that it allows collecting both data in the real space, *i.e.* images of the sample, and in the reciprocal space, that is, electron diffraction patterns of the sample. In the case of crystalline samples, electron diffraction patterns supply information about the reciprocal lattice geometry for a certain crystal orientation presenting a projection axis as the optical axis of the microscope [142]. Finally, a fluorescent screen converts the electron image into a visible image. The resolution of TEM depends on the properties of the electron beam, such as electron wavelength and divergence of the beam, and the

properties of the electromagnetic lenses, such as their spherical aberration coefficient. In high resolution transmission electron microscopy (HRTEM) the point-to-point resolution is usually ~0.2 nm [142].

In SEM a probe lens, on top of the specimen, substitutes the objective lens used in TEM [142]. It focuses the electron beam that impinges on the specimen and determines the resolution of the acquired image, which depends on the beam size. Usually, the maximum point-to-point resolution in SEM is of the order of few nanometers [142]. The microstructural information is provided by the low energy *secondary electrons*, which are inelastically scattered from the surface of the specimen. Therefore, contrary to TEM, there is no limit on the maximum thickness of the specimen to be analysed by SEM. However, the fundamental difference in the operation of TEM and SEM lies in the way the signal from the sample is collected to form the image. While TEM collects simultaneously the signal over the full field of view, SEM collects the signal sequentially from each point of the surface while the electron beam is scanned across the sample field of view [142]. The scan rate must be restricted in order to ensure that the signal recorded for each data point is statistically adequate. The final image of the surface of the sample is the sum of all the point images and it is projected on a monitor.

Apart from providing a magnified image of the sample, electron microscopy can integrate microanalytical techniques, such as **energy dispersive X-ray spectrometry (EDX)**, to determine the composition of the sample under investigation. EDX detects the X-rays photons emitted from the specimen upon the interaction with the electron beam. The energy of the emitted X-ray photons is characteristic of each element; therefore, the composition of the sample can be determined at a nanometric scale [142].

The need for a very thin specimen restricts sometimes the use of TEM analysis to thin films since the thinning of a bulk sample is a nontrivial and time consuming task. Mechanical or electrochemical thinning, focused ion-beam (FIB) milling or the replica method are some of the techniques used to prepare TEM specimens. In the present thesis, FIB milling and the replica method have been used to prepare specimens of glass-ceramic samples.

FIB milling is a versatile tool for removing the final surface layers from samples intended for TEM [142]. In general, two ion guns are used to sputter from both sides of the sample. The angle of incidence and the energy of the ion beam are usually restricted

to no more than 15º and 5 kV, respectively, in order to avoid sub-surface radiation damage and topographic surface irregularities. In addition, inert gases (typically argon) are used as sputtering ions in order to avoid ion-induced chemical reactions.

The replica method overcomes the necessity of thinning the sample to be examined by TEM. Figure 3.9 illustrates the preparation of a replica from the surface of the glass-ceramic sample. First, a carbon film was deposited on the surface of the sample. Then, the carbon replica was released by etching of the glass matrix, preserving the nanocrystals in their original configuration. Finally, the replica was collected on a copper grid for TEM examination.

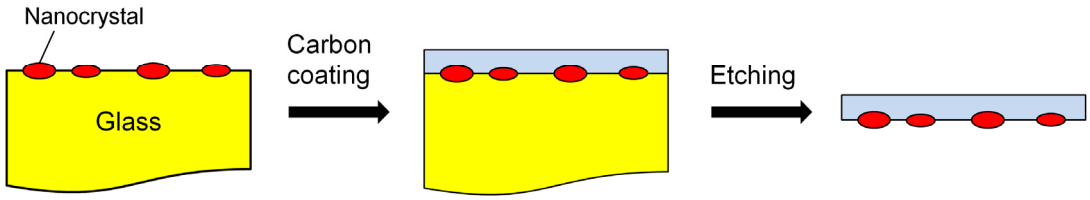

Figure 3.9: Sketch of the replica method applied to glass-ceramic samples to prepare specimens for TEM analysis.

The specimen prepared by FIB was examined by a JEOL 2010F TEM operating at 200 kV coupled with a Gatan image filter (energy resolution of 0.8 eV) at the *Centros Científicos y Tecnológicos* (*Universitat de Barcelona*), to study the inner microstructure of glass-ceramics. The glass-ceramic specimen prepared using the replica method was analyzed through a JEOL JEM 2100 TEM operating at 200 kV (point-to-point resolution of 0.25 nm) at the *Centro Nacional de Microscopía Electrónica* (*Universidad Complutense de Madrid*), to study the microstructure of the surface of glass-ceramics. This last TEM was equipped with an energy dispersive X-ray detector which allowed the analysis of the nanocrystals and the determination of their composition.

Finally, SEM measurements of thin film fluorotellurite glasses were performed at the *Instituto de Ciencia y Tecnología de Polímeros* (CSIC, Madrid) using a Hitachi SU 8000 microscope operating at 1 kV.

3.4 Optical characterization

Optical characterisation of rare earth doped TeO_2–ZnO–ZnF_2 glasses has included: *i*) determination of their linear optical constants, *n* and *k*, by spectroscopic ellipsometry and transmittance measurements; *ii*) measurement of their transparency range by spectrophotometry; and finally, *iii*) determination of their emission spectra as well as the time evolution of the photoluminescence signal by steady-state and time-resolved photoluminescence spectroscopy, respectively.

3.4.1 Spectroscopic ellipsometry

Ellipsometry is based on the change of the polarization of light when it is reflected at the interface between two media. Figure 3.10 schematizes the polarization change occurring between the incident and the reflected beams on a sample interface. The polarization change is related to the linear optical constants, *i.e.* the refractive index *n* and the absorption coefficient *k*, as well as to the characteristics of the interface, such as its smoothness.

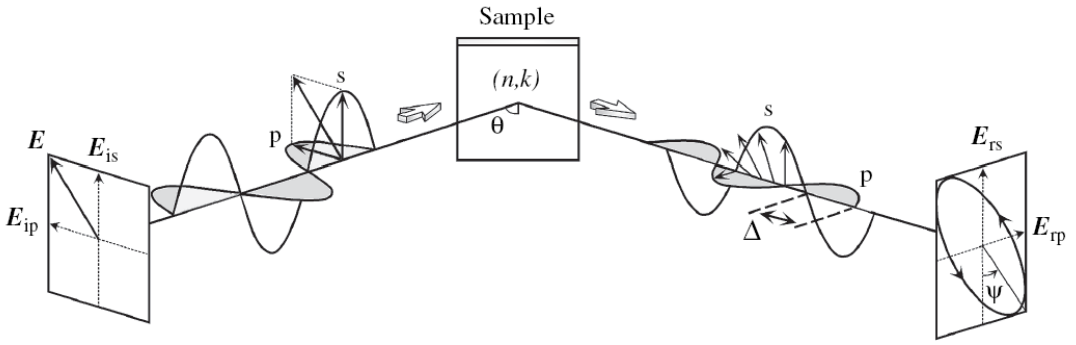

Figure 3.10: Scheme of the measuring principle of ellipsometry.

Usually, the quantity measured by ellipsometry is the ratio (ρ) between the Fresnel reflection coefficients for the *p* (R_p) and *s* (R_s) polarization components of the beam, which is a complex number. This quantity is expressed in terms of [143]:

$$\rho = \frac{R_p}{R_s} = \tan\Psi e^{i\Delta} \tag{3.3}$$

where tanΨ gives the modulus of R_p/R_s and Δ the phase shift between the *p*- and *s*-components of the reflected beam. TanΨ and Δ are related to the refractive index (*n*) and absorption coefficient (*k*) of the sample, respectively. Moreover, the components R_p and R_s are function of the incidence angle, being the difference between them maximum at the Brewster's angle [76]. Therefore, ellipsometry measurements are generally performed at the Brewster's angle in order to have a larger signal to noise ratio [143].
Once the ellipsometric parameters of the sample have been measured in the wavelength range of interest, the optical constants and the thickness of the sample can be deduced through data analysis. It consists of three major parts: *i*) dielectric function modelling, when this is unknown (*e.g.* Sellmeier's or Cauchy's equation is used for modelling transparent dielectrics); *ii*) construction of an optical model (*e.g.* substrate + film + roughness layers); and finally, *iii*) fitting of the ellipsometric data produced by the model to the experimental ellipsometric spectra.

In the present work, bulk and thin film glasses were modelled using a **Cauchy-type** dispersion for the refractive index (3.4), and an exponential decay for the extinction coefficient (3.5) [143]:

$$n = A_n + \frac{B_n}{\lambda^2} + \frac{C_n}{\lambda^4} \tag{3.4}$$

$$k = A_k + \exp\left[B_k\left(\frac{1}{\lambda} + \frac{1}{\gamma}\right)\right] \tag{3.5}$$

where A_n, B_n, C_n, A_k, and B_k are adjustable parameters and γ is the optical gap of the material (in nm).
The experimental ellipsometric parameters have been measured using a commercial variable angle spectroscopic ellipsometer (VASE, J.A. Woollam Co.). The light source is a lamp emitting unpolarized light in the range from 250 to 1700 nm. The wavelength and the polarization of the incident beam are selected by means of a monochromator and a linear polarizer, respectively. Then, the intensities of the *p*- and *s*-components of the beam reflected by the sample are measured using a continuously rotating analyzer and a solid state photodetector. Furthermore, the light source and the detector are mounted on a motorized goniometer, which allows moving them in order to measure at different angles of incidence.

Ellipsometric data analysis of glass samples of this thesis was made by considering two optical models [143]:

i) A transparent dielectric layer and a top roughness layer in the case of bulk glasses, since they have a thickness larger than $5d_p$ (d_p: penetration depth of light). In this case, optical interferences due to backside reflection were negligible;

ii) A multilayer composed by the Si substrate as bottom layer, a transparent dielectric layer, and a top roughness layer in the case of film glasses, that in all cases had a thickness between 100 and 1500 nm (smaller than d_p). They present interference fringes arising from the combination of the reflected beams at the air-film and film-substrate interfaces, which depend on the thickness of the film.

Fitting of the experimental data to the model was made using the software Wvase32 (Woolam) and the Marquardt-Levenberg iterative algorithm to find the parameters that minimized the mean square error between the simulated and experimental data [144].

Figure 3.11a shows the experimental spectra of the ellipsometric parameters (Ψ and Δ) in the case of a TeO_2–ZnO–ZnF_2 glass film deposited on silicon substrate, measured at an incident angle of 65º. The best fit of the experimental ellipsometric data, obtained by using the model of the inset, is also shown in Fig. 3.11a. Besides, Fig. 3.11b shows the dispersion of the optical constants *n* and *k*, which are two fitting parameters in Fig. 3.11a.

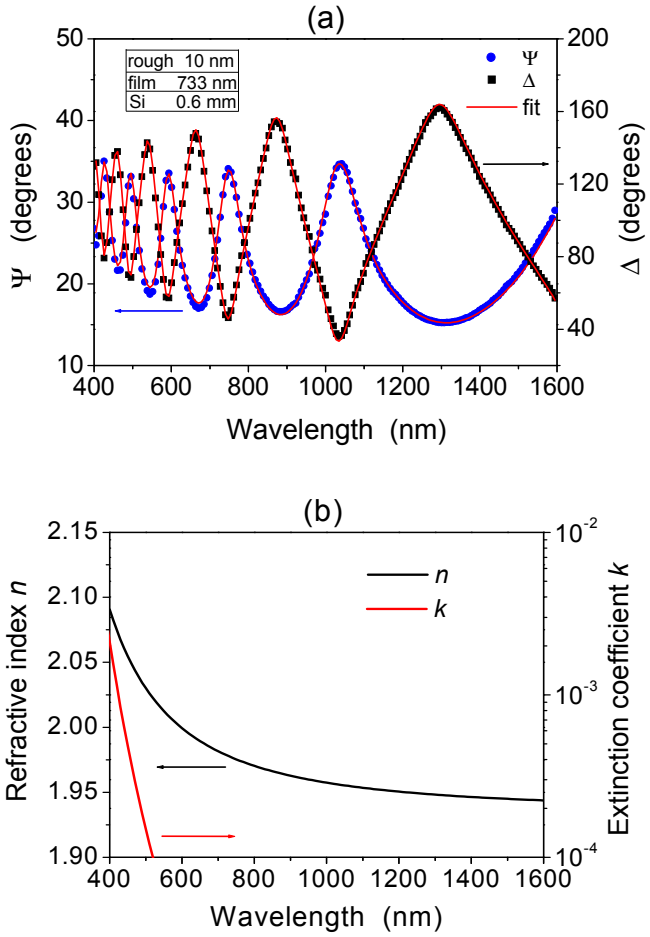

Figure 3.11: (a) Ellipsometric experimental data of a TeO_2–ZnO–ZnF_2 glass film on a Si substrate measured at an incidence angle of 65º and their fitting using the model shown in the inset. (b) Dispersion of the linear refractive index (n and k) deduced from the ellipsometric data presented in (a).

The thickness of the measured film, which is the third fitting parameter, is ~730 nm. The experimental error for n is ± 0.005, while for k is 1% of its value. We want to stress that it is not possible to determine the value of k in the wavelength range where the sample is transparent (*i.e.* from 700 to 3000 nm) since our experimental detection limit for k is 10^{-4}, a value that is orders of magnitude larger than the typical k value of transparent materials.

3.4.2 Spectrophotometry

As it has been described in chapter 2, glasses are characterised by a very low intrinsic scattering and by two intrinsic absorption edges in the ultraviolet and infrared wavelength range, which define their transparency region, that is the wavelength range

where the transmittance has a high value or, analogously, the absorbance has a negligible value.

The **transmittance** (T) of a sample is defined as the relation between the intensity of transmitted light (I_t), *i.e.* after passing through the sample, and the intensity of incident light on the sample (I_{in}), at normal incidence. Moreover, the transmittance is related to the optical and physical properties of the sample through the **Beer-Lambert law** [60]:

$$T = \frac{\mathrm{I_t}}{\mathrm{I_{in}}} = (1 - \mathrm{r})^2 \mathrm{e}^{-\alpha \mathrm{L}} \tag{3.6}$$

where α is the absorption coefficient, L is the thickness of the sample, and r is the Fresnel reflection coefficient at normal incidence at the interface air-sample, that depends on the real part of the refractive index (n) [60]:

$$r = \left(\frac{\mathrm{n} - 1}{\mathrm{n} + 1}\right)^2 \tag{3.7}$$

Therefore, the absorption coefficient α can be easily calculated once T, n and L are known. Besides, the relation between the absorption coefficient, $\alpha(\lambda)$, in cm^{-1}, and the extinction coefficient, $k(\lambda)$, is [60]:

$$k(\lambda) = \frac{\alpha(\lambda)\lambda}{4\pi} \tag{3.8}$$

where λ is the wavelength of light (in cm). In addition, sometimes it is convenient to use the **absorbance** (A), rather than transmittance. The absorbance is defined as: $A = ln(1/T)$ so it varies linearly with the absorption coefficient and the thickness of the sample.

In this thesis we have determined the transparency region of TeO_2–ZnO–ZnF_2 glasses in the ultraviolet, visible and near infrared wavelength range with a commercial spectrophotometer (Cary 5000) operating at normal incidence in the range 200-3000 nm. In the case of bulk glasses, we have measured the transmittance of optically polished plano-parallel glass slabs ~1 mm thick; whereas in the case of thin film glasses produced by PLD, they were grown on transparent substrates, such as fused silica, to measure their transmittance in this wavelength range. Since the ultraviolet absorption edge of the substrate is blue shifted with respect to the absorption edge of the glass film, the transmittance measurement of glass films was not affected by the presence of the

substrate. We estimated the ultraviolet absorption edge of bulk glasses by calculating the value of their ***cut-off wavelength*** (λ_c), defined as the wavelength at which $T(\lambda_c)= 0.5T_{max}$ [76].

However, we cannot compare the cut-off wavelength of bulk and film glasses since the accuracy of the measurements depends on the thickness of the sample, as we describe next. Figure 3.12 shows the visible and near-infrared transmittance of a TeO_2–ZnO–ZnF_2 bulk glass (1 mm thick) and of a thin film glass (100s nm thick) deposited on fused silica (SiO_2), both with the same nominal composition.

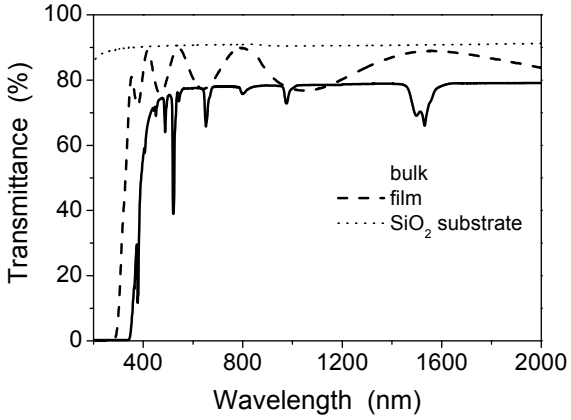

Figure 3.12: Transmittance spectra of bulk and film Er-doped TeO_2–ZnO–ZnF_2 glasses with similar composition. The transmittance spectrum of the fused silica substrate, where the film was grown, is included for comparison.

From Fig. 3.12, we note that the cut-off wavelength (λ_c) of the film and bulk glasses are apparently very different. Even if a small difference in λ_c between the two types of glasses could arise from their slightly different composition and structure originated by the different fabrication methods; the large difference observed in Fig. 3.12 is an artefact that is due to the maximum sensitivity of the spectrophotometer detector, which is able to measure a minimum value of transmittance equal to $5\cdot10^{-4}$ (assuming the maximum transmittance is 1). Since T scales as $\exp(-\alpha L)$, the transmittance reaches zero (*i.e.* $5\cdot10^{-4}$) when $\alpha L= -\ln(5\cdot10^{-4})$, neglecting the reflection coefficient ($r\approx 0$). Therefore, the maximum α value measured by the spectrophotometer depends on the thickness of the sample (L), this value being larger for thinner samples. For example, a bulk glass (L= 0.1 cm) will have $T= 5\cdot10^{-4}$ at a wavelength for which $\alpha= 76$ cm^{-1}, while for a thin film glass ($L= 10^{-4}$ cm) the value $T= 5\cdot10^{-4}$ will be reached for a wavelength corresponding to $\alpha= 76\cdot10^3$ cm^{-1}. Therefore, since the cut-off wavelength of the film corresponds to a much larger α than in the case of the bulk glass, it will be blue shifted

with respect to that of the bulk, as shown in Fig. 3.12. For this reason, we cannot compare the cut-off wavelength of glasses with very different thickness as film and bulk glasses.

The upper wavelength limit of the Cary 5000 spectrophotometer in the infrared region (3000 nm) did not allow us to determine the position of the infrared absorption edge of TeO_2–ZnO–ZnF_2 glasses neither the magnitude of the infrared absorption bands due to OH^- molecular vibrations. Therefore, we have performed Fourier transform infrared (FTIR) absorption measurements of bulk and thin film glasses in collaboration with B. Maté from the *Instituto de Estructura de la Materia* (CSIC, Madrid). We have used a Bruker IFS 66 spectrophotometer in the range 1.5-10 μm, subtracting the contribution of atmospheric OH^-s from each measured spectra. Moreover, in the case of thin film glasses, deposited on transparent substrates (borosilicate glasses), the contribution of the substrate was subtracted from the measured spectra (film + substrate) in order to determine the absorption spectra of film glasses.

We have determined the concentration of OH^- groups (ions cm^{-3}) in TeO_2–ZnO–ZnF_2 glasses through the Beer-Lambert law:

$$N_{OH} = \frac{N_A}{\varepsilon}\,\alpha_{OH} \tag{3.9}$$

where N_A is the Avogadro's number; $\varepsilon = 49.1 \cdot 10^3$ $cm^2\,mol^{-1}$ is the molar absorptivity of OH^- groups in silicate glasses [98]; α_{OH} (in cm^{-1}) is the absorption coefficient corresponding to OH^- groups in the infrared absorption spectrum of glass.
We have also estimated the parts per million (*ppm*) of OH^- groups in bulk glasses using the equation [145]:

$$C_{OH} = \frac{N_{OH} W_{OH}}{N_{OH} W_{OH} + N_{glass} W_{glass}} \tag{3.10}$$

where W_{OH} and W_{glass} are the molecular weight of OH^- and glass, respectively, while N_{OH} and N_{glass} are the number of OH^- and glass molecules in 1 cm^3, respectively.

3.4.3 Steady-state and time-resolved photoluminescence spectroscopy

Photoluminescence (PL) spectroscopy was employed to investigate the photoluminescence response of rare earth doped TeO_2–ZnO–ZnF_2 glasses. The experimental measurements of PL spectroscopy can be classified into: steady-state and time-resolved measurements. The main difference between them lies in the type of illumination used to excite the sample and in the system used to detect the PL signal. Steady-state measurements are performed under constant illumination conditions while time resolved measurements are performed with a pulsed illumination. In steady-state spectroscopy, the glass sample is illuminated with a continuous laser beam and the emission spectrum is recorded by means of a monochromator and a photodetector. Because of the short timescale of photoluminescence from rare earth ions in glasses (μs up to ms range), steady-state is reached almost immediately when the sample is first exposed to light [86]. Thus, most PL measurements are steady-state. Instead, in time-resolved spectroscopy the sample is exposed to a pulse of light that has duration shorter than the one of the PL signal. Then, the **intensity** of PL is recorded as a function of time by a photodetector and an oscilloscope. In this case, the intensity $I(t)$ of PL that results from exciting the sample with light, whose intensity $K(t)$ varies with time t in an arbitrary way, can be expressed by [86]:

$$I(t) = \int_0^\infty \mathrm{K}(\mathrm{t}-\mathrm{t}')\,\varphi(\mathrm{t}')d\mathrm{t}' \tag{3.11}$$

where $\varphi(t)$ is the photoluminescence decay function. This relation is generally valid if the number of excited molecules in a system is small compared with the total number of molecules and the system does not undergo a permanent change under light excitation. For the particular case of a steady-state excitation turned off at $t = 0$ ($K(t)= 1$ for $t< 0$ and $K(t)= 0$ for $t> 0$ in eq. (3.11)) then, the PL intensity is given by:

$$I(t) = \int_0^\infty \varphi(\mathrm{t}')d\mathrm{t}' \tag{3.12}$$

The advantage of using a pulsed excitation is the possibility of extracting information about the relaxation mechanisms of the photoluminescent ions. In particular, the PL *decay time*, or *lifetime* of the emitting state, can be determined.

It general, the ***mean lifetime*** of the PL emission is determined as [86]:

$$\tau_m = \frac{\int_0^\infty t\varphi(t)dt}{\int_0^\infty \varphi(t)dt} \tag{3.13}$$

In the particular case when the photoluminescence decay function ($\varphi(t)$) is purely exponential, *i.e.* $\varphi(t)= \varphi(0)\exp(-t/\tau)$, then $\tau_m = \tau = \varphi(0)/e$. The $\boldsymbol{\tau}$ value is usually called the ***lifetime*** of the PL emission or *1/e decay time*. A single exponential decay of the PL emission is associated with fast diffusion of the excitation energy among rare earth ions, that is, spatial equilibrium of the excitation is reached in a time shorter than the decay time [146]. Nevertheless, sometimes the PL decay function is not a single exponential function but it can be fitted by using two different single exponential functions. This fact may be due to local inhomogeneities in the environment of rare earth ions [146]. For example, in chapter 5, the exponential decay of the $^4I_{13/2} \rightarrow {}^4I_{15/2}$ Er^{3+} emission in glass-ceramic samples is fitted by two single exponential functions due to the presence of Er^{3+} ions in crystalline and amorphous environments.

The characterization of the PL response of rare earth doped TeO_2–ZnO–ZnF_2 bulk and film glasses was performed in collaboration with A. Miguel and R. Balda from the *Departamento de Física Aplicada I* (*Universidad del País Vasco*, Bilbao). Figure 3.13 shows a schematic representation of the experimental system used to acquire the PL emission spectra of rare earth doped TeO_2–ZnO–ZnF_2 glasses through steady-state measurements.

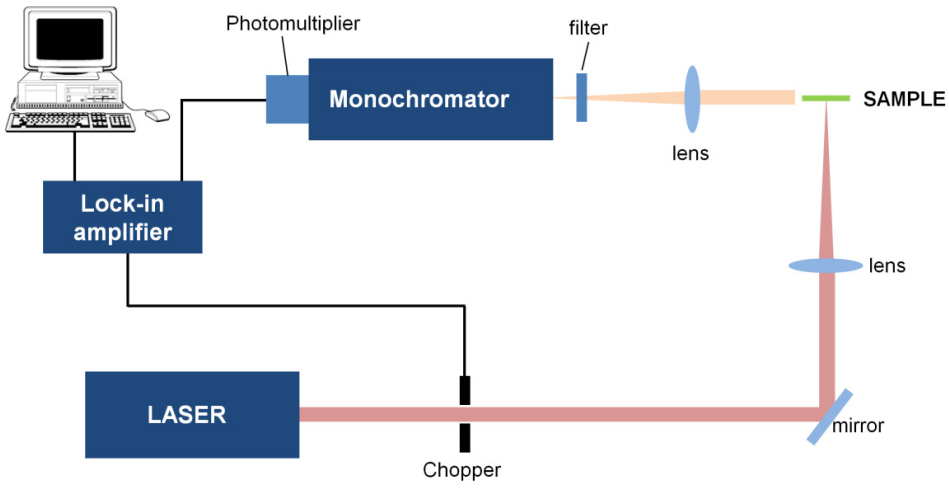

Figure 3.13: Scheme of the set-up employed to perform steady-state photoluminescence measurements.

The sample were excited either by an Ar laser (visible range) or a Ti:sapphire ring laser (near infrared range). Then, the PL signal was analyzed with a 0.19 m monochromator (Horiba Jobin-Ivon) equipped with three diffraction gratings with blaze wavelength 500 nm, 1000 nm, and 1500 nm, respectively. The monochromator is coupled to a photomultiplier (Hamamatsu R928 or H10330A-75 for visible and near infrared detection, respectively) to collect the PL signal and convert it into an electrical signal. Finally, the PL signal was amplified by a standard lock-in technique and the PL spectrum was recorded with the help of a computer software.

The PL decay signal of rare earth doped TeO_2–ZnO–ZnF_2 glasses was recorded with a set-up similar to that of Fig. 3.13 through time-resolved measurements. Contrary to steady-state measurement, pulsed excitation light sources were used in this case: a dye laser pumped by a pulsed nitrogen laser as visible excitation (1 ns pulse duration) or a Ti:sapphire laser pumped by a pulsed frequency doubled Nd:YAG laser as near infrared excitation (9 ns pulse duration). The PL emission was detected by the adequate photomultiplier and finally the PL decay signal was obtained by processing the signal with a digital oscilloscope and recorded by a computer software.

As an example, Figure 3.14 shows the emission spectrum and the photoluminescence decay of the near infrared transition $^4I_{13/2} \rightarrow {}^4I_{15/2}$, measured in an Er doped TeO_2–ZnO–ZnF_2 bulk glass.

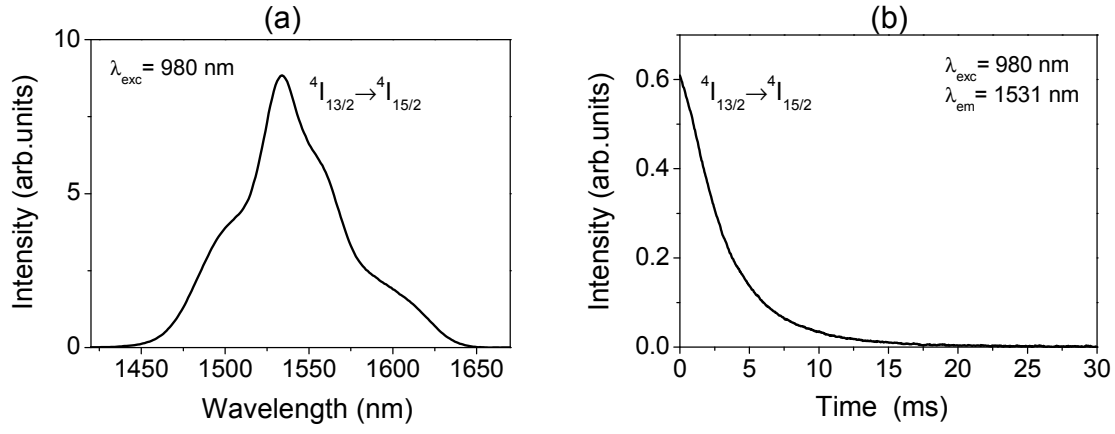

Figure 3.14: (a) Emission spectrum of the Er^{3+} transition $^4I_{13/2} \rightarrow {}^4I_{15/2}$ by pumping a TeO_2–ZnO–ZnF_2 glass at 980 nm (cw). (b) Photoluminescence decay function of the maximum intensity of the emission $^4I_{13/2} \rightarrow {}^4I_{15/2}$ (at 1531 nm) by pumping the sample with a laser pulse of 9 ns, at 980 nm.

4

Rare earth doped TeO_2–ZnO–ZnF_2 glasses

4.1 Introduction

As described in the introductory chapters, **fluorotellurite glasses** present improved properties with respect to tellurite glasses, in particular when considered as hosts for rare-earth ions. The introduction of fluorine improves the mid-IR transmission of fluorotellurite glasses by reducing the content of hydroxyl groups [37, 147]. Moreover, the efficiency of rare earth radiative transitions increases by decreasing the OH^- concentration in glasses since these groups are nonradiative quenching centres for excited rare earth ions, as described in chapter 2. Actually, Zhan and co-authors reported an intense infrared emission at 2.7 μm ($^4I_{11/2} \rightarrow {}^4I_{13/2}$) in Er^{3+}-doped fluorotellurite glasses, that is usually quenched in tellurite glasses. They relate this emission to the very small OH^- concentration in their glasses that led to a larger population of the $^4I_{11/2}$ level [148]. Furthermore, the introduction of fluorine modifies the local electrostatic field symmetry around rare earth ions, which results in a reduction of the electron-phonon coupling. Thus, nonradiative deexcitation via multiphonon relaxation is reduced and the efficiency of radiative transitions increases in doped fluorotellurite glasses with respect to tellurite glasses [38, 149].

In this chapter we report and discuss the results obtained in the study of the TeO_2–ZnO–ZnF_2 glass system as host for RE ions. This system has already been reported to show good structural and optical properties [149, 150, 151]. We dedicate the first part of the chapter to the characterisation of the composition, thermal behaviour and structure of the produced glasses. Then, we present their transmittance and their linear refractive index. In the second part of the chapter, we study the photoluminescence response of rare earth doped glasses by varying the type and concentration of the dopant ion. We start with the study of a series of Er-doped TeO_2–ZnO–ZnF_2 glasses to find out the most

suitable doped glasses for optical applications. In fact, both the properties of the glass host and concentration quenching effects, arising when increasing the dopant concentration, have to be taken into account for practical applications. Moreover, the exhaustive characterization of these Er-doped glasses served as preliminary step to select adequate candidates for the production of Er-doped TeO_2–ZnO–ZnF_2 glass-ceramics, as it will be shown in chapter 5, which has never been reported before.

The chapter ends with the photoluminescence characterisation of the selected TeO_2–ZnO–ZnF_2 host co-doped with different Er^{3+}-Yb^{3+} and Er^{3+}-Tm^{3+} concentrations to improve the pumping efficiency of Er^{3+} ions and generate an ultra broad near infrared emission, respectively.

4.2 Composition and density

TeO_2–ZnO–ZnF_2 glasses were produced by the conventional melt-quenching technique, described in chapter 3. We have selected two TeO_2–ZnO–ZnF_2 glass hosts (DF-1 and DF-2) having different Zn/Te and F/O ratios, from the study of Nazabal and coworkers [151]. Their nominal composition is:

- **DF-1**: 74.6 TeO_2–8.8 ZnO–16.6 ZnF_2 (mol%) **Zn/Te**≈ 0.34; **F/O**≈ 0.21
- **DF-2**: 46.6 TeO_2–18.2 ZnO–35.2 ZnF_2 (mol%) **Zn/Te**≈ 1.15; **F/O**≈ 0.63

Each glass matrix was doped with an increasing concentration of ErF_3: 0.5, 1, 2 and 3 wt% (corresponding to 0.35, 0.7, 1.4 and 2.1 mol%, respectively).

We have measured the density of DF-1 and DF-2 by applying the Archimedes' principle, using bromonaphthalene at room temperature ($C_{10}H_7Br$, ρ_{20^oC}= 1.48 g/cm^3) as immersion liquid, whereas the composition of the fluorotellurite bulk glasses was determined by combining Rutherford backscattering spectrometry (RBS) and proton-induced gamma ray emission (PIGE) techniques, as described in chapter 3. As an example, Figure 4.1 presents the experimental and simulated RBS spectra of DF-1 and DF-2 glasses doped with 1 wt% ErF_3.

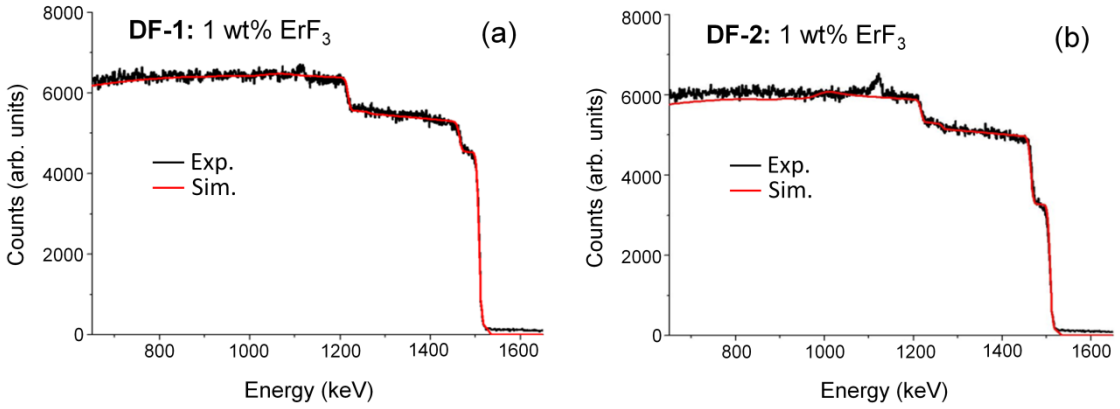

Figure 4.1: Experimental and simulated RBS spectra of: (a) DF-1: 1 wt% ErF_3; (b) DF-2: 1 wt% ErF_3.

We clearly observe three edges in the RBS spectra of Fig. 4.1 at ~1520, ~1480, and ~1200 keV which belong to Te, Zn and O signals, respectively. Moreover, their height is related to the content of each element in the glass. Thus, we infer that the Te content is larger in DF-1 than in DF-2 while the Zn content is smaller in DF-1 than in DF-2.

Table 4.1 summarizes the relative nominal and experimental compositions as well as the density of DF-1 and DF-2, doped with 1 wt% ErF_3. The density and the atomic concentration of Te, Zn, O and F are similar in the other DF-1 and DF-2 glasses doped with different ErF_3 concentrations within the resolution of the experimental set-up used, and therefore they are not reported here.

The relative concentration of each element, $[X]_{rel}$, was calculated by normalizing the atomic concentration of the element, X (% at.), determined from RBS or PIGE analysis, to the total cationic concentration: $[X]_{rel} = (X/\Sigma X_{i,cat})x100$. The estimated experimental error is ± 10 % for the concentration of Te, Zn, O and F while is ± 30 % for the Er concentration, due to its small RBS signal (see chapter 3). The maximum experimental error affecting the density measurements is ± 0.5 %.

Table 4.1: Nominal and experimental relative composition and density of DF-1 and DF-2 glasses doped with 1 wt% ErF_3.

Sample		$[Te]_{rel}$ (%)	$[Zn]_{rel}$ (%)	$[Er]_{rel}$ (%)	$[O]_{rel}$ (%)	$[F]_{rel}$ (%)	Density (g/cm^3)
DF-1	Nominal	74	25	0.6	157	35	
	Experimental	68 ± 7	31 ± 3	0.8 ± 0.3	152 ± 15	19 ± 2	5.48 ± 0.03
DF-2	Nominal	47	52	0.5	110	73	
	Experimental	38 ± 4	61 ± 6	0.3 ± 0.1	108 ± 18	37 ± 4	5.36 ± 0.03

The density values presented in Table 4.1 for DF-1 and DF-2 are in good agreement with those reported in the literature for glasses of similar composition [151]. DF-2, which has a larger Zn and F content and a smaller Te content with respect to DF-1, presents a density smaller than DF-1. This behaviour stems from the higher atomic weight of Te (127.6) compared to Zn (65.4), as it has been described in the literature for zinc-tellurite glasses with varying Te/Zn ratio [149, 152].

The measured fluorine relative concentration shows that both DF glasses present large fluorine losses that are about 45-50 % of their nominal value, while the relative oxygen content is similar to the nominal one. Concerning the cationic concentration, a relative enrichment of Zn with respect to Te is observed both in DF-1 and DF-2. As described above, the small Er content is affected by a large experimental error and thus it is not

possible to extract any conclusion about its relative concentration with respect to Te or Zn.

From the results of RBS-PIGE analysis, we have calculated the real composition of DF-1 and DF-2 glasses:

- **DF-1**: 68 TeO_2–22 ZnO–10 ZnF_2 (mol%) **Zn/Te**≈ 0.47; **F/O**≈ 0.12

- **DF-2**: 35 TeO_2–46 ZnO–19 ZnF_2 (mol%) **Zn/Te**≈ 1.86; **F/O**≈ 0.33

We clearly observe in both glasses a reduction in TeO_2 and ZnF_2 with respect to ZnO content. Finally, the difference between the real and nominal composition is larger for DF-2, which has the largest F content, than for DF1-1.

Fluorine losses are usually observed during the melting of fluorotellurite glasses [37, 147, 151] and it is difficult to avoid them even when using a covered crucible, as it was done in this work. The addition of fluorine to the batch, in the form of ZnF_2, chemically dehydrates the melt by eliminating both the OH^-s inside the glass melt (in the form of [≡Te-OH]) and, at the same time, adventitious atmospheric water dissolved in the melt (H_2O). The chemical reactions taking place between ZnF_2 and the OH^-s inside the glass melt (4.1) and between ZnF_2 and the atmospheric water (4.2), generate HF which is volatile and leads to the partial loss of fluorine [37, 147]:

$$2\ [\equiv Te\text{-}OH] + ZnF_2 \rightarrow \equiv Te–O–Te \equiv + ZnO + 2HF\uparrow \quad (4.1)$$

$$ZnF_2 + H_2O \rightarrow ZnO + 2HF\uparrow \quad (4.2)$$

Furthermore, according to the reactions 4.1 and 4.2, ZnF_2 is converted in ZnO during the melting dehydration. In addition, Zn enrichment, *i.e.* the increase in the Zn/Te ratio, can be attributed to a partial loss of Te during the melting. Te losses have been previously observed in glasses of similar composition and attributed to evaporation from the glass melt of highly volatile compounds, such as TeF_4 [151].

4.3 Thermal analysis

An important parameter to consider in the manufacture and technological applications of glass is its stability, which is defined in terms of glass resistance to crystallisation during heating. Glass stability, or thermal stability, is measured as the difference between the crystallisation (T_c) and the glass transition (T_g) temperatures, for a sample heated at a specified linear rate. In order to be more conservative and to follow the same criterion used by Nazabal and co-authors [151], we have calculated the glass thermal stability as the difference between the onset of crystallisation (T_{on}) and the glass transition temperatures.

Figure 4.2 shows the experimental DSC curves for the two TeO_2–ZnO–ZnF_2 glasses considered in this work, with an increasing concentration of ErF_3. The heating rate used in the DSC measurements was 10 ºC/min. From the DSC curves we have determined the glass transition (T_g), onset of crystallisation (T_{on}), crystallisation (T_c) and melting (T_m) temperatures as described in chapter 3.

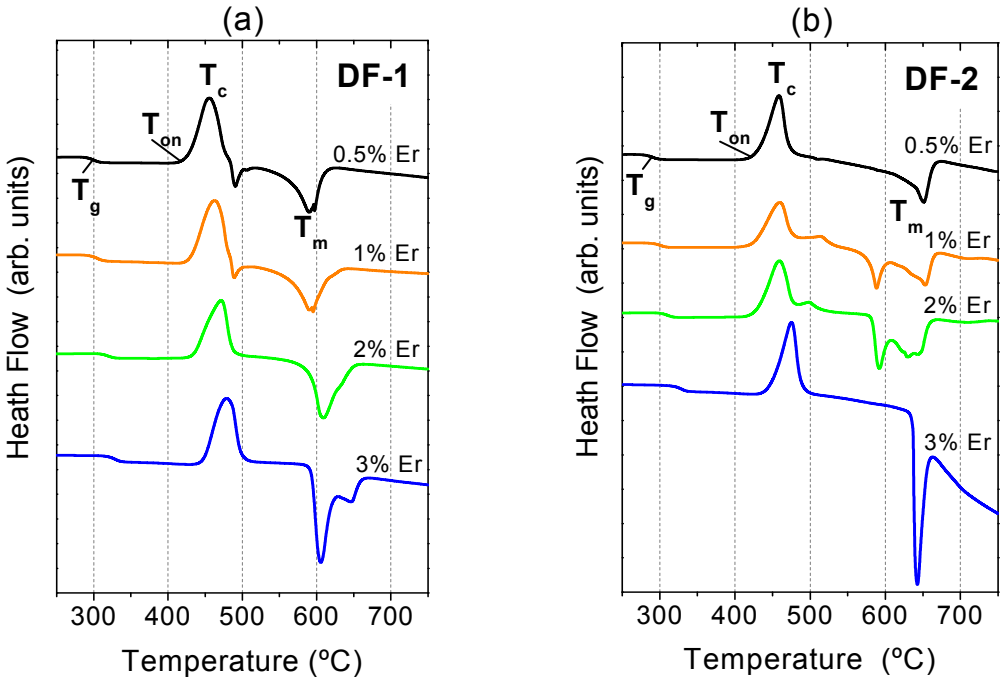

Figure 4.2: DSC curves of TeO_2–ZnO–ZnF_2 glasses doped with ErF_3 (0.5-3 wt%): (a) DF-1; (b) DF-2.

Table 4.2 summarizes the experimental values of T_g, T_{on}, T_c and T_m for each glass composition, together with the glass thermal stability calculated as ($T_{on} - T_g$).

Table 4.2: Glass transition (T_g), onset of crystallisation (T_{on}), peak crystallisation (T_c), peak melting (T_m) temperatures, and glass thermal stability ($T_{on} - T_g$) for DF-1 and DF-2 doped with increasing ErF_3 content (wt%).

Sample	T_g (ºC)	T_{on} (ºC)	T_c (ºC)	T_m (ºC)	$T_{on} - T_g$ (ºC)
DF-1:					
0.5 % Er	300	418	456	491, 591	118
1 % Er	305	425	463	490, 592	120
2 % Er	318	430	471	609	112
3 % Er	328	443	480	606, 647	115
DF-2:					
0.5 % Er	290	417	458	652	127
1 % Er	301	420	461, 514	589, 655	119
2 % Er	310	422	460, 498	592, 638	112
3 % Er	327	440	476	643	103

Both DF-1 and DF-2 glasses have a large thermal stability range: ($T_{on} - T_g$)> 110 ºC, except glass DF-2: 3% Er which has a smaller value, but still > 100 ºC. Therefore, these Er-doped fluorotellurite glasses should be suitable for optical fibre drawing. Moreover, they show a similar trend with the increase of ErF_3 content: T_g, T_{on} and T_c shifts towards higher values, while T_m seems to be not affected by the increase of ErF_3. Jha and co-authors reported this behaviour in Er doped tellurite glasses where they related the increase of T_g and T_c to the strong bonding of Er^{3+} with nonbringing oxygens, which led to an increase of the rigidity of the glass network [153]. We also observe that T_g is lower in DF-2 than in DF-1 for glasses with the same Er content. This fact has been previously described by Nazabal and co-authors [151]. They relate it to the breaking of the strong TeO_2 covalent network upon addition of F and Zn. The first forms ionic, non-bridging bonds with Te atoms, enabling the glass-forming liquid to be more fluid at low temperatures; hence the isoviscous point, *i.e.* T_g, decreases as fluorine concentration increases [37]. In a similar way, the addition of Zn, which is a network modifier, decreases the rigidity of the glass network too by decreasing the number of bridging oxygens and the coordination number of Te [151, 153].

The crystallisation of zinc-fluorotellurite and zinc-tellurite glasses has been studied by Nazabal and Nukui, respectively, by using in-situ high-temperature X-ray diffractometry (XRD) [151, 154]. This technique consists in recording rapid X-ray diffraction patterns while the sample is heated. Therefore, the structural changes and the crystalline phases which form when heating the glass can be identified and related to the

DSC curve of the sample. They observed that the principal crystalline phases that nucleate in zinc-fluorotellurite and zinc-tellurite glasses are: α-TeO_2 (paratellurite) and $Zn_2Te_3O_8$ [151, 154]. These crystalline phases are present in the XRD patterns of zinc-fluorotellurite and zinc-tellurite glasses until reaching their main melting temperature (~600 ºC), when they disappear [151, 154].

We have performed XRD measurements on an annealed DF sample (DF-1: 1 wt% ErF_3) which showed clear sign of crystallisation, *i.e.* it was opaque after the annealing treatments. We have identified α-TeO_2 and $Zn_2Te_3O_8$ crystalline phases in the XRD pattern of the sample (Fig. 4.3), in agreement with the study by Nazabal and Nukui. For this reason, we also attribute the endothermic peaks observed close to 600 °C in the DSC curves of DF-1 and DF-2 glasses (Fig. 4.2) to the melting of these phases.

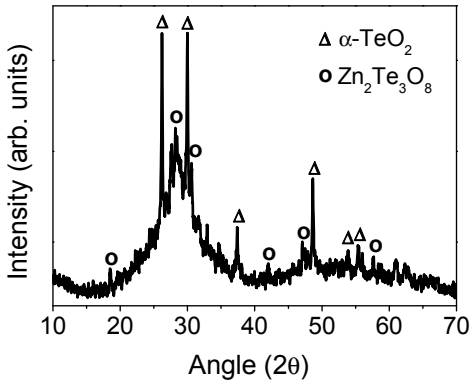

Figure 4.3: XRD pattern of a partially crystallized glass (DF-1: 1 wt% ErF_3). Diffraction peaks belong to α-TeO_2 (**Δ**) and $Zn_2Te_3O_8$ (**O**) crystalline phases.

Besides, we observe additional crystallisation and melting peaks in some of DF glasses, such as in the case of DF-2: 1, 2 wt% ErF_3 (Fig. 4.2b). Nazabal identified an additional crystalline phase ($ZnTeO_3$) through in-situ high-temperature XRD analysis in a glass with similar composition [151]. This phase crystallised in crystallised in correspondence of the main crystallisation peak (~460 °C). Furthermore, the crystallisation temperature of the α-TeO_2 phase was shifted to a higher temperature in this sample, which might explain the additional crystallisation peak observed at ~500 ºC in the DSC curves of DF-2: 1, 2 wt% ErF_3 (Fig. 4.2b). However, the additional melting peak at ~650 ºC observed for some of DF glasses (Fig. 4.2), could not be attributed to the melting of any known phase [151].

Finally, the small endothermic peak present at ~490 ºC in the case of DF-1: 0.5, 1 wt% ErF_3 (Fig. 4.2a) was assigned by Nazabal to the melting of γ-TeO_2, an instable crystalline phase found in glasses with similar composition to DF-1, which disappeared at lower temperatures than α-TeO_2 and $Zn_2Te_3O_8$ [151].

4.4 Structural characterization

Fourier-transform (FT) Raman spectroscopy has been employed to study the glass network structure of DF glasses. Er-doped DF-1 and DF-2 samples were excited at 1064 nm with an incident power of 30 mW. Experimental Raman spectra have been normalized to their maximum intensity and reduced to ease their comparison, as described in chapter 3. Figure 4.4 presents the Raman spectra of Er-doped DF-1 and DF-2 glasses (0.5-3 wt% ErF_3) in the 200-1000 cm^{-1} range. They show three broad bands, peaking at about 440, 660 and 740-770 cm^{-1}, which are characteristic of zinc-tellurite glasses [152, 153, 155, 156, 157] and zinc-fluorotellurite glasses, obtained by partial substitution of ZnO with ZnF_2 [149, 150, 151]. The increase in ErF_3 content does not affect the glass network, since all DF-1 and DF-2 spectra are very similar between them. Of course, this is related to the small percentage of erbium present in the glass. However, Jha and co-authors have addressed the role Er^{3+} plays in the network of tellurite glasses and have suggested that Er^{3+} ions most likely act as network modifiers [153].

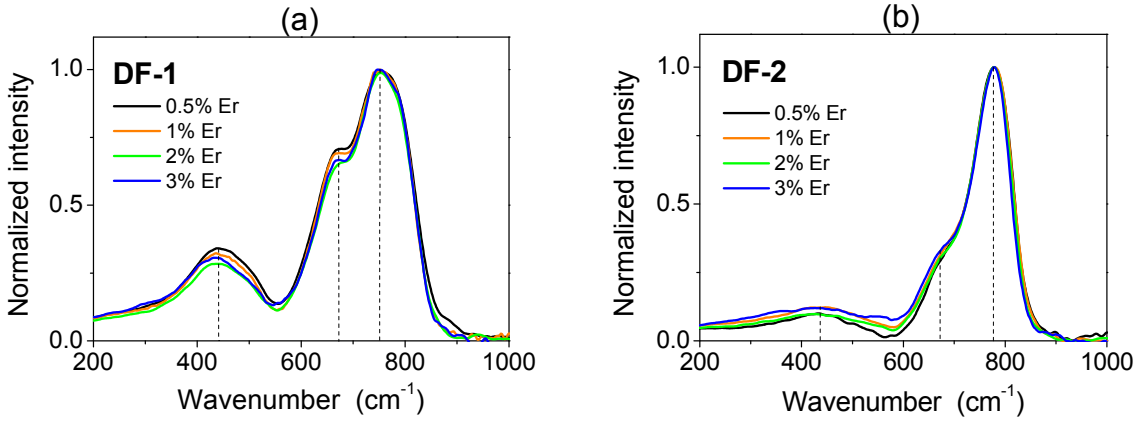

Figure 4.4: Normalized reduced Raman spectra of the Er-doped TeO_2–ZnO–ZnF_2 glasses (0.5-3 wt% ErF_3). (a) DF-1; (b) DF-2.

An excellent starting point to understand the network structure of DF-1 and DF-2 glasses is to consider the structure of α-TeO_2 and $Zn_2Te_3O_8$, which are the main crystalline phases that nucleate in these types of glasses, as described in the previous section. Moreover, Raman vibrations are mainly sensitive to the polarizability of tellurium entities, therefore we first describe the structural units formed by Te in these glasses. The structure of α-TeO_2 is formed by a three-dimensional network of TeO_4 trigonal bipyramids (tbp) connected in infinite chains by shared vertices. In each TeO_4 group, Te forms two equatorial bonds (Te-O_{eq}) and two axial bonds (Te-O_{ax}) with oxygen with a bond length of 1.9 and 2.08 Å, respectively [158]. TeO_4 tbp are linked by sharing an oxygen atom, being in axial position in one polyhedron and in equatorial position in the other, and so forming Te-$_{ax}O_{eq}$-Te bonds (see Fig. 4.5a) [159]. The structure of $Zn_2Te_3O_8$ is built up of infinite chains of Te_3O_8 groups, which are formed by one TeO_4 tbp and two TeO_{3+1} polyhedra, which are distorted TeO_4 tbp. They are connected by a long Te-O bond (~2.4 Å) in infinite chains, as represented in Fig. 4.5b [157, 160].

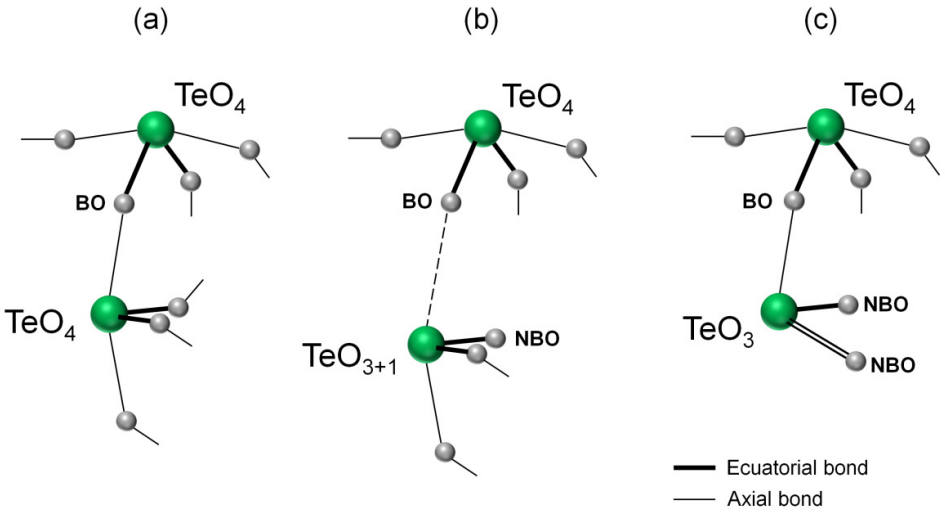

Figure 4.5: Schematic drawing of the structural units in tellurite crystals and glasses. (a) TeO_4 trigonal bipyramids (tbp); (b) TeO_4 tbp linked to a TeO_{3+1} polyhedron; (c) TeO_4 tbp linked to a TeO_3 trigonal pyramid. Bridging oxygen (BO) and non-bridging oxygen (NBO) atoms are indicated in the figure.

A pure tellurite glass would present a structure similar to that of α-TeO_2. However, during the vitrification process of a zinc-tellurite glass, the introduction of ZnO leads to a progressive transformation of the α-TeO_2 structure to a $Zn_2Te_3O_8$ structure due to the addition of a glass modifier cation, such as Zn^{2+}, which leads to the deformation and

breaking of Te-O_{ax} bonds in TeO_4 tbp [152, 156, 157]. When one of the axial bonds of a TeO_4 tbp is stretched, this becomes a TeO_{3+1} polyhedron (Fig. 4.5b). In the limit, a Te-O_{ax} bond can be cleaved and thus a TeO_3 trigonal pyramidal (tp) structural unit is produced (Fig. 4.5c). Therefore, Te will have a reduced coordination number in the resulting glass network [155, 161]. Moreover, the formation of TeO_{3+1} and TeO_3 units leads to the conversion of some of the single bonded bridging oxygens (BO) into single bonded or doubly bonded non-bridging oxygens (NBO), as shown in Fig. 4.5b-c.

The described structural modifications in zinc-tellurite glasses have been confirmed by neutron diffraction experiments, which show that ZnO forms ZnO_6 polyhedra in these glasses, which are incorporated in infinite chains of TeO_4-TeO_3 units and lead to the formation of TeO_3 and TeO_{3+1} polyhedra [158]. Figure 4.6 shows a structural model adapted from Kozhukharov et al. [158] that illustrate the atomic arrangement of a zinc-tellurite glass (80 TeO_2–20 ZnO mol%).

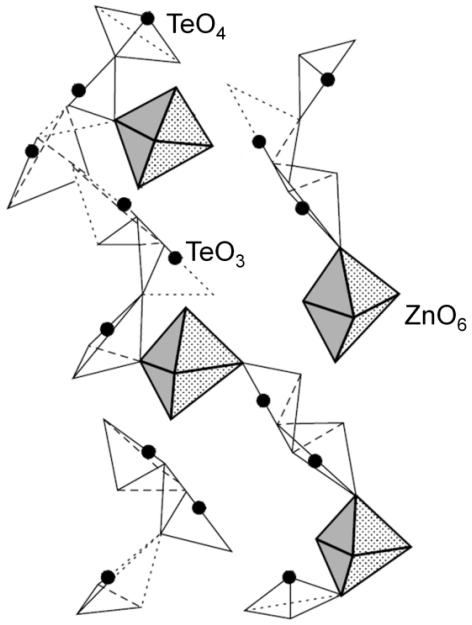

Figure 4.6: Model representing the atomic arrangement of a 80 TeO_2–20 ZnO mol% glass. A fraction of ZnO_6 polyhedra are incorporated into and between the infinite chains of TeO_4–TeO_3 units. Adapted from Ref. [158].

In order to assign the Raman bands in the spectra of DF glasses (Fig. 4.4) to molecular vibrations in the structural units TeO_4, TeO_{3+1} and TeO_3 described above, we have first deconvoluted the Raman spectra of DF-1 and DF-2, doped with 1 wt% ErF_3, into 5 Gaussian bands. The number of bands and their initial position was set according to the Raman bands of α-TeO_2 [153]. Then, a fitting was realized to determine the peak

position, width and intensity of each Gaussian band, by minimizing the mean square error (MSE) between the experimental and calculated Raman envelopes [162]. The Gaussian bands obtained with this procedure are shown in Figure 4.7 for DF-1 and DF-2 and indicated as A, B, C, D and E. They have been assigned to the stretching and bending vibrations of Te-O, Te-O-Te and Te-O_{NBO} bonds in the TeO_4, TeO_{3+1} and TeO_3 structural units according to the literature on the structure of zinc-tellurite and zinc-fluorotellurite glasses [151, 150, 152, 153, 155, 157].

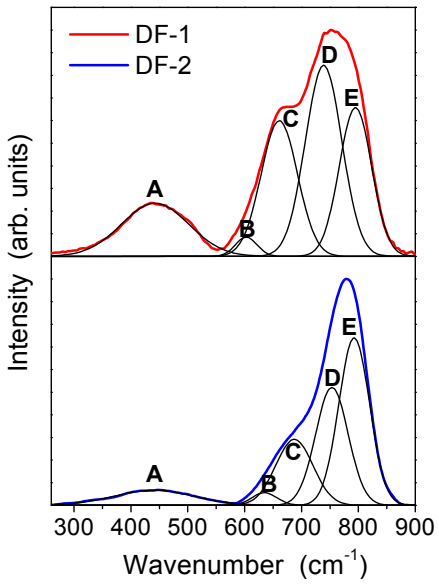

Figure 4.7: Deconvolution of the Raman spectra of DF-1 and DF-2, doped with 1 wt% ErF_3, in five Gaussian bands: A, B, C, D and E. Spectra have been shifted vertically to ease their comparison.

Band A, at ~440cm^{-1}, corresponds to the low energy broad band in the Raman spectra of DF glasses. It is assigned to symmetric and bending vibrations of Te-O-Te bonds at corner sharing sites of TeO_4, TeO_{3+1} and TeO_3 polyhedra. Its intensity is related to the network connectivity.

The middle broad Raman band, at ~660 cm^{-1}, has been deconvoluted into two Gaussian bands (B and C). Band B is associated to vibration of a continuous TeO_3/TeO_4 network while band C is assigned to the symmetric stretching of Te-O bonds in TeO_4 units together with coupled symmetric vibrations along Te-O-Te links in TeO_4/TeO_3 pairs. Finally, the broad band at the highest energy, ~740-770 cm^{-1}, has been deconvoluted into two Guassian bands (D and E) as well. Band D is assigned to the symmetric stretching of Te-O bonds in TeO_{3+1} units and to vibrations of Te-O_{NBO} bonds in TeO_{3+1}/TeO_3 units, whereas band E is assigned to the symmetric stretching of Te-O

bonds in TeO_3 polyhedra. Table 4.3 summarizes the position and the band assignment for each Gaussian band of Fig. 4.7.

Table 4.3: Band assignment, peak position (Peak) and normalized intensity (I_N) of the Gaussian bands obtained by deconvolution of the Raman spectra of DF-1 and DF-2 doped with 1 wt% ErF_3.

Raman band	DF-1 Peak (cm^{-1}); I_N	DF-2 Peak (cm^{-1}); I_N	Assigned vibrational modes
A	442; 0.23	441; 0.07	Symmetric and bending vibrations of Te-O-Te bonds at corning sharing sites.
B	603; 0.08	635; 0.06	Vibration of continuous TeO_3/TeO_4 network.
C	661; 0.59	687; 0.30	Symmetric stretching of Te-O in TeO_4 units. Coupled symm. vib. along Te-O-Te in TeO_4/TeO_3 pairs.
D	734; 0.84	753; 0.52	Symm. stretching of Te-O in TeO_{3+1} units. Vibrations of Te-O_{NBO} in TeO_{3+1}/TeO_3 units.
E	795; 0.65	792; 0.74	Symm. stretching of Te-O in TeO_3 units.

We note that the most intense band in the Raman spectrum of DF-1 is band D, related to TeO_{3+1} units, while the most intense band in the spectrum of DF-2 is band E, related to TeO_3 units (Fig. 4.7). In addition, by considering the intensity of the deconvoluted bands (Table 4.3), we can infer that the structure of DF-1 (Zn/Te≈ 0.47) is mainly composed by TeO_{3+1} units (band D), followed by TeO_3 (band E) and TeO_4 (band C) polyhedra in almost equal parts. On the contrary, the network structure of DF-2 (Zn/Te≈ 1.86) is mainly composed by TeO_3 trigonal pyramids (band E) followed by TeO_{3+1} polyhedra (band D) and by only few TeO_4 trigonal bipyramids (band C). Besides, the glass network is well connected in DF-1 while is poorly connected in the case of DF-2, as indicated by the reduced intensity of band A in the latter case. However, both DF glasses present a continuous network formed by TeO_3/TeO_4 polyhedra (band B).

Both the reduced intensity and the peak positions of bands B, C, and D in the case of DF-2, which shifts towards higher energy values with respect to DF-1 (see Table 4.3), have been associated to a large Zn content in zinc-tellurite glasses [152]. As described above, Zn^{2+} cations break up the tellurite network by converting TeO_4 units into TeO_{3+1} and TeO_3 units and thus leading to a poorly connected and less rigid network. Therefore, the structure of DF glasses is mostly affected by the Zn/Te ratio, which determines the type and the quantity of structural units composing the glass network.
With respect to the influence of the F/O ratio on the structure of zinc-fluorotellurite glasses, this has been studied by Sidebottom and co-workers [150]. They compared the

Raman spectra of TeO_2−ZnO−ZnF_2 glasses with a fixed Zn/Te ratio and varying F/O ratio and observed that the increase in the F/O ratio did not affect the intensity of the high frequency Raman bands. However, it affected the relative intensity of the bending mode, *i.e.* band A, which increases due to the conversion of TeO_3 units into $Te(O,F)_{3+1}$ units. They concluded that F is easily dissolved into the tellurite network by replacing O without producing any further breakup.

Finally, it is worth mentioning that the cut-off frequency of vibrational modes, related to the maximum phonon energy of the glass network, occurs at ~850 cm^{-1} in both DF glasses (Fig. 4.7). A similar value is found in the literature for zinc-tellurite and zinc-fluorotellurite glasses [151, 150, 155]. This leads to a reduction of the multiphonon relaxation of rare earth ions in these glasses with respect to other oxide glasses, as it was discussed in chapter 2 [33].

4.5 Optical characterization

The transmittance spectra and the dispersion of the real part of the refractive index (n) of DF glasses, in the visible and near infrared wavelength range, were determined by spectroscopic measurements and ellipsometry, respectively, while their infrared absorption was investigated by means of Fourier transform infrared spectroscopy. All the measurements were performed on polished glass slabs of ~1mm thick.

4.5.1 Transmittance and refractive index

Figure 4.8 shows the transmittance spectra of DF-1 doped with increasing ErF_3 content, 1-3 wt% (Fig. 4.8a), and with the same content (1 wt%) of different rare earth ions: Er^{3+}, Tm^{3+}, and Yb^{3+} (Fig. 4.8b). Absorption bands due to rare earth's transitions from the ground level to excited levels in the 400-1800 nm wavelength range have been identified and assigned in Fig. 4.8b. As it can be deduced from Fig. 4.8, the general features of the transmittance spectra, *i.e.* absorption edge and maximum transmittance of both DF glasses, do not depend on the type of rare earth dopant and its concentration.

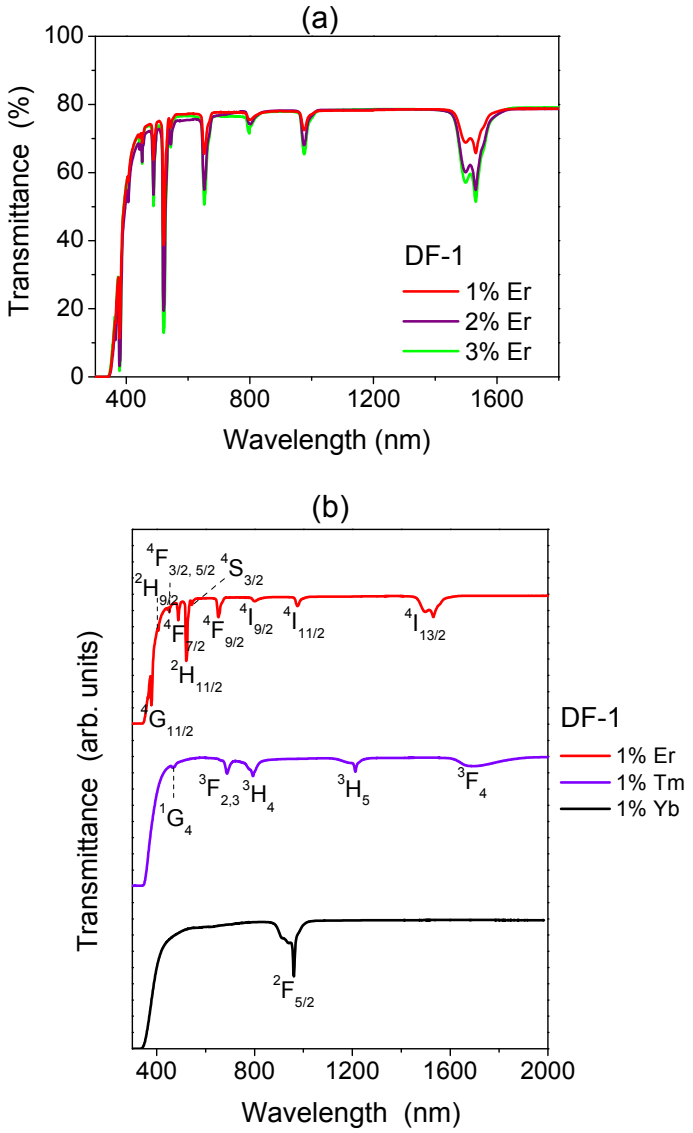

Figure 4.8: (a) Transmittance spectra of DF-1 doped with increasing ErF_3 content (1-3 wt%). (b) Transmittance spectra of DF-1 doped with 1 wt% of different rare earths (ErF_3, TmF_3, YbF_3). Er^{3+}, Tm^{3+}, and Yb^{3+} absorption bands are labelled in (b) with the upper levels of the transitions, originated in the ground level. The spectra in (b) have been shifted vertically to ease their comparison.

Similarly to the transmittance, the dispersion of the linear refractive index (n) is not sensitive to the type and concentration of rare earths ions doping the glass. Therefore, we will focus in the following analysis only on DF-1 and DF-2 doped with 1 wt% ErF_3 in order to compare the optical properties of the two glass matrices. The experimental transmittance and the calculated dispersion of n are presented in Fig. 4.9 for DF-1 and DF-2.

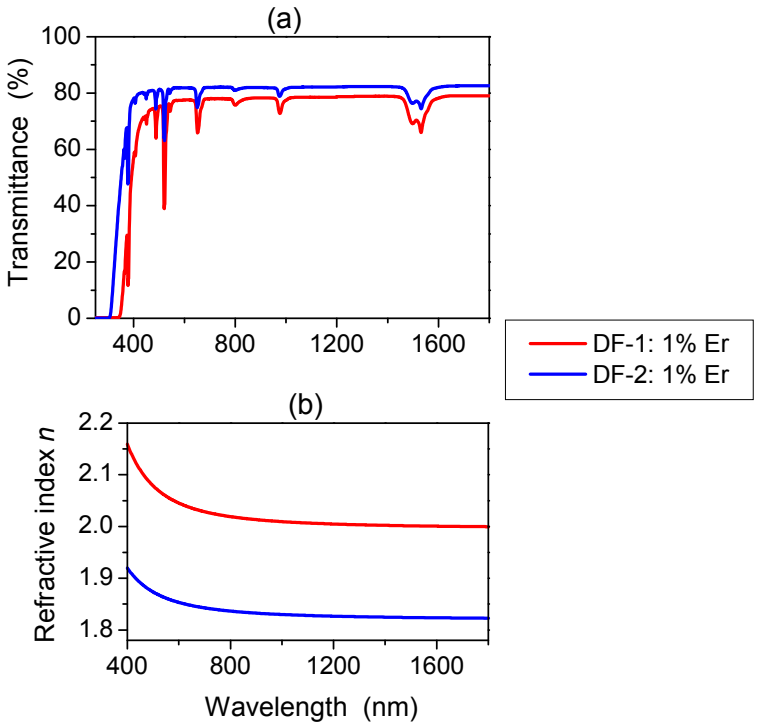

Figure 4.9: (a) Transmittance spectra and (b) refractive index dispersion of DF-1 and DF-2 glasses, doped with 1 wt% ErF_3.

Both DF-1 and DF-2 present sharp absorption edges in the ultraviolet (UV) region and a high transmittance in the visible and near infrared regions (Fig. 4.9a). DF-2 shows a slightly higher maximum transmittance (82 vs 79 %) and a blue-shifted UV absorption edge when compared to DF-1. The UV absorption edges of DF-1 and DF-2, calculated according as the wavelength for which $T(\lambda_c)= 0.5 \cdot T_{MAX}$ (chapter 3), are $\lambda_c \approx$ 343 nm for DF-2 and $\lambda_c \approx$ 385 nm for DF-1.

The dispersion of *n* shows a strong decay up to the near infrared region for both glasses. Then, for $\lambda >$ 900 nm the refractive index stays at an approximately constant value of 1.82 for DF-2 and of 2.00 for DF-1 (Fig. 4.9b). The imaginary part of the refractive index (*k*) is under the experimental resolution limit (10^{-4}) of our experimental set-up for wavelengths larger than 500 nm, except for the wavelength ranges where rare earth absorption bands occur.

It is well known that the optical properties of glass such as its transmittance (or absorption) and refractive index, depend on the glass composition.

In the case of DF glasses we observe that the absorption edge (λ_c) blue shifts and the refractive index (*n*) decreases as the Zn/Te ratio increases. This behaviour arises from the structural changes induced by the breakup of the covalent tellurite network upon

Zn^{2+} introduction. As described in the previous section, the increase of the Zn/Te ratio in zinc-tellurite and zinc-fluorotellurite glasses leads to a decrease of the rigidity and strength of the glass network. Moreover, the degree of covalency and polarizability of the glass network decrease too when the Zn/Te ratio increases (Zn has a smaller polarizability than Te) [151, 152, 153]. Another consequence of the increase of the Zn/Te ratio is the reduction in the glass density, as seen in section 4.2. The resulting effect is the decrease of the refractive index according to the Lorentz-Lorenz formula (Eq. 2.1). In addition, the reduction of the electronegativity difference among anionic and cationic elements in the glass network with the increase of the Zn/Te ratio (Zn has a lower electronegativity than Te) leads to an increase of the band gap energy, *i.e.* λ_c shifts to shorter wavelengths [151].

4.5.2 Infrared absorption

In chapter 2 we described the effect that OH^- groups present in the glass matrix may have on the nonradiative decay of rare earth ions. High energy vibrations of OH^- groups not only quench the radiative emissions of rare earth ions but also limit strongly the mid-infrared transparency of glasses (see Fig. 2.6). Thus, we have measured the infrared absorption of DF-1 and DF-2, doped with 1 wt% ErF_3, in the 6000-1500 cm^{-1} region (corresponding to 1.7-6.7 μm) to determine both their mid-infrared absorption edge and the magnitude of their OH^- absorption bands. Figure 4.10 shows the experimental spectra, which are similar to those of other rare earth doped DF glasses.

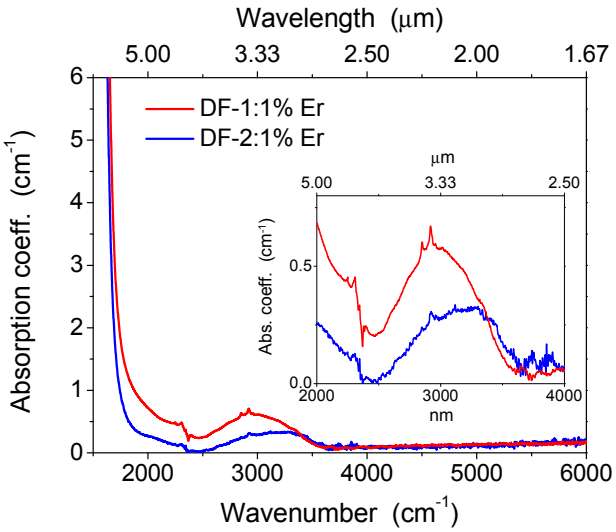

Figure 4.10: Infrared absorption spectra of DF-1 and DF-2 doped with 1 wt% ErF_3. The inset zooms in the region between 2000-4000 cm^{-1} where are observed the absorption bands attributed to molecular vibrations of OH^- groups.

We clearly observe in both cases the multiphonon absorption edge at ~1600 cm^{-1} (~6 μm), which represents the long wavelength (low energy) limit in the transparency region of glasses. This value is similar to that of other tellurite and fluorotellurite glasses described in the literature [151, 163]. In addition, both spectra present a broad absorption band between 2000-4000 cm^{-1}, which is attributed to stretching vibrations of OH^- groups present in the glass [98, 37, 163]. The maximum intensity of this absorption band is ~0.6 cm^{-1} (at ~3000 cm^{-1}) in the case of DF-1 and ~0.35 cm^{-1} (at ~3200 cm^{-1}) in the case of DF-2 (inset Fig. 4.10). Moreover, we observe as well a small band peaking at ~2900 cm^{-1} in both spectra, that can be due to molecular vibrations of $CH/CH_2/CH_3$ doublets coming from contaminants on the glass surface, such as wax or oil [37]. Finally, the infrared absorption spectrum of DF-2 shows small bands at ~3600 cm^{-1}, which are related to the presence of atmospheric water during the measurement [37].

The position of OH^- absorption bands depends on the type of hydrogen bonding between OH^- groups and the cations of the glass network [98]. O'Donnell *et al.* [37] have assigned them in the case of fluorotellurite glasses. They attributed the absorption band peaking at ~2300 cm^{-1} to strongly H-bonded Te-OH groups (*strong OH⁻s*); the band at ~3000 cm^{-1} to weakly H-bonded Te-OH groups (*weak OH⁻s*); and finally, the high energy shoulder of this last band to free Te-OH groups (*free OH⁻s*), *i.e.* not H-bonded to the glass network, and/or molecular water [37].

Thus, we have deconvoluted the OH^- absorption bands observed in the infrared absorption spectra of DF-1 and DF-2 to quantify the contribution of strong, weak, and

free OH^-s. To do that we have first subtracted the contribution of the multiphonon edge, which partially hides the lower energy OH^- band due to strong OH^-s [37]. The results are showed in Fig. 4.11.

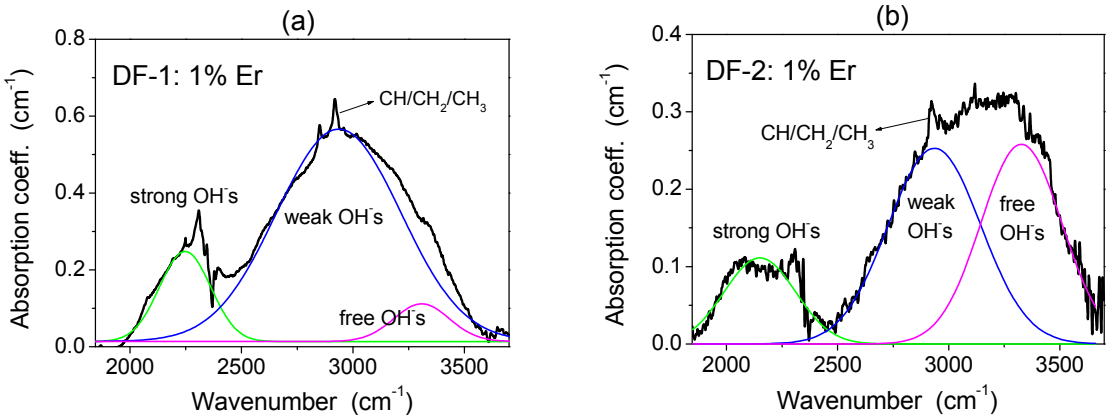

Figure 4.11: Gaussian deconvolution of the absorption band due to OH^- groups in the case of (a) DF-1 and (b) DF-2, doped with 1 wt% ErF_3.

We observe the presence of the three types of OH^- groups in the glasses. However, the main contribution to the absorption band is due weak OH^-s in the case of DF-1 while is due to both weak and free OH^-s for DF-2 (Fig. 4.11). Table 4.4 summarizes the results of the Gaussian deconvolution: peak position, intensity and area of the different types of OH^- groups in DF-1 and DF-2. Moreover, we have determined the OH^- concentration (N_{OH}) and OH^- *parts per million* (C_{OH}) corresponding to each sub-band in Fig. 4.11 from Eq. 3.9 and 3.10, respectively.

Table 4.4: Peak position (λ_P); peak intensity (I_P); band area (A_B); OH^- concentration (N_{OH}); and OH^- parts per million (C_{OH}) corresponding to each sub-band obtained by Gaussian deconvolution of the OH^- absorption bands in the infrared spectra of DF-1 and DF-2.

	λ_P (cm^{-1})	I_P (cm^{-1})	A_B	N_{OH} (10^{18} ions/cm^3)	C_{OH} (ppm)
DF-1					
Strong OH^-s	2248	0.25	68	3.1	15.4
Weak OH^-s	2937	0.56	386	6.9	35.3
Free OH^-s	3308	0.11	31	1.3	6.6
DF-2					
Strong OH^-s	2150	0.11	45	1.3	6.9
Weak OH^-s	2936	0.25	132	3.1	15.9
Free OH^-s	3327	0.26	118	3.2	17.0

We have estimated the total OH^- content in DF-1 and DF-2 from the concentration of the different types of OH^- groups included in Table 4.4. This value is 56.3 *ppm* (1.13 10^{19} ions/cm^3) in the case of DF-1, while is 39.8 *ppm* (0.76 10^{19} ions/cm^3) for DF-2. These values are lower than those reported by Massera and coauthors in the TeO_2–Bi_2O_3–ZnO glass system [36].

The small OH^- content of DF glasses stems from the dehydration of the glass melt according to the chemical reactions between fluorine and water described in section 4.2 (Eq. 4.1 and 4.2). The dehydration process is proportional to both fluorine content and duration of the melting, which was the same for all DF glasses. Therefore, the smaller OH^- content estimated for DF-2 is in agreement with the larger fluorine content (and fluorine losses!) of this glass with respect to DF-1. A similar behaviour has been described by Nazabal *et al.* in fluorotellurite glasses with similar composition [151] and by O'Donnell *et al.* in the TeO_2–ZnF_2–Na_2O glass system [37].

Finally, it is worth mentioning that the small magnitude of the infrared absorption bands due to OH^-s stretching vibrations do not limit the infrared transparency region of DF-1 and DF-2, contrary to what is reported for other tellurite glasses [98, 163].

4.6 Photoluminescence response of Er^{3+} doped TeO_2–ZnO–ZnF_2 glasses

Erbium is the element of choice when considering doping of glasses with rare earths. This is due to the multiplicity of possible applications of Er-doped glasses both in the near-infrared and in the visible spectral regions. In fact, besides the main Er^{3+} emission in the optical C-band (1530 to 1565 nm), that is currently used by EDFAs and EDWAs to amplify optical signals in telecommunication networks (chapter 1 and 2), green and red upconverted Er^{3+} emissions may be employed in applications such as visible lasers, temperature sensors, and even to improve the efficiency of solar cells [164, 165, 166].

In order to have indications on the site symmetry and bonding of Er^{3+} ions in DF-1 and DF-2 hosts, we have determined the Judd-Ofelt parameters Ω_t (t= 2, 4, 6) by calculating the experimental oscillator strength of Er^{3+} transitions from the experimental absorption

cross-section (σ_a) of DF-1 and DF-2 doped with 2wt% ErF_3 (Fig. 4.12) [167], using the procedure described in chapter 2.

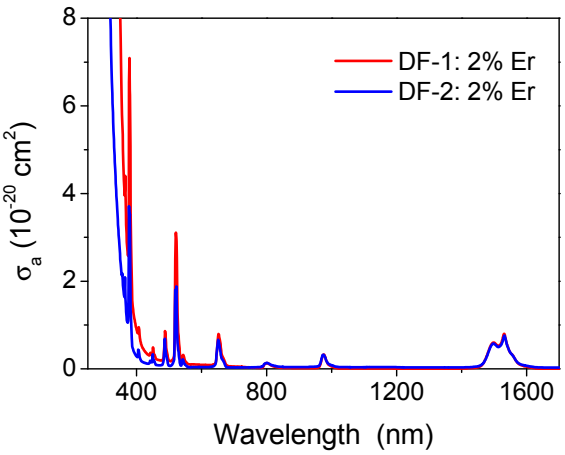

Figure 4.12: Absorption cross-section (σ_a) of DF-1 and DF-2 doped with 2 wt% ErF_3.

Table 4.5 reports the Judd-Ofelt parameters as well as the spectroscopy quality factor (Ω_4/Ω_6) of DF glasses and of a zinc-tellurite glass (80 TeO_2–19 ZnO–1 Er_2O_3 mol%) reported in the literature [168]. The spectroscopy quality factor is considered an important indicator of the intensity of the major laser transitions of the considered rare earth ion, in this case Er^{3+} [169].

Table 4.5: Judd-Ofelt parameters Ω_t (t= 2, 4, 6) and spectroscopy quality factor (Ω_4/Ω_6) obtained for Er^{3+} in DF-1, DF-2 glass hosts. Ω_t values obtained in Ref. [168] for a TeO_2–ZnO glass (80 TeO_2–19 ZnO–1 Er_2O_3 mol%) are included for comparison.

Host	Ω_2 (10^{-20} cm^2)	Ω_4 (10^{-20} cm^2)	Ω_6 (10^{-20} cm^2)	Ω_4/Ω_6
DF-1	4.71	1.57	1.13	1.39
DF-2	3.02	1.28	1.14	1.12
TeO_2– ZnO[168]	6.30	1.55	1.29	1.20

It is well known that the value of the parameter Ω_2 is indicative of the amount of covalent bonding between the rare earth ions and their ligand anions [170]. Therefore, the reduction of Ω_2 in DF hosts with respect to the zinc-tellurite host indicates that Er^{3+} ions are in a less covalent (or more ionic) environment, *i.e.* around fluorine anions, in DF glasses. Moreover, Ω_2 is lower in DF-2 with respect to DF-1, in good agreement with the higher F/O ratio in the first host. Finally, the spectroscopy quality factor of both DF glasses is quite high when compared to other glass hosts, whose quality factor

is in the range 0.43-1.5 [171]. In particular, DF-1 has a spectroscopy quality factor of 1.39, which is larger than that of DF-2 and the zinc-tellurite reference glass (Table 4.5). Thus, DF-1 is in principle the most promising host between DF glasses to achieve stimulated Er^{3+} emissions, as we have in fact demonstrated in the case of Nd^{3+} doped glasses [172].

4.6.1 Near infrared emissions

The near infrared emission was measured at room temperature for all the Er^{3+} doped DF-1 and DF-2 glasses, by exciting them at 801 nm, in resonance with the $^4I_{9/2}$ level (Fig. 4.13). Due to the small energy gap (~2200 cm^{-1}) between the $^4I_{9/2}$ level and the next lower level ($^4I_{11/2}$), level $^4I_{9/2}$ is mainly depopulated by multiphonon relaxation. Then, from the $^4I_{11/2}$ level, emission to the ground level ($^4I_{15/2}$) and nonradiative decay to the $^4I_{13/2}$ level occur. Finally, from the $^4I_{13/2}$ level, the fundamental Er^{3+} emission ($^4I_{13/2}\rightarrow{}^4I_{15/2}$) takes place (Fig. 4.13).

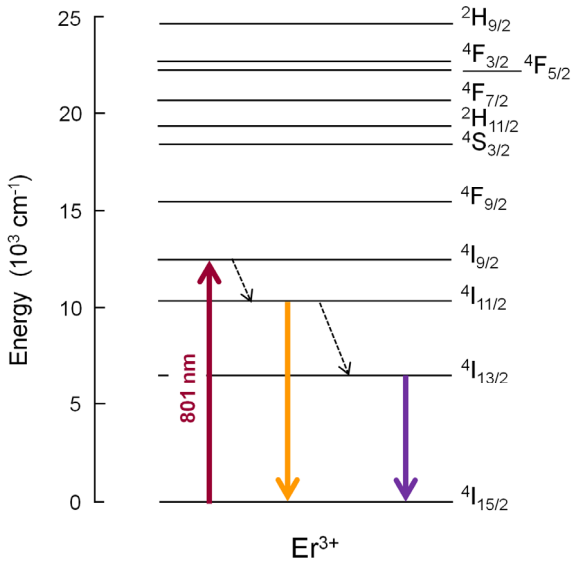

Figure 4.13: Energy level diagram of Er^{3+} ion excited at 801 nm, in resonance with the $^4I_{9/2}$ level. Dashed down arrows indicate nonradiative transitions. The $^4I_{11/2}\rightarrow{}^4I_{15/2}$ and $^4I_{13/2}\rightarrow{}^4I_{15/2}$ near infrared emissions are indicated as down arrows.

Figure 4.14a-b presents the near infrared emission spectra measured for DF-1 and DF-2 glasses doped with increasing Er^{3+} concentration (0.5-3 wt% ErF_3), while Figure 4.14c compares the emission spectra of DF-1 and DF-2 doped with 1 wt% ErF_3.

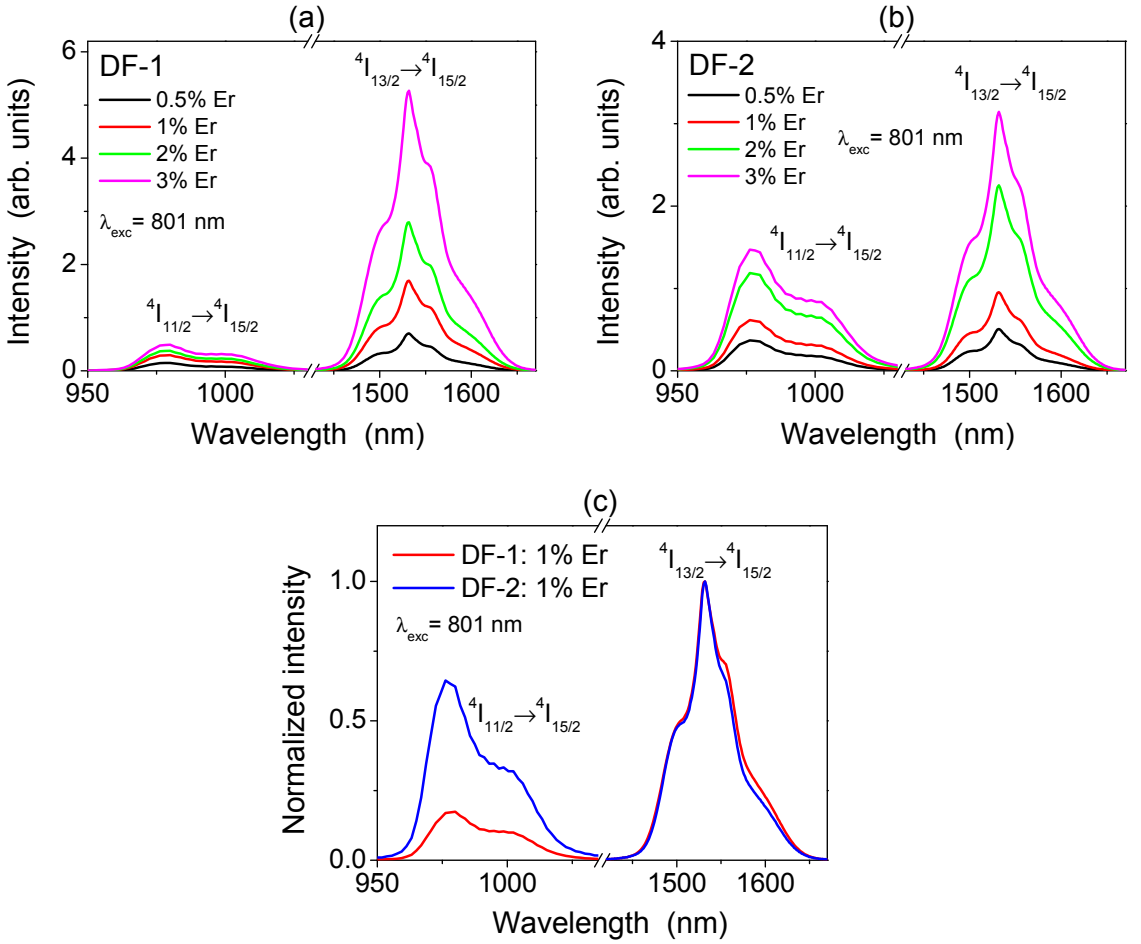

Figure 4.14: Room temperature near infrared emission spectra of Er^{3+} doped (a) DF-1 and (b) DF-2 glasses excited at 801 nm. (c) Normalized near infrared emission spectra of DF-1 and DF-2 glasses, doped with 1 wt% ErF_3.

In all DF glasses, the maximum intensity of $^4I_{11/2}\rightarrow{}^4I_{15/2}$ and $^4I_{13/2}\rightarrow{}^4I_{15/2}$ emissions is at 980 nm and 1532 nm, respectively, and their value increases with the ErF_3 content. The intensity at 980 nm increase 3 times in DF-1 and 4 times in DF-2 while the intensity at 1532 nm increase 7 times in DF-1 and 6 times in DF-2 with the increase of ErF_3 content. However, DF-2 shows a more intense $^4I_{11/2}\rightarrow{}^4I_{15/2}$ and a less intense $^4I_{13/2}\rightarrow{}^4I_{15/2}$ emission with respect to DF-1. In particular, if we compare DF-1 and DF-2 doped with 1 wt% ErF_3 (Fig. 4.14c), we observe that the emission intensity at 980 nm is only ~20 % of the maximum emission intensity (at 1532 nm) for DF-1, while it reaches ~60 % in the case of DF-2 (Fig. 4.14b).

If we consider the energy gap between $^4I_{11/2}$ and $^4I_{13/2}$ levels (~3600 cm^{-1}, Fig. 4.13), nonradiative decay from $^4I_{11/2}$ to $^4I_{13/2}$ may be induced both by multiphonon deexcitation and by the vibrations in OH^- groups, which are maximum at ~3000 cm^{-1} in the case of DF-1 and ~3200 cm^{-1} in the case of DF-2 (Fig. 4.9). Both processes may contribute to

reduce the intensity of the $^4I_{11/2} \rightarrow {}^4I_{15/2}$ emission in DF-1; however, the probability of these nonradiative processes is smaller in the case of DF-2 host. This stems from the larger fluorine concentration of DF-2, which leads to a smaller OH^- content in this glass with respect to DF-1, as described in section 4.5.2. Furthermore, as indicated by the value of the Judd-Ofelt parameter Ω_2 (Table 4.5), Er^{3+} ions in DF-2 are in a more ionic environment with respect to DF-1, which also contributes to decrease their multiphonon deexcitation rate. The global effect is that the $^4I_{11/2}$ level is more populated in DF-2 than in DF-1 and by consequence the $^4I_{13/2}$ is less populate in DF-2 than in DF-1 and thus, the relative intensity at 980 nm with respect to 1532 nm is higher in DF-2 than in DF-1.

Since the main Er^{3+} transition, $^4I_{13/2} \rightarrow {}^4I_{15/2}$, is relevant for application of Er doped DF glasses as optical amplifiers and lasers in the optical C-band, we have determined the parameters that characterize this transition in DF-1 and DF-2, in order to compare their value with those of other glasses. These parameters are:

i) The **full width at half maximum** (FWHM), that is commonly employed as an estimation of the available bandwidth for optical amplification at 1.5 μm. A large value of FWHM is particularly relevant for systems based on wavelength division multiplexing (WMD) [31]. Another way to estimate the bandwidth of the $^4I_{13/2} \rightarrow {}^4I_{15/2}$ emission is by calculating the **effective bandwidth**, defined as [173]: $\Delta\lambda_{eff} = \int I(\lambda) d\lambda / I_{max}$. This is considered a more accurate estimation of the $^4I_{13/2} \rightarrow {}^4I_{15/2}$ emission bandwidth than the FWHM, due to the asymmetry of the emission band [174, 175].

ii) The **peak of the emission cross-section** (σ_e^{peak}), calculated from the McCumber's relation (Eq. 2.8). It is used to quantify the probability of spontaneous/stimulated $^4I_{13/2} \rightarrow {}^4I_{15/2}$ emission events [87]. A large value of σ_e^{peak} is therefore beneficial for signal amplification.

iii) The **experimental lifetime** (τ), obtained by fitting the photoluminescence decay signal of the $^4I_{13/2}$ level to a single exponential function (see chapter 3). It is an important parameter in optical amplifiers since a long lifetime leads to slow gain dynamics, which are desirable when amplifying high-rate signals [102].

Figure 4.15 shows the experimental decay of the $^4I_{13/2}$ level in DF-1 glasses.

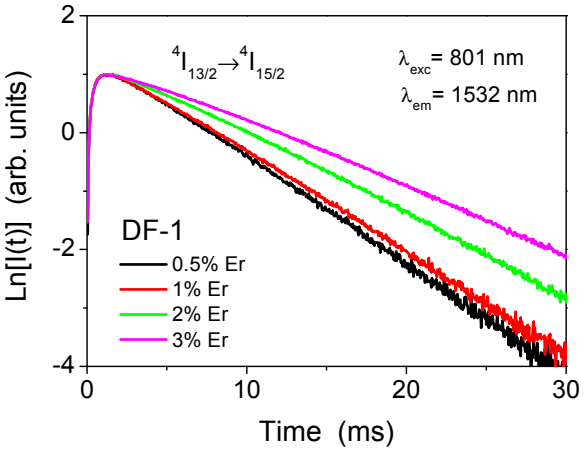

Figure 4.15: Semilogarithmic plot of the room temperature photoluminescence decay of the $^4I_{13/2}$ level for DF-1 glasses excited at 801 nm.

We note that, contrary to what we may expect, the experimental decay of the $^4I_{13/2}$ level becomes longer when the Er concentration increases in DF-1 glasses. This behaviour is similar also in the case of Er doped DF-2 glasses. Instead, the usual trend for the fluorescence lifetime is that it decreases when the dopant concentration increases, due to concentration quenching effects (chapter 2). However, another phenomenon that may influence the experimental fluorescence decay is *self-absorption* that causes a delay in the detected fluorescence signal due to successive reabsorption and re-emission of photons inside the sample [175, 176]. It is proportional to the thickness (L), absorption cross-section (σ_a) and rare earth concentration (N) of the sample and becomes important when the emission and absorption bands overlap as it occurs for Er^{3+} at 1.5 μm. Following the approach of Auzel and coauthors [177], the fluorescence lifetime corrected for self-absorption can be determined as: $\tau_{PL} = \tau/(1 + \sigma_a NL)$ from the experimental lifetime τ.

Finally, we have calculated two **figures of merit** (FOM), which are commonly used to quantify the performance of Er-doped glasses as optical amplifiers in terms of their emission cross-section, bandwidth and lifetime [31, 178]. The FOM for the bandwidth of the amplifier (FOM-BW), is calculated as the product of the peak value of the emission cross-section (σ_e^{peak}) by the FWHM. The FOM for the gain of the amplifier (FOM-Gain), is calculated as the product of the emission cross-section (σ_e^{peak}) by the lifetime (τ). The value of FOM-Gain is inversely proportional to the threshold for laser action for continuous wave operation while for pulsed operation the threshold becomes independent of τ when the pump pulse duration is much shorter than τ [99].

Table 4.6 summarizes the values of the parameters described above for all the Er^{3+} doped DF-1 and DF-2 glasses. The values of these parameters in other Er-doped tellurite/fluorotellurite or commonly used glasses are included in Table 4.6 for comparison [31, 178, 179, 180].

Table 4.6: Properties of the $^4I_{13/2} \rightarrow {}^4I_{15/2}$ emission (peaking at 1532 nm) for DF-1 and DF-2 glasses, doped with 0.5-3 wt% ErF_3. N is the concentration of Er^{3+} ions per unit volume; $\Delta\lambda_{eff}$ is the experimental effective bandwidth; FWHM is the full width at half maximum; σ_e^{peak} is the peak value of the emission cross-section; τ is the experimental lifetime; τ_{PL} is the emission lifetime corrected for self-absorption; FOM-BW is the figure of merit for the amplifier bandwidth; FOM-Gain is the figure of merit for the amplifier gain. The values found in the literature for tellurite/fluorotellurite hosts and other types of glass hosts are included for comparison.

Sample	N (Er^{3+}) (10^{20} cm^{-3})	$\Delta\lambda_{eff}$ (nm)	FWHM (nm)	σ_e^{peak} (10^{-21} cm^2)	τ (ms)	τ_{PL} (ms)	FOM-BW (10^{-21} cm^2 nm)	FOM-Gain (10^{-24} cm^2 s)
DF-1:								
0.5 % Er	0.73	67.7	53	8.2	5.4	5.1	435	44
1 % Er	1.47	73.4	63	8.8	5.9	5.3	554	52
2 % Er	2.97	74.6	66	8.7	6.1	4.9	574	53
3 % Er	4.44	77.0	68	9.2	6.8	4.8	626	63
DF-2:								
0.5 % Er	0.71	66.7	51	7.1	7.7	7.3	362	55
1 % Er	1.44	68.8	55	7.5	8.2	7.4	412	61
2 % Er	2.85	74.5	65	7.5	8.5	6.8	487	64
3 % Er	4.35	75.1	65	7.8	7.6	5.5	507	59
Tellurite/Fluorotellurite hosts*								
TZNE1 [178]	-	-	56	6.9	2.5	-	374	17
TZN [31]	-	-	75	8.6	7.6	-	650	65
TG1 [179]	-	-	72	8.4	3.0	-	605	25
TBN3 [180]	-	-	73	9.1	2.1	-	663	19
Non-tellurite hosts								
Al/SiO_2 [31]	-	-	45	5.5	10	-	250	55
ZBLAN [31]	-	-	65	4.8	10	-	300	48
Phosphate [180]	-	-	37	6.4	-	-	237	-
Germanate [180]	-	-	53	5.7	-	-	302	-

***** **TZNE1**: 75TeO_2–20ZnO–4Na_2CO_3–1Er_2O_3 (mol%); **TZN**: 80TeO_2–10Na_2O–9ZnO–1Er_2O_3 (mol%); **TG1**: 85TeO_2–10PbF_2–4AlF_3−1ErF_3 (mol%); **TBN3**: 70TeO_2–12B_2O_3–3Nb_2O_5–15ZnO (mol%): 1 wt% Er_2O_3.

The emission band broadens ($\Delta\lambda_{eff}$ and FWHM in Table 4.6) for DF glasses as the Er^{3+} concentration increases. In particular, the emission FWHM increases from 53 to 68 nm in DF-1 and from 51 to 65 in DF-2 when the Er^{3+} concentration goes from 0.5 to 3 wt% ErF_3. However, the absorption FWHM ($^4I_{15/2} \rightarrow {}^4I_{13/2}$) does not change when increasing Er^{3+} concentration in both DF glasses. As an example, Fig. 4.16 shows that the

absorption FWHM of DF-1 glasses does not change (inset) even if the intensity of the $^4I_{15/2} \rightarrow {}^4I_{13/2}$ absorption band scales with Er concentration.

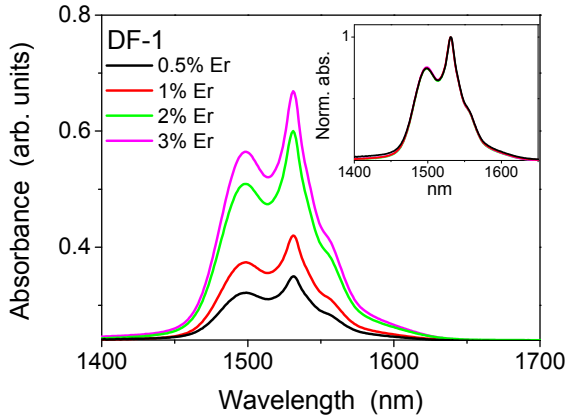

Figure 4.16: $^4I_{15/2} \rightarrow {}^4I_{13/2}$ absorption band as a function of wt% ErF_3 in DF-1. In the inset the absorption bands have been normalized to their maximum value to compare their width.

Thus, the broadening of the emission band ($^4I_{13/2} \rightarrow {}^4I_{15/2}$) cannot be attributed to changes in the sites occupied by Er^{3+} ions when their concentration increases, since if this was the case, both absorption and emission bandwidths should increase [167, 175]. Similarly, this phenomenon has been observed in other tellurite and fluorotellurite glasses and attributed to self-absorption [175, 176, 179], that is also responsible for the lengthening of the experimental lifetime (τ) with the increase of Er^{3+} concentration, as described above. The lifetime of the $^4I_{13/2}$ level corrected for self-absorption (τ_{PL}), contrary to τ, decreases with Er^{3+} content in DF-1 and DF-2 (Table 4.6). Moreover, τ and τ_{PL} are similar for DF samples with the lowest Er concentration (0.5 wt%), for which self-absorption is small, while their difference is maximum for the samples with the highest Er concentration (3 wt%).

Finally, we compare the bandwidth (FOM-BW) and gain (FOM-Gain) figures of merit of DF glasses with those of other glass hosts listed in Table 4.6. In particular, we focus on DF-1 and DF-2 doped with 1 wt% ErF_3, since they have a similar Er^{3+} content than the rest of doped glasses.

If we compare the FOM-BW and FOM-Gain of DF-1 and DF-2 with those of tellurite and fluorotellurite glass hosts, we note that, except for TZN [31] and TZNE1 [178] glasses, the other tellurite/fluorotellurite glasses [179, 180] present a larger FOM-BW but a smaller FOM-Gain than DF glasses. This is mainly due to the larger FWHM and

the smaller lifetime of the $^4I_{13/2}$ level (τ) in the case of these glasses with respect to DF glasses. A large value of τ has been related to the reduction of the hydroxyl content in rare earth doped zinc-fluorotellurite glasses [38, 151].

From the data summarized in Table 4.6 we conclude that DF glasses, and DF-1 in particular DF-1, present simultaneously large bandwidth, emission cross-section and lifetime values, which are reflected on their large FOMs. In fact, DF glasses have a larger FOM-BW than silicate, fluorozirconate (ZBLAN), phosphate and germanate glasses and comparable FOM-Gain with respect to those of silicate and fluorozirconate glasses (see Table 4.6) [31, 180]. Their larger FOM-BW is related to their larger FWHM and emission cross-section with respect to non-tellurite hosts. In particular, the large FWHM of tellurite glasses is a consequence of their network structure, which presents different sites, and so different crystal fields, that can be occupied by rare earth ions (*inhomogeneous* broadening) [153]; while their large cross-section stems from the large refractive index of tellurite glasses ($n \approx 2$), which increases the local field correction for rare earth ions in the glass matrix (chapter 2) [173].

These results suggest that DF-1 is the most promising candidate for developing broadband amplifiers in the optical C band. In fact, it presents, simultaneously, large FOM-BW and FOM-Gain values, and furthermore they increase with Er^{3+} concentration.

4.6.2 Visible *upconverted* emissions

Near infrared (NIR) to visible upconverted photoluminescence was measured at room temperature for all Er doped DF glasses by exciting them at 801 nm with a Ti-sapphire laser. Figure 4.17 presents the experimental upconverted emission spectra of DF glasses doped with increasing Er^{3+} concentration (0.5-3 wt% ErF_3). They show three emission bands centred at around 525, 545 and 660 nm. The two bands in the green region corresponds to ($^2H_{11/2}$, $^4S_{3/2}$)→$^4I_{15/2}$ transitions while the band in the red is attributed to the $^4F_{9/2}$→$^4I_{15/2}$ transition (Fig. 4.13).

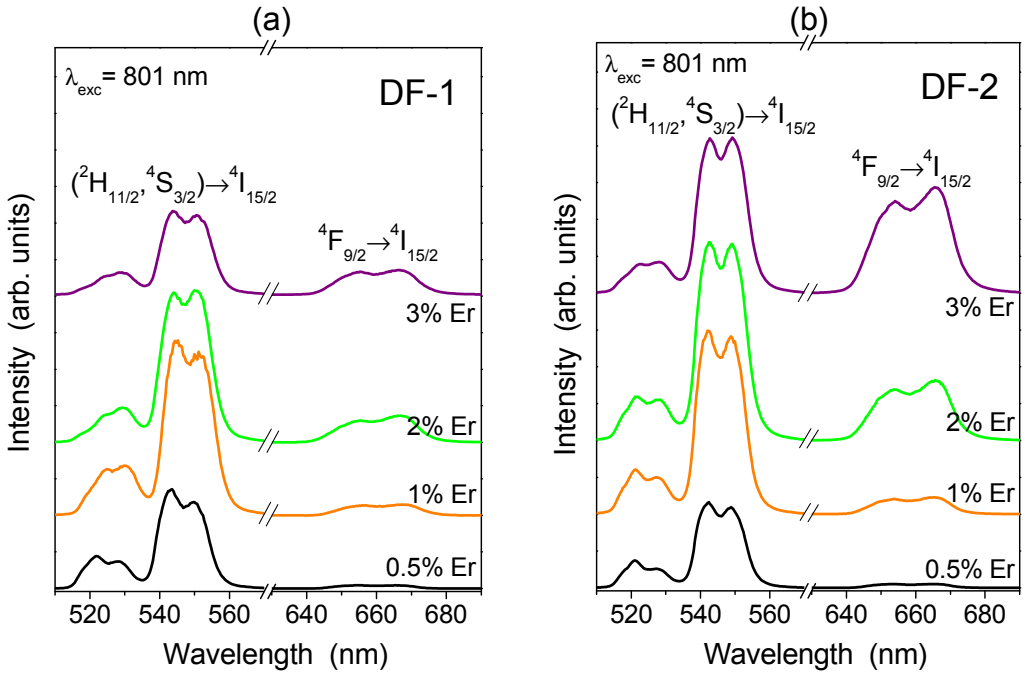

Figure 4.17: Room temperature visible upconverted emission spectra of Er^{3+} doped (a) DF-1 and (b) DF-2 glasses excited at 801 nm.

The most intense emission in both glasses is the green emission from the $^4S_{3/2}$ level, which is visible also by naked eyes. The weaker green emission from the $^2H_{11/2}$ level is observed too, since this level is populated at room temperature through thermocoupling with the $^4S_{3/2}$ level. Finally, the red emission from level $^4F_{9/2}$ is quite weak compared to the green emission for samples with Er concentrations lower than 1 wt% ErF_3. However, the intensity of the red emission increases with Er concentration and becomes comparable to the green one for DF-2 doped with 3 wt% ErF_3 (Fig. 4.17b). In order to quantify the increase of the red emission band with Er concentration, we have calculated the red to green ($^4S_{3/2}$) intensity ratio (I_{RED}/I_{GREEN}) for all the doped glasses and the results obtained are presented in Fig. 4.18.

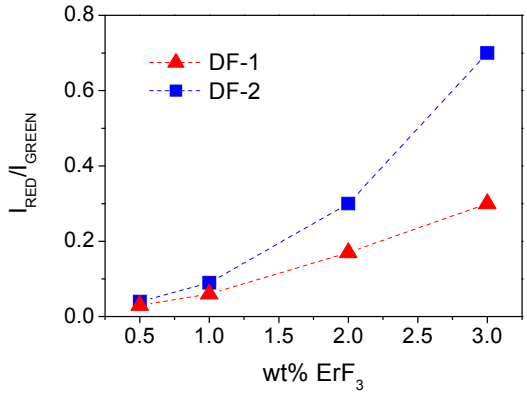

Figure 4.18: Red ($^4F_{9/2}$) to green ($^4S_{3/2}$) intensity ratio (I_{RED}/I_{GREEN}) as a function of Er concentration (0.5-3 wt% ErF_3) for DF-1 and DF-2 glasses excited at 801 nm. Dashed lines are guides to the eye.

The increase of the I_{RED}/I_{GREEN} ratio is more pronounced in DF-2 than in DF-1. While it increases from 0.03 to 0.3 for DF-1, it goes from 0.04 to 0.7 as ErF_3 increases from 0.5 to 3 wt% in the case of DF-2.

In order to analyze the mechanisms involved in the green and red upconversion, we have first studied the dependence of their intensities (I_{UP}) on the laser pump power (P_{exc}) at 801 nm. Actually, $I_{UP} \propto (P_{exc})^m$ where m is the number of IR photons involved in the upconversion pumping mechanism [96]. Figure 4.19 shows the dependence of the intensity of green and red emissions on the pump power in the case of DF-1 doped with 2 wt% ErF_3.

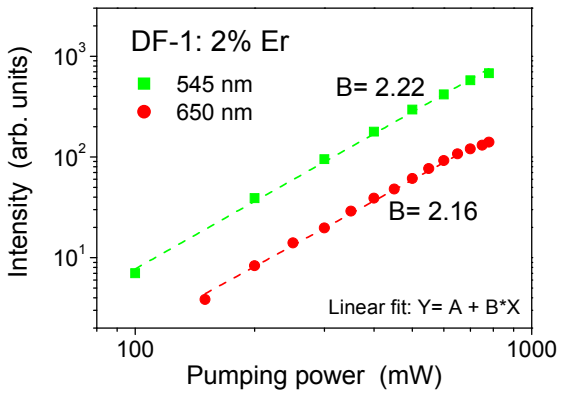

Figure 4.19: Room temperature upconversion emission intensities as a function of pumping power at 801 nm in DF-1 doped with 2 wt% ErF_3. Dashed lines are the linear fitting of experimental measurements, which lead to a slope of 2.22 and 2.16 for the green and red emissions, respectively.

DF-2 shows also a quadratic dependence ($m \approx 2$) of I_{UP} with P_{exc}. This behaviour suggests that the upconverted emission of DF glasses is likely related to excited state

absorption (ESA) or energy transfer (ET) mechanisms, since they are two photons processes. In order to distinguish which mechanism, ESA or ET, dominates in the population of $^4S_{3/2}$ and $^4F_{9/2}$ levels in DF glasses, we have compared the experimental lifetime of these levels under infrared excitation (λ_{exc}= 801 nm) and visible, or direct, excitation (λ_{exc}= 488 nm). In this last case, Er^{3+} ions are excited in resonance with the $^4F_{7/2}$ level and the $^4S_{3/2}$ and $^4F_{9/2}$ levels are populated by multiphonon relaxation (Fig. 4.13). As an example, Fig. 4.20 shows the experimental decay of the $^4S_{3/2}$ and $^4F_{9/2}$ levels in DF-1 and DF-2 doped with 3 wt% ErF_3. The values obtained for all Er doped DF glasses are summarized in Table 4.7.

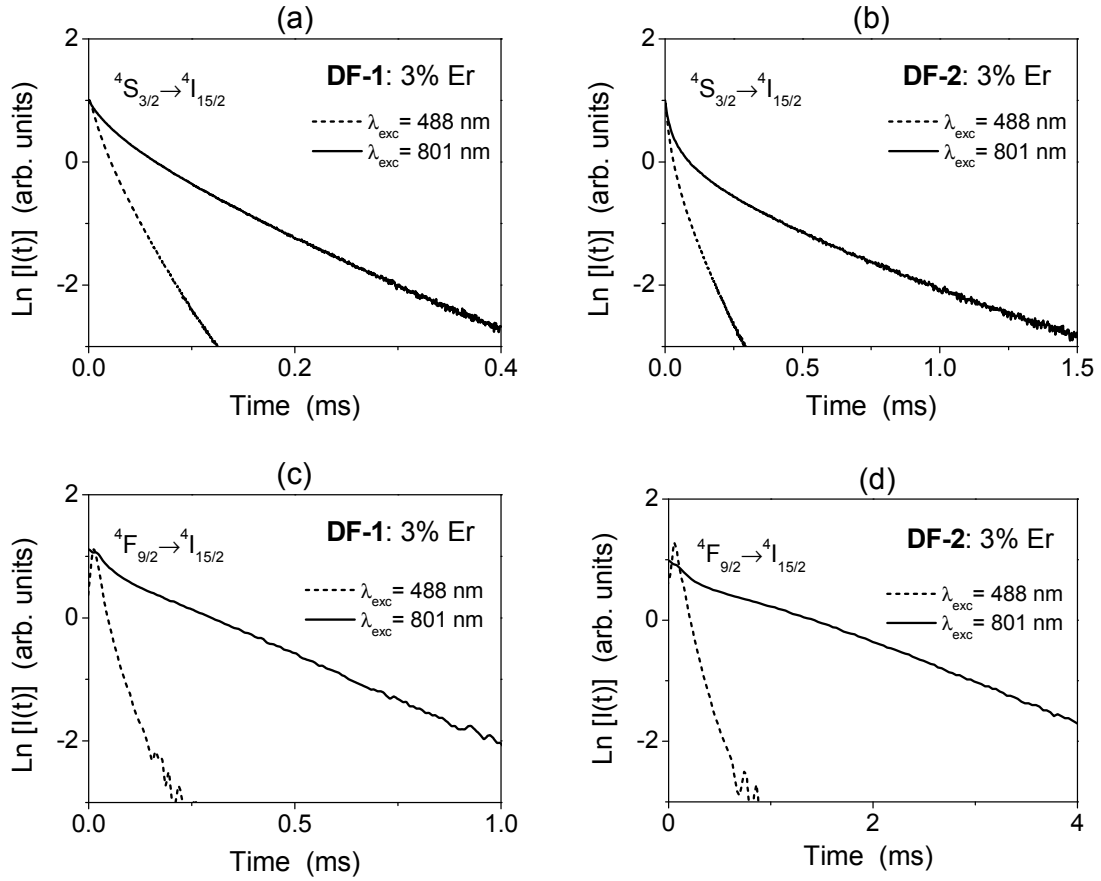

Figure 4.20: Semilogarithmic plot of the room temperature photoluminescence decay of $^4S_{3/2}$ and $^4F_{9/2}$ levels under visible excitation (λ_{exc}= 488 nm) and near infrared excitation (λ_{exc}= 801 nm) in (a, c) DF-1 and (b, d) DF-2, doped with 3 wt% ErF_3.

We note that the fluorescence decay from $^4S_{3/2}$ and $^4F_{9/2}$ levels under infrared and visible excitation do not follow a single-exponential function. However, the decay from the $^4F_{9/2}$ level under infrared excitation shows a two-exponential behaviour. Thus, in this case, we have fitted the decay signal using a short (τ_s) and long (τ_l) time constants.

In the other cases, we have calculated the mean lifetime of the $^4S_{3/2}$ and $^4F_{9/2}$ emissions using Eq. 3.13. Moreover, the lifetime of the $^4S_{3/2}$ level is slightly longer under infrared excitation than under visible excitation, whereas the lifetime of the $^4F_{9/2}$ level is strongly enhanced under infrared excitation with respect to visible excitation in both DF glasses (Fig. 4.20).

Table 4.7: Lifetime of the $^4S_{3/2}$ and $^4F_{9/2}$ levels under visible excitation (λ_{exc}= 488 nm) and infrared excitation (λ_{exc}= 801 nm) in Er-doped DF glasses. The signal was too weak to measure the lifetime of the $^4F_{9/2}$ level in the samples doped with 0.5 wt% ErF_3. The lifetime of the $^4I_{11/2}$ level (λ_{exc}= 801 nm) is included for comparison.

Sample	$^4S_{3/2}$ lifetime (ms)		$^4F_{9/2}$ lifetime (ms)		$^4I_{11/2}$ τ_m (ms)
	λ_{exc}= 488 nm	λ_{exc}= 801 nm	λ_{exc}= 488 nm	λ_{exc}= 801 nm	λ_{exc}= 801 nm
DF-1:					
0.5 % Er	0.071	0.108	0.075	-	0.49
1 % Er	0.054	0.082	0.061	τ_s=0.061; τ_l=0.377	0.42
2 % Er	0.036	0.058	0.048	τ_s=0.047; τ_l=0.409	0.36
3 % Er	0.035	0.055	0.034	τ_s=0.030; τ_l=0.375	0.32
DF-2:					
0.5 % Er	0.178	0.776	0.204	-	1.9
1 % Er	0.143	0.445	0.196	τ_s=0.199; τ_l=1.770	2.0
2 % Er	0.083	0.252	0.150	τ_s=0.163; τ_l=1.720	1.7
3 % Er	0.048	0.192	0.122	τ_s=0.121; τ_l=1.640	1.5

Upconverted emissions originated from ESA processes show a similar lifetime under visible and infrared excitation. Moreover, ESA occurs during the excitation pulse width, and leads to an immediate decay of the luminescence after excitation. On the contrary, upconverted emissions that are originated by ET processes show a characteristic rise time in their decay curves, that is the delay from the laser pulse to the population of the emitting level by energy transfer. Another characteristic of the upconversion generated by ET is that its lifetime is longer under infrared excitation than under visible excitation and it depends on the lifetime of the intermediate and emitting levels as well as on the dopant concentration. [96]

In the present case, the photoluminescence decay from the $^4S_{3/2}$ level does not show any rise time under infrared excitation (Fig. 4.20a and b), which may indicate ESA processes from the $^4I_{13/2}$ and $^4I_{11/2}$ levels which populate the $^4S_{3/2}$ level. However, since the lifetime measured under infrared excitation is longer than the one measured under visible excitation (see Table 4.7), additional ET processes should populate the $^4S_{3/2}$ level. For example, ET processes may occur between two close Er^{3+} ions, both in the

$^4I_{11/2}$ level. One ion passes its energy to the other and goes to the ground state. Then, the other ion reaches the $^4F_{7/2}$ level from which the $^4S_{3/2}$ level is populated by multiphonon relaxation. ESA and ET processes described above are schematically represented in Fig. 4.21.

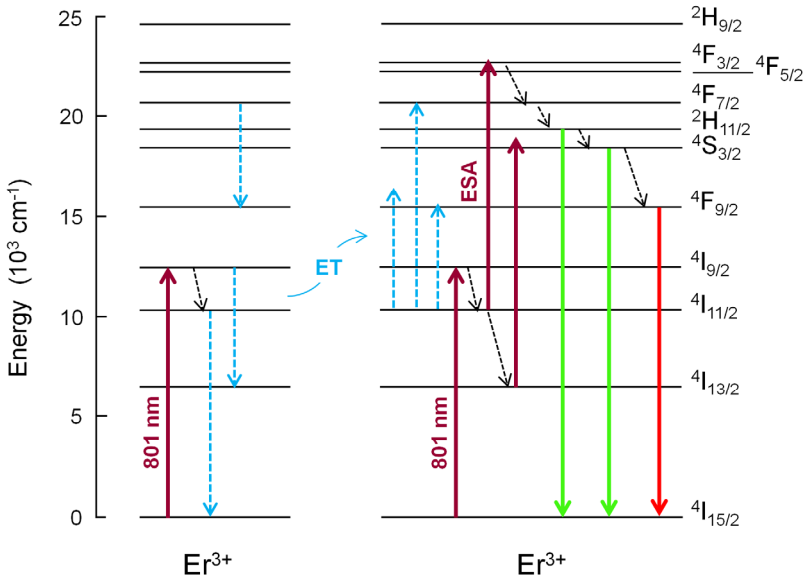

Figure 4.21: Energy level diagrams of Er^{3+} ions in DF glasses. Visible emissions from the $^2H_{11/2}$, $^4S_{3/2}$ and $^4F_{9/2}$ levels are indicated as down arrows while absorption from the ground state or from an excited state (ESA: excited state absorption) are indicated as up arrows. Dashed down arrows indicate nonradiative transitions. Energy transfer (ET) processes, when exciting at 801 nm in resonance with level $^4I_{9/2}$, are represented as dashed cyan arrows.

Regarding the upconverted red emission, there are different mechanisms that may populate the $^4F_{9/2}$ level in DF glasses, depending on Er concentration. When the Er^{3+} concentration is low (0.5 wt% ErF_3), the $^4F_{9/2}$ level can be mainly populated by multiphonon relaxation from the $^4S_{3/2}$ level. In this case, the intensity of the $^4F_{9/2}\rightarrow{}^4I_{15/2}$ transition is very low, compared to the green emission (Fig. 4.17). However, when the Er^{3+} concentration increases, the intensity of the red upconverted emission show a dramatic enhancement (see Fig. 4.18). As described above, this behaviour indicates that the $^4F_{9/2}$ level is mainly populated by ET mechanisms. Moreover, Table 4.7 shows that the short lifetime (τ_s) components of the $^4F_{9/2}$ level, under infrared excitation, have a similar value than the lifetime of the $^4F_{9/2}$ level under visible excitation; whereas, the long lifetime (τ_l) components of the $^4F_{9/2}$ level, under infrared excitation, are very close to the lifetime of the $^4I_{11/2}$ level (λ_{exc}= 801 nm). This behaviour suggests that the intermediate level where ET is originated is the $^4I_{11/2}$ level. For example, as sketched in

Fig. 4.21, an Er^{3+} ion in the $^4I_{11/2}$ level may be promoted to the $^4F_{9/2}$ level ($^4I_{11/2}\rightarrow{}^4F_{9/2}$) by receiving the energy from a close Er^{3+} that undergo the nonradiative transition $^4I_{9/2}\rightarrow{}^4I_{13/2}$. Another ET process able to populate the $^4F_{9/2}$ level is between an Er^{3+} in the $^4F_{7/2}$ level and another in the $^4I_{11/2}$ both ending in the $^4F_{9/2}$ level through the transitions $^4F_{7/2}\rightarrow{}^4F_{9/2}$ and $^4I_{11/2}\rightarrow{}^4F_{9/2}$ (Fig. 4.21).

The results presented have shown that Er doped DF-2 glasses have stronger upconverted emissions, both in intensity and lifetime, than DF-1 glasses. This stems from the larger probability of ESA and ET processes between adjacent Er^{3+} ions in DF-2 than in DF-1, which is proportional to the lifetime of intermediate levels, such as $^4I_{11/2}$, where these processes are originated [96]. As described in the previous sections, this is due to the larger fluorine concentration, and hence larger F/O ratio in DF-2 which reduces both the nonradiative processes due to multiphonon relaxation and OH^-s molecular vibrations. Thus, the lifetime of Er^{3+} excited levels becomes longer in DF-2 than in DF-1.

However, the mechanisms that originate the visible upconverted emissions are similar in DF glasses: the green emission ($^4S_{3/2}\rightarrow{}^4I_{15/2}$) is attributed mainly to ESA processes with a small contribution of ET processes, while the red emission ($^4F_{9/2}\rightarrow{}^4I_{15/2}$) is due mainly to ET processes.

4.7 Photoluminescence response of codoped TeO_2–ZnO–ZnF_2 glasses

As described in the introduction, suitable combinations of rare earth ions may lead to achieve improved emissions from RE doped glasses. For example, Yb^{3+} is well known to act as a sensitizer for Er^{3+}, increasing the pumping efficiency of Er doped glasses at 980 nm [181, 182]. This is due to the larger absorption cross-section of Yb^{3+} with respect to Er^{3+}, at 980 nm, and to its broader absorption band, which extends from ~900 to ~1000 nm. In addition, due to the matching between the $^2F_{7/2}\rightarrow{}^2F_{5/2}$ (Yb^{3+}) emission and the $^4I_{15/2}\rightarrow{}^4I_{11/2}$ (Er^{3+}) absorption, the energy is transferred from Yb^{3+} to Er^{3+} through cross-relaxation. Another possibility is codoping glasses with Er^{3+}-Tm^{3+} to achieve broadband optical amplifiers in the near infrared region. In fact, Tm^{3+} ions

present an emission ($^3H_4 \rightarrow {}^3F_4$) peaking at 1460 nm, in the short wavelength window of optical communications (S band), and another ($^3F_4 \rightarrow {}^3H_6$) peaking at 1800 nm, which covers the long wavelength window of optical communications (L, U bands). These emissions along with the Er^{3+} emission at 1530 nm (C band) may provide optical amplifiers covering the entire optical telecommunication transmission window for multi-channel wavelength division multiplexing (WDM) systems [183, 184, 185].

However, in order to have efficient energy transfer processes between RE ions, it is fundamental that the glass host in which they are embedded possesses a low non-radiative deexcitation rate in order to avoid quenching of energy transfer processes. In this regard, as described in the previous sections, DF glasses are idoneous candidates to be co-doped with RE ions since their maximum phonon energy is around 850 cm^{-1}. In particular, we chose the DF-1 glass host to be codoped with Er^{3+}-Yb^{3+} and Er^{3+}-Tm^{3+} since this is a promising host for broadband optical amplifier at 1.5 μm when doped with Er^{3+}, as we have shown in section 4.6.1.

In the following we present the most relevant results obtained in the photoluminescence characterization of codoped DF-1 glasses.

4.7.1 Er^{3+}-Yb^{3+} codoping

The sensitisation effect of Yb^{3+} in Er-doped DF-1 glasses was studied in three Er^{3+}-Yb^{3+} codoped samples with a fixed Er concentration (0.5 wt% ErF_3) and an increasing Yb concentration (0.5-2 wt% YbF_3), that were produced by melt-quenching (Table 4.8). Moreover, Er^{3+} and Yb^{3+} single-doped glasses were produced too as references.

Table 4.8: Nominal Er and Yb content in the three Er^{3+}-Yb^{3+} codoped DF-1 glasses.

ErF_3 (wt%)	**N(Er)** (10^{20} ions/cm^3)	**YbF_3** (wt%)	**N(Yb)** (10^{20} ions/cm^3)
0.5	0.73	0.5	0.72
0.5	0.73	1	1.5
0.5	0.73	2	2.9

Yb^{3+} is characterised by having only one excited level ($^2F_{5/2}$) at a similar energy (~10000 cm^{-1}) than the $^4I_{11/2}$ (Er^{3+}) level. This is illustrated in Fig. 4.22 where we

compare the absorption spectra of the Er single-doped sample (0.5 wt% ErF_3) and that of an Er-Yb codoped sample (0.5 wt% ErF_3–2 wt% YbF_3).

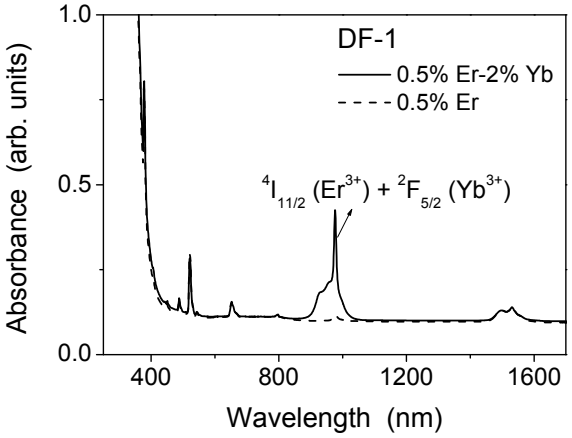

Figure 4.22: Absorption spectra of DF-1 glasses single-doped with 0.5 wt% ErF_3 and codoped with 0.5 wt% ErF_3–2 wt% YbF_3.

They only differ in the wide and intense absorption band in the 900-1000 nm range that peaks at 980 nm. This band is due to the overlap of the $^4I_{15/2}\rightarrow{}^4I_{11/2}$ (Er^{3+}) and the $^2F_{7/2}\rightarrow{}^2F_{5/2}$ (Yb^{3+}) absorption bands. The introduction of Yb^{3+} increases the absorption cross-section at 980 nm by one order of magnitude with respect to the Er^{3+} single-doped sample ($\sigma_{Er\text{-}Yb}= 2.93\cdot10^{-20}$ cm^2 vs. $\sigma_{Er}= 3.18\cdot10^{-21}$ cm^2). Thus, to exploit this large absorption cross-section, we have excited the codoped samples with a Ti-sapphire laser at 980 nm (room temperature) and compared the near infrared $^4I_{13/2}\rightarrow{}^4I_{15/2}$ (Er^{3+}) emission of Er-Yb codoped samples with that of the Er single-doped sample. The experimental room temperature emission spectra are presented in Fig. 4.23.

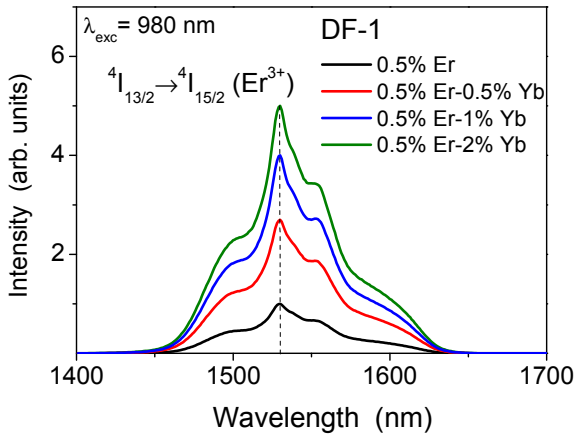

Figure 4.23: Room temperature infrared emission spectra of the $^4I_{13/2}\rightarrow{}^4I_{15/2}$ (Er^{3+}) transition for DF-1 single-doped with 0.5 wt% ErF_3 and codoped with 0.5 wt% ErF_3 and 0.5, 1, and 2 wt% YbF_3 excited at 980 nm.

All emission spectra have a very similar shape, which is independent from Yb^{3+} content. They peak at ~1530 nm and their FWHM is close to 52 nm, as in the case of the Er single-doped glass. However, the intensity of the $^4I_{13/2} \rightarrow {}^4I_{15/2}$ (Er^{3+}) emission increases with Yb^{3+} concentration. It becomes 5 times larger in the codoped glass with 0.5 wt% ErF_3 and 2 wt% YbF_3, with respect to the Er^{3+} single-doped glass (0.5 wt% ErF_3). This behaviour stems from the fact that Yb^{3+} ions can decay either radiatively by emitting at ~980 nm ($^2F_{5/2} \rightarrow {}^2F_{7/2}$) or nonradiatively by transferring their energy to nearby Er^{3+} ions since the probability of multiphonon deexcitation of the $^2F_{5/2}$ level is negligible due to its large energy gap with respect to the ground level (~10000 cm^{-1}). In the last case, the population of the $^4I_{13/2}$ (Er^{3+}) level is increased by energy transfer (ET) processes from Yb^{3+} ions and thus the intensity of the $^4I_{13/2} \rightarrow {}^4I_{15/2}$ (Er^{3+}) emission increases too.

The comparison between the photoluminescence decay of the $^2F_{5/2}$ (Yb^{3+}) level in Yb^{3+} single-doped and Er^{3+}-Yb^{3+} codoped DF-1 samples may offer another proof of energy transfer from Yb^{3+} to Er^{3+}. We have measured the decay of the $^2F_{5/2}$ (Yb^{3+}) level at room temperature, under excitation at 980 nm, by recording the photoluminescence signal at 1070 nm in order to avoid any signal from the $^4I_{11/2} \rightarrow {}^4I_{15/2}$ (Er^{3+}) emission. Figure 5.24a compares the experimental decay curves of the $^2F_{5/2}$ (Yb^{3+}) level in the 2 wt% YbF_3 single-doped sample and in the 0.5 wt% ErF_3–2 wt% YbF_3 codoped sample. We have also studied the temporal evolution of the $^4I_{13/2} \rightarrow {}^4I_{15/2}$ (Er^{3+}) emission in the series of Er-Yb codoped glasses excited at 980 nm (Fig. 4.24b).

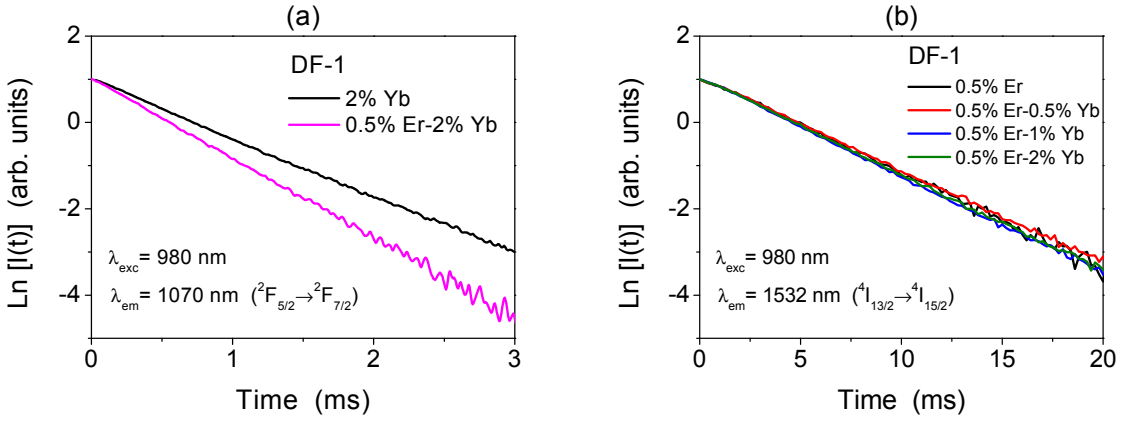

Figure 4.24: (a) Semilogarithmic plot of the room temperature photoluminescence decay of the $^2F_{5/2}$ (Yb^{3+}) level for DF-1 doped with 2 wt% YbF_3 and codoped with 0.5 wt% ErF_3–2 wt% YbF_3 excited at 980 nm. (b) Semilogarithmic plot of the room temperature photoluminescence decay of the $^4I_{13/2}$ (Er^{3+}) level for DF-1 doped with 0.5 wt% ErF_3 and codoped with 0.5 wt% ErF_3 and 0.5, 1, 2 wt% YbF_3 excited at 980 nm.

The decay curves presented in Fig. 4.24 can be fitted by a single exponential function which gives us the lifetime of the emitting $^2F_{5/2}$ (Yb^{3+}) and $^4I_{13/2}$ (Er^{3+}) levels. The lifetime of the $^2F_{5/2}$ level is shorter in the Er-Yb codoped sample (~0.54 ms) than in the Yb^{3+} single-doped sample (~0.70 ms), which confirms the existence of nonradiative energy transfer from Yb^{3+} to Er^{3+}. Similarly, the lifetime of the $^4I_{13/2}$ (Er^{3+}) level is slightly reduced by the addition of YbF_3, as Fig. 4.24b shows. For example, the lifetime of the $^4I_{13/2}$ level is 4.7 ms in the Er^{3+} single-doped sample while is 4.4 ms in the sample codoped with 0.5 wt% ErF_3–2 wt% YbF_3. This fact indicates that little ET, or back transfer, from Er^{3+} to Yb^{3+} occurs in the codoped samples.

The energy transfer efficiency from Yb^{3+} to Er^{3+} can be calculated as: $\eta_{Yb-Er} = 1 - \tau_{Yb-Er}/\tau_{Yb}$, where $\tau_{Yb\text{-}Er}$ and τ_{Yb} are the lifetime of the $^2F_{5/2}$ (Yb^{3+}) level in codoped and single-doped samples, respectively [186]. We have determined that the energy transfer efficiency increases with Yb^{3+} concentration: it goes from 0.05 for the 0.5 wt% ErF_3–0.5 wt% YbF_3 sample to 0.22 for the sample with the higher Yb^{3+} content (0.5 wt% ErF_3–2 wt% YbF_3) [186]. This is due to the reduction of Er^{3+}-Yb^{3+} distance when Yb^{3+} concentration increases, thus energy transfer processes are favoured. However, the largest η_{Yb-Er} calculated for DF-1 glasses (0.22) is lower than the values reported in the literature for tellurite and halide modified tellurite glasses, having similar Er^{3+} and Yb^{3+} contents, which are close to 0.6 [187, 188]. A low value of the $Yb^{3+}\rightarrow Er^{3+}$ ET efficiency has been related with the presence of back transfer from Er^{3+} to Yb^{3+}, which becomes more important when the lifetime of the $^4I_{11/2}$ (Er^{3+}) level increases. In this regard, Gapontsev *et al.* reported that the $Yb^{3+}\rightarrow Er^{3+}$ ET rate mainly depends on the ratio between the back transfer rate ($Er^{3+}\rightarrow Yb^{3+}$) and the multiphonon relaxation rate of the $^4I_{11/2}$ (Er^{3+}) level [189]. Thus, both the presence of $Er^{3+}\rightarrow Yb^{3+}$ back transfer and the low multiphonon relaxation rate of the $^4I_{11/2}$ (Er^{3+}) level in the zinc-fluorotellurite host DF-1 (see section 4.6.1) may be considered the causes for the small value of η_{Yb-Er}.

We have finally investigated the evolution of the visible upconverted emissions with Yb^{3+} concentration in Er^{3+}-Yb^{3+} codoped DF-1 glasses by measuring them at room temperature after exciting the samples at 980 nm. As discussed in section 4.6.2, the green and red emissions are due to the ($^2H_{11/2}$, $^4S_{3/2}$)$\rightarrow$$^4I_{15/2}$ and $^4F_{9/2}\rightarrow$$^4I_{15/2}$ (Er^{3+}) transitions, respectively. Figure 4.25a shows that the overall intensity of both the green and red upconverted emissions increases with Yb^{3+} concentration while Fig. 4.25b

presents the intensity of the green ($^4S_{3/2}$) and red upconverted emission as a function of the YbF_3 content in DF-1 glasses.

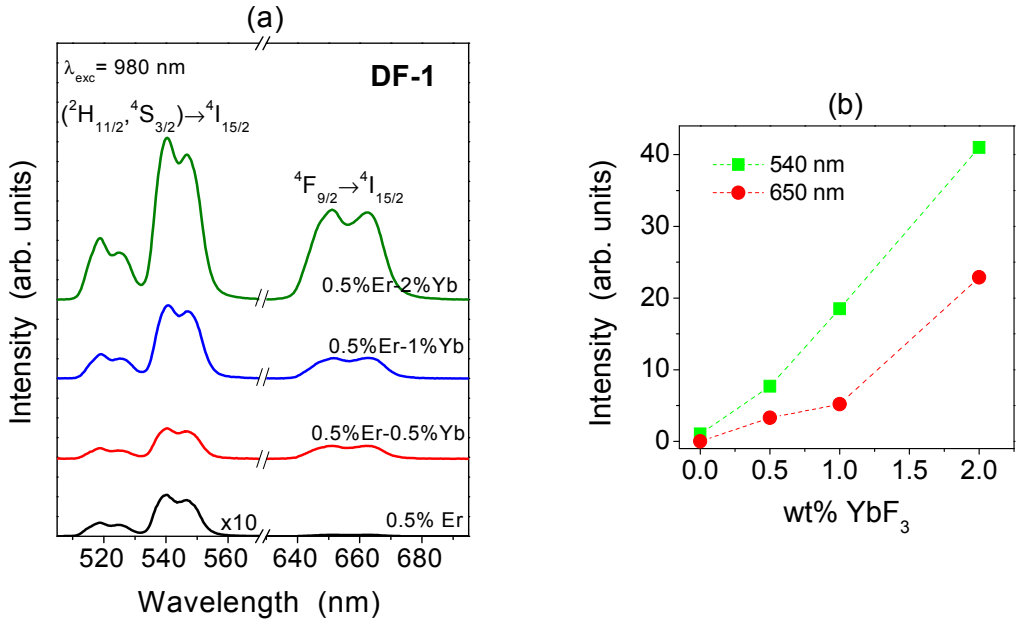

Figure 4.25: (a) Room temperature Er^{3+} visible upconverted emission spectra in the glass host DF-1 codoped with increasing Yb^{3+} concentration (0.5-2 wt% YbF_3) excited at 980 nm. (b) Maximum intensity of the green and red emissions as a function of the YbF_3 content. Dashed lines are guides to the eye.

The intensity of the visible upconverted emissions is maximum in the sample codoped with 0.5 wt% ErF_3–2 wt% YbF_3. In particular, the green emission ($^4S_{3/2}\rightarrow{}^4I_{15/2}$) is ~40 times stronger in this sample than in the case of the Er^{3+} single-doped sample (0.5 wt% ErF_3) and the red emission is ~800 times stronger (Fig. 4.25b). Moreover, the ratio between the intensity of the red and green ($^4S_{3/2}$) emissions increases from 0.03, in the reference Er single-doped sample (0.5 wt% ErF_3), up to 0.55, in the sample codoped with 2 wt% YbF_3. We have calculated the *standardized upconversion efficiency*, which is defined as the ratio between the visible power density emitted and the absorbed infrared power density (fixed to 1 W/cm^2) [190], to quantify the upconverted emissions of DF-1 glasses and to compare it that of other glasses. The standardized upconversion efficiency for the $^4S_{3/2}\rightarrow{}^4I_{15/2}$ emission of the DF-1 glass codoped with the largest YbF_3 content is $1.06\cdot10^{-4}$ [186]. This values is three orders of magnitude larger than that of silicate glasses ($2\cdot10^{-7}$) but it is smaller than the upconversion efficiency of fluoride glasses ($1\cdot10^{-3}$) [190]. Yet, it is large enough to make this glass a good candidate for optical applications in the visible.

The intensity of the green ($^4S_{3/2}$) and red ($^4F_{9/2}$) upconverted emissions shows a quadratic dependence on the excitation laser power (Fig. 4.26), similarly to what it was observed in the case of Er^{3+} doped DF glasses; thus indicating that both the $^4S_{3/2}$ and $^4F_{9/2}$ levels are populated by two photon processes such as exited state absorption (ESA) or energy transfer (ET) [96].

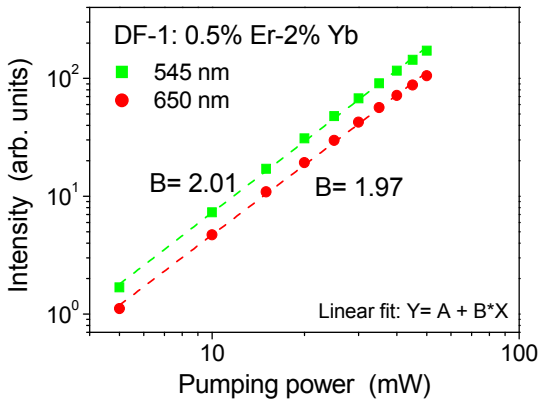

Figure 4.26: Room temperature upconversion emission intensities as a function of pumping power at 980 nm in DF-1 codoped with 0.5 wt% ErF_3–2 wt% YbF_3. Dashed lines are the linear fitting of experimental measurements, which give a slope of 2.01 at 545 nm and of 1.97 at 650 nm.

Figure 4.27 shows the possible upconversion mechanisms responsible for the green and red Er^{3+} emissions when exciting the codoped DF-1 glasses at 980 nm.

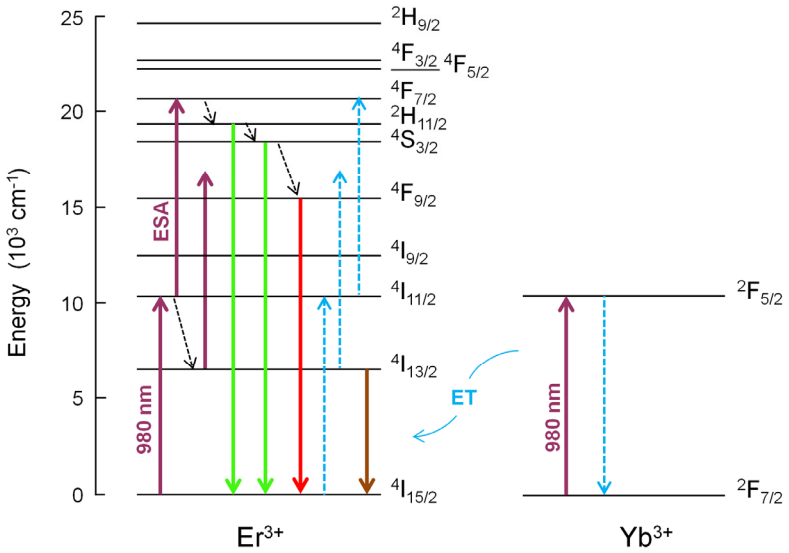

Figure 4.27: Energy level diagrams of Er^{3+} and Yb^{3+} in the codoped DF-1 glasses. Absorptions transitions are indicated as up arrows from the ground state or from an excited state (ESA), while emission transitions as down arrows. Black dashed arrows indicate multiphonon deexcitation while cyan dashed arrows indicate energy transfer (ET) processes between Yb^{3+} and Er^{3+} excited at 980 nm.

Er^{3+} ions can be excited to the $^4I_{11/2}$ state by ground state absorption and by resonant energy transfer from Yb^{3+} ions through the transitions: $^2F_{5/2}\rightarrow{}^2F_{7/2}$ (Yb^{3+}) and $^4I_{15/2}\rightarrow{}^4I_{11/2}$ (Er^{3+}). Therefore, the population of the $^4I_{11/2}$ (Er^{3+}) level increases with Yb^{3+} co-doping and thus the probability of ESA and ET processes which involve this level. For example, once Er^{3+} ions have been excited to the $^4I_{11/2}$ level, they can be promoted to the $^4F_{7/2}$ level by excited state absorption of a second infrared photon or by energy transfer from a close Yb^{3+} ion (Fig. 4.27). We can neglect Er^{3+}-Er^{3+} ET processes since the Er^{3+} content in the glasses considered here is too low ($0.73\cdot10^{20}$ ions/cm^3). Finally, multiphonon deexcitation of the $^4F_{7/2}$ (Er^{3+}) level lead to the population of the lower levels ($^2H_{11/2}$; $^4S_{3/2}$) from which the green emission is originated (Fig.4.27). Further multiphonon relaxation of the $^4S_{3/2}$ level can populate the $^4F_{9/2}$ level from which is originated the red emission.

However, we observe in Fig. 4.25b that the green emission increases at a faster rate than the red emission in DF-1 codoped samples with Yb^{3+} concentration in the range 0.5-1 wt% YbF_3; but both green and red emissions increases at a similar rate in the range 1-2 wt% YbF_3. For this reason, the $^4F_{9/2}$ (Er^{3+}) level should be populated not only by multiphonon relaxation of the $^4S_{3/2}$ level but also by ET/ESA processes, when the YbF_3 content is between 1-2 wt%. Two likely processes that can increase the population of the $^4F_{9/2}$ level in DF-1 codoped glasses are: *i*) ESA from the $^4I_{13/2}$ (Er^{3+}) level; and *ii*) ET from Yb^{3+} ions which decay nonradiatively to the ground level ($^4F_{5/2}\rightarrow{}^4F_{7/2}$) passing their energy to nearby Er^{3+} ions in the $^4I_{13/2}$ level, that thus are promoted to the $^4F_{9/2}$ (Er^{3+}) level (see Fig. 4.27).

To conclude, the DF-1 glass co-doped with the largest Yb^{3+} concentration (0.5 wt% ErF_3–2 wt% YbF_3) has shown strongly enhanced near infrared (5-fold) and visible upconverted Er^{3+} emissions (green: 40-fold, red: 800 -fold) with respect to the Er single-doped DF-1 glass. Thus, it is an adequate candidate to develop broadband amplifiers in the optical C band as well as devices based on the visible upcoverted Er^{3+} emissions.

4.7.2 Er^{3+}-Tm^{3+} codoping

To end this chapter, we investigate the effect of Tm^{3+} codoping on the near infrared photoluminescence response of DF glasses. We have produced a series of four Er^{3+}-Tm^{3+} codoped glasses having a fixed Er content and increasing Tm content by

melt-quenching, as summarized in Table 4.9. Er^{3+} and Tm^{3+} single doped DF-1 glasses were produced too as references.

Table 4.9: Nominal Er and Tm content in the four Er^{3+}-Tm^{3+} co-doped DF-1 glasses.

ErF_3 (wt%)	**N(Er)** (10^{20} ions/cm^3)	**TmF_3** (wt%)	**N(Tm)** (10^{20} ions/cm^3)
0.3	0.43	0.3	0.43
0.3	0.43	0.5	0.72
0.3	0.43	0.7	1
0.3	0.43	1	1.4

Figure 4.28 compares the absorption spectrum of the Er single-doped (0.3 wt% ErF_3) and an Er-Tm codoped DF-1 glasses. In this case, the $^4I_{9/2}$ (Er^{3+}) and $^3H_4$ (Tm^{3+}) levels overlap in a region close to 800 nm. Thus, in order to excite both rare earth ions at the same time, codoped samples have been excited with a Ti-sapphire laser at 792 nm, in resonance with the $^4I_{9/2}$ (Er^{3+}) and the $^3H_4$ (Tm^{3+}) levels.

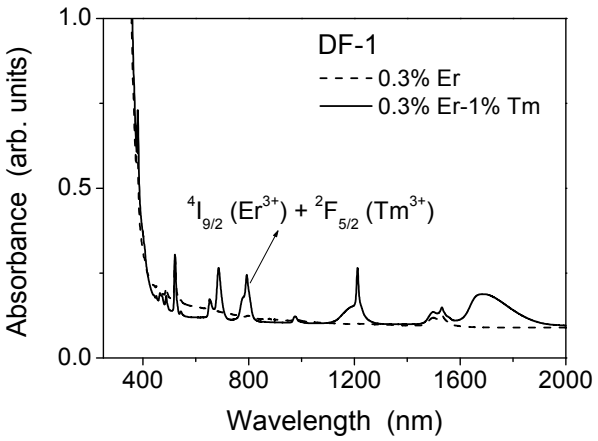

Figure 4.28: Absorption spectra of DF-1 single-doped with 0.3 wt% ErF_3 and codoped with 0.3 wt% ErF_3–1 wt% TmF_3.

Figure 4.29a shows the room temperature near infrared emission spectra collected from Er-Tm codoped DF-1 glasses and from the reference Er single-doped glass (0.3 wt% ErF_3). All emission spectra have been normalized to the peak of the $^4I_{13/2}\rightarrow{}^4I_{15/2}$ (Er^{3+}) emission (at 1532 nm) in order to ease their comparison.

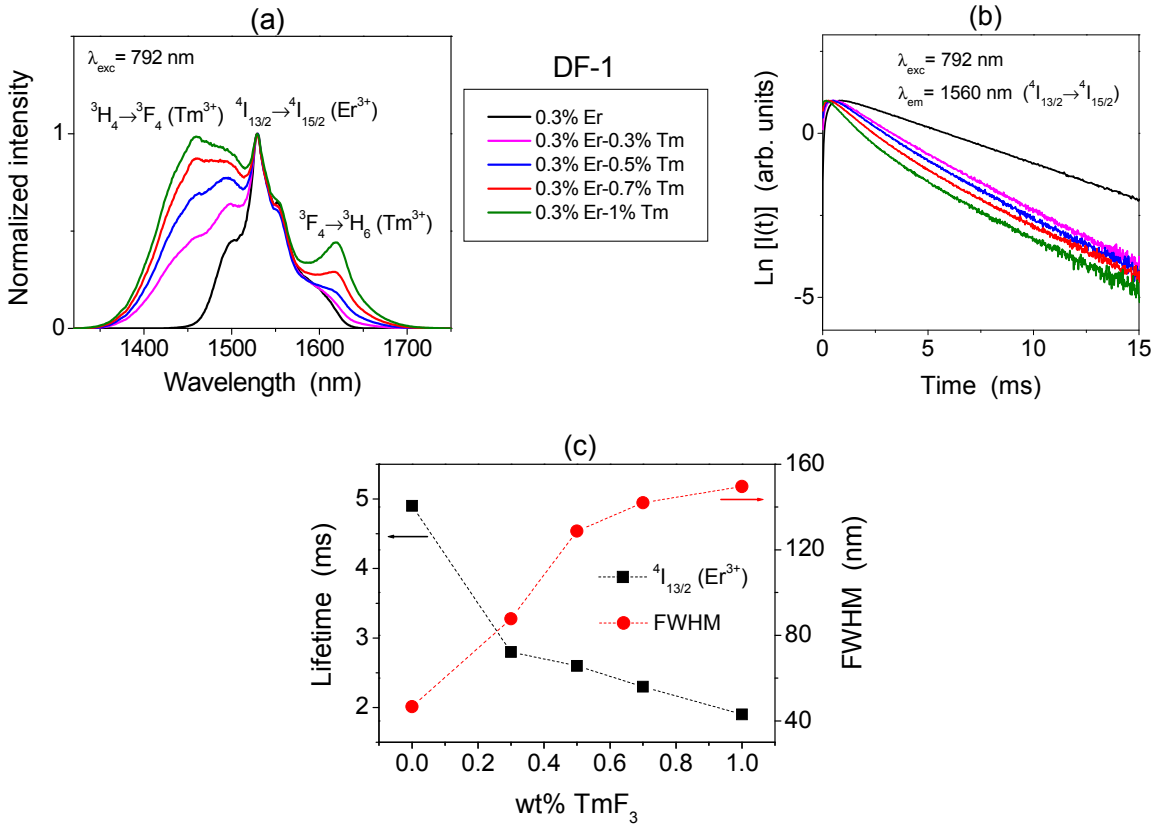

Figure 4.29: (a) Room temperature normalized near infrared emission spectra of Er-Tm codoped and Er single-doped DF-1 glasses excited at 792 nm. (b) Semilogarthmic plot of the room temperature photoluminescence decay of the $^4I_{13/2}$ (Er^{3+}) level under excitation at 792 nm in Er-Tm codoped and Er single-doped DF-1 glasses. (c) Full width at half maximum (FWHM) of the emission spectra in (a) and mean lifetime of the $^4I_{13/2}$ (Er^{3+}) level. Dashed lines are guides to the eye.

We can clearly distinguish three overlapping bands in the spectra of codoped glasses (Fig. 4.29a), which belong to Er^{3+} and Tm^{3+} transitions: the band peaking at 1460 nm corresponds to the $^3H_4 \rightarrow {}^3F_4$ (Tm^{3+}) transition; the one peaking at 1532 nm corresponds to the $^4I_{13/2} \rightarrow {}^4I_{15/2}$ (Er^{3+}) transition; and finally, the small band at 1620 nm is the short wavelength tail of the $^3F_4 \rightarrow {}^3H_6$ (Tm^{3+}) transition. Unfortunately, we were not able to measure the entire $^3F_4 \rightarrow {}^3H_6$ (Tm^{3+}) transition due to the upper limit of the detector at 1700 nm. The relative intensity of the $^3H_4 \rightarrow {}^3F_4$ and $^3F_4 \rightarrow {}^3H_6$ (Tm^{3+}) emission bands increases with Tm^{3+} content. Moreover, the full width at half maximum (FWHM) of the near infrared emission spectra increases too with Tm^{3+} concentration, as shown in Fig. 4.29c. In particular, the FWHM increases from 50 nm, in the reference Er single-doped sample (0.3 wt% ErF_3), up to 150 nm, in the sample codoped with 1 wt% TmF_3. This value is larger than the one reported in Er-Tm codoped tellurite glasses (134 nm) [183] and it is only 10 nm less than the FWHM of Er-Tm codoped chalcohalide glasses [184] and tungsten-tellurite glasses [185]. Thus, the near infrared Tm^{3+} and Er^{3+} emissions in

DF-1 glasses (from 1430 to 1680 nm) would allow covering the entire optical communication window, that is: the S, C, L and U bands in wavelength division multiplexing transmission systems [12].

In addition to the FWHM value, the lifetime of the $^4I_{13/2} \rightarrow {}^4I_{15/2}$ (Er^{3+}) near infrared emission is another relevant parameter used to characterize the amplifier performance. We have obtained the experimental decay of the $^4I_{13/2}$ (Er^{3+}) level by exciting the DF-1 codoped glasses at 792 and collecting the photoluminescent signal at 1560 nm in order to avoid contributions from the $^3H_4 \rightarrow {}^3F_4$ (Tm^{3+}) transition. As we can appreciate in Fig. 4.29b, the decay of the $^4I_{13/2}$ (Er^{3+}) level in Er-Tm codoped samples cannot be fitted by a single exponential function as in the case of the Er single-doped glass. Thus, we have calculated the mean lifetime of the $^4I_{13/2}$ (Er^{3+}) level in the co-doped glasses by using Eq. 3.13. The obtained lifetime values are plotted in Fig. 4.29c as a function of TmF_3 content in DF-1 glasses. We observe that the lifetime of the $^4I_{13/2}$ (Er^{3+}) level shortens as Tm^{3+} concentration increases. It decreases from 4.9 ms, for the Er single-doped (0.3 wt% ErF_3) glass, to 1.9 ms, for the Er-Tm codoped glass with 0.3 wt% ErF_3–1 wt% TmF_3. This phenomenon can be attributed to a higher probability of nonradiative decay of Er^{3+} ions through energy transfer processes, when Tm^{3+} concentration increases. As illustrated in Fig. 4.30, the 792 nm excitation promotes Er^{3+} ions to the $^4I_{9/2}$ level from which nonradiative de-excitation occurs, leading to the population of the $^4I_{11/2}$ and $^4I_{13/2}$ levels. While some Er^{3+} ions decay radiatively to the ground state ($^4I_{13/2} \rightarrow {}^4I_{15/2}$), others ions can transfer their energy to the $^3F_4$ (Tm^{3+}) level through the $^4I_{13/2} \rightarrow {}^4I_{15/2}$ (Er^{3+}) and $^3H_6 \rightarrow {}^3F_4$ (Tm^{3+}) transitions. This process depopulates the $^4I_{13/2}$ (Er^{3+}) level and thus reduces its lifetime.

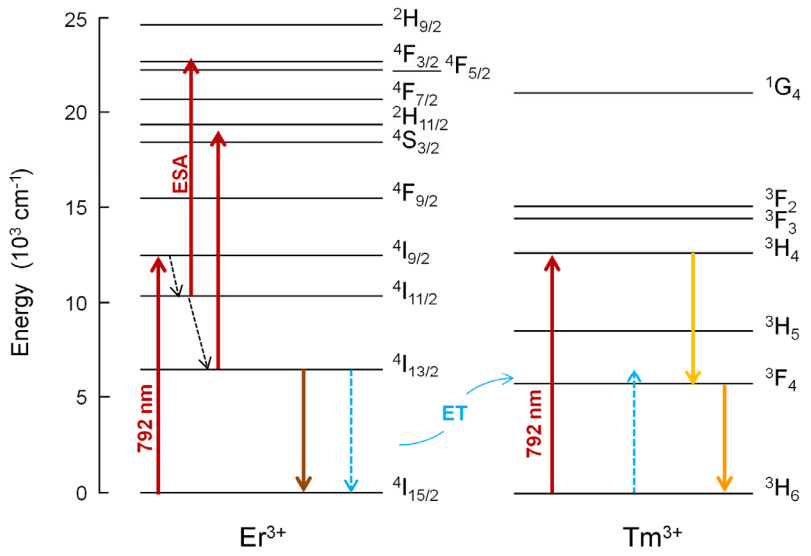

Figure 4.30: Energy level diagrams of Er^{3+} and Tm^{3+} in DF-1 glasses. Absorptions transitions are indicated as up arrows from the ground state or from an excited state (ESA), while the emission transitions as down arrows. Black dashed arrows indicate multiphonon deexcitation while cyan dashed arrows indicate energy transfer (ET) processes between Er^{3+} and Tm^{3+} excited at 792 nm.

As in the case of Er-Yb codoped glasses, we have calculated the Er^{3+}→Tm^{3+} energy transfer efficiency (η_{Er-Tm}) to quantify the Er^{3+}→Tm^{3+} energy transfer in the codoped glasses. It is defined as: $\eta_{Er-Tm} = 1 - \tau_{Er-Tm}/\tau_{Er}$, where $\tau_{Er\text{-}Tm}$ and τ_{Er} are the lifetime of the $^4I_{13/2}$ (Er^{3+}) level in co-doped and single-doped samples, respectively [191]. η_{Er-Tm} ranges from 0.45 for the 0.3 wt% ErF_3–0.3 wt% YbF_3 sample to 0.60 for the sample with the highest Tm^{3+} content (0.3 wt% ErF_3–1 wt% YbF_3). These values are quite large if we compare them with those of Er-Yb codoped DF-1 glasses. However, they are similar to the Er^{3+}→Tm^{3+} energy transfer efficiency reported for zinc-tellurite glasses [192] but they are lower than the η_{Er-Tm} of tungsten-tellurite glasses [185].

In conclusion, among the studied DF-1 glasses co-doped with Er^{3+}-Tm^{3+}, the glass co-doped with the largest Tm concentration (0.3 wt% ErF_3–1 wt% TmF_3) has shown the widest FWHM (150 nm) and the largest Er^{3+}→Tm^{3+} energy transfer efficiency (0.60). Therefore, we consider that this co-doped glass is a suitable candidate to implement broadband amplifiers in the entire telecommunication window of WDM systems.

4.8 Summary and conclusions

In this chapter we have studied the structural and optical properties of rare earth doped TeO_2–ZnO–ZnF_2 glasses. We selected two different glass hosts whose nominal composition was: 74.6 TeO_2–8.8 ZnO–16.6 ZnF_2 mol% (**DF-1**) and 46.6 TeO_2–18.2 ZnO–35.2 ZnF_2 mol% (**DF-2**). Both glass hosts were doped with Er^{3+} and in addition, DF-1 was codoped with Er^{3+}-Yb^{3+} and Er^{3+}-Tm^{3+}.

We have first analyzed the **composition** of DF-1 and DF-2. A large fluorine loss (~45-50 %), due to the chemical reaction between fluorine and water during glass melting, and a relative enrichment of Zn with respect to Te (~40-60 %) are observed in both glasses. Thus, the actual composition of the fluorotellurite glasses is: 68 TeO_2–22 ZnO–10 ZnF_2 mol% (DF-1) and 35 TeO_2–46 ZnO–19 ZnF_2 mol% (DF-2).

Thermal analysis of DF-1 and DF-2 glasses has shown that both have a large thermal stability range ($T_{on} - T_g \approx$ 100-130 ºC), which slightly decreases when the dopant concentration (ErF_3) increases. Besides, X-ray diffractometry measurements have shown that the main crystalline phases that nucleate at ~420 ºC and melt at ~600 ºC in these glasses are α-TeO_2 and $Zn_2Te_3O_8$.

The **structure** of TeO_2–ZnO–ZnF_2 glasses mainly depends on the Zn/Te ratio. This is due to the action of the glass modifier cation (Zn^{2+}), which breaks up the strong tellurite network by converting TeO_4 units into TeO_{3+1} and TeO_3 units. Therefore, the glass with the larger Zn/Te ratio (DF-2: Zn/Te≈ 1.86) shows a loose network structure composed mainly by TeO_3 units and TeO_{3+1} units, with only few TeO_4 units. On the contrary, the glass with the smaller Zn/Te ratio (DF-1: Zn/Te≈ 0.47), shows a strongly connected glass network which is mainly composed by TeO_{3+1} units and by TeO_3/TeO_4 units in almost equal parts. Finally, the maximum phonon energy of DF-1 and DF-2 glass networks is ~850 cm^{-1}.

The **optical characterization** of DF-1 and DF-2 has shown, as already described in the literature, that the position of the UV absorption edge and the value of the refractive index depend on the Zn/Te ratio. As the content of Te^{4+} decreases and the content of the modifying cation (Zn^{2+}) increases, the UV absorption edge shifts to shorter wavelengths, *i.e.* from ~385 nm (DF-1) to ~343 nm (DF-2), whereas the value of the refractive index decreases, *i.e.* from 2.00 (DF-1) to 1.82 (DF-2) at 1500 nm. However,

both DF-1 and DF-2 showed a broad transparency region from the visible to the infrared region (up to ~6 μm). Moreover, they present very small absorption bands due to O-H stretching vibrations in OH^- groups (at ~3.3 μm). From the intensity of these bands, we have estimated the total OH^- content in DF glasses. This is 56.3 *ppm* (corresponding to $1.12 \cdot 10^{19}$ ions/cm^3) in DF-1 while it is only 39.8 *ppm* (corresponding to $0.75 \cdot 10^{19}$ ions/cm^3) in DF-2. This small OH^- content is a consequence of the melting dehydration caused by the reaction of fluorine with water related.

The second part of the chapter is devoted to the study of the **photoluminescence response** of **Er doped DF glasses**. In particular, we have considered the $^4I_{13/2} \rightarrow {}^4I_{15/2}$ near infrared emission and the green ($^4S_{3/2} \rightarrow {}^4I_{15/2}$) and red ($^4F_{9/2} \rightarrow {}^4I_{15/2}$) visible upconverted emissions. The emission spectra and the lifetime of these emissions were measured at room temperature by exciting at 801 nm in resonance with the $^4I_{9/2}$ level.
Due to the importance of the $^4I_{13/2} \rightarrow {}^4I_{15/2}$ emission in optical amplifiers for telecommunication networks, we have determined the parameters of this emission and two figures of merit (FOM) on the performance of optical amplifiers. Especially, DF-1 presents a wider emission bandwidth (FWHM= 63 nm for 1 wt% ErF_3) and a larger cross-section ($\sigma_e^{peak} = 8.8 \cdot 10^{-21}$ cm^2 for 1 wt% ErF_3) with respect to DF-2 (FWHM= 55 nm, $\sigma_e^{peak} = 7.5 \cdot 10^{-21}$ cm^2 for 1 wt% ErF_3), due to its larger refractive index. Thus, DF-1 is a promising candidate for developing **broadband optical amplifier in the C band** (1.5 μm). On the contrary, DF-2 presents stronger infrared to visible upconverted emissions than DF-1. In particular, DF-2 doped with 3 wt% ErF_3 presents both strong green and red emissions that make this glass suitable for devices such as **phosphors** and upconverters. The strong upconversion of DF-2 is related to the large probability of excited state absorption and energy transfer processes for Er^{3+} ions in this glass, which populate the $^4S_{3/2}$ and $^4F_{9/2}$ levels. The probability of these processes is related to the radiative lifetime of intermediate levels, which depends on the environment of Er^{3+} ions. An ionic environment and a low OH^- content, as in the case of DF-2, reduce the nonradiative relaxation of rare earth ions thus increasing the radiative lifetime of intermediate levels.

Finally, we have studied the photoluminescence response of **DF-1 glasses codoped** with **Er-Yb** and **Er-Tm**. In the first case, the objective was to increase the pumping efficiency of Er^{3+} at 980 nm, since Yb^{3+} presents only one excited level ($^2F_{5/2}$) at the same energy of the $^4I_{11/2}$ (Er^{3+}) level but with a larger absorption cross-section. We have

achieved an enhancement of the $^4I_{13/2}\rightarrow{}^4I_{15/2}$ (Er^{3+}) near infrared emission (5-fold); the $^4S_{3/2}\rightarrow{}^4I_{15/2}$ (Er^{3+}) green upconverted emission (40-fold); the $^4F_{9/2}\rightarrow{}^4I_{15/2}$ (Er^{3+}) red upconverted emission (800-fold), for the glass codoped with 0.5 wt% ErF_3–2 wt% YbF_3 with respect to the single Er doped glass. This is due to $Yb^{3+}\rightarrow Er^{3+}$ energy transfer processes that have a larger probability to occur than energy transfer processes between Er^{3+} ions, due to the larger absorption cross-section of Yb^{3+} ions (at 980 nm) with respect to Er^{3+} ions. Thus, the DF-1 glass codoped with 0.5 wt% ErF_3–2 wt% YbF_3 shows improved photoluminescence emissions with respect to the Er single-doped glass and it is therefore an adequate candidate to develop broadband amplifiers in the optical C band as well as devices based on the upconverted visible emissions.

Instead, codoping with Tm^{3+} was aimed at increasing the emission bandwidth available for signal amplification in the near infrared region, which is used in WDM transmission systems. When pumped at 792 nm, in resonance with the $^4I_{9/2}$ (Er^{3+}) and the $^3H_4$ (Tm^{3+}) levels, the DF-1 glass codoped with 0.3 wt ErF_3–1 wt% TmF_3 shows a full width at half maximum three times larger than that of the Er single-doped glass (150 nm vs. 50 nm). The large emission bandwidth of the Er-Tm codoped glass is due to the superposition of Tm^{3+} and Er^{3+} emission bands in the infrared region and to energy transfer processes between these ions. Thus, the DF-1 glass codoped with 0.3 wt ErF_3–1 wt% TmF_3 is a suitable candidate to implement **broadband amplifiers in the S, C, L and U bands** of the optical telecommunication transmission window.

5

Transparent Er^{3+} doped TeO_2–ZnO–ZnF_2 glass-ceramics

5.1 Introduction

In chapter 4 we discussed the structural and optical properties of rare earth doped TeO_2–ZnO–ZnF_2 glasses with two different compositions: 68 TeO_2–22 ZnO–10 ZnF_2 mol% (DF-1) and 35 TeO_2–46 ZnO–19 ZnF_2 mol% (DF-2). We studied the photoluminescence response of these glasses as a function of Er^{3+} concentration to find out that DF-1 possessed a more intense near infrared emission (at 1.5 μm) than DF-2, although the latter showed stronger upconverted visible emissions. These results were related to the glass structure and to the environment of Er^{3+} ions, which are strongly connected with the glass composition and its fabrication process. Therefore, it is possible to increase the emission efficiency of rare earth ions by choosing an optimised glass host composition.

However, there is another way to increase the emission efficiency of rare earth ions that is based on the engineering of their environment at the nanoscale, by transforming the glass host into a glass-ceramic [39, 110]. This allows the combination of the properties of glass and a crystalline nano-phase in the same host leading to an improved photoluminescence response [111, 112]. In particular, oxyfluoride glasses have been indicated as the best candidates to produce rare earth doped glass-ceramics since they are able to provide a fluoride crystalline environment for rare earth ions inside an oxide amorphous matrix [42, 44]. Thus, oxyfluoride glass-ceramics behave mostly like oxide glasses in terms of preparation and processing, *e.g.* they can be easily fiberized, but in addition they allow rare earth ions to be in a low phonon energy environment, which increases the efficiency of their emissions.

Most rare earth doped glass-ceramics prepared to date have been synthesized from oxyfluoride silicate glasses. This is most likely due to the fact that controlled crystallisation of these glasses is feasible and their nucleation and crystallisation mechanisms have been studied in detail [42, 193, 194]. For example, the ability of LaF_3 crystallisation upon thermal treatments, was related to the $NaO_2/(SiO_2+Al_2O_3)$ ratio and to a La/Si phase separation in the Na_2O–Al_2O_3–SiO_2–LaF_3 system [42, 193].
On the contrary, very little information can be found in the literature on oxyfluoride tellurite (or fluorotellurite) glass-ceramics and only few authors reported results on rare earth glass-ceramics of these systems. For example, Rojo and coauthors studied the relation between the ionic conductivity and nanocrystals formation in a Li_2O-LiF-TeO_2 glass [195] whereas Yu and coauthors reported glass-ceramics in the TeO_2–ZnO–ZnF_2–YF_3–ErF_3 system [196]. They detected the formation of $Y_2Te_6O_{15}$ or $Er_2Te_5O_{13}$ crystalline phases and observed a stronger upconversion and near infrared emission, at 1.5 μm, in the case of glass-ceramic samples. Besides, Hou and coauthors reported the precipitation of CaF_2 nanocrystals in the TeO_2–SiO_2–AlF_3–CaO–NaF–ErF_3 system [197]. This glass-ceramic showed a slightly more intense near infrared emission, at 1.5 μm, than the glass sample. Finally, Joshi et al. reported the precipitation of nano-crystals of different oxide phases in a TeO_2–Li_2CO_3–PbF_2–$PbCl_2$ glass co-doped with Er^{3+}/Yb^{3+} [198]. They observed intense visible upconversion in glass-ceramic and ceramic samples.

In this chapter we study in detail the preparation, the microstructure and the photoluminescence response of transparent fluorotellurite glass-ceramics obtained from the glass DF-1 doped with 1 wt% ErF_3. To our knowledge, this is the first time that transparent Er^{3+} doped glass-ceramics are synthesized in this glass matrix.

5.2 Synthesis of glass-ceramic samples

As described in chapter 2, the most common procedure to obtain glass-ceramics from glasses is though controlled thermal treatments [41]. In particular, it is usually employed a two-step thermal treatment, which consists in heating the precursor glass from room temperature (RT) to a temperature T_1 during a time D_1 to induce nuclei formation and then, to further increase the annealing temperature to a value T_2 and holding the sample at this temperature a time D_2 to induce the crystal growth [41]. Once the second annealing step is ended the sample is cooled down to room temperature. Figure 5.1 represents schematically the two-step thermal treatment described.

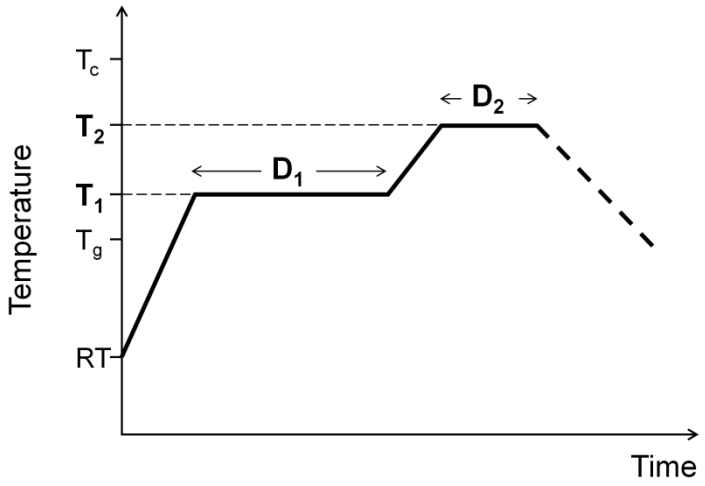

Figure 5.1: Two-step thermal treatment used to produce glass-ceramic samples. The glass is heated at a fixed rate until a temperature T_1 at which is maintained during a time D_1 to induce nuclei formation. Then, the annealing temperature is increased to the value T_2 at which the sample stays for a time D_2 to induce crystal growth. Finally the sample is cooled down to room temperature.

There are general rules on the optimal range for the nucleation temperature (T_1) that goes from T_g up to ~50 ºC above it, and the crystal growth temperature (T_2), which should be kept close to T_1 in order to have a low crystal growth rate and so small crystals [43]. Nevertheless, the optimal values of T_1 and T_2 together with the duration and heating rate of each annealing step depend on the glass composition and its thermodynamic properties. Therefore, we study in detail in the following section the nucleation and crystal growth behaviour of DF glasses to design the optimum thermal treatments for their nanocrystallisation.

5.2.1 Nucleation and crystal growth behaviour of TeO_2–ZnO–ZnF_2 glasses

In chapter 4 we calculated the thermal stability range ($T_{on} - T_g$) of DF glasses from their DSC curves obtained from glass chips heated at a constant rate of 10 ºC/min. Both glasses showed to be thermally stable since their $T_{on} - T_g$ was larger than 100 ºC. In order to investigate the effect of the heating rate on the thermal properties and the crystallisation behaviour of DF glasses, we have performed DSC measurements on grinded glass samples in the 200-500 ºC interval at different heating rates (5, 10, 15 ºC/min). The resulting DSC curves are shown in Fig. 5.2a and b, for DF-1 and DF-2 glasses doped with 1 wt% ErF_3, respectively. We note that the glass transition (T_g), onset of crystallisation (T_{on}) and crystallisation (T_c) temperatures shift to higher values with increasing heating rates. Moreover, the dependence of these temperatures on the heating rate can be fitted linearly in the plot Ln(T) versus the heating rate (q) as shown in Fig. 5.2c and d.

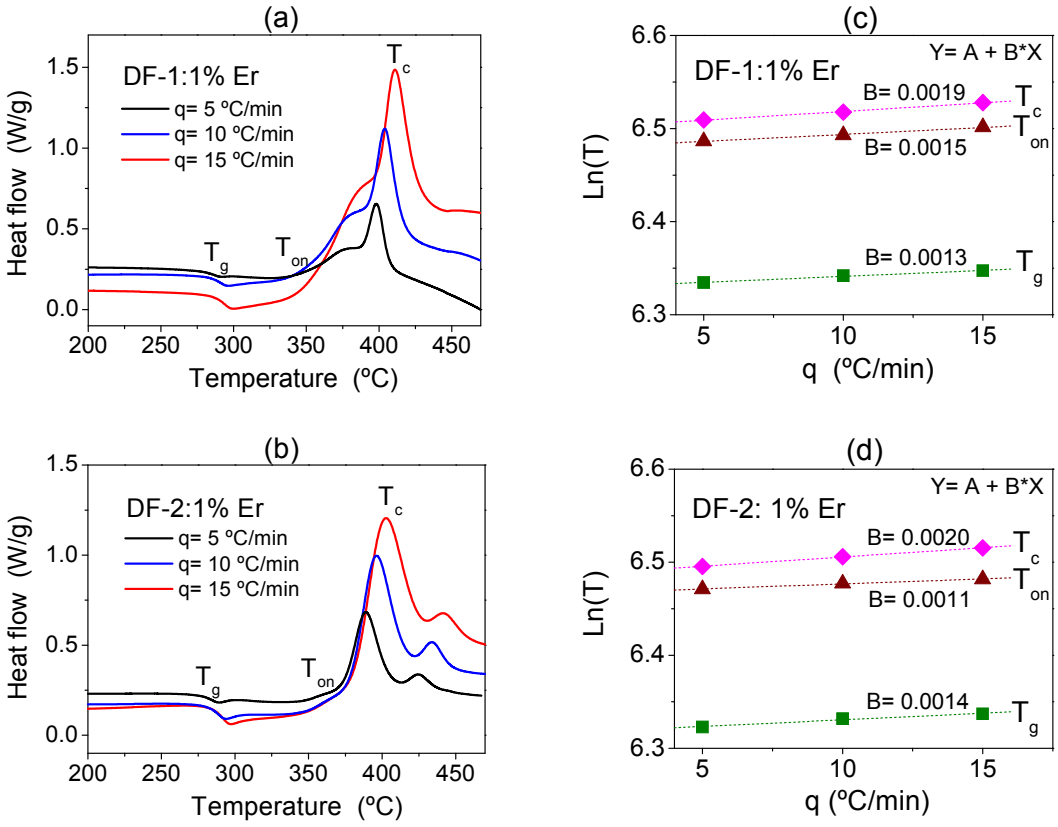

Figure 5.2: (a, b) DSC measurements at the heating rates of 5, 10, and 15 ºC/min and (c, d) plot of Ln(T) versus the heating rate for glass transition temperature (T_g); onset of crystallisation temperature (T_{on}); and main crystallisation temperature (T_c) for (a, c) DF-1 and (b, d) DF-2 doped with 1 wt% ErF_3. Dashed lines in (c) and (d) correspond to the linear fit to experimental data.

The variation of the characteristic temperatures with the heating rate, represented by the slope of the linear fit (B in Fig. 5.2c and d), is quite small for both DF glasses. The crystallisation temperature (T_c), which corresponds to the value of the main crystallisation peak of Fig. 5.2a and b, is the most sensitive to the heating rate in both cases but, even in this case, its variation with the heating rate is small: T_c varies from 398 to 411 ºC in the case of DF-1 and from 389 to 402 ºC in DF-2, as the heating rate increases from 5 to 15 ºC/min.

The variation of T_c with the heating rate (q) allows us to determine an important kinetic parameter for glass crystallisation, that is the activation energy for crystallisation (E_c), through the Kissinger equation [199]:

$$\mathrm{Ln}\left(\frac{q}{T_c^2}\right) = -\frac{E_c}{RT_c} + \mathrm{Constant} \qquad (5.1)$$

where R is the gas constant (R= 8.314 J/K·mol). E_c is inversely proportional to the rate of crystal growth at a temperature lower than T_c; therefore, it is related to the glass resistance to crystallisation [199].

From Eq. 5.1, the slope of the linear fit to experimental data in the plot of $Ln(q/T_c^2)$ vs. $(1000/T_c)$[1] corresponds to $-E_c/R$. Figure 5.3 shows the $Ln(q/T_c^2)$ vs. $1000/T_c$ plot with the experimental data obtained for DF-1 and DF-2 glasses.

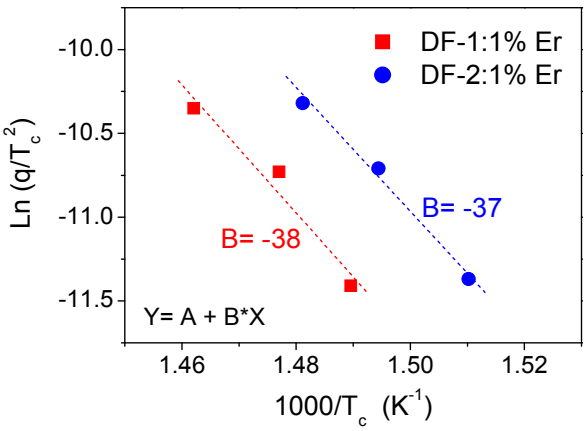

Figure 5.3: Plot of $Ln(q/T_c^2)$ versus $1000/T_c$ for DF-1 and DF-2 doped with 1 wt% ErF_3. Dashed lines correspond to the linear fit to experimental data.

We observe in Fig. 5.3 that E_c is similar for both DF glasses, being ~309 kJ/mol and ~301 kJ/mol in the case of DF-1 and DF-2, respectively, for the phase transformations

[1] We choose $1000/T_c$ instead of $1/T_c$ in order to obtain E_c in kJ/mol.

corresponding to the main crystallisation peak. Moreover, we have also calculated the activation energy for crystallisation ($E_{c'}$) for the phase transformation corresponding to the smaller crystallisation peaks present in the DSC curves of DF-1 and DF-2 at ~360 and ~420 ºC, respectively (Fig. 5.2a and b). We have found that $E_{c'} \approx 374$ kJ/mol in the first, while $E_{c'} \approx 258$ kJ/mol in the latter.

The activation energy for crystallisation of DF glasses is moderate, which indicate that their crystal growth rate is moderate too and that they do not show a large resistance to crystallisation. If we compare the TeO_2–ZnO–ZnF_2 glasses considered in this work with other tellurite systems we observe that they show a larger E_c than TeO_2–LiO_2–WO_3 [200] and TeO_2–Bi_2O_3–ZnO [201] glasses ($E_c \approx$ 150-250 kJ/mol), but smaller than a 75 TeO_2–20 ZnO–4 Na_2CO_3 glass ($E_c \approx$ 900 kJ/mol) [178].

If we focus on the DSC curves of DF glasses obtained from grinded glass samples, in form of powder (Fig. 5.2a-b), and we compare them with the traces presented in chapter 4, obtained from chips of the same glasses, we can observe important differences. These are clearly seen in Fig. 5.4 where we compare the DSC curves (q= 10 ºC/min) from both types of samples in the case of DF-1. The same behaviour has been also observed in the case of DF-2.

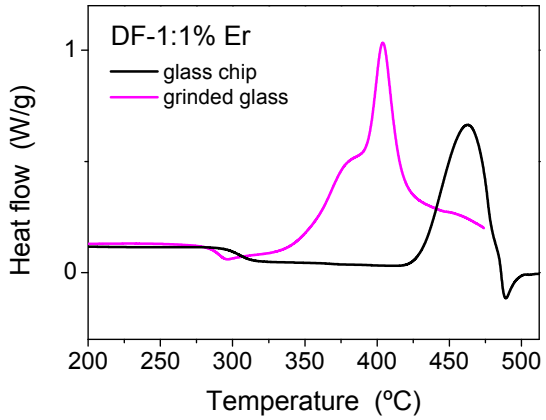

Figure 5.4: DSC curves at a fixed heating rate of 10 ºC/min for a glass chip (sphere of few mm) and grinded glass (particles of ~0.01 mm) in the case of DF-1 doped with 1wt% ErF_3.

We observe in the figure that both crystallisation and glass transition temperatures shift to lower values when the size of glass samples is reduced from a diameter of a few mm to ~0.01 mm. Moreover, the DSC curve belonging to the glass chip shows a very broad crystallisation peak compared to the curve of the grinded glass. These differences

cannot be related to bulk (or volume) nucleation, since in that case the crystallisation peak would not be affected by the size of glass samples used in the measurements. Instead, the strong dependence of T_c with the size of glass samples can be attributed to surface nucleation, since a small sample (*i.e.* grinded glass) would crystallise easier, that is at a lower temperature, than a large sample (*i.e.* glass chip), due to the larger surface to volume ratio in the first case [41].

Finally, we have followed the methods proposes by Marotta [202] and Ray [203] to determine the nucleation and crystal growth rate-like curves for DF glasses, respectively, through differential thermal analysis experiments. While these curves are not quantitative, they indicate the temperature range where the nucleation and crystal growth rates increase. The first method consists in comparing the temperature corresponding to the crystallisation peak with (T_c) and without (T_c^0) an isothermal hold for 30 min at a potential nucleation temperature (T_n), as schematically represented in Fig. 5.5a. The heating rate employed is 20 °C/min to neglect nuclei formation during heating [202]. The nucleation rate-like curve is then obtained from the plot of ($1/T_c - 1/T_c^0$) as a function of T_n, since the number of nuclei formed during the isothermal hold is proportional to the shift of T_c to lower values [202].

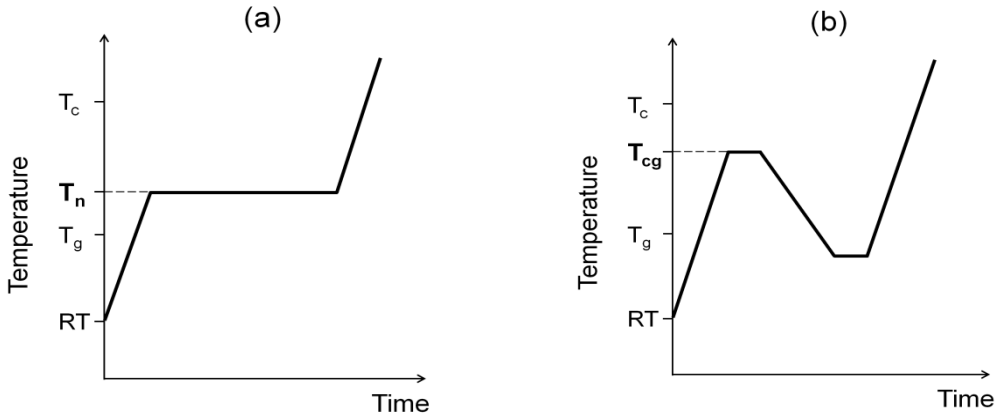

Figure 5.5: Schematic representation of thermal treatments performed with the DSC to determine the (a) nucleation rate and (b) crystal growth rate-like curves.

The method employed to determine the crystal growth rate-like curve is based on the comparison between the area of the crystallisation peak with (A_T) and without (A) an isothermal hold of the sample during 5 minutes at a potential crystal growth temperature (T_{cg}) [203]. A fixed amount of grinded glass (~50 mg) and a heating rate of 20 °C/min were employed in all measurements. After the isothermal hold at T_{cg}, the sample is

cooled down below T_g and stabilised during 5 minutes. In the last step the sample is heated again until a temperature larger than T_c. Figure 5.5b represents the thermal cycle described above. Then, the crystal growth rate-like curve is obtained from the plot $\Delta A = A - A_T$ versus T_{cg}, due to the fact that the area of the crystallisation peak is linearly proportional to the amorphous phase volume [203].

Figure 5.6 presents the nucleation and crystal growth rate-like curves obtained for two representative fluorotellurite glasses applying the methods described above.

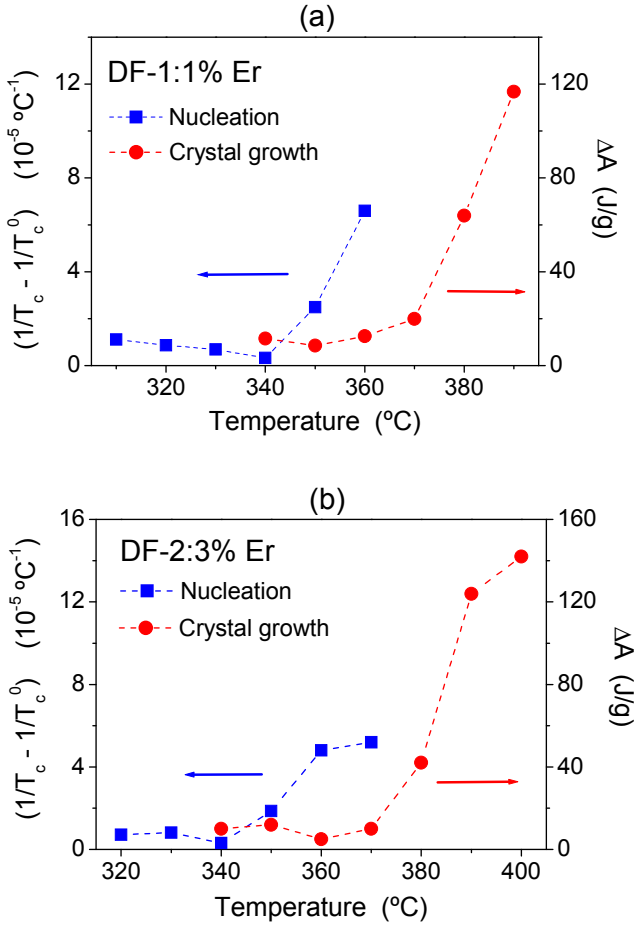

Figure 5.6: Nucleation and crystal growth rate-like curves for (a) DF-1 doped with 1 wt% ErF_3 and (b) DF-2 doped with 3 wt% ErF_3. Dashed lines are guides to the eye.

We note that the nucleation and crystal growth rate-like curves overlap significantly for both DF glasses. In the case of DF-1 (Fig. 5.6a), the nucleation rate is low for temperatures lower than 340 ºC. From this temperature it grows very fast reaching its maximum close to 360 ºC. The isothermal hold of 30 min at 370 ºC did not allow determining another point of the nucleation curve since there was no crystallisation peak in the DSC trace of this sample, due to the fact that the sample crystallised completely.

The crystal growth rate of DF-1 starts to grow at 360 ºC and reaches its maximum at 390 ºC, for which $A_T = 0$. Therefore, both nucleation and crystal growth take place at the same time for DF-1 in the 350-390 ºC range. Similarly, in the case of DF-2 (Fig. 5.6b), the nucleation rate is maximum around 370 ºC and the crystal growth rate at 400 ºC. Thus, nucleation and crystal growth should occur simultaneously between 360-400 ºC in DF-2. As indicated by Massera and coauthors, thermal treatments at temperatures in the range where nucleation and crystal growth curves overlap should be avoided if a controlled formation of nanocrystals is desired, since they lead to crystals with a broad size distribution [201].

Our study on the nucleation and crystal growth behaviour of DF glasses allow us to conclude that:

i) They present a moderate activation energy for crystallisation (~300 kJ/mol) which indicates that these glasses do not show large resistance to crystallisation;

ii) They show a marked tendency towards surface crystallisation;

iii) They present overlapping nucleation and crystal growth curves in the 350-400 ºC range.

These results are relevant for the design of thermal treatments to synthesize transparent rare earth doped glass-ceramics through controlled crystallisation of DF glasses.

5.2.2 Two-step thermal treatments

As described in the previous pages, the most common form to obtain glass-ceramic is by two-step thermal treatments in a proper temperature range and for an adequate time. Thermal treatments of DF glasses were performed on glass slices, few mm thick, in a muffle furnace in air. The temperature and duration of each annealing step were chosen according to the T_g and T_c temperatures of each glass and taking care to avoid the temperature range where the nucleation and growth curves overlap. Thus, as shown in the previous section, the maximum annealing temperature should be limited to 350-360 ºC. In particular, the temperature of the first step (T_1) was chosen to be close to T_g (up to 30 ºC higher) while the temperature of the second step (T_2) was ~30-60 ºC lower than T_c. The duration of the annealing steps was different for each of them: it was

larger for the first step (between 10 and 20 hours), since the nucleation rate is very low close to T_g, and shorter for the second one (2.5–3 hours) in order to grow nanocrystals. The heating rates were maintained fixes in all cases: 5 ºC/min for the RT-T_1 ramp and 2 ºC/min for the T_1-T_2 ramp (Fig. 5.1). Since it was no possible to control the cooling rate of the furnace, the samples were cooled down to room temperature by turning off the heater and keeping them inside the furnace in order to avoid thermal stress that could break them. The estimated free cooling rate was ~1-2 ºC/min.

As an example, table 5.1 lists the thermal treatments performed on DF-1 glasses doped with 1 wt% ErF_3 (T_g≈ 300 ºC; T_c≈ 390 ºC). We do not show here the thermal treatment performed on other DF glasses (DF-2 and DF-1 with different dopant content) since they did not lead to the production of transparent glass-ceramic samples.

Table 5.1: Two-step thermal treatments performed on DF-1: 1 wt% ErF_3 samples. The temperature and the duration of the first and second step are indicated as T_1; D_1 and T_2; D_2, respectively.

DF-1:1% Er annealed sample	**T_1; D_1** (ºC; hours)	**T_2; D_2** (ºC; hours)	**Comments**
T-1	300; 10	330; 3	No changes in transmittance spectrum
T-2	300; 14	330; 3	No changes in transmittance spectrum
T-3	300; 18	330; 3	Increase of Er^{3+} absorption bands
T-4	330; 10	360; 2.5	Total loss of transparency
T-5 (GC0)	300; 10	345; 2.5	Stark transitions in Er^{3+} absorption bands → Glass-ceramic
T-6 (GC1)	310; 10	340; 3	Stark transitions in Er^{3+} absorption bands → Glass-ceramic
T-7	310; 15	340; 2.5	Sample broken during annealing
T-8 (GC2)	305; 15	340; 2.5	Stark transitions in Er^{3+} absorption bands → Glass-ceramic
T-9 (GC3)	305; 20	340; 2.5	Stark transitions in Er^{3+} absorption bands → Glass-ceramic

The easiest and fastest way of checking whether the annealed samples show signs of crystallisation and maintain a high degree of transparency is through the measurement of their transmittance. This is because we expect that the absorption bands of rare earth ions change according to their environment. In particular, the inhomogeneous broadening of rare earth ions absorptions/emissions which is observed in glasses is strongly reduced when rare earths are in a crystalline environment. Moreover, in this last case, transitions from individual Stark sublevels may be well distinguished, as we

will show in the next section. In the case of DF-1 doped with 1 wt% ErF_3, the annealed T-5, T-6, T-8 and T-9 samples (Table 5.1) showed signs of crystallisation in their transmittance spectrum while they maintained a high transparency. Further structural characterization, presented in the next sections, actually proved that these samples were glass-ceramics.

These successful treatments have in common a similar T_1 temperature (300-310 ºC) and the second annealing step (T_2= 340-345 ºC and D_2= 2.5 hours), whereas the duration of the first annealing step (D_1) varied between 10-20 hours in these treatments. Therefore, we conclude that D_1 does not seem to be a critical variable to obtain transparent glass-ceramic samples. The optimal temperature interval for T_2 seems to be very narrow as well (T_2= 340-345 ºC) since in the case of T-1, T-2, and T-3 samples a slightly lower T_2 (330 ºC) precluded the growth of nanocrystals even if the first annealing step was similar to that of T-5, T-8, and T-9 samples, respectively (Table 5.1). At the same time, annealing at T_2= 360 ºC, in the range where the nucleation and crystal growth curves overlap (Fig. 5.6a), avoids the synthesis of transparent glass-ceramics due to formation of crystals larger than the wavelength of visible light (T-4 sample).
The fact that the nucleation and crystal growth curves of DF glasses overlap over a large temperature range strongly limits the synthesis of transparent glass-ceramic samples. From one side, the first annealing step has to be done at a temperature for which the nucleation rate is very low and thus, it is difficult to generate a high density of nuclei in the annealed glasses. Form the other side, the second annealing step is even more critical since a too long treatment or a slightly larger temperature may lead to nucleation and crystal growth at the same time with the consequent generation of large crystals and the loss of transparency.

5.3 Optical characterization

Once the glass samples had been annealed, they were polished until having planoparallel surfaces and ~1 mm thickness to perform transmittance and ellipsometry measurements.

As an example, Fig. 5.7 presents the transmittance spectra, at room temperature, of the precursor DF-1 glass (PG), *i.e.* not annealed, and of T-3, T-6, and T-9 annealed samples (Table 5.1). We do not show the transmittance spectra of T-5 and T-8 samples since they are very similar to those of T-6 and T-9 samples, respectively.

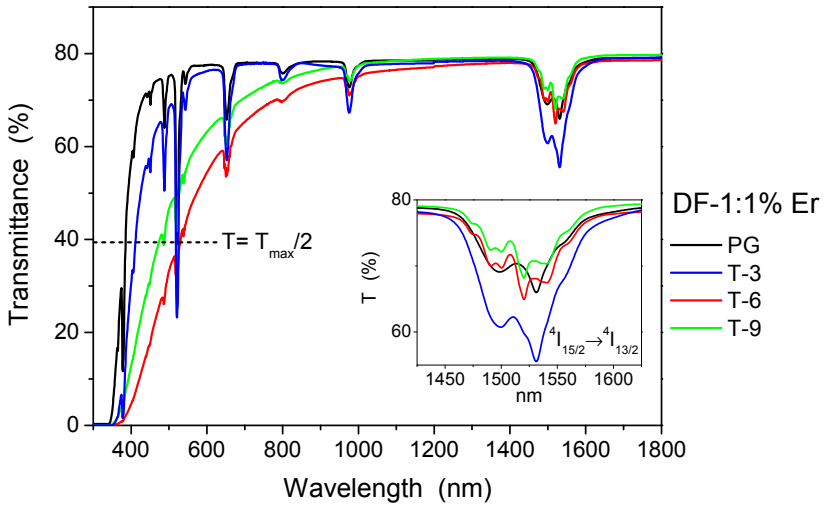

Figure 5.7: Transmittance spectra of precursor and annealed DF-1: 1wt% ErF_3 samples. The inset shows an enlarged view of the region between 1450-1600 nm where the absorption band due to the $^4I_{15/2}\rightarrow{}^4I_{13/2}$ Er^{3+} transition lies.

We observe in Fig. 5.7 that the spectra of annealed DF-1 samples present a red shifted UV absorption edge compared to the PG sample. In particular, the cut-off wavelength λ_c ($T(\lambda_c)= T_{max}/2$) shifts from 385 nm (PG) to 530 nm in the case of T-6 sample, which presents the most red-shifted absorption edge. However, all the annealed samples shown in Fig. 5.7 present a high transmittance in the infrared spectral region (~80 %). This suggests that the partial loss of transparency in the visible may be attributed to Rayleigh scattering due to the presence of nanometric particles, such as nanocrystals, embedded in the glass matrix, as it has been reported for other glass-ceramics [204]. We remind here that scattering losses are proportional to the size of particles (see chapter 2); therefore, T-6 should have the largest particles among the annealed samples included in Fig. 5.7.

Furthermore, we note important differences in Fig. 5.7 among the Er^{3+} absorption bands of the PG and the annealed samples. They can be attributed to the changes induced by thermal treatments in the environment (and ligand field) of Er^{3+} ions. In particular, T-6 and T-9 samples show a splitting of the Er^{3+} absorption bands, clearly observed in the $^4I_{15/2}\rightarrow{}^4I_{13/2}$ transition (inset Fig. 5.7). This behaviour stems from a reduction of

inhomogeneous broadening due to an "ordered" environment for rare earth ions. Thus, individual transitions between Stark sublevels may be clearly observed even at room temperature when rare earth ions are segregated in a crystalline phase in glass-ceramics [205].

We have also determined the linear refractive index of the annealed sample T-9 by ellipsometric data fitting (chapter 3). Figure 5.8a compares PG and T-9 samples whereas Fig. 5.8b presents the dispersion of the real part of their refractive index in the 400-1800 nm range.

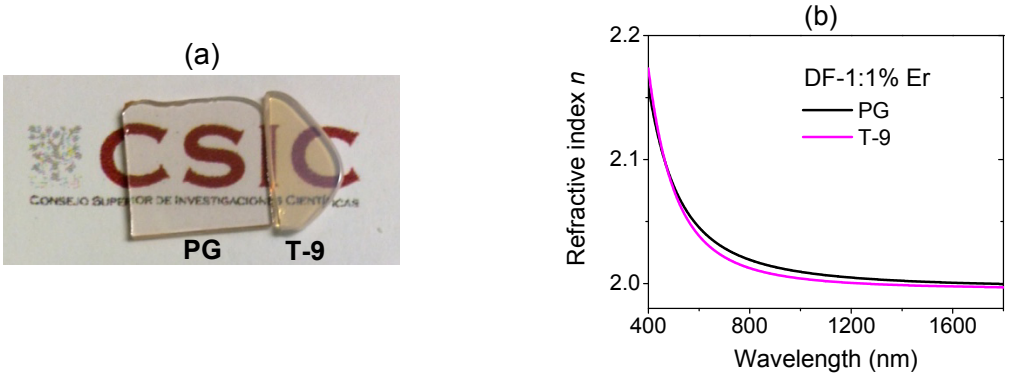

Figure 5.8: (a) Image of precursor and annealed (T-9) DF-1: 1wt% ErF_3 samples. (b) Refractive index dispersion of PG and T-9 samples.

As shown in Fig. 5.8a, a visual inspection of the annealed sample T-9 shows that it maintains a good transparency in the visible. The most noticeable difference between PG and T-9 samples is their colour: the first one has a pale pink colour while the second present an orange colour, probably due to the scattering of light observed in the blue visible spectral region (Fig. 5.7). The dispersion of the refractive is very similar for both PG and T-9 (Fig. 5.8b). The refractive index shows a strong decay in the visible region and then a slow decrease in the infrared, maintaining almost a constant value for wavelengths longer than 1000 nm. The value of *n* at 1550 nm is 2.00 for the PG and 1.99 for T-9.

5.4 Structural characterization

Transmittance spectra of T-6 and T-9 strongly indicate that Er^{3+} ions are in a crystalline environment in these samples. Thus, we have performed a detailed structural characterization of T-6 to determine the crystalline phases formed and the size of crystals dispersed in the glass matrix. With this aim, we initially performed X-ray diffraction measurements. Then, we compared the structure of the annealed sample to that of the precursor glass sample by Raman spectroscopy. Finally, we analysed the microstructure of T-6 by transmission electron microscopy.

5.4.1 X-ray diffraction analysis

X-ray diffraction (XRD) analysis is widely employed to characterize the crystalline phases and to estimate the size of crystals present in glass-ceramics. Moreover, XRD analysis allows evaluating the crystalline to amorphous ratio of glass-ceramics. XRD measurements were performed at room temperature on the annealed T-4 (completely opaque) and T-6 (transparent) samples by using an X'Pert diffractometer (PANalytical) employing the Bragg-Brentano geometry (2θ= 10º-70º; incident beam: CuKα, λ= 1.54 Å).

Figure 5.9 compares the XRD patterns obtained for the precursor glass and the annealed T-4 and T-6 samples.

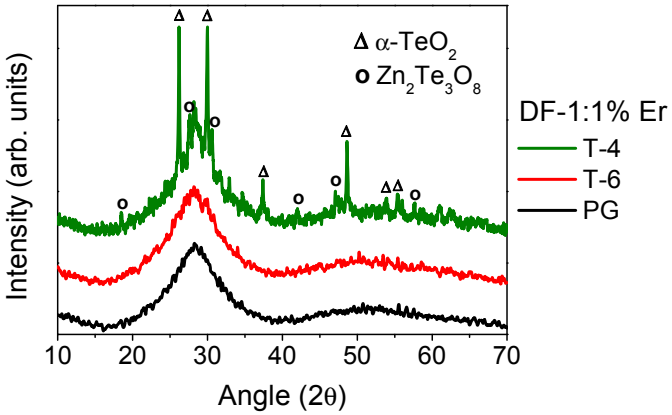

Figure 5.9: XRD patterns of PG, T-6 and T-4 samples. The peaks in the pattern of the T-4 sample have been assigned to α-TeO_2 and $Zn_2Te_3O_8$ crystalline phases.

XRD patterns of PG and T-6 samples are similar: they present a broad halo, typical of amorphous solids, which peaks at 2θ≈ 29º. Moreover, the pattern of T-6 does not show any narrow peak which could indicate the presence of crystalline phases. On the contrary, the XRD pattern of T-4 shows several diffraction peaks superimposed on the same broad halo observed for PG and T-6 samples.
We have employed the POWD-12++ software (1997) together with the ICSD (Inorganic Crystal Structure Database [206]) to assign the observed diffraction peaks. Taking into account the sample composition (TeO_2–ZnO–ZnF_2: ErF_3) we have identified the alpha-tellurite (α-TeO_2) [207] and zinc tellurium oxide ($Zn_2Te_3O_8$) [208] crystalline phases.

Since the diffraction peaks attributed to the α-TeO_2 phase present larger intensity than those attributed to the $Zn_2Te_3O_8$ phase (Fig. 5.9), we conclude that the first phase develops in major proportion than the second one in the case of T-4. This result agrees with the study of Nazabal [151] which indicates that the α-TeO_2 phase prevails over the $Zn_2Te_3O_8$ phase in similar fluorotellurite glasses annealed at temperatures lower than 400 ºC. However, even if T-4 is opaque in the visible, the fraction of the amorphous phase is large since its diffraction pattern clearly shows the broad halo characteristic of amorphous materials (Fig. 5.9).

Finally, even if no diffraction peaks are observed in the pattern of T-6 (Fig. 5.9) we cannot rule out the presence of a small crystalline fraction since the minimum crystalline/amorphous ratio that can be detected with the diffractometer used is ≈ 1-2 %. Thus, the results provided by XRD analysis suggest that the crystalline fraction of T-6 should be lower than the sensitivity threshold of the diffractometer.

5.4.2 Raman and micro-Raman spectroscopy analysis

We have employed Raman spectroscopy (λ_{exc}= 785 nm) to study eventual structural changes in the annealed samples. Figure 5.10 shows the normalized reduced Raman spectra corresponding to the precursor glass (PG) and annealed T-4 and T-6 samples. In addition, we include the Raman spectra of TeO_2 and ErF_3 polycrystalline reagents used to produce PG.

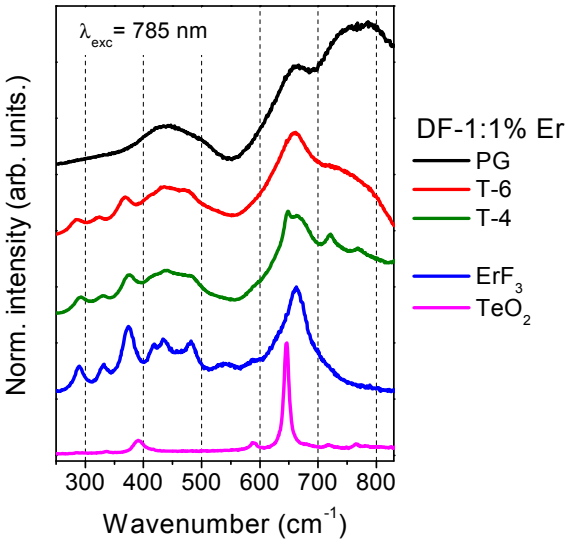

Figure 5.10: Normalized reduced Raman spectra (λ_{exc}= 785 nm) of PG and annealed T-4 (opaque) and T-6 (transparent) samples. Raman spectra of TeO_2 and ErF_3 reagents are included for comparison. Spectra have been shifted vertically to ease their comparison.

Both annealed samples show different Raman spectra than the PG. They do not show the three distinctive broad bands of zinc-tellurite glasses (see chapter 4) as PG but they show sharper bands. Some of them peak at similar positions than ErF_3 Raman bands. In particular, in the spectra of T-4 and T-6 samples we observe bands at ~286, ~323, ~367, and ~660 cm^{-1} as well as two much less intense bands at ~433, and ~473 cm^{-1}. In addition, the spectrum of T-4 shows small bands peaking at ~648, ~720, and ~768 cm^{-1} that have been assigned to α-TeO_2 and γ-TeO_2 phases, respectively [178]. The fact that the bands attributed to the α-TeO_2 and γ-TeO_2 phases are observed only in the Raman spectrum of T-4 agrees with the results of the XRD analysis.

The fact that the Raman spectra of T-4 and T-6 samples show bands at the same wavenumbers than the ErF_3 polycristalline reagent suggests the presence of ErF_3 crystals in these samples. The excitation wavelength at 785 nm corresponds to a photon energy of ~12739 cm^{-1} that is very close to the energy gap between the $^4I_{9/2}$–$^4I_{15/2}$ Er^{3+} multiplets in ErF_3 crystals (= 12334 ± 358 cm^{-1}) [171]. Thus, the Raman signal from ErF_3 crystals is enhanced due to excitation of quasi-resonant electronic Raman transitions, similarly to what has been reported by Becker and coauthors in the case of $ErPO_4$ crystals [209].

To prove this hypothesis, we have compared the Raman spectra of PG, T-4 and T-6 samples obtained by exciting them at 1064 nm (Fig. 5.11).

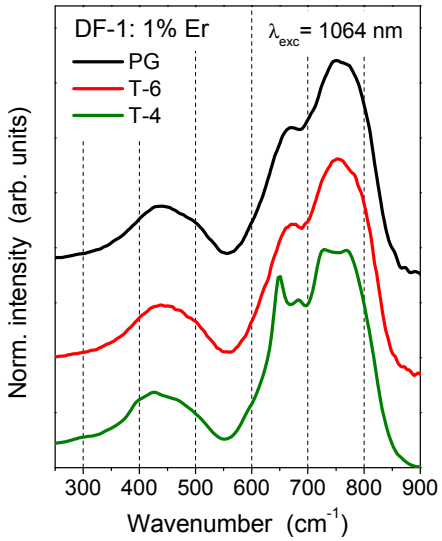

Figure 5.11: Normalized reduced Raman spectra (λ_{exc}= 1064 nm) of PG, T-4, and T-6 samples. Spectra have been shifted vertically to ease their comparison.

In this case, only the spectrum of sample T-4 shows some sharp bands (~648, ~683, ~730, and ~768 cm^{-1}) that are superimposed on the three broad bands observed in the spectrum of PG and T-6 samples. The sharp bands are found at similar positions than those of TeO_2 (Fig. 5.10) which once more supports the presence of tellurite crystalline phases in T-4. However, contrary to Fig. 5.10 no sharp bands are observed in the spectrum of T-6 due to the fact that quasi-resonant electronic Raman transitions in ErF_3 crystals cannot be excited at 1064 nm.

Finally, we have carried out a micro-Raman analysis of the surface of T-6 to search for evidences of phase separation in its microstructure, which could affect its homogeneity at a micrometric scale. For that purpose, we have acquired a Raman spectrum (λ_{exc}= 442 nm) every 2 µm on a surface of 20x20 μm^2. As an example, Figure 5.12a compares a Raman spectrum acquired on the surface of T-6 with the Raman spectrum of PG. We have determined the peak position and the full-width at half maximum (FWHM) of the most intense Raman band (at ~742 cm^{-1} in Fig. 5.12a) over the analysed surface of T-6. The resulting 2D Raman mapping is presented in Fig. 5.12b.

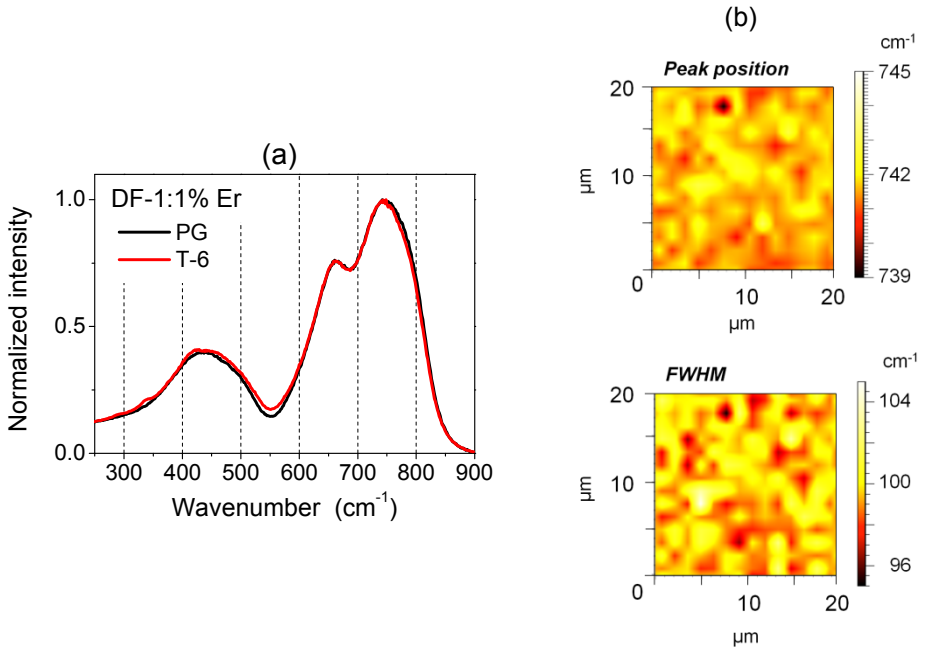

Figure 5.12: (a) Normalized reduced Raman spectra (λ_{exc}= 442 nm) of PG and T-6 samples. (b) 2D Raman mapping of the surface of T-6: peak position (top) and FWHM (bottom) of the most intense Raman band.

As expected from the Raman spectra obtained by exciting PG and T-6 at 1064 nm, Raman spectra of these samples excited at 442 nm are very similar too (Fig. 5.12a). In addition, the 2D Raman mapping (Fig. 5.12b) of T-6 shows no signs of phase separation or structural modifications in the analysed surface since the variation of the peak position (± 3 cm^{-1}) and FWHM (± 5 cm^{-1}) are very small compared to the reference (PG) values: 742 cm^{-1} and 100 cm^{-1}, respectively.

5.4.3 Transmission electron microscopy analysis

Despite the optical and structural characterization of sample T-6 clearly suggest the presence of nanocrystals in an amorphous matrix, the decisive proof requires the direct observation of nanocrystals by transmission electron microscopy (TEM). Thus, we have acquired TEM images of both the surface and the volume of T-6. As we described in chapter 3, an adequate specimen was prepared by the replica method in the first case; while, in the second case, focused ion-beam (FIB) milling was used to thin the bulk sample. Figure 5.13a shows a plane-view TEM image of a replica of T-6.

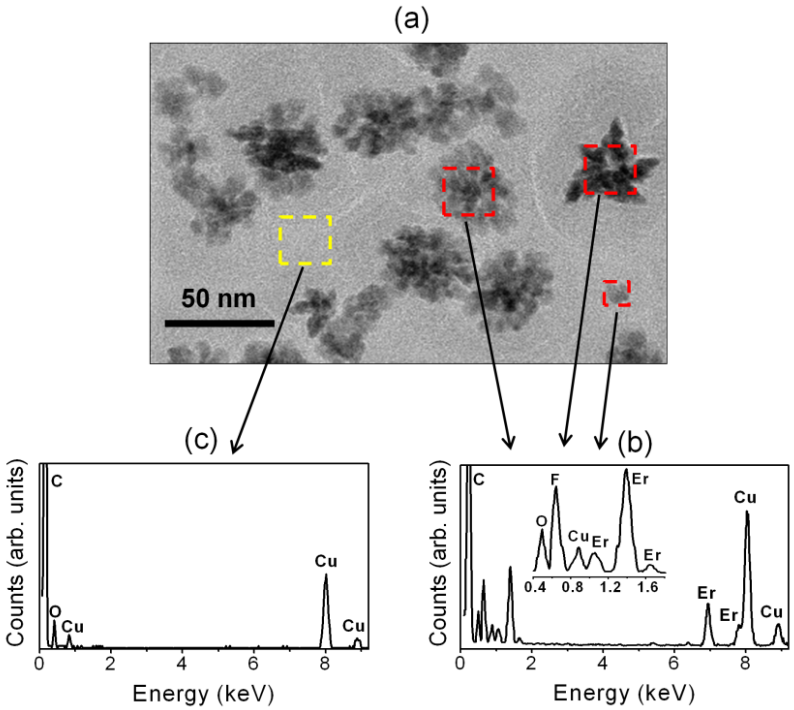

Figure 5.13: (a) Plane-view TEM image of a replica of T-6. (b) EDX spectrum of the nanoparticles observed in (a). The inset shows the 0.4-1.7 keV region in more detail. (c) EDX spectrum of the region without nanoparticles. Peak assignment is included in (b) and (c).

The replica of T-6 presents several agglomerated nanoparticles (dark grey areas in Fig. 5.13a) with a dendritic structure and an average size of 50 ± 10 nm. We have performed energy dispersive X-ray (EDX) analysis to investigate the composition of the observed nanoparticles. The results are shown in Fig. 5.13b and they indicate that the nanoparticles are composed by erbium and fluorine. Carbon, copper and oxygen signals are also present in the EDX spectrum of the nanoparticles but they come from the carbon film and copper grid, respectively, as it is confirmed by the EDX spectrum of the light grey area (Fig. 5.13c). We remember here that the replica method only allows collecting the crystalline fraction on the sample surface (chapter 3). No signals from Te and Zn are detected in the nanoparticles, even if these elements are the principal constituents of T-6. This fact agrees with the structural analysis of T-6 described in the previous pages which indicates that the sample does not contain any Te and Zn crystalline phases. In order to confirm that the nanoparticles observed in Fig. 5.13a are nanocrystals, Figure 5.14a shows the enlarged TEM image of a nanoparticle.

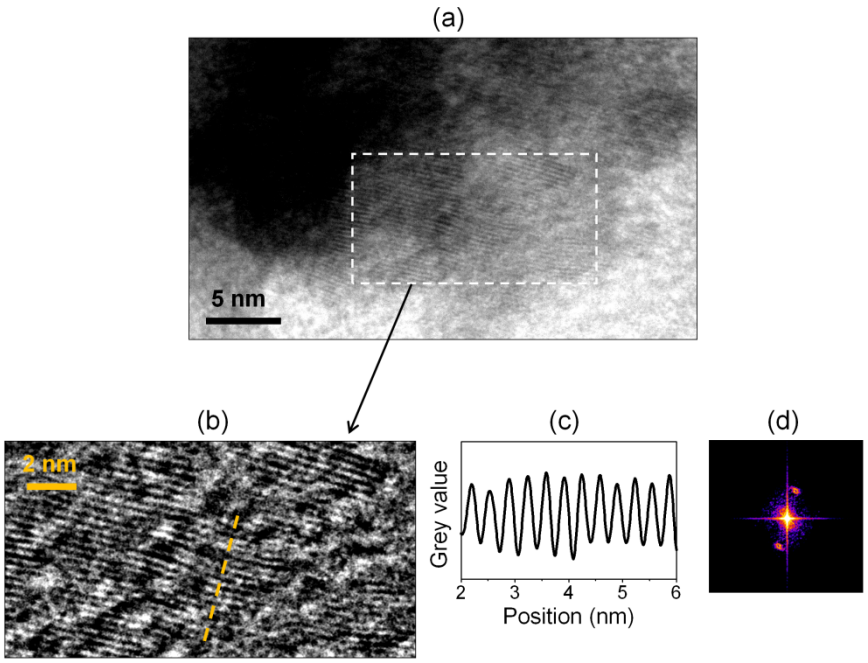

Figure 5.14: (a) Plane-view TEM image of a nanoparticle observed in the replica of T-6. (b) Enlarged view of the region selected in (a). (c) Oscillations corresponding to grey value along the dashed line in (b). (d) FFT of the TEM image in (b).

We observe lattice fringes in Fig. 5.14a, which confirm that the nanoparticles are actually nanocrystals [142]. A further zoom-in on the region where the lattice fringes are clearer (Fig. 5.14b) allow us to determine the lattice spacings which are a fingerprint of crystalline compounds. We have employed two complementary methods to determine the lattice spacings. The first one follows the approach described by Prathibha et al. [210]. It consists in representing the grey value along a line perpendicular to the lattice fringes by means of ImageJ [211] software. The period of the oscillations represents the lattice spacing. The second method makes use of the fast Fourier transform (FFT) algorithm to collect information about the reciprocal lattice geometry analogously to electron diffraction patterns [142]. In the reciprocal space, each lattice spacing produces a brilliant spot.

The first method (Fig. 5.14c) leads to a lattice spacing of 3.4 ± 0.2 Å for the lattice fringes intercepted by the dashed line in Fig 5.14b; while the FFT of Fig. 5.14b shows two brilliant spots at a distance of 3.3 ± 0.2 Å (Fig. 5.14d). These values match well with the (111) and (020) planes of ErF_3 crystals (orthorhombic unit cell), which have a lattice spacing of 3.19 and 3.42 Å, respectively [212].

Due to the marked tendency of DF glasses to surface crystallisation, we have performed additional TEM measurements of the core of sample T-6 to be sure of the presence of ErF_3 nanocrystals in the volume too. Figure 5.15a presents the TEM image of the core of T-6.

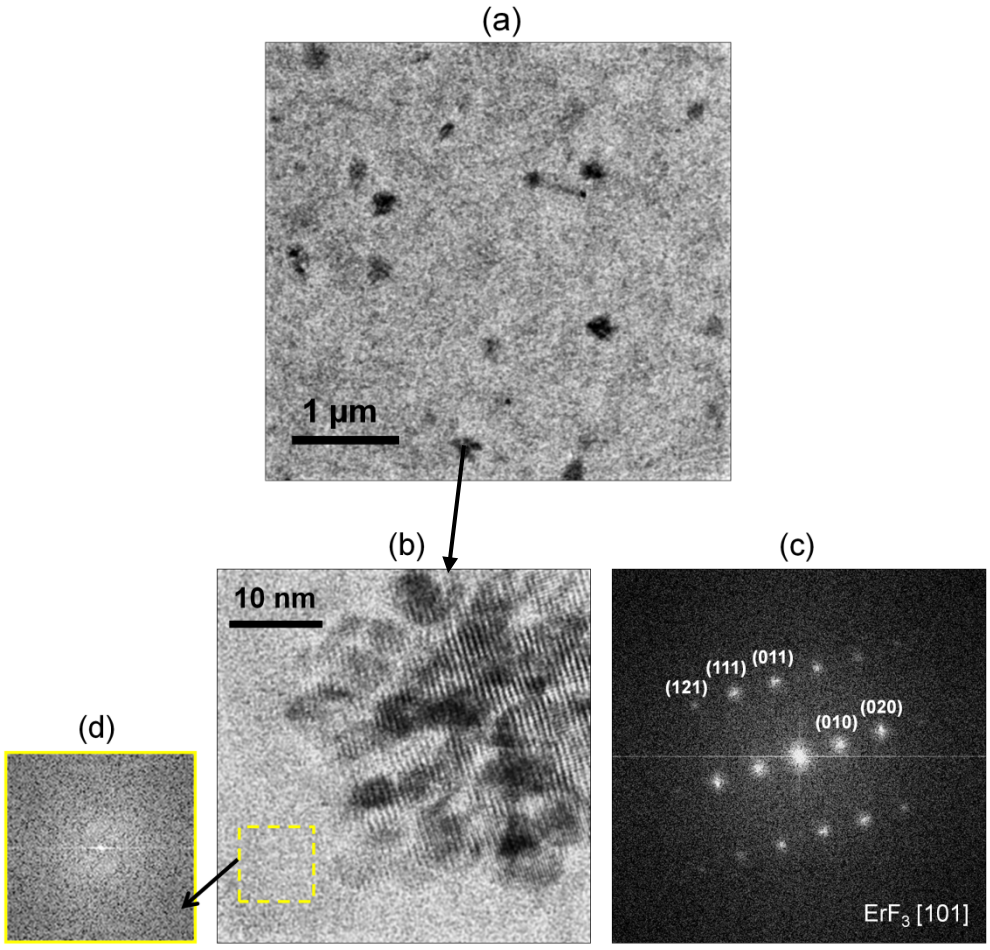

Figure 5.15: (a) Plane-view TEM image of the core of T-6. (b) High resolution TEM image of a nanocrystal corresponding to dark grey regions in (a). (c) FFT of the TEM image in (b) indexed according to ErF_3 crystalline planes. (d) FFT of the region inside the dashed square in (b).

We observe agglomerated nanocrystals in the core of T-6 that are well dispersed (Fig. 5.15a). Due to the low resolution, we can distinguish well only the biggest ones having a size of ~200 nm. High resolution TEM image of a nanocrystal shows clearly its lattice fringes (Fig. 5.15b). The FFT of this image shows different brilliant spots in the reciprocal space which can be indexed as: (121), (111), (011), (010), and (020) planes of ErF_3 crystals oriented in the [101] direction (Fig. 5.15c). On the contrary, FFT of an amorphous region (Fig. 5.15d) shows no brilliant spots, as we expected. Table 5.2 summarizes the experimental lattice spacings from Fig. 5.15c and compares them with the tabulated ones [212] for ErF_3 crystals.

Table 5.2: Experimental lattice spacings observed in Fig. 5.15c (d_{exp}); tabulated lattice spacing for ErF_3 and corresponding crystalline planes [212].

d_{exp} (Å)	d_{ErF3} (Å) [212]	Plane (hkl) [212]
2.49	2.482	(121)
3.19	3.190	(111)
3.38	3.420	(020)
3.68	3.689	(011)
6.85	-	(010)

Therefore, TEM analysis of sample T-6 confirms the presence of ErF_3 nanocrystals in all the volume of the sample and thus, the success in the synthesis of transparent Er^{3+} doped TeO_2–ZnO–ZnF_2 glass-ceramics.

5.5 Photoluminescence response

The transparent glass-ceramic (GC) samples obtained by two-step thermal treatments of the DF-1: 1 wt% ErF_3 precursor glass (PG) are composed by an amorphous glass matrix, with the same structure as PG, but with embedded ErF_3 nanocrystals. Thus, the Er^{3+} environment in glass-ceramic samples changes with respect to PG. We have determined the Judd-Ofelt parameters Ω_t (t= 2, 4, 6) of a glass-ceramic sample (T-8 or GC2 in Table 5.1) to estimate the variations of Er^{3+} environment upon annealing. They have been calculated from the absorption spectra of GC2, shown in Fig. 5.16, following the procedure described in chapter 2 [213].

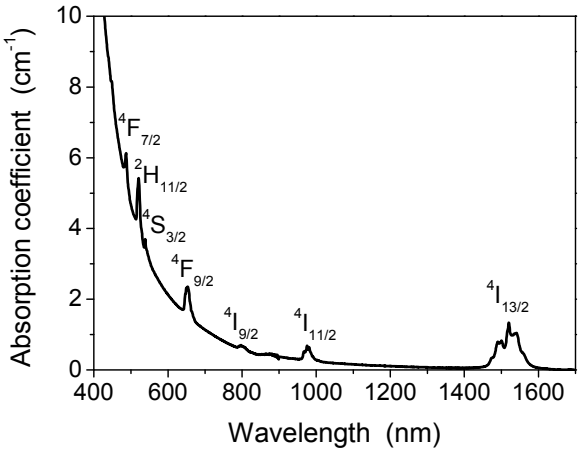

Figure 5.16: Absorption spectra of GC2. Er^{3+} absorption bands are labelled with the upper level of the transition, originated in the ground level.

Table 5.3 lists the Ω_t (t= 2, 4, 6) values and the spectroscopy quality factor (Ω_4/Ω_6) for the GC2 sample and compares them to those of PG, discussed in chapter 4.

Table 5.3: Judd-Ofelt parameters Ω_t (t= 2, 4, 6) and spectroscopy quality factor (Ω_4/Ω_6) of Er^{3+} in GC2 sample. The values calculated for PG are included for comparison.

Sample	Ω_2 (10^{-20} cm^2)	Ω_4 (10^{-20} cm^2)	Ω_6 (10^{-20} cm^2)	Ω_4/Ω_6
GC2	1.28	1.04	1.00	1.04
PG	4.71	1.57	1.13	1.39

The reduction of the Ω_2 parameter indicates that the Er^{3+} environment is less covalent, or analogously more ionic, in the case of GC2 than for PG [170]. Moreover, the Ω_2 value of GC2 is similar to the value reported for an Er doped fluoride glass of the PbF_2–GaF_3–ZnF_3 system ($\Omega_2 = 1.54 \cdot 10^{-20}$ cm^2) [214]. Thus, the Er^{3+} environment has become ionic in the GC2 sample, while it was mainly covalent in the PG. This result agrees with the structural characterisation of GC samples which showed the formation of ErF_3 nanocrystals. The variations of Er^{3+} environment in GC samples affect both the crystal field and the maximum phonon energy of the host (chapter 2). In particular, the maximum phonon energy is ~300 cm^{-1} for the fluoride crystalline phase [42] while is 850 cm^{-1} for the amorphous fluorotellurite glass matrix (chapter 4). Therefore, we expect that the efficiency of Er^{3+} emissions increases dramatically in glass-ceramic samples due to the reduction of the probability of multiphonon relaxation of excited levels.

Finally, the spectroscopy quality factor of GC2 (Table 5.3) is slightly smaller than that of PG, yet is larger enough to make it a promising candidate for stimulated emission [171].

In the next sections we study the photoluminescence response of GC1 and GC2 (see Table 5.1) and compare it to the response of PG that was presented in chapter 4.

5.5.1 Near infrared emissions

We have characterized the room temperature near infrared emissions of GC1 and GC2 samples by exciting them at 801 nm, in resonance with the $^4I_{9/2}$ level.

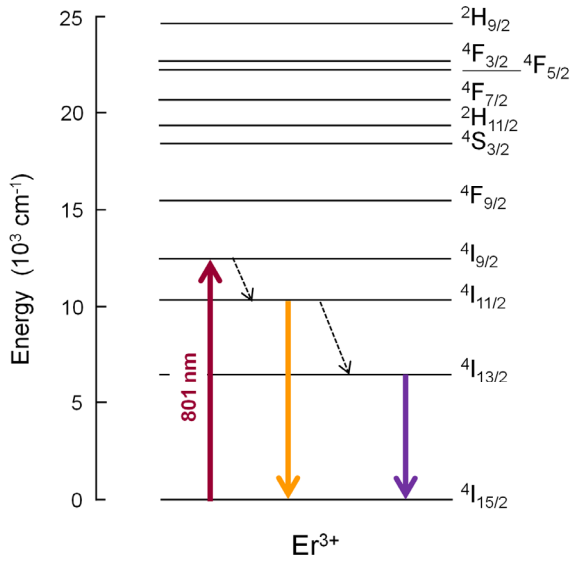

Figure 5.17: Energy level diagram of Er^{3+} ion excited at 801 nm, in resonance with the $^4I_{9/2}$ level. Dashed down arrows indicate nonradiative transitions. The $^4I_{11/2}\rightarrow{}^4I_{15/2}$ and $^4I_{13/2}\rightarrow{}^4I_{15/2}$ near infrared emissions are indicated as down arrows.

As represented in the Er^{3+} transition diagram (Fig. 5.17), the lower energy levels, $^4I_{11/2}$ and $^4I_{13/2}$, are populated by multiphonon relaxation. Then, radiative transitions from these levels to the ground level lead to the infrared emission at ~980 nm ($^4I_{11/2}\rightarrow{}^4I_{15/2}$) and to the main Er^{3+} emission at ~1530 nm ($^4I_{13/2}\rightarrow{}^4I_{15/2}$).

Figure 5.18a compares the near infrared emission spectra of glass-ceramic samples with that of PG while Fig. 5.18b compares the fluorescence decay of the $^4I_{13/2}$ level.

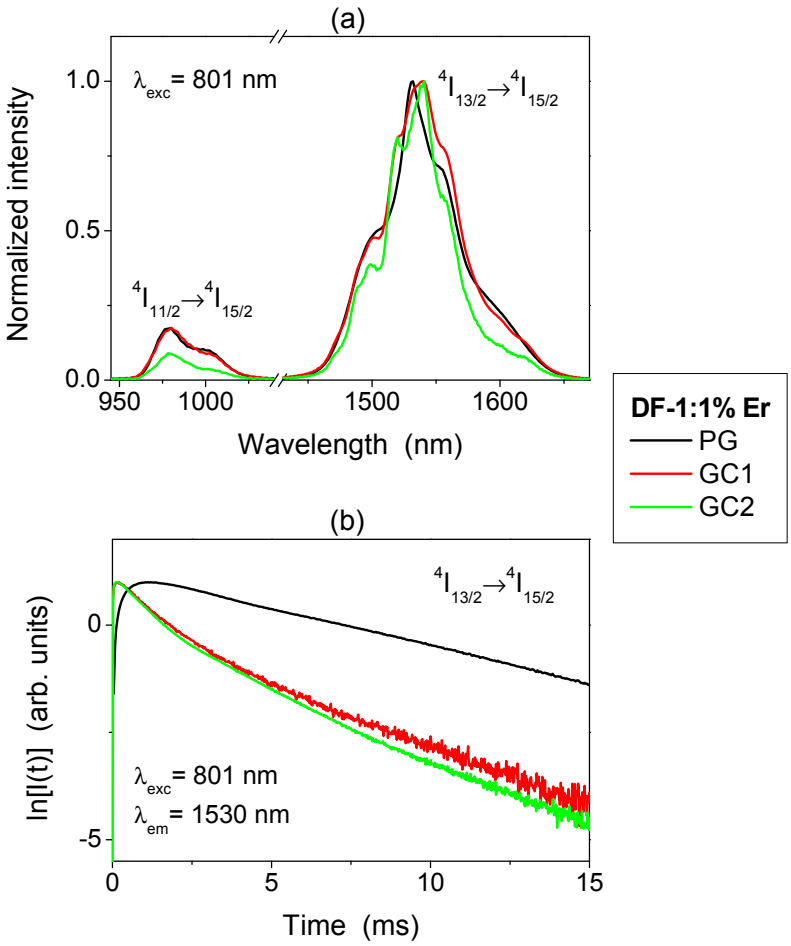

Figure 5.18: (a) Room temperature normalized near infrared emission spectra of GC1 and GC2 samples excited at 801 nm. PG spectrum is included for comparison. (b) Semilogarithmic plot of the fluorescence decay of the $^4I_{13/2}$ level (λ_{em}= 1530 nm) for PG, GC1 and GC2 samples.

The shape of the $^4I_{13/2}\rightarrow{}^4I_{15/2}$ emission band changes for GC samples with respect to that of the PG, while the $^4I_{11/2}\rightarrow{}^4I_{15/2}$ emission band presents a similar shape for all the samples. The $^4I_{13/2}\rightarrow{}^4I_{15/2}$ band is composed by four broad sub-bands in the case of PG that split up in one more sub-band in the case of GC samples. In particular, the most intense sub-band peaks at ~1530 nm in the spectrum of PG while it peaks at ~1540 nm in the spectra of GC samples. In addition, the $^4I_{13/2}\rightarrow{}^4I_{15/2}$ emission presents a reduced full width at half maximum (FWHM) in the case of GC2 (51 nm) while it does not change in the case of GC1 (62 nm) with respect to the PG (63 nm). We described in chapter 2 that the shape of absorption and emission bands of rare earth ions is mainly affected by their environment (ligand field). The characteristics of the $^4I_{13/2}\rightarrow{}^4I_{15/2}$ emission band in the case of GC samples suggest that Er^{3+} ions are in a crystalline

environment, since this leads to a reduction of inhomogeneous broadening and to well-resolved sub-bands due to the high degree of symmetry of Er^{3+} sites [30].

The experimental fluorescence decay curves of the $^4I_{13/2}$ level (Fig. 5.18b) show a reduced lifetime of the $^4I_{13/2} \rightarrow {}^4I_{15/2}$ emission for GC1 and GC2 with respect to PG. In addition, the decay curves of GC samples cannot be fitted by a single exponential function as in the case of PG. They can be fitted instead by two single exponential functions, with short (τ_s) and long (τ_l) time constants, respectively. Table 5.4 lists the values of τ_s and τ_l for GC samples and the lifetime (τ) of the $^4I_{13/2}$ level for PG.

Table 5.4: Lifetime of the $^4I_{13/2}$ level in PG, GC1, and GC2 samples excited at 801 nm (room temperature).

Sample	**$^4I_{13/2}$ lifetime** (ms)
PG	τ= 5.9
GC1	τ_s= 1.1; τ_l= 3.7
GC2	τ_s= 1.1; τ_l= 3.1

The fact that the lifetime of the $^4I_{13/2}$ level is fitted by two single exponential functions in the case of GC samples suggests that Er^{3+} ions are partitioned in two different environments, which are most likely the crystalline (ErF_3 nanocrystals) and the amorphous (glass matrix) ones, as it has been described by Goutaland and coauthors for aluminosilcate oxyfluoride glass-ceramics [215]. Moreover, the smaller lifetime values of both GC samples (Table 5.4), with respect to the PG, may be due to a reduced distance between adjacent Er^{3+} ions in the nanocrystals which would favour dipole-dipole energy transfer processes that would depopulate $^4I_{11/2}$ and $^4I_{13/2}$ levels, as described for other glass-ceramics [216].

Finally, we have calculated the emission cross-section (σ_e) of the $^4I_{13/2} \rightarrow {}^4I_{15/2}$ transition in GC1 and GC2 through the McCumber's relation (Eq. 2.8) [87]. They are compared in Fig. 5.19 with that of PG.

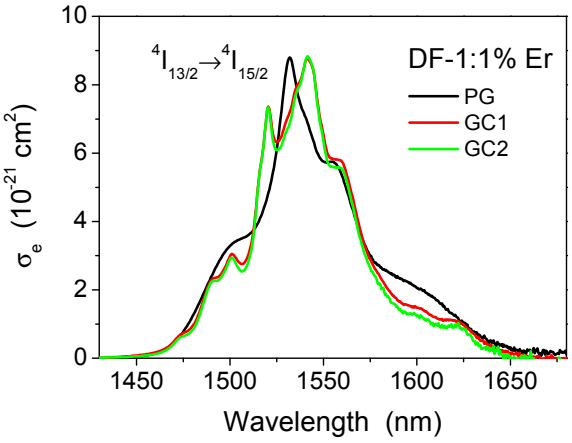

Figure 5.19: Room temperature emission cross-section of the $^4I_{13/2}\rightarrow{}^4I_{15/2}$ transition determined for PG, GC1, and GC2 samples using the McCumber's relation.

We note that the emission cross-section of the two GC samples is similar. It differs from that of PG in shape and width, since it presents several sub-bands and it becomes slightly broader. However, the maximum σ_e value, which indicates the probability of $^4I_{13/2}\rightarrow{}^4I_{15/2}$ emission events, is similar for both GC and PG samples (~$8.8\cdot10^{-21}$ cm^2).

5.5.2 Visible *upconverted* emissions

In chapter 4 we studied the near infrared to visible upconversion of Er-doped fluorotellurite glasses. Fluorotellurite glasses with ErF_3 content lower than 2 wt% presented a strong green emission but a very weak red emission. In this section we compare the visible upconverted emissions of GC samples with that of the PG. The three samples have been excited at room temperature at 801 nm, in resonance with the $^4I_{9/2}$ level (Fig. 5.17). Figure 5.20a shows the experimental emission spectra, normalized to their maximum intensity (at 545 nm).

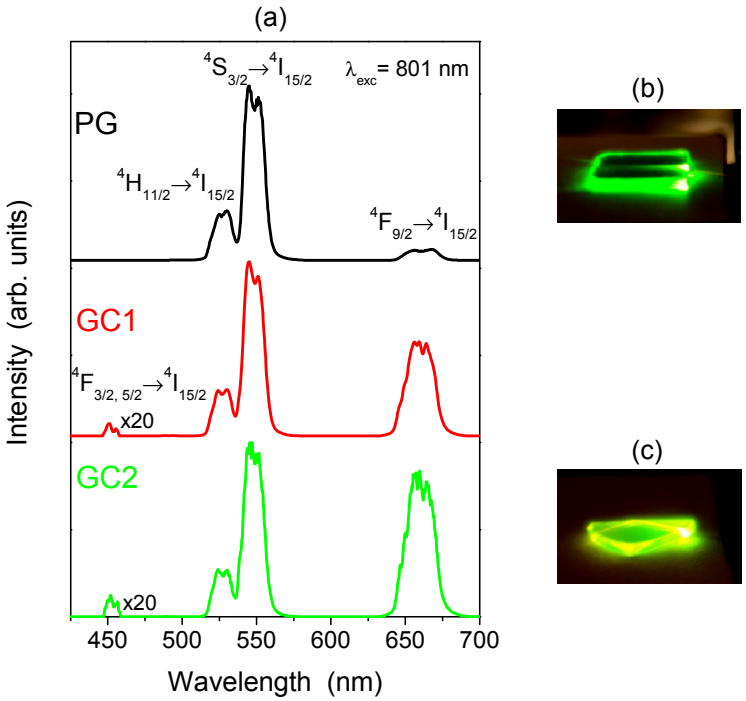

Figure 5.20: (a) Room temperature normalized visible upconversion emission spectra of GC1, GC2 and PG samples excited at 801 nm. (b) Image of the visible emission in (b) PG and (c) GC2 samples.

Both GC and PG samples present three emission bands, two of them in the green and the third one in the red spectral regions. The green emission bands are attributed to the $(^2H_{11/2},\ ^4S_{3/2})\rightarrow{}^4I_{15/2}$ transitions while the red emission is attributed to the $^4F_{9/2}\rightarrow{}^4I_{15/2}$ transition. In addition, the emission spectra of GC samples show another very weak emission at ~450 nm, that is attributed to the $(^4F_{3/2},\ ^4F_{5/2})\rightarrow{}^4I_{15/2}$ transitions (Fig. 5.17). The detection of this emission as well as the observation of well resolved sub-bands in the spectra of GC samples are due to the low phonon energy of Er^{3+} environment and to its high symmetry, respectively, which are a consequence of the formation of ErF_3 nanocrystals in the glass-ceramics.

However, the most remarkable difference between the spectra of PG and GC samples is the relative intensity of the red emission with respect to the green one. In particular, the red to green intensity ratio (I_{RED}/I_{GREEN}) is ~0.06 for the PG ant it increases up to ~0.54 and ~0.84 in the case of GC1 and GC2, respectively. The variation of I_{RED}/I_{GREEN} can be observed also by naked eye: PG sample shows a bright apple green emission (Fig. 5.20b), while the GC2 sample shows a green-yellowish emission (Fig. 5.20c), due to the contribution of the strong red emission.

We have finally determined the dependence of the intensity of upconversion emissions (at 550 and 660 nm) on the laser pump power (λ_{exc}= 801 nm) in the case of GC1 (Fig. 5.21). The dependence is quadratic, which indicates that excited state absorption (ESA) or energy transfer (ET) processes populate the $^4S_{3/2}$ and $^4F_{9/2}$ levels [96], as in the case of DF glasses (chapter 4).

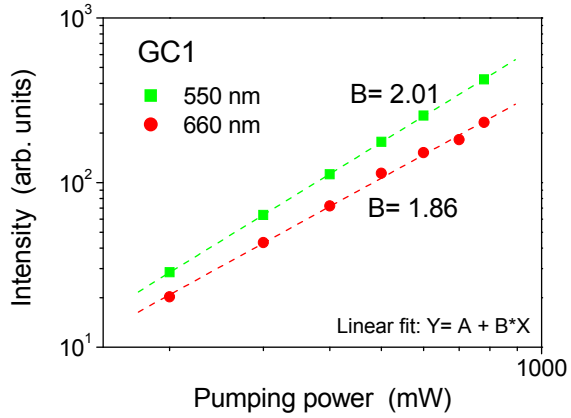

Figure 5.21: Room temperature upconversion emission intensities as a function of pumping power at 801 nm for GC1. Dashed lines are the linear fitting of experimental measurements, which lead to a slope of 2.01 at 550 nm and of 1.86 at 660 nm.

As we did for the PG in chapter 4, we have studied the lifetime of the visible emissions under near infrared (λ_{exc}= 801 nm) and visible (λ_{exc}= 488 nm) excitation to determine whether ESA or ET processes are responsible for the upconverted emissions [96]. To illustrate this, we present in Fig. 5.22 the fluorescence decay curves of $^4S_{3/2}$ and $^4F_{9/2}$ levels for GC2.

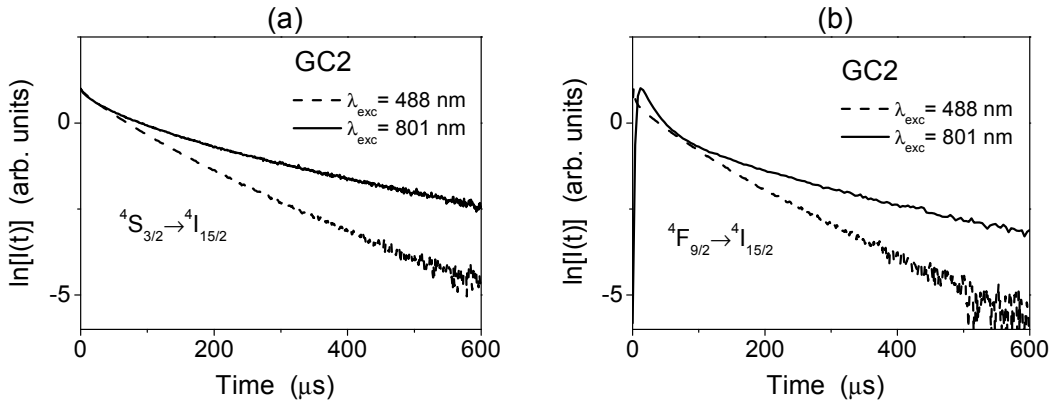

Figure 5.22: Semilogarithmic plot of the room temperature fluorescence decay of (a) $^4S_{3/2}$ and (b) $^4F_{9/2}$ levels under direct excitation (λ_{exc}= 488 nm) and near infrared excitation (λ_{exc}= 801 nm) for GC2.

The decay curves can be fitted by two single exponential functions, with a short (τ_s) and long (τ_l) time constants. The values of τ_s and τ_l for the $^4S_{3/2}$ and $^4F_{9/2}$ levels are listed in Table 5.5 for GC1 and GC2. We also include the average lifetime (Eq. 3.13) of the $^4I_{11/2}$ level in Table 5.5.

Table 5.5: Lifetime of the $^4S_{3/2}$ and $^4F_{9/2}$ levels under visible excitation (λ_{exc}= 488 nm) and infrared excitation (λ_{exc}= 801 nm) in GC1 and GC2. The lifetime of the $^4I_{11/2}$ level is included for comparison.

Sample	$^4S_{3/2}$ lifetime (μs)		$^4F_{9/2}$ lifetime (μs)		$^4I_{11/2}$ τ_m (μs)
	λ_{exc}= 488 nm	λ_{exc}= 801 nm	λ_{exc}= 488 nm	λ_{exc}= 801 nm	λ_{exc}= 801 nm
GC1	τ_s= 45; τ_l= 105	τ_s= 37; τ_l= 154	τ_s= 49; τ_l= 114	τ_s= 22; τ_l= 206	275
GC2	τ_s= 36; τ_l= 107	τ_s= 41; τ_l= 129	τ_s= 21; τ_l= 89	τ_s= 23; τ_l= 183	220

We note in Fig. 5.22a that the photoluminescence decay curve of the $^4S_{3/2}$ level does not show an initial rise time under infrared excitation. This fact indicates that ESA processes from the $^4I_{13/2}$ and $^4I_{11/2}$ levels followed by multiphonon relaxation of the upper $^4F_{3/2}$, $^4F_{7/2}$, and $^2H_{11/2}$ levels are mainly populating the $^4S_{3/2}$ level (Fig. 5.23). However, at the same time, the fact that the lifetime of the $^4S_{3/2}$ level is longer when pumping at 801 nm with respect to direct pumping (Table 5.5) is an indication of the presence of additional ET processes such as the $^4I_{11/2} \rightarrow {}^4I_{15/2}$; $^4I_{11/2} \rightarrow {}^4F_{7/2}$ transitions, which would contribute to populate the $^4S_{3/2}$ level (Fig. 5.23).

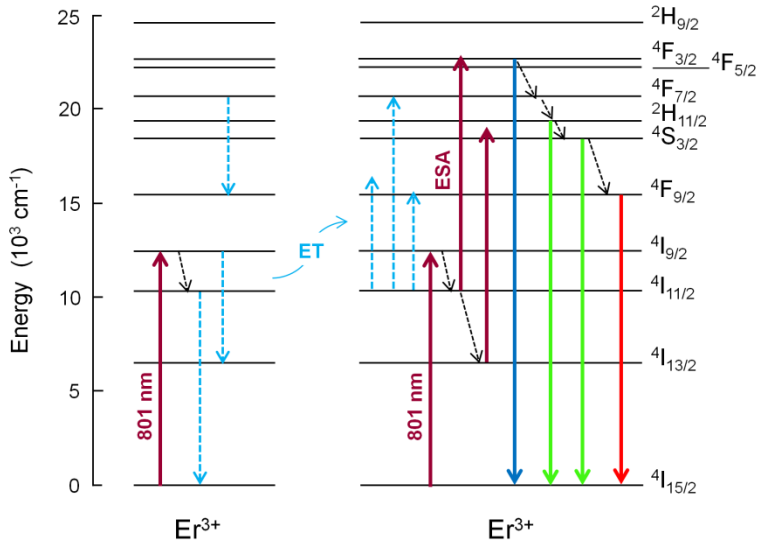

Figure 5.23: Energy level diagram of Er^{3+} in GC samples. Magenta up arrows indicate photon absorption from the ground state or from an excited state (ESA). Visible emissions are indicated as blue, green and red down arrows. Black dashed down arrows indicate nonradiative transitions. Energy transfer (ET) processes, when exciting at 801 nm in resonance with level $^4I_{9/2}$, are represented as cyan dashed arrows.

On the other hand, the decay curve of the $^4F_{9/2}$ level under infrared excitation (Fig. 5.22b) shows a rise time just after the end of the excitation pulse, which is characteristic of ET processes [96]. As discussed in the previous section, it is likely that Er^{3+} ions segregated in the fluoride nanocrystals have a shorter distance between them with respect to the ions dispersed in the amorphous glass matrix (PG). Thus, the large increase of the red upconverted emission in GC samples may be attributed to the increased probability of ET processes between nearby Er^{3+} ions in the nanocrystals. We note that the τ_l value of the $^4F_{9/2}$ level under infrared excitation is close to the lifetime of the $^4I_{11/2}$ level for both GC samples (Table 5.5). This suggests that the $^4I_{11/2}$ level is the intermediate level for ET processes in GC1 and GC2. In this way, two ET processes that may populate the $^4F_{9/2}$ level in GC samples are: $^4I_{9/2}\rightarrow{}^4I_{13/2}$; $^4I_{11/2}\rightarrow{}^4F_{9/2}$ and $^4F_{7/2}\rightarrow{}^4F_{9/2}$; $^4I_{11/2}\rightarrow{}^4F_{9/2}$ as illustrated in Fig. 5.23.

Finally, it is worth mentioning that the small phonon energy of the fluoride crystalline phase may also lead to an increase of the population of the $^4F_{9/2}$ level by reducing its multiphonon deexcitation.

5.6 Summary and conclusions

In this chapter we have studied the nucleation and crystal growth behaviour of TeO_2–ZnO–ZnF_2 glasses to design thermal treatments that allow the production of **transparent rare earth doped glass-ceramics** through controlled crystallisation of precursor glass samples. We have succeeded only for a specific glass composition: 68 TeO_2– 22 ZnO– 10 ZnF_2 (mol%): 1 wt% ErF_3. The difficulty encountered for synthesizing transparent TeO_2–ZnO–ZnF_2 glass-ceramics has been attributed to the small temperature interval for the optimal crystal growth temperature which lead to the formation of nanometric-size crystals in the glass matrix. Moreover, we have found that this temperature interval depends on both the glass composition and the dopant concentration of TeO_2–ZnO–ZnF_2 glasses.

We have performed an exhaustive structural characterization of the produced transparent glass-ceramic samples. While XRD analysis did not show any evidence of the presence of crystalline phases, Raman spectroscopy showed that transparent glass-ceramic samples have a structure similar to that of the precursor glass, even at a micron scale (micro-Raman analysis). The observation of quasi-resonant electronic Raman transitions when λ_{exc}= 785 nm suggested the presence of ErF_3 crystals. TEM allowed us to confirm the presence of **dendritic ErF_3 nanocrystals** in all the volume of glass-ceramics. The nanocrystals have characteristic sizes of ~50 nm and sometimes they aggregate together in clusters of up to 200 nm. The crystalline to amorphous ratio in glass-ceramic samples is low (< 1%) due to their low ErF_3 content (1 wt%). Thus, even if glass-ceramics are mainly amorphous as indicated by XRD and Raman, large part of Er^{3+} ions in these samples are segregated into the fluoride nanocrystals.

The optical characterization of glass-ceramic samples through transmittance measurements has shown that they are highly transparent in the visible and near infrared spectral regions even if they present a red shifted UV absorption edge. This shift may be attributed to Rayleigh scattering from the nanocrystals dispersed in the glass matrix. Moreover, the Er^{3+} absorption bands observed in the spectra of glass-ceramics show well resolved sub-bands that confirm a crystalline environment for Er^{3+} ions. The absorption and the refractive index of glass-ceramics samples are similar to those of the precursor glass. In particular, the linear refractive index is close to 2 in the infrared region.

The fact that Er^{3+} ions in glass-ceramic samples are segregated in a fluoride crystalline environment affects their photoluminescence response at room temperature since they "see" an environment different from the one of the amorphous glass matrix, which is characterized by a **low phonon energy** (~300 cm^{-1}).

The $^4I_{13/2} \rightarrow {}^4I_{15/2}$ (~1.5 μm) near-infrared emission spectra of glass-ceramics showed well-resolved sub-bands and a slightly reduced width, compared to the precursor glass, which indicate that the environment of Er^{3+} ions is ordered. However, the fluorescence decay of the $^4I_{13/2}$ level in glass-ceramics was fitted by two single exponential functions with a shorter lifetime than the precursor glass. We have attributed this behaviour to the presence of Er^{3+} in amorphous and crystalline environments at the same time. In the last case, the distances between neighbour Er^{3+} ions are reduced, which would favour energy transfer processes with a consequent depopulation of $^4I_{11/2}$ and $^4I_{13/2}$ levels. However, the reduced distances between Er^{3+} ions in the nanocrystals led to a strong red upconverted emission ($^4F_{9/2} \rightarrow {}^4I_{15/2}$) in glass-ceramic samples due to the larger probability of energy transfer processes between nearby Er^{3+} ions. In particular, the red to green ($^4S_{3/2} \rightarrow {}^4I_{15/2}$) intensity ratio was up to 14 times larger for a glass-ceramic sample than in the precursor glass sample, becoming the red and green emissions of comparable intensity. Finally, the reduced phonon energy of the fluoride nanocrystals may also contribute to increase the population of the $^4F_{9/2}$ level by reducing its multiphonon relaxation.

6

Er^{3+} doped TeO_2–ZnO–ZnF_2 thin film glasses

6.1 Introduction

We have shown in the previous chapters that rare earth doped TeO_2–ZnO–ZnF_2 glasses and glass-ceramics are excellent hosts for rare earth ions. They show intense near infrared and upconverted visible emissions that can be employed in optical amplifiers or phosphors, respectively. However, in order to develop integrated optical devices such as erbium doped waveguide amplifiers (EDWA) operating in the optical C-band (1.5 μm), the configuration usually adopted is that of Er doped film glasses deposited on Si substrates [16, 217]. Among the different chemical and physical techniques to produce rare earth doped film glasses such as sol-gel, flame hydrolysis, chemical vapour deposition, or pulsed laser deposition (PLD) [27, 125, 218]; we choose this last one since it allows the synthesis of multicomponent film glasses maintaining their complex stoichiometry and at the same time with a good optical quality [51, 53, 219, 220].

In this chapter we investigate the synthesis of Er^{3+} doped TeO_2–ZnO–ZnF_2 films by PLD. We choose the glass DF-1 (68 TeO_2– 22 ZnO– 10 ZnF_2 mol%) doped with 1 wt% ErF_3 since, as we have shown in chapter 4, it is a promising candidate to develop broadband optical amplifiers in the optical C band. As grown film show a weak $^4I_{13/2} \rightarrow {}^4I_{15/2}$ emission at 1.5 μm, thus we determine the thermal treatments able to enhance the near infrared emission. Finally, we relate the enhanced near infrared emission to the modifications induced on the structure and composition of Er doped TeO_2–ZnO–ZnF_2 films.

6.2 Optical characterization of as-grown films

Er doped TeO_2–ZnO–ZnF_2 films were grown by PLD at room temperature by using the optimum laser fluence (2 J/cm^2) and oxygen pressure (10 Pa), as described in chapter 3. As-grown films showed a high transparency by naked eye. We have characterized their optical properties by measuring the transmittance of as-grown films deposited on fused silica substrates and the linear refractive index of films deposited on Si substrates. Figure 6.1 shows the transmittance of a representative fluorotellurite film and compares it with that of the bulk glass used as target for PLD.

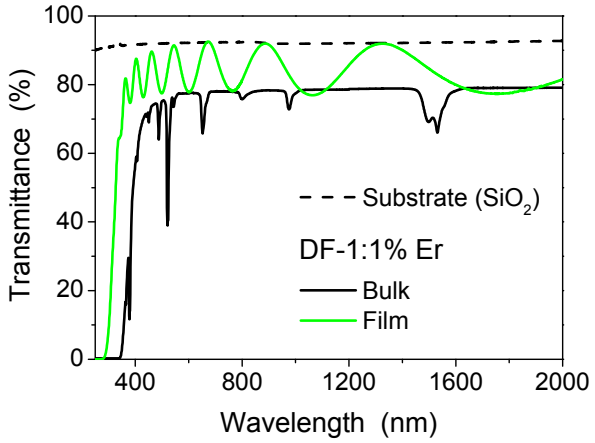

Figure 6.1: Transmittance spectrum of a representative DF-1: 1 wt% ErF_3 film glass. The transmittance spectra of the fused silica substrate and the bulk glass used as PLD target are included for comparison.

The transmittance spectrum of the film shows a high average transmittance (> 85 % for λ> 360 nm) and interference fringes, whose number and intensity are related to the thickness of the film and to the refractive index contrast (Δn) between the film and the substrate, respectively. Contrary to the spectrum of the bulk glass, the characteristic Er^{3+} absorption bands are not observed in the case of the film glass due to its reduced thickness that generates interference fringes which hide these bands. As commented in chapter 3, it is not possible to compare the cut-off wavelength (λ_c) of the film and target glasses due to their very different thickness (~10^{-7} vs ~10^{-3} m). However, while the target has a $\lambda_c \approx$ 385 nm the film shows a $\lambda_c \approx$ 320 nm.

We have determined as well the linear refractive index (n) dispersion of fluorotellurite films by spectroscopic ellipsometry (chapter 3). We do not report the absorption coefficient (k) of the films since it was below our experimental resolution limit ($k < 10^{-4}$) for λ> 500 nm.

Figure 6.2 presents the dispersion of for a representative as-grown film in the 400-1600 nm spectral range. The refractive index of the bulk glass is included for comparison.

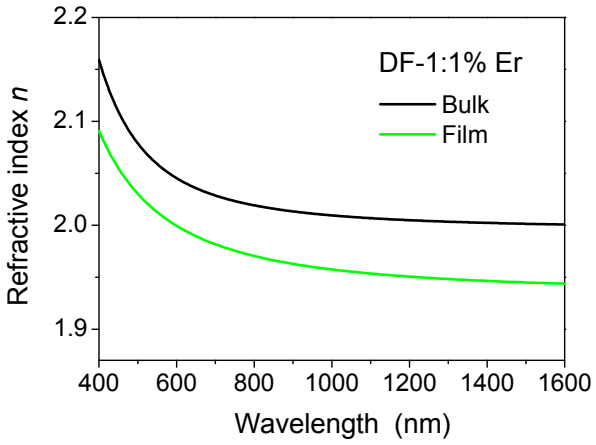

Figure 6.2: Linear refractive index of a representative DF-1: 1 wt% ErF_3 film. The refractive index of the bulk glass is included for comparison.

The refractive index of the film (n_F) is smaller than the refractive index of the bulk (n_B) in all the spectral range considered. In particular, $n_F = 1.94$ while $n_B = 2.00$ at 1500 nm, thus the film refractive index is reduced by 3 % with respect to the bulk. This reduction may stem from compositional changes or/and a reduced density of the films due to the fabrication technique, as it has been previously observed in both transparent tellurite and germanate film glasses produced by PLD [53, 221]. However, its value is large enough to guarantee a high confinement for the light propagating in the film due to large index contrast with respect to the substrate ($n_{SiO2} \approx 1.44$ at 1500 nm).

6.3 Near infrared emission

In the previous section we have shown that as-grown fluorotellurite films possess very good optical properties. However, the practical application of these films requires combining them with a strong photoluminescence emission at 1.5 μm. Thus, we have measured the $^4I_{13/2} \rightarrow {}^4I_{15/2}$ emission spectrum and lifetime by exciting the samples at 980 nm in resonance with the $^4I_{11/2}$ level. As we have described in chapter 4 for bulk glasses, multiphonon relaxation of the $^4I_{11/2}$ level lead to the population of the $^4I_{13/2}$ level, which decays radiatively to the ground level emitting at ~1.5 μm.

Unfortunately, as-grown films showed a weak near infrared emission with a signal to noise ratio too low to determine the lifetime of the $^4I_{13/2}$ level. Thus, we have performed annealing treatments of the as-grown films in air with the aim of enhancing the near infrared emission. We have performed step annealing at increasing temperatures (270 ºC; 300 ºC; 310 ºC; 315 ºC; and 320 ºC) for 2-3 hours at each temperature. After each annealing step we have measured the near infrared emission spectrum to study the dependence of the photoluminescence intensity (I_{PL}) at 1.53 µm with the annealing temperature (T_{ANN}). Figure 6.3 shows the results obtained.

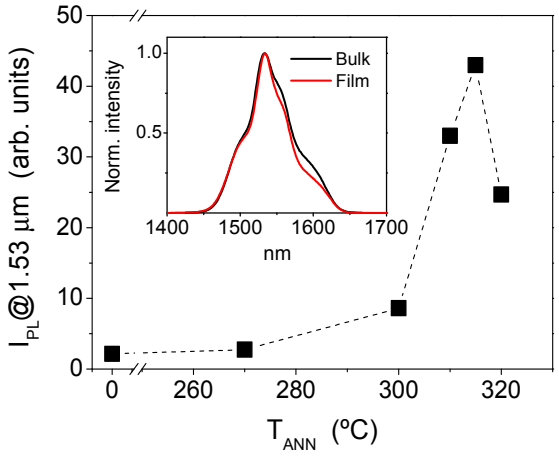

Figure 6.3: Room temperature intensity (I_{PL} at 1.53 µm) of the $^4I_{13/2} \rightarrow {}^4I_{15/2}$ near infrared emission as a function of the annealing temperature (T_{ANN}) for fluorotellurite films excited at 980 nm. The inset compares the normalized emission spectra of film and bulk samples.

We observe in Fig. 6.3 that I_{PL} shows a moderate increase for $T_{ANN} \leq 300$ ºC while it increases significantly for T_{ANN} = 310-315 ºC. In particular, I_{PL} is 20 times larger with respect to the as-grown film after annealing at 315 ºC. Instead, a further annealing at 320 ºC led to a decrease of I_{PL} and to a partial detachment of the film from the substrate. In addition, films annealed at temperatures higher than 320 ºC showed a loss of transparency probably due to their partial crystallisation. We have also investigated the effect of the duration of the annealing treatment on I_{PL} for $T_{ANN} < 315$ ºC and we have found that I_{PL} did not change noticeably when increasing the annealing time from 1 hour up to 6 hours at a given temperature. Finally, we have observed that films annealed in consecutive steps from a lower T_{ANN} to a higher one showed a better adherence to the substrate and a larger I_{PL} compared to films annealed only in a single step at the highest temperature.

Contrary to I_{PL}, the emission spectrum of fluorotellurite films (annealed or not) did not change with T_{ANN}, which suggests that annealing treatments did not alter the Er^{3+} environment in the film glasses. However, the emission spectrum of a film has a slightly reduced width than that of the bulk (inset Fig. 6.3). The full width at half maximum is 57 nm for the film while is 65 nm for the bulk sample. This behaviour is most likely related to structural or compositional variations between the bulk and film glasses, as we discuss in the next sections.

Finally, we have studied the dependence of the lifetime of the $^4I_{13/2}$ level (τ) with T_{ANN} by annealing a film in three consecutive steps: *i*) at 300 ºC for 3 hours (sample **AF-1**); *ii*) at 310 ºC for 3 hours (sample **AF-2**); and *iii*) at 315 ºC for 2 hours (sample **AF-3**); and measuring the decay of the $^4I_{13/2}$ level after each annealing step. Figure 6.4a compares the experimental decay of the $^4I_{13/2}$ level for AF-1 and AF-3 films with that of the bulk glass. The decay curves can be fitted by a single exponential function whose time constant is τ. The decay of the $^4I_{13/2}$ level for AF-2, not shown in Fig. 6.4, is fitted by a single exponential function too. Figure 6.4b shows the dependence of the measured τ on T_{ANN}.

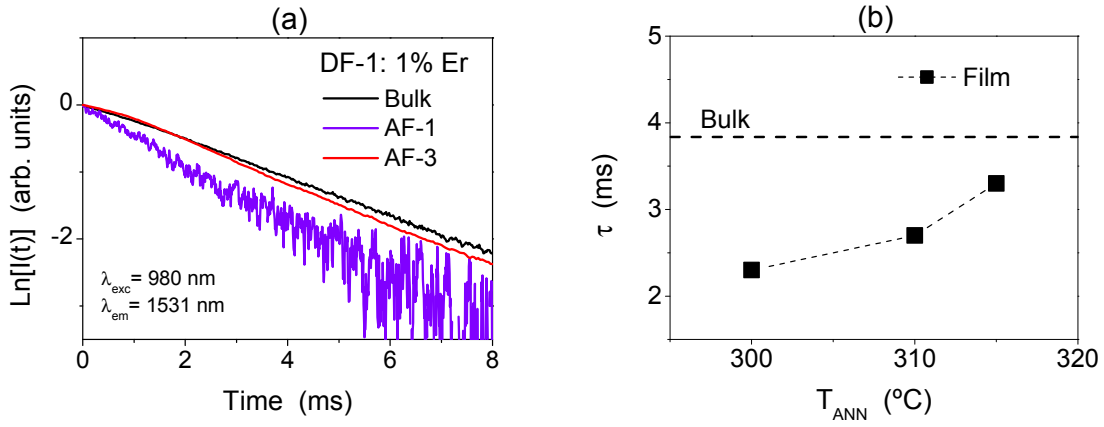

Figure 6.4: (a) Semilogarithmic plot of the room temperature fluorescence decays from the $^4I_{13/2}$ level (λ_{em}= 1531 nm) for bulk, AF-1 and AF-3 samples. (b) Relation between the lifetime of the $^4I_{13/2}$ level (τ) and T_{ANN} for fluorotellurite films. Dashed lines between points are guides to the eye. The horizontal dashed line in (b) indicates the τ of the bulk glass.

τ increases from 2.3 ms (AF-1) up to 3.3 ms (AF-3) by increasing the annealing temperature from 300 to 315 ºC (Fig. 6.4b). However, the maximum τ (3.3 ms) measured for the annealed fluorotellurite film AF-3 is still lower than the τ of the bulk glass, which is equal to 3.8 ms. As we have described in chapter 2, the most frequent causes for photoluminescence quenching of rare earth ions in glasses there are: a high

concentration or clustering of rare earth ions, a high OH^- concentration, structural defects in the glass matrix. We analyze in the next section the composition and structure of as-grown and annealed fluorotellurite films to reveal their effect on the photoluminescence response.

6.4 Compositional and structural analysis

We have determined the composition of as-grown (AGF) and annealed (AF-3) fluorotellurite film glasses through Rutherford backscattering spectrometry (RBS) and proton-induced gamma ray emission (PIGE) techniques that were described in chapter 3. Figure 6.5 presents the experimental and simulated RBS spectra of the AGF sample.

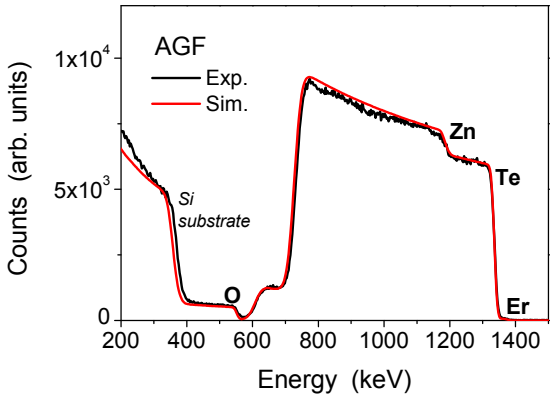

Figure 6.5: Experimental and simulated RBS spectra of a representative as-grown film (AGF).

We clearly observe in the figure the edges associated to Te, Zn, O and Si (substrate) while the one associated to Er is barely seen due to its small intensity. The atomic content of these elements was determined from the fitting of the experimental RBS spectrum through the SIMRA software [134]. Instead, F content was determined trough PIGE analysis. The estimated experimental error is ± 10 % for the Te, Zn, O, and F concentration while is ± 100 % for the Er concentration. The experimental composition determined for bulk, as-grown film (AGF) and annealed film (AF-3) glasses is presented in Table 6.1.

Table 6.1: Experimental atomic composition ([X] in at.%) of bulk, as-grown film (AGF) and annealed film (AF-3) glasses.

Sample	[Te]	[Zn]	[Er]	[O]	[F]
Bulk	23.7 ± 2.4	11.6 ± 1.2	0.3 ± 0.1	58.4 ± 5.8	6.0 ± 1.2
AGF	22.4 ± 2.2	8.2 ± 0.8	0.1 ± 0.1	66.0 ± 6.6	3.3 ± 0.3
AF-3	24.4 ± 2.4	8.6 ± 0.9	0.1 ± 0.1	64.2 ± 6.4	2.7 ± 0.3

Table 6.1 shows that both AGF and AF-3 are enriched in [Te] with respect to [Zn] compared to the bulk glass, while the comparison between the films and the bulk fluorotellurite glasses is complicated due to its small content and the large error in its determination in the case of [Er]. However, the results obtained suggest that Er content in the films is comparable to that of the bulk so Er clustering seems unlikely in AGF and AF-3 samples. Finally, the most significant compositional change between the film and bulk glasses regards their anionic content. While [O] increases, [F] decreases in the film glasses, especially in the AF-3 sample. The fact that AGF and AF-3 have a similar composition indicates that annealing the films at $T_{ANN} \leq 315$ ºC does not lead to any significant compositional variation within the experimental error of our measurements.

The composition variations observed in AGF can be attributed to the deposition technique. Thin films that are deposited by PLD in the presence of a background gas usually are enriched in the heaviest elements [222]. This fact can be attributed to the collisions between the ablated species and the background gas molecules which lead to a reduction of the kinetic energy and to a modification of the angular distribution of the ablated species during their expansion [222]. Scattering of the ablated species by the background gas becomes important at pressures above 10 Pa and it is more intense for species with masses similar to those of the background gas molecules, *i.e.* the lightest species [223]. In our case this should lead to a relative enrichment of [Te] (at. weight= 127.6) with respect to [Zn] (at. weight= 65.4), as experimentally observed (Table 6.1). Enrichment in [O] has been previously observed in either oxide or oxyfluoride tellurite film glasses produced by PLD in an O_2 atmosphere [224, 225, 226]. It may have different origins such as the incorporation of background oxygen to films during the deposition process or through the oxidation of a fraction of the ablated species by reaction with background O_2 molecules. With respect to the reduction of [F] observed in fluorotellurite films this may be attributed to its light weight [223] and its high

electronegativity which make it a highly reactive element. In this regard we remember that reaction of F with H_2O led to the dehydration of DF glasses during their melt (chapter 4).

The excess of oxygen may lead to structural modifications in the case of film glasses. Thus, we have analysed the structure of AGF and AF-3 samples through Raman spectroscopy (λ_{exc}= 442 nm). Figure 6.6 compares the Raman spectra of fluorotellurite film glasses with that of the bulk glass.

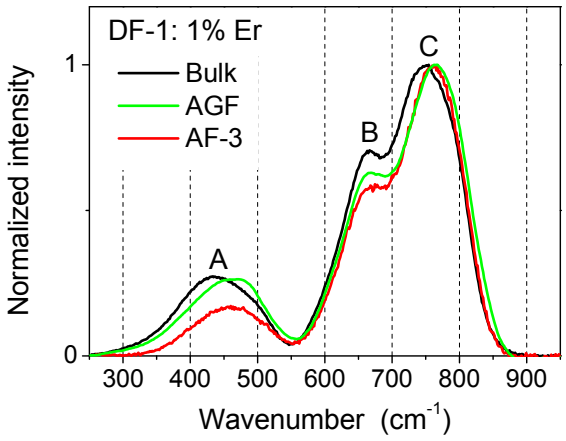

Figure 6.6: Normalized and reduced Raman spectra of bulk, as-grown film (AGF) and annealed film (AF-3) glasses.

Raman spectra of bulk, AGF and AF-3 samples present the same cut-off frequency of optical phonon modes (at ~850 cm^{-1}) and show the three distinctive bands of tellurite glasses at 400-500 cm^{-1}, 600-700 cm^{-1} and 700-800 cm^{-1}, which are indicated in Fig. 6.6 as A, B, and C, respectively. As it was described in chapter 4, these bands are associated to: symmetric and bending vibrations of Te-O-Te bonds at corning sharing sites of [TeO_4], [TeO_{3+1}], and [TeO_3] units (band A); symmetric stretching of Te-O bonds in [TeO_4] units (band B); vibrations of Te-O and Te-O_{NBO} bonds in [TeO_{3+1}]/[TeO_3] units (band C). We have determined the intensity, peak position and area of A, B, and C bands by Gaussian deconvolution of the Raman spectra of bulk, AGF and AF-3 samples to ease their comparison. Table 6.2 summarizes these values.

Table 6.2: Peak position (Peak), relative intensity (I_p) and area of the bands obtained by Gaussian deconvolution of Raman spectra of bulk, AGF and AF-3 fluorotellurite glasses.

Band	Bulk			AGF			AF-3		
	Peak (cm^{-1})	I_p	Area	Peak (cm^{-1})	I_p	Area	Peak (cm^{-1})	I_p	Area
A	438	0.27	40	455	0.24	30	457	0.17	23
B	658	0.7	62	662	0.63	58	663	0.59	58
C	760	1	106	769	1	108	766	1	97

As we observe in Fig. 6.6, the Raman spectra of bulk and film glasses show small differences. The peak position of A, B, and C bands shifts toward higher wavenumbers in the case of film glasses with respect to the bulk glass. In addition, the relative intensity (and area) of bands A and B decreases with respect to the band C. The intensity of the band A has been related to the glass network connectivity and to the F/O ratio [150]. Thus, its reduction may be related to the composition of film glasses (Table 6.1) and the increase of non-bridging oxygens (NBO) in these samples, which leads to a decrease in the network connectivity. We have qualitatively estimated the fraction of NBO in the bulk and film glasses from the intensity ratio between C and B bands (I_C/I_B). This ratio is found to increase from 1.43 in the case of the bulk to 1.59 (AGF) and 1.69 (AF-3).

The analysis of the structure of fluorotellurite film glasses indicates that their glass network connectivity is smaller than in the bulk glass as well as the number of [TeO_4] units, while the number of number of NBO and [TeO_3] units increases. However, these structural modifications cannot be responsible for the quenching of the near infrared emission observed in AGF since the AF-3 sample presents a strong PL emission at 1.5 μm while having a similar structure to AGF.

6.5 Surface morphology analysis

Film glasses for active applications such as EDWA or EDWL should present a smooth surface free of voids or large particles to allow propagation of light with low losses [16, 219, 220]. We have studied the surface morphology of as-grown (AGF) and annealed AF-3 films by scanning electron microscopy (SEM) and atomic force

microscopy (AFM). Figure 6.7 shows the plane-view SEM images of the AGF and AF-3 fluorotellurite film glasses.

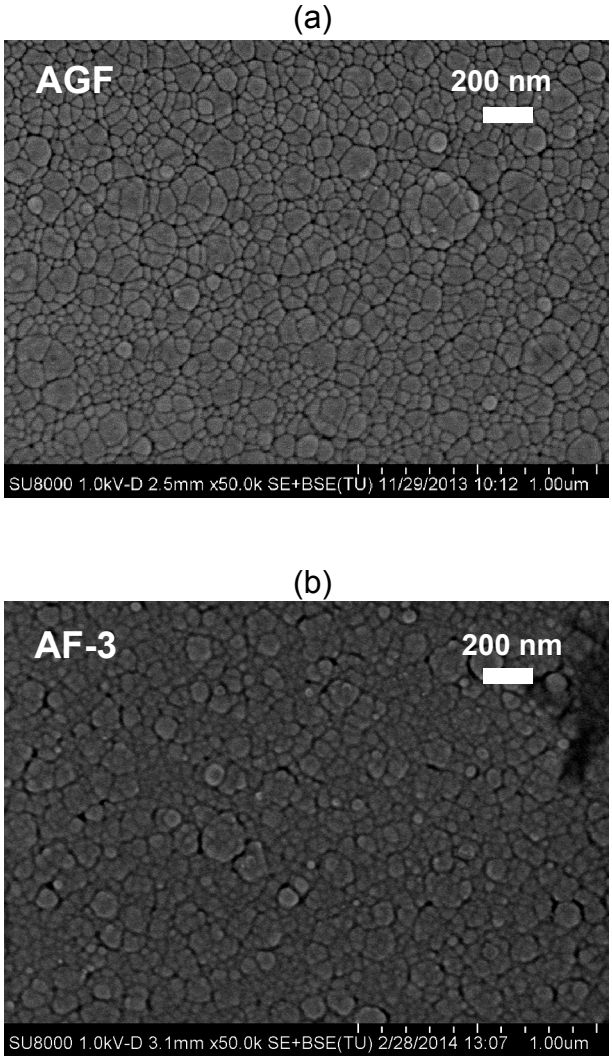

Figure 6.7: Plane-view SEM images of (a) as-grown (AGF); and (b) annealed AF-3 fluorotellurite film glasses.

Both as-grown and annealed films show a uniform surface composed by small particles with typical diameters ∅< 100 nm, that belong to the same plane. Only few large particles and clusters of agglomerated particles are observed in the AGF and AF-3 samples. However, we note that in the case of AGF (Fig. 6.7a) the boundaries between the particles can be well distinguished which imply that the microstructure of the film presents interconnection voids which increase the film porosity. On the contrary, the annealed film (Fig. 6.7b) shows a more compact microstructure where only few boundaries between adjacent particles are observed. This fact should lead to a reduction

of the surface roughness and porosity of the annealed film with a consequent improvement of its optical quality. Thus, we have determined the mean surface roughness (root mean squared, *rms*) of AGF and AF-3 by AFM (not shown here). As we expected, the *rms* roughness is ~12 nm for AGF while it reduces to only 8 nm for AF-3 (–30 %). These values are well below the typical mean roughness (16 nm) reported by Caricato and coauthors [227] for oxyfluoride silicate films synthesized by PLD at 200 ºC.

In addition, the reduced porosity of AF-3 should lead to a higher density and thus to a larger refractive index with respect to the AGF. Since the films were deposited on a transparent substrate it has not been possible to determine their refractive index by spectroscopy ellipsometry. However, we have compared the transmittance spectra of these films (Fig. 6.8).

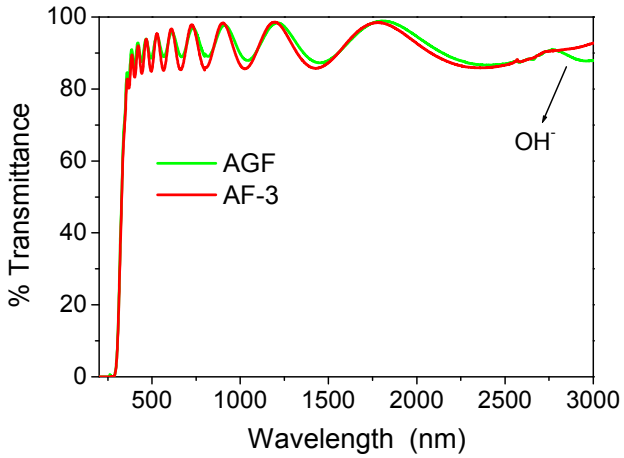

Figure 6.8: Transmittance spectra of as-grown (AGF) and annealed AF-3 fluorotellurite film glasses. Spectra have been normalized to the substrate transmittance spectrum.

The spectra of as-grown and annealed films present a high transmittance and the same number of oscillations which indicates that their thickness is similar. However, we observe in Fig. 6.8 that the amplitude of interferences fringes is slightly larger in the case of AF-3. We have already described in section 6.1 that the amplitude of the interferences fringes in the transmittance spectrum of a thin film is related to the Δn between the film and the substrate. Therefore, the transmittance spectra in Fig. 6.8 suggest that Δn increases and so the refractive index of the film glass upon annealing, which is in good agreement with the results of SEM analysis that indicate a less porous structure in the case of the AF-3 sample (Fig. 6.7b). In addition, a second difference

between the transmittance spectra of AGF and AF-3 is the presence of an absorption band in the 2800-3000 nm range in the spectrum of AGF. We observe that this band is strongly reduced in the case of the AF-3 sample, which suggests that the responsible process is less intense in the annealed film. Similar bands in the transmittance spectra of glasses have been attributed to OH^- vibrations [163]. Thus, in the next section we investigate the OH^- content of fluorotellurite films and how it is affected by annealing treatments.

6.6 OH^- content

We have measured the infrared absorption spectra of fluorotellurite films by FTIR. The substrate (borosilicate glass) employed to deposit the film glasses hides their multiphonon absorption edge. Thus, we focus here only on the infrared region where the OH^- absorption bands are observed. Figure 6.9 compares the absorption coefficient of bulk and film glasses obtained as described in chapter 4 for bulk fluorotellurite glasses.

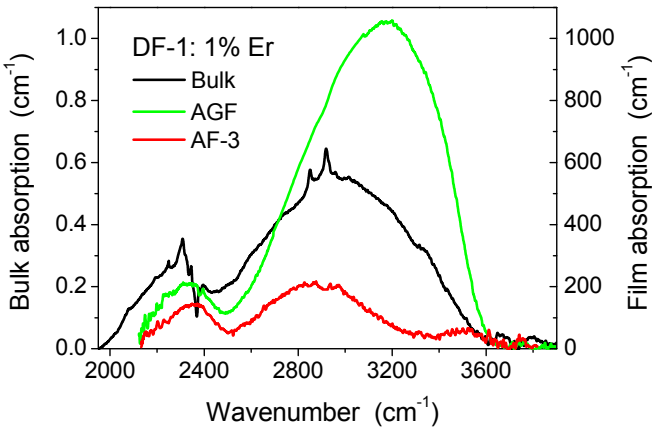

Figure 6.9: Absorption coefficient of DF-1: 1 wt% ErF_3 bulk, as-grown film (AGF) and annealed film (AF-3) glasses in the infrared spectral region.

We immediately note that the intensity of the absorption band due to OH^- vibrations (α_{OH}) is more than 3 orders of magnitude larger in the as-grown film (AGF) than in the bulk glass. Even if post-deposition annealing leads to a strong reduction of α_{OH}, as we observe in the case of AF-3 sample, this is still ~400 times larger than α_{OH} of the bulk glass. This result is not surprising since film glasses synthesized by PLD usually shows a large OH^- content [220, 226]. In particular, Irannejad et al. [226] reported that

phospho-tellurite films synthesized by PLD with a substrate held at 100-200 ºC showed a 10^3-10^4 times larger infrared absorption than the bulk glass.

Post-deposition annealing not only reduces the maximum α_{OH} of fluorotellurite films but it leads to a modification of the shape of the infrared absorption spectrum which becomes similar to that of the bulk glass (Fig. 6.9). As discussed in chapter 4, the broad absorption band due to OH^- vibrations can be deconvoluted into three sub-bands that are attributed to strong, weak and free OH^-s according to the strength of the hydrogen-matrix bond [37, 98]. The strongest the bond, the smallest is the vibration energy (or wavenumber) of OH^- groups. Thus, we can relate the different AFG and AF-3 spectra to a variation in the relative amount of strong, weak and free OH^-s in the two samples. Figure 6.10 shows the Gaussian deconvolution of the OH^- absorption band in the spectra of AGF and AF-3 samples.

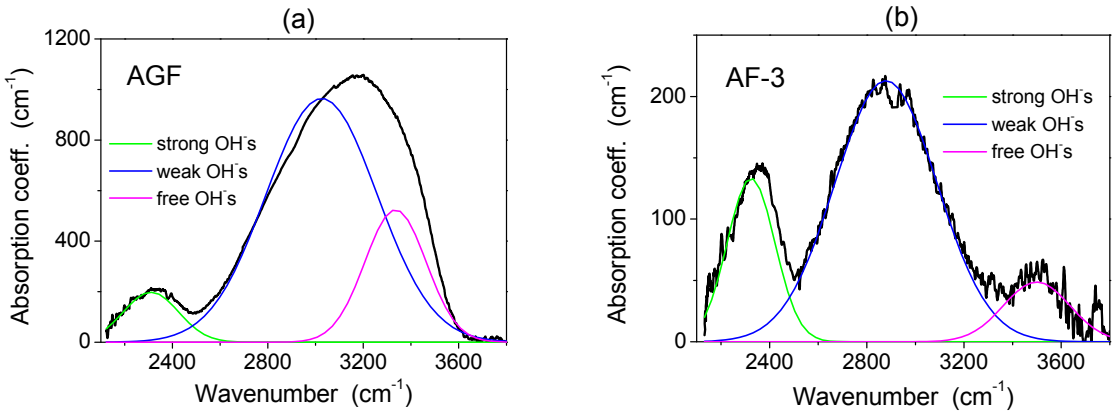

Figure 6.10: Gaussian deconvolution of the absorption band due to OH^- groups in the case of (a) as-grown (AGF); and (b) annealed AF-3 fluorotellurite film glasses.

Table 6.3 summarizes the peak position, intensity, and relative area of strong, weak, and free OH^- groups in AGF and AF-3 samples. In addition, the OH^- concentration (N_{OH}) associated to each type of OH^- groups has been calculated by Eq. 3.9 and included in the table. We have also included in the table the values calculated for the DF-1: 1 wt% ErF_3 bulk glass (chapter 4).

Table 6.3: Peak position (λ_P); peak intensity (I_P); relative area (A_B); and OH^- concentration (N_{OH}) corresponding to each sub-band obtained by Gaussian deconvolution of the OH^- absorption band in the infrared spectra of AGF and AF-3. The values calculated for the bulk glass are included for comparison.

	λ_P (cm^{-1})	I_P (cm^{-1})	A_B (%)	N_{OH} (10^{20} ions/cm^3)
AGF				
Strong OH^-s	2310	192	7	24
Weak OH^-s	3025	960	72	118
Free OH^-s	3335	520	21	64
AF-3				
Strong OH^-s	2324	132	20	16
Weak OH^-s	2879	212	70	26
Free OH^-s	3499	49	10	6
Bulk				
Strong OH^-s	2248	0.25	14	0.03
Weak OH^-s	2937	0.56	80	0.07
Free OH^-s	3308	0.11	6	0.01

We can estimate the total OH^- concentration in the case of AGF and AF-3 samples from Table 6.3. AGF presents a $N_{OH} = 2.0\ 10^{22}$ ions/cm^3 which is reduced to $N_{OH} = 4.8\ 10^{21}$ ions/cm^3 for AF-3. Thus, AGF shows an OH^- density 10^3 times larger than the bulk glass ($N_{OH} = 1.1\ 10^{19}$ ions/cm^3) while the AF-3 still presents a N_{OH} more than 10^2 times larger. Interestingly, if we look in detail to the relative content of the different types of OH^- groups in the film and bulk glasses, we observe that AGF possesses the largest relative content of free OH^-s. Upon annealing, the content of free OH^-s decreases by a factor of ~10 whereas that of weak OH^-s by a factor of ~5. However, the content of strong OH^-s is only slightly affected by the annealing since it only decreases by a factor of ~1.5.

The large OH- content of fluorotellurite films, even in the annealed one, is most likely the responsible of photoluminescence quenching. We have estimated the ratio N_{OH}/[Er] (nominal [Er]= $1.47\ 10^{20}$ ions/cm^3) for bulk and film glasses. It is 0.08 for the bulk glass; 33 for AF-3; and 136 for AGF. This implies that in the AGF Er^{3+} ions are most likely surrounded by OH^- groups that quench their photoluminescence emission, while a similar process is negligible in the case of bulk glass. The situation of AF-3 is somewhat intermediate: Er^{3+} ions are likely surrounded by OH- groups but at a lower extent than in the case of AGF. This leads to a partial quenching of the near infrared

emission at 1.5 μm of AF-3, as demonstrated by the reduced experimental lifetime of the emission in the case of AF-3 with respect to the bulk glass (Fig. 6.4b).

The large OH^- content in the films has to be related to either the fabrication process by PLD or to post-growth incorporation of molecular water. The presence of interconnection voids on the film surface and its porous structure (Fig. 6.7a) would support this last possibility. In fact, Irannejad and coworkers observed the incorporation of molecular water (absorption band at 3700 cm^{-1}) in phospho-tellurite films produced by PLD [220]. The deposition of a silica capping layer on the top of the films was enough to avoid this process [220]. In order to check this possibility, we compared the FTIR absorption spectra of *"just"* annealed films and the spectrum of the same film measured one year after its annealing. They did not show noticeable differences, which suggest that in the present case, OH^- incorporation takes place during the synthesis process itself.

The PLD deposition chamber was evacuated in all cases to a residual pressure of 10^{-4} Pa prior to the deposition of any film. Thus, residual water vapour present in the deposition chamber cannot justify such a large OH^- content in the as-grown films. Neither the OH^- content in the target bulk glass seems to be the origin, since as it is shown in Table 6.3, its OH^- content is 10^3 times lower than in AGF, nor the O_2 gas used as dynamic background during the synthesis of the films, since it has a high purity (99.995 %) and a OH^- content < 3 *ppm*. Thus, the origin of such a large OH^- content has to be related to a possible contamination with H_2O of the O_2 inlet in the chamber during film deposition. In this case, the dehydration process due to the reaction between fluorine and water during the melting, which undoubtedly takes place in the case of bulk glasses as it was discussed in chapter 4, will be limited in the case of thin films due to their reduced fluorine content and therefore, its role in the control of OH^- concentration would be limited.

6.7 Summary and conclusions

In this chapter we demonstrate that Er^{3+} doped fluorotellurite film glasses with very good optical quality can be synthesized by pulsed laser deposition at room temperature in an O_2 atmosphere (10 Pa). The films show a high transmittance (> 85 %) for wavelengths larger than 360 nm and a refractive index slightly smaller than 2 in the near-infrared spectral region. However, the near-infrared $^4I_{13/2} \rightarrow {}^4I_{15/2}$ emission at 1.5 μm is strongly quenched in as-grown film glasses. Post-deposition annealing treatments largely improve the near infrared Er^{3+} photoluminescence emission at 1.5 μm. We have obtained the best results for 2-3 hours annealing steps in the range 300-315 ºC. In particular, we have achieved up to a 20-fold increase of the emission intensity (at 1.53 μm) and a single-exponential decay of the $^4I_{13/2}$ level with a maximum lifetime of 3.3 ms, while the shape of the emission spectrum is similar to that of the bulk glass and little affected by the annealing, thus indicating that Er^{3+} environment remained unchanged.

We have investigated the modifications induced by the annealing in order to determine the origin of photoluminescence quenching in as-grown films. The **composition and structure** of fluorotellurite films, even if slightly different from that of the bulk glass, are similar in as-grown and annealed films so we consider that they are not responsible for the photoluminescence quenching. On the contrary, the **surface morphology** of the annealed film improves upon annealing: it shows a reduced roughness (8 vs 12 nm) and fewer particles/voids with respect to the as-grown film. This contributes to improve the optical properties of the annealed film, which may lead to improve its photoluminescence response in return. However, the main responsible for the photoluminescence quenching of as-grown films is their large **OH^- content** which leads to nonradiative deexcitation of the $^4I_{13/2}$ level through stretching vibrations of O-H bonds. In particular, we have estimated that the OH^- concentration is 10^3 times larger in the as-grown film and more than 10^2 times larger in the annealed film, with respect to the bulk glass. Therefore, even if the OH^- content of annealed films has been strongly reduced it is still large enough to induce nonradiative deexcitation of Er^{3+} ions, as evidenced by the fact that the lifetime measured for the bulk glass is larger than for the annealed film (3.8 ms vs. 3.3 ms). OH^- groups in the produced fluorotellurite films are part of the glass network and they do not come from molecular water incorporated to

the films after their deposition, as reported in the case of phospho-tellurite films [220, 226]. The OH^- content of as-grown films could be likely reduced by using a heated substrate, increasing the duration of post-deposition annealing treatments, and finally by avoiding any contamination of the deposition chamber with water vapour.

7

Conclusions/Conclusiones

Conclusions

In this thesis we investigate fluorotellurite glasses, glass-ceramics, and film glasses belonging to the TeO_2–ZnO–ZnF_2 system as hosts for rare earth ions and we analyze their potential as base materials for active photonic devices. The main conclusions achieved are summarized in the following.

- **Rare earth doped TeO_2–ZnO–ZnF_2 glasses**

We have studied the effect of Zn/Te and F/O ratios on the properties of TeO_2–ZnO–ZnF_2 glasses. For this purpose we have considered two glass hosts with real compositions: 68 TeO_2–22 ZnO–10 ZnF_2 mol% (DF-1) and 35 TeO_2–46 ZnO–19 ZnF_2 mol% (DF-2). We have determined that the glass having the larger Zn/Te and F/O ratios (DF-2) presents a poorly connected network structure mainly composed by TeO_3 units; a lower refractive index (1.82 *vs.* 2.00 nm at 1500 nm); a lower OH^- content (39.8 *ppm vs.* 56.3 *ppm*) and a blue shifted ultraviolet absorption edge (~343 nm *vs.* ~385 nm), with respect to the glass with the lower Zn/Te and F/O ratios (DF-1). However, both glasses are characterized by a maximum phonon energy of ~850 cm^{-1}; a large thermal stability ($T_{on} - T_g$) ≥ 100 ºC and a broad transparency region from the visible up to ~6 μm, which make them promising for practical applications. The study of the photoluminescence response of **Er^{3+} doped** DF-1 and DF-2 glasses (λ_{exc}= 801 nm at room temperature), as a function of the dopant concentration, has demonstrated that DF-1 is a promising candidate for its application in broadband optical amplifiers in the C band (1.5 μm) due to its large emission cross-section and bandwidth, while DF-2 doped with 3 wt% ErF_3 is suitable for implementing devices based on the infrared to visible (green and red) upconverted emissions due to the strong intensity and large lifetime of these emissions.

Finally, we have studied the room temperature photoluminescence response of **Er^{3+}-Yb^{3+}** and **Er^{3+}-Tm^{3+} codoped** DF-1 glasses. The glass codoped with the largest Yb^{3+} content (0.5 wt% ErF_3–2 wt% YbF_3) is suitable to develop broadband amplifiers in the optical C band as well as devices based on the infrared to visible (green and red) upconverted emissions since it shows enhanced near infrared emission at 1.5 μm (5-fold) and visible upconverted emissions (green: 40-fold; red: 800-fold) with respect to the single Er^{3+} doped glass (0.5 wt% ErF_3), due to energy transfer processes from Yb^{3+} to Er^{3+} ions. In the case of Er^{3+}-Tm^{3+} codoped DF-1 glasses, we have demonstrated that the glass with the largest Tm^{3+} content (0.3 wt% ErF_3–1 wt% TmF_3) is a suitable candidate to implement ultra broadband amplifiers covering the S, C, L, and U bands of the optical telecommunication transmission window since it presents a 150 nm-wide emission spectra due to the superposition of the near infrared emission of Er^{3+} and Tm^{3+} ions.

- **Transparent Er^{3+} doped TeO_2–ZnO–ZnF_2 glass-ceramics**

We have studied the thermodynamic behavior of TeO_2–ZnO–ZnF_2 glasses with the objective of producing transparent rare earth doped glass-ceramics through two-step thermal treatments of precursor glass samples. We have determined that transparent glass-ceramic samples can be produced by controlled crystallisation in a small temperature range (340-345 ºC) in the case of the glass with composition: 68 TeO_2– 22 ZnO– 10 ZnF_2 (mol%): 1 wt% ErF_3. Moreover, this interval is strongly dependent on both the glass composition and the dopant concentration. Glass-ceramics are highly transparent in the visible (> 500 nm) and near infrared spectral regions and they present a linear refractive index similar to those of the precursor glass (1.99 at 1500 nm). Transmission electron microscopy analysis has evidenced the presence of **dendritic ErF_3 nanocrystals** in the amorphous glass matrix, with characteristic sizes of ~50 nm. The crystalline to amorphous ratio is low (< 1 %) in glass-ceramics due to their low ErF_3 content (1 wt%) but the fraction of Er^{3+} ions segregated into the fluoride nanocrystals is large. Thus, the local environment of Er^{3+} ions changes from the amorphous environment of the glass matrix to the polycrystalline environment of fluoride nanocrystals, which is characterized by a **low maximum phonon energy** (~300 cm^{-1}). This fact has important effects on the photoluminescence response of Er^{3+} ions: their absorption and emission bands

sharpen and transitions between individual Stark levels can be well resolved at room temperature; their upconverted red emission is dramatically enhanced and it becomes of comparable intensity to the green one (I_{RED}/I_{GREEN}≈ 0.54-0.84). Thus, glass-ceramics may be adequate candidates to develop devices based on Er^{3+} visible upconverted emission such as phosphors and upconvertes.

- **Er^{3+} doped TeO_2–ZnO–ZnF_2 thin film glasses**

We have synthesized film glasses by pulsed laser deposition at room temperature from the 68 TeO_2– 22 ZnO– 10 ZnF_2 (mol%): 1 wt% ErF_3 bulk glass. The glass structure of as-grown films is similar to that of the bulk glass, although they show a larger fraction of non bridging oxygens and TeO_3 units. They present a very good optical quality (linear refractive index: 1.94 at 1500 nm, transmittance larger than 85 % for λ> 360 nm). Unfortunately, the near infrared emission at 1.5 μm of as-grown films is too weak to be useful for practical applications. However, this was improved through optimized annealing treatments in air in the 300-315 ºC range. In particular, a 20-fold increase of the maximum emission intensity with respect to as-grown films, and a single-exponential decay of the $^4I_{13/2}$ level with a maximum lifetime of 3.3 ms were achieved. This improvement was attributed to the significant decrease of the OH^- content in the annealed film (1 order of magnitude). OH^- content remained stable with time, thus suggesting that the incorporation of hydroxyl ions to the films takes place during their deposition. Finally, we propose the use of a heated substrate and the increase of the annealing time to reduce further the OH^- content of film glasses.

Conclusiones

En esta tesis investigamos vidrios, vitrocerámicos, y láminas delgadas de vidrios de fluoroteluritos pertenecientes al sistema TeO_2–ZnO–ZnF_2 como matrices para iones de tierras raras, así como analizamos su posible aplicación para el desarrollo de dispositivos fotónicos activos. Los principales resultados obtenidos se resumen a continuación.

- **Vidrios de TeO_2–ZnO–ZnF_2 dopados con iones de tierras raras**

Hemos estudiado el efecto del contenido relativo de Zn/Te y F/O en las propiedades de de vidrios de TeO_2–ZnO–ZnF_2. Para ello, hemos considerado dos vidrios con composiciones reales: 68 TeO_2–22 ZnO–10 ZnF_2 mol% (DF-1) and 35 TeO_2–46 ZnO–19 ZnF_2 mol% (DF-2). El vidrio con un cociente de Zn/Te y de F/O mayor (DF-2) posee una estructura de red vítrea débilmente conectada, compuesta principalmente por unidades TeO_3; un índice de refracción menor (1.82 *vs.* 2.00 nm a 1500 nm); un contenido de OH^- inferior (39.8 *ppm vs.* 56.3 *ppm*) y, por último, un borde de absorción ultravioleta desplazado hacía longitudes de onda menores (~343 nm *vs.* ~385 nm), en comparación con el vidrio con cociente de Zn/Te y F/O menores (DF-1). Sin embargo, ambos vidrios se caracterizan por una máxima energía de fonón máxima similar (~850 cm^{-1}); una gran estabilidad térmica ($T_{on} - T_g$) ≥ 100 ºC y una amplia región de transparencia desde el visible hasta ~6 μm, que los hacen prometedores para aplicaciones prácticas.

El estudio de la respuesta fotoluminiscente de los vidrios DF-1 y DF-2 **dopados con Er^{3+}** (λ_{exc}= 801 nm a temperatura ambiente), en función de la concentración de dopante, ha demostrado que DF-1 es un candidato prometedor para el desarrollo de amplificadores ópticos de banda ancha en la ventana de transmisión C (1,5 μm) dadas su amplia anchura de banda y elevada sección eficaz, mientras que el vidrio DF-2 dopado con el 3 % de ErF_3 es adecuado para desarrollar dispositivos basados en las emisiones visibles (verde y roja) por procesos de conversión de energía (*upconversion*) gracias a la elevada intensidad y largo tiempo de vida de estas emisiones.

Por último, hemos estudiado la respuesta fotoluminiscente a temperatura ambiente de vidrios DF-1 **codopados con Er^{3+}-Yb^{3+}** e **Er^{3+}-Tm^{3+}**. El vidrio codopado con el mayor contenido de Yb^{3+} (0.5 % ErF_3–2 % YbF_3) es un candidato potencial para

desarrollar amplificadores ópticos de banda ancha en la ventana de transmisión C, así como dispositivos basados en las emisiones visibles del Er^{3+} por procesos de *upconversion*, dado a que muestra un aumento significativo tanto de la emisión a 1.5 μm (factor 5), como de las emisiones visibles (verde: factor 40; roja: factor 800) con respecto al vidrio dopado solo con Er^{3+} (0.5 % ErF_3), lo que se relaciona con los procesos de transferencia de energía desde Yb^{3+} hacia Er^{3+}. En el caso de los vidrios codopados con Er^{3+}-Tm^{3+}, el vidrio con el mayor contenido de Tm^{3+} (0.3 % ErF_3–1 % TmF_3) ha demostrado ser un candidato adecuado para implementar amplificadores de banda ultra ancha que cubran las ventanas de transmisión en telecomunicaciones S, C, L, y U debido a que presenta un espectro de emisión con un anchura de banda de 150 nm gracias a la superposición de las emisiones de Er^{3+} y Tm^{3+} en el infrarrojo cercano.

- **Vitro-cerámicos transparentes de TeO_2–ZnO–ZnF_2 dopados con Er^{3+}**

Hemos estudiado el comportamiento termodinámico de los vidrios de TeO_2–ZnO–ZnF_2 con el objetivo de producir vitrocerámicos transparentes dopados con tierras raras mediante tratamientos térmicos en dos etapas de muestras de vidrios. Hemos determinado que es posible producir vitrocerámicos transparentes por cristalización controlada, pero solo en un pequeño intervalo de temperaturas (340-345 ºC) y en el caso del vidrio: 68 TeO_2– 22 ZnO– 10 ZnF_2 (mol%) dopado con 1 % en peso de ErF_3. Además, este intervalo depende fuertemente de la composición del vidrio y de la concentración del dopante. Los vitrocerámicos son muy transparentes en el visible (> 500 nm) y en el infrarrojo cercano y poseen un índice de refracción lineal similar al del vidrio de partida (1,99 a 1500 nm). El análisis por microscopia electrónica ha evidenciado la presencia de **nanocristales dendríticos de ErF_3**, con dimensiones características de ~50 nm, embebidos en la matriz amorfa. La relación entre las fases cristalina y amorfa en las muestras vitrocerámicas transparentes es pequeña (< 1 %) debido al pequeño contenido de ErF_3 (1 % en peso). Sin embargo, la mayoría de iones de Er^{3+} se encuentran segregados en los nanocristales de fluoruro presentes en los vitrocerámicos. Por ello, el entorno local de los iones de Er^{3+} cambia desde el amorfo de la matriz vítrea al policristalino de los nanocristales de fluoruro, que se caracterizan por una máxima energía de fonón muy baja (~300 cm^{-1}). Este hecho tiene un importante efecto en la respuesta fotoluminiscente de los iones de Er^{3+}: sus

bandas de absorción y emisión se hacen más definidas, pudiéndose resolver transiciones entre niveles Stark a temperatura ambiente; su emisión roja por *upconversion* aumenta mucho, siendo su intensidad similar a la de la emisión verde ($I_{ROJO}/I_{VERDE}\approx$ 0.54-0.84). Por ello, consideramos que los vitrocerámicos son candidatos adecuados para el desarrollo de dispositivos basados en las emisiones visibles del Er^{3+} por procesos de *upconversion*.

- **Láminas delgadas de vidrios de TeO_2–ZnO–ZnF_2 dopados con Er^{3+}**

Hemos sintetizado láminas delgadas mediante depósito por láser pulsado a temperatura ambiente a partir del vidrio 68 TeO_2– 22 ZnO– 10 ZnF_2 (mol%) dopado con 1 % en peso de ErF_3. La estructura de estas láminas es similar a la del vidrio masivo, aunque presentan una fracción mayor de *oxígenos no puente*, así como de unidades TeO_3. La calidad óptica de las láminas es muy buena (índice de refracción lineal de 1,94 a 1500 nm y transmitancia mayor del 85 % $\lambda>$ 360 nm). Sin embargo, las laminas crecidas a temperatura ambiente muestran una emisión en el infrarrojo cercano (1,5 μm) demasiado débil para su aplicación práctica. Hemos determinado que el tratamiento térmico post-depósito óptimo se encuentra en un intervalo de temperaturas de 300-315 ºC en aire. En particular, hemos conseguido aumentar 20 veces la intensidad máxima de emisión y alcanzar un tiempo de vida del nivel $^4I_{13/2}$ de 3.3 ms. Esta mejoría se ha atribuido a una reducción del contenido de OH^- de 1 orden de magnitud en la lámina recocida. Además, este contenido permanece estable a lo largo del tiempo, lo cual sugiere que los iones hidroxilos se incorporan a las láminas durante su crecimiento y no después. Por último, se propone el empleo de un sustrato caliente y de recocidos de mayor duración para reducir aún más la concentración de OH^- en las láminas.

References

[1] B.E.A. Saleh and M.C. Teich: Fundamentals of Photonics (John Wiley & Sons, Inc., New York, 1991).

[2] J. Hecht: Understanding fiber optics, 2nd ed. (Indianapolis: Sams Publishing, 1993).

[3] T.H. Maiman: “Stimulated optical radiation in ruby”, Nature 187 (1960), p. 493-494.

[4] R.N. Hall, G.E. Fenner, J.D. Kingsley, T.J. Soltys, R.O. Carlson: “Coherent light emission from GaAs junctions”, Phys. Rev. Lett. 9 (1962), p. 366-368.

[5] K.C. Kao, and G.A. Hockman: “Dielectric-fibre surface waveguides for optical frequencies”, Proc. IEE 113 (1966), p. 1151-1158.

[6] F.P. Kapron, D.B. Keck, R.D. Maurer: “Radiation losses in glass optical waveguides”, Appl. Phys. Lett. 17 (1970), p. 423-425.

[7] T. Miya, Y. Terunuma, T. Hosaka, T. Miyashita: “Ultimate low-loss single mode fiber at 1.55 μm”, Electron. Lett. 15 (1979), p. 106-108.

[8] Available at http://www.ecse.rpi.edu/~schubert/Light-Emitting-Diodes-dot-org/chap22/chap22.htm (accessed on February 2015)

[9] R.J. Mears, L. Reekie, I.M. Jauncey, D.N. Payne: “Low-noise erbium-doped fibre amplifier operating at 1.54 μm”, Electron. Lett. 23 (1987), p. 1026-1028.

[10] N.S. Bergano, J. Aspell, C.R. Davidson, P.R. Trischitta, B.M. Nyman, F.W. Kerfoot: "Feasibility demonstration of transoceanic EDFA transmission," *Proceedings of SPIE*, vol. 1581 (1995), p. 182-187.

[11] P.J. Winzer, R.-J Essiambre: “Advanced optical modulation formats”, Proc. IEEE 94 (2006), p. 952-981.

[12] R. Ramaswami: “Optical fiber communication: from transmission to networking”, IEEE Commun. Mag. 40 (2002), p. 138-147.

[13] D.J. Richardson, J.M. Fini, L.E. Nelson: “Space-division multiplexing in optical fibres”, Nature Photon. 7 (2013), p. 354-362.

[14] D. Cotter, R.J. Manning, K.J. Blow, A.D. Ellis, A.E. Kelly, D. Nesset, I.D. Phillips, A.J. Poustie, D.C. Rogers: “Nonlinear Optics for High-Speed Digital Information Processing”, Science 286 (1999), p. 1523-1528.

[15] G. Lifante, Integrated Photonics: Fundamentals (John Wiley & Sons Ltd, 2003).

[16] J.D.B. Bradley and M. Pollnau: “Erbium-doped integrated waveguide amplifiers and lasers”, Laser Photonics Rev. 5 (2011), p. 368-403.

[17] The Current Trend in Optics and Photonics, Edited by C.-C. Lee (Springer, 2015).

[18] Available at http://www.photonics.com/Article.aspx?AID=54399 (accessed on February 2015)

[19] Editorial: “Extending opportunities”, Nature Photon. 6 (2012), p. 407.

[20] S.D. Jackson: “Towards high-power mid-infrared emission from a fibre laser”, Nature Photon. 6 (2012), p. 423-431.

[21] A.J. Kenyon: “Recent developments in rare-earth doped materials for optoelectronics”, Prog. Quant. Electron. 26 (2002), p. 225-284.

[22] J. Clark and G. Lanzani: “Organic photonics for communications”, Nature Photon. 4 (2010), p. 438-446.

[23] D.K. Gramotnev, S.I. Bozhevolnyi: “Plasmonics beyond the diffraction limit”, Nature Photon. 4 (2010), p. 83-91.

[24] B. Jalali, S. Fathpour: “Silicon photonics”, J. Lightw. Technol. 24 (2006), p. 4600-4615

[25] L. Pavesi: “Will silicon be the photonic material of the third millenium?”, J. Phys-Condens Mat. 15 (2003), p. R1169-R1196.

[26] D. Liang and J.E. Bowers: “Recent progress in lasers on silicon”, Nature Photon. 4 (2010), p. 511-517.

[27] M. Yamane and Y. Asahara: Glasses for photonics (Cambridge University Press, 2000).

[28] K. Richardson, D. Krol, K. Hirao: “Glasses for Photonic Applications”, Int. J. Appl. Glass Science 1 (2010), p. 74-86.

[29] E.M. Vogel, M.J. Weber, D.M. Krol: “Nonlinear optical phenomena in glass”, Phys. Chem. Glasses 32 (1991), p. 231-254.

[30] Rare-Earth-Doped Fiber Lasers and Amplifiers, Edited by M.J.F. Digonnet (CRC Press, 2001), p. 19-133.

[31] S. Shen, A. Jha, X. Liu, M. Naftaly, K. Bindra, H.J. Bookey, A.K. Kar: “Tellurite glasses for broadband amplifiers and integrated optics”, J. Am. Ceram. Soc. 85 (2002), p. 1391-1395.

[32] S.J. Madden and K.T. Vu: “High-Performance Integrated Optics with Tellurite Glasses: Status and Prospects”, Int. J. Appl. Glass Science 3 (2012), p. 289-298.

[33] J.S. Wang, E.M. Vogel, E. Snitzer: “Tellurite glass: a new candidate for fiber devices”, Opt. Mater. 3 (1994), p. 187-203.

[34] A. Jha, B. Richards, G. Jose, T. Teddy-Fernandez, P. Joshi, X. Jiang, J. Lousteau: “Rare-earth ion doped TeO_2 and GeO_2 glasses as laser materials”, Prog. Mater. Sci. 57 (2012), p. 1426-1491.

[35] A. Jha, B.D.O. Richards, G. Jose, T.T. Fernandez, C.J. Hill, J. Lousteau, P. Joshi: “Review on structural, thermal, optical and spectroscopic properties of tellurium oxide based glasses for fibre optic and waveguide applications”, Int. Mater. Rev. 57 (2012), p. 357-382.

[36] J. Massera, A. Haldeman, J. Jackson, C. Rivero-Baleine, L. Petit, K. Richardsonz: “Processing of Tellurite-Based Glass with Low OH Content”, J. Am. Ceram. Soc. 94 (2011), p. 130-136.

[37] M.D. O'Donnell, C.A. Miller, D. Furniss, V.K. Tikhomirov, A.B. Seddon: “Fluorotellurite glasses with improved mid-infrared transmission”, J. Non-Cryst. Solids 331 (2003), p. 48-57.

[38] D.L. Sidebottom, M.A. Hruschka, B.G. Potter, R.K. Brow: “Increased radiative lifetime of rare earth-doped zinc oxyhalide tellurite glasses”, Appl. Phys. Lett. 71 (1997), p. 1963-1965.

[39] Y. Teng, K. Sharafudeen, S. Zhou, J. Qiu: “Glass-ceramics for photonic devices”, J. Ceram. Soc. Jpn. 120 (2012), p. 458-466.

[40] M. Mortier: “Between glass and crystal: glass-ceramics, a new way for optical materials”, Philos. Mag. B 82 (2002), p. 745-753.

[41] N. Karpukhina, R.G. Hill, R.V. Law: “Crystallisation in oxide glasses – a tutorial review”, Chem. Soc. Rev. 43 (2014), p. 2174-2186.

[42] A. de Pablos-Martín, A. Durán, M.J. Pascual: “Nanocrystallisation in oxyfluoride systems: mechanisms of crystallisation and photonic properties”, Int. Mater. Rev. 57 (2012), p. 165-186.

[43] G.H. Beall, L.R. Pinckney: “Nanophase Glass-Ceramics”, J. Am. Ceram. Soc. 82 (1999), p. 5-16.

[44] M. Mortier and G. Dantelle: "Oxyfluoride Transparent Glass Ceramics" in Functionalized Inorganic Fluorides, Edited by A. Tressaud (John Wiley & Sons Ltd, 2010).

[45] A. Suárez-García, J. Gonzalo, C.N. Afonso: “Low-loss Al_2O_3 waveguides produced by pulsed laser deposition at room temperature”, Appl. Phys. A – Mater. Sci. Process. 77 (2003), p. 779-783.

[46] R. Serna, C.N. Afonso: “In situ growth of optically active erbium doped Al_2O_3 thin films by pulsed laser deposition”, Appl. Phys. Lett. 69 (1996), p. 1541-1543.

[47] Z. Xiao, R. Serna, C.N. Afonso, I. Vickridge: “Broadband infrared emission from Er–Tm: Al_2O_3 thin films”, Appl. Phys. Lett. 87 (2005), Art. 111103.

[48] A.O.G. Dikovska, P.A. Atanasov, M. Jiménez De Castro, A. Perea, J. Gonzalo, C.N. Afonso, J. García López: “Optically active Er^{3+}-Yb^{3+} codoped Y_2O_3 films produced by pulsed laser deposition”, Thin Solid Films 500 (2006), p. 336-340.

[49] C.N. Afonso, J.M. Ballesteros, J. Gonzalo, G.C. Righini, S. Pelli: "Rare-earth doped glass waveguides prepared by pulsed laser deposition", Appl. Surf. Sci. 96-98 (1996), p. 760-763.

[50] R. Serna, J.M. Ballesteros, M. Jiménez de Castro, J. Solis, C.N. Afonso: "Optically active Er–Yb doped glass films prepared by pulsed laser deposition", J. Appl. Phys. 84 (1998), p. 2352-2354.

[51] J. Gonzalo, O. Sanz, A. Perea, J.M. Fernández-Navarro, C.N. Afonso, J. García López: "High refractive index and transparent heavy metal oxide glassy thin films", Appl. Phys. A – Mater. Sci. Process. 76 (2003), p. 943-946.

[52] J. Gonzalo, H. Fernandez, J. Solis, D. Munoz-Martin, J.M. Fernandez-Navarro, C.N. Afonso, J.L.G. Fierro: "Enhanced nonlinear optical properties of oxygen deficient lead-mobium-germanate film glasses", Appl. Phys. Lett. 90 (2007), Art. 251907.

[53] D. Munoz-Martin, H. Fernandez, J.M. Fernandez-Navarro, J. Gonzalo, J. Solis, J.L.G. Fierro, C. Domingo, J.V. Garcia-Ramos: "Nonlinear optical susceptibility of multicomponent tellurite thin film glasses", J. Appl. Phys. 104 (2008), Art. 113510.

[54] D. Munoz-Martín, M.A. Villegas, J. Gonzalo, J.M. Fernández-Navarro: "Characterisation of glasses in the TeO_2–WO_3–PbO system", J. Eur. Ceram. Soc. 29 (2009), p. 2903-2913.

[55] J. Siegel, J.M. Fernández-Navarro, A. García-Navarro, V. Diez-Blanco, O. Sanz, J. Solis, F. Vega, J. Armengol: "Waveguide structures in heavy metal oxide glass written with femtosecond laser pulses above the critical self-focusing threshold", Appl. Phys. Lett. 86 (2005), Art. 121109.

[56] V. Díez-Blanco, J. Siegel, J. Solís: "Waveguide structures written in SF57 glass with fs-laser pulses above the critical self-focusing threshold", Appl. Surf. Sci. 252 (2006), p. 4523-4526.

[57] F. Xu, R. Serna, M. Jiménez De Castro, J.M. Fernández Navarro, Z. Xiao: "Broadband infrared emission of erbium-thulium-codoped calcium boroaluminate glasses", Appl. Phys. B: Lasers Opt. 99 (2010), p. 263-270.

[58] M. Jiménez De Castro, J.M. Fernández Navarro: "Infrared luminescence of erbium-doped sodium lead germanate glass", Appl. Phys. B: Lasers Opt. 106 (2012), p. 669-675.

[59] J.M. Fernández Navarro: El vidrio (CSIC-SECM, 2003).

[60] The Properties of Optical Glass, Edited by H. Bach and N. Neuroth (Springer-Verlag, Berlin, 1995).

[61] A. Sakamoto and S. Yamamoto: "Glass-ceramics: Engineering Principles and Applications", Int. J. Appl. Glass Science 1 (2010), p. 237-247.

[62] V.M. Fokin, E.D. Zanotto, N.S. Yuritsyn, J.W.P. Schmelzer: "Homogeneous crystal nucleation in silicate glasses: A 40 years perspective", J. Non-Cryst. Solids 352 (2006), p. 2681-2714.

[63] S.D. Stookey: “Catalyzed crystallization of glass in theory and practice”, Ind. Eng. Chem. 51 (1959), p. 805-808.

[64] K.F. Kelton: “Crystal Nucleation in Liquids and Glasses”, Solid State Phys. 45 (1991), p. 75-177.

[65] M.C. Weinberg: “Glass-forming ability and glass stability in simple systems”, J. Non-Cryst. Solids 167 (1994), p. 81-88.

[66] R.A.H. El-Mallawany: Tellurite Glasses Handbook - Physical Properties and Data (CRC Boca Raton, FL, 2001).

[67] E.F. Lambson, G.A. Saunders, B. Bridge, R.A. El-Mallawany: “The elastic behaviour of TeO_2 glass under uniaxial and hydrostatic pressure”, J. Non-Cryst. Solids 69 (1984), p. 117-133.

[68] B.E. Warren: “The Diffraction of X-Rays in Glass”, Phys. Rev. 45 (1934), p. 657-661.

[69] W.H. Zachariasen: “The atomic arrangement in glass”, J. Am. Chem. Soc. 54 (1932), p. 3841-3851.

[70] A.C. Wright: “Neutron scattering from vitreous silica. V. The structure of vitreous silica: What have we learned from 60 years of diffraction studies?”, J. Non-Cryst. Solids 179 (1994), p. 84-115

[71] S.R. Elliott: “Medium-range structural order in covalent amorphous solids”, Nature 354 (1991), p. 445-452.

[72] A.P. Sokolov, A. Kisliuk, M. Soltwisch, D. Quitmann: “Medium-range order in glasses: Comparison of Raman and diffraction measurements”, Phys. Rev. Lett. 69 (1992), p. 1540-1543.

[73] P.H. Gaskell, M.C. Eckersley, A.C. Barnes, P. Chieux: “Medium-range order in the cation distribution of a calcium silicate glass”, Nature 350 (1991), p. 675- 677.

[74] B.E. Warren: “The Basic Principles Involved in the Glassy State”, J. Appl. Phys. 13 (1942), p. 602-610.

[75] Treatise on material science and technology, Volume 12, Glass I: Interaction with Electromagnetic Radiation, Edited by: M. Tomozawa, R.H. Doremus (Academic Press, Inc. Ltd. 1977).

[76] M. Born and E. Wolf: Principles of Optics 6^{th} edition (Pergamon Press, Oxford, 1993).

[77] R.W. Boyd: Nonlinear Optics (Academic press, San Diego, 1992).

[78] R. Righini: “Ultrafast optical Kerr effect in liquids and solids”, Science 262 (1993), p. 1386-1390.

[79] M.E. Lines: “Oxide glasses for fast photonic switching: A comparative study”, J. Appl. Phys. 69 (1991), p. 6876-6884.

[80] D.W. Hall, M.A. Newhouse, N.F. Borrelli, W.H. Dumbaugh, D.L Weidman: "Nonlinear optical susceptibilities of high-index glasses", Appl. Phys. Lett. 54 (1989), p. 1293-1295.

[81] Handbook of the pysics and chemistry of Rare Earths Vol. 32, Edited by K.A. Gschneidner Jr., L. Eyring, G. H. Lander (Elsevier Science B.V. 2001).

[82] J.H. Van Vleck: "The puzzle of rare-earth spectra in solids", J. Phys. Chem. 41 (1937), p. 67-80.

[83] H.N. Russell and F.A. Saunders: "New Regularities in the Spectra of the Alkaline Earths", Astrophysical Journal. 61 (1925), p. 38-69.

[84] M.J. Dejneka, A. Streltsov, S. Pal, A.G. Frutos, C.L. Powell, K. Yost, P.K. Yuen, U. Müller, J. Lahiri: "Rare earth-doped glass microbarcodes", Proc. Natl. Acad. Sci. USA 100 (2003), p. 389-393.

[85] R. Reisfeld: "Radiative and nonradiative transition of rare earths in glasses", Struct. Bonding 22 (1975), p. 123-175.

[86] G.C. Righini, M. Ferrari: "Photoluminescence of rare-earth-doped glasses", Rivista del Nuovo Cimento 28 (2005), p. 1-53.

[87] D.E. McCumber: "Einstein Relations Connecting Broadband Emission and Absorption Spectra", Phys. Rev 136 (1964), p. A954-A957.

[88] W.J. Miniscalco, R.S. Quimby: "General procedure for the analysis of Er^{3+} cross-sections", Opt. Lett. 16 (1991), p. 258-260.

[89] B.R. Judd: "Optical absorption intensities of rare-earth ions", Phys. Rev. 127 (1962), p. 750-761.

[90] G.S. Ofelt: "Intensities of Crystal Spectra of Rare-Earth Ions", J. Chem. Phys. 37 (1962), p. 511-520.

[91] C.A. Morrison, R.P. Leavitt: Handbook on the Physics and Chemistry of Rare Earths 5; Chapter 46: Spectroscopic properties of triply ionized lanthanides in transparent host crystals (K.A. Gschneidner and L. Eyring, North Holland, Amsterdam, 1982), p. 461-692.

[92] S. Tanabe, T. Ohyagi, N. Soga, T. Hanada: "Compositional dependence of Judd-Ofelt parameters of Er^{3+} ions in alkali-metal borate glasses", Phys. Rev. B 46 (1992), p. 3305-3310.

[93] L.A. Riseberg and H.W. Moos: "Multiphonon orbit-lattice relaxation of excited states of rare-earth ions in crystals", Phys. Rev. 174 (1968), p. 429-438.

[94] C.B. Layne, W.H. Lowdermilk, M.J. Weber: "Multiphonon relaxation of rare-earth ions in oxide glasses", Phys. Rev. B 16 (1977), p. 10-20.

[95] E. Snoeks, P.G. Kik, A. Polman: "Concentration quenching in erbium implanted alkali silicate glasses", Opt. Mater. 5 (1996), p. 159-167.

[96] F. Auzel: “Upconversion and Anti-Stokes Processes with f and d Ions in Solids”, Chem. Rev. 104 (2004), p. 139-173.

[97] Y. Yan, A.J. Faber, H. de Waal: “Luminescence quenching by OH groups in highly Er-doped phosphate glasses”, J. Non-Cryst. Solids 181 (1995), p. 283-290.

[98] X. Feng, S. Tanabe, T. Hanada: “Hydroxyl groups in erbium-doped germanotellurite glasses”, J. Non-Cryst. Solids 281 (2001), p. 48-54.

[99] W. Koechner: Solid-state Laser Engineering, Sixth edition (Springer 2006).

[100] E. Snitzer: “Optical Maser Action of Nd^{+3} in a Barium Crown Glass”, Phys. Rev. Lett. 7 (1961), p. 444-446.

[101] C.J. Koester and E. Snitzer: “Amplification in a Fiber Laser”, Appl. Opt. 3 (1964), p. 1182-1186.

[102] D.R. Zimmerman, L.H. Spiekman, “Amplifiers for the Masses: EDFA, EDWA, and SOA Amplets for Metro and Access Applications”, IEEE J. Lightwave Technol. 9 (1991), p. 234-250.

[103] W.J. Miniscalco: “Erbium-doped glasses for fiber amplifiers at 1500 nm”, IEEE J. Lightwave Technol. 9 (1991), p. 234-250.

[104] J.S. Wang, D.P. Machewirth, F. Wu, E. Snitzer, E.M. Vogel: “Neodymium-doped tellurite single-mode fiber laser”, Opt. Lett. 19 (1994), p. 1448-1450.

[105] M. Yamada, A. Mori, K. Kobayashi, H. Ono, T. Kanamori, K. Oikawa, Y. Nishida, Y. Ohishi: “Gain-flattened tellurite-based EDFA with a flat amplification bandwidth of 76 nm”, IEEE Photon. Technol. Lett. 10 (1998), p. 1244-1246.

[106] J.-L. Adam: “Lanthanides in non-oxide glasses”, Chem. Rev. 102 (2002), p. 2461-2476.

[107] M. Dejneka, E. Snitzer, R.E. Riman: “Blue, green and red fluorescence and energy transfer of Eu^{3+} in fluoride glasses”, J. Lumin. 65 (1995), p. 227-245.

[108] E. Downing, L. Hesselink, J. Ralston, R. Macfarlane: “A three-color, solid-state, three-dimensional display”, Science 273 (1996), p. 1185-1189.

[109] L.B. Shaw, B. Cole, P.A. Thielen, J.S. Sanghera, I.D. Aggarwal: “Mid-wave IR and long-wave IR laser potential of rare-earth doped chalcogenide glass fiber”, IEEE J. Quantum. Elect. 37 (2001), p. 1127-1137.

[110] M.C. Gonçalves, L.F. Santos, R.M. Almeida: “Rare-earth-doped transparent glass ceramics”, C. R. Chimie 5 (2002), p. 845-854.

[111] Y. Wang and J. Ohwaki: “New transparent vitroceramics codoped with Er^{3+} and Yb^{3+} for efficient frequency upconversion”, Appl. Phys. Lett. 63 (1993), p. 3268-3270.

[112] M.J. Dejneka: “The luminescence and structure of novel transparent oxyfluoride glass-ceramics”, J. Non-Cryst. Solids 239 (1998), p. 149-155.

[113] M.J. Weber: "Probabilities for radiative and nonradiative decay of Er^{3+} in LaF_3", Phys. Rev. 157 (1967), p. 262-272.

[114] Z. Hu, Y. Wang, F. Bao, W. Luo: "Crystallization behavior and microstructure investigations on LaF_3 containing oxyfluoride glass ceramics", J. Non-Cryst. Solids 351 (2005), p. 722-728.

[115] V. Lavín, I. Iparraguirre, J. Azkargorta, A. Mendioroz, J. González-Platas, R. Balda, J. Fernández: "Stimulated and upconverted emissions of Nd^{3+} in a transparent oxyfluoride glass-ceramic", Opt. Mater. 25 (2004), p. 201-208.

[116] P.A. Tick, N.F. Borrelli, L.K. Cornelius, M.A. Newhouse: "Transparent glass ceramics for 1300 nm amplifier applications", J. Appl. Phys. 78 (1995), p. 6367-6374.

[117] B.N. Samson, P.A. Tick, N.F. Borrelli: "Efficient neodymium-doped glass-ceramic fiber laser and amplifier", Opt. Lett. 26 (2001), p. 145-147.

[118] J. Méndez-Ramos, V.K. Tikhomirov, V.D. Rodríguez, D. Furniss: "Infrared tuneable up-conversion phosphor based on Er^{3+}-doped nano-glass–ceramics", J. Alloys Compd. 440 (2007), p. 328-332.

[119] Y. Ledemi, A.-A. Trudel, V.A.G. Rivera, S. Chenu, E. Véron, L.A. Nunes, M. Allix, Y. Messaddeq: "White light and multicolor emission tuning in triply doped $Yb^{3+}/Tm^{3+}/Er^{3+}$ novel fluoro-phosphate transparent glass-ceramics", J. Mater. Chem. C 2 (2014), p. 5046-5056.

[120] D. Chen, Y. Wang, N. Yu, P. Huang, F. Weng: "Near-infrared quantum cutting in transparent nanostructured glass ceramics", Opt. Lett. 33 (2008), p. 1884-1886.

[121] F. Brech and L. Cross: "Optical microemission stimulated by a ruby MASER", Appl. Spectrosc. 16 (1962), p. 59.

[122] H.M. Smith and A.F. Turner: "Vacuum Deposited Thin Films Using a Ruby Laser", Appl. Opt. 4 (1965), p. 147-148.

[123] D. Dijkkamp, T. Venkatesan, X.D. Wu, S.A. Shaheen, N. Jisrawi, Y.H. Min-Lee, W.L. McLean, M. Croft: "Preparation of Y-Ba-Cu oxide superconductor thin films using pulsed laser evaporation from high T_c bulk material", Appl. Phys. Lett. 51 (1987), p. 619-621.

[124] K.L. Saenger: "Pulsed laser deposition: Part I A review of process characteristics and capabilieties", Processing of Advanced Materials 2 (1993), p. 1-24.

[125] Pulsed Laser Deposition of Thin Films, Edited by R. Eason (John Wiley & Sons Ltd, 2006).

[126] J.T. Cheung, H. Sankur: "Growth of thin films by laser-induced evaporation", CRC Critical Reviews in Solid State and Materials Sciences 15 (1988), p. 63-109.

[127] K.L. Saenger: "Pulsed laser deposition: Part II A review of process mechanisms", Processing of Advanced Materials 3 (1993), p. 63-82.

[128] C.N. Afonso and J. Gonzalo: Láminas Delgadas y Recubrimientos: Preparación, Propiedades y Aplicaciones (J. Albella, CSIC, 2003), p. 2-26.

[129] P.R. Willmott and J.R. Huber: "Pulsed laser vaporization and deposition", Rev. Mod. Phys. 72 (2000), p. 315-328.

[130] E. Backen, S. Haindl, T. Niemeier, R. Hühne, T. Freudenberg, J. Werner, G. Behr, L. Schultz, B. Holzapfel: "Growth and anisotropy of La(O, F)FeAs thin films deposited by pulsed laser deposition", Supercond. Sci. Tech. 21 (2008), Art. 122001.

[131] J.R. Tesmer and M. Nastasi: Handbook of Modern Ion Beam Materials Analysis (Materials Research Society, Pittsburgh, Pennsylvania, 1995).

[132] H-J. Gossmann, L.C. Feldman: "Materials Analysis with High Energy Ion Beams. Part I: Rutherford Backscattering", MRS Bull. 12 (1987), p. 26-28.

[133] G. Vizkelethy: Nuclear Reaction Analysis and Proton-Induced Gamma Ray Emission in Characterization of Materials 1st edition (John Wiley & Sons Ltd, 2007) p. 269-293.

[134] M. Mayer: SIMNRA User's Guide, Report IPP 9/113 (Max Planck Institut für Plasmaphysik, Garching, Germany, 1997).

[135] A. Caciolli, M. Chiari, A. Climent-Font, M.T Fernández-Jiménez, G. García-López, F. Lucarelli, S. Nava, A. Zucchiatti: "Measurements of γ-ray emission induced by protons on fluorine and lithium", Nucl. Instr. and Meth. in Phys. Res. B 249 (2006), p. 98-100.

[136] F.J. Ferrer, J. Gil-Rostra, A. Terriza, G. Rey, C. Jimenez, J. Garcia-Lopez, F. Yubero: "Quantification of low levels of fluorine content in thin films", Nucl. Instrum. Method Phys. Res. B 274 (2012), p. 65-69.

[137] P.J. Haines: Principles of Thermal Analysis and Calorimetry (Royal Society of Chemistry, Great Britain, 2002).

[138] C.V. Raman, K.S. Krishnan: "A new type of secondary radiation", Nature 121 (1928), p. 501-502.

[139] E. Smith and G. Dent: Modern Raman Spectroscopy - A Practical Approach (John Wiley & Sons Ltd, 2005).

[140] R. Shuker and R.W. Gammon: "Raman-scattering selection-rule breaking and the density of states in amorphous materials", Phys. Rev. Lett. 25 (1970), p. 222-225.

[141] F.L. Galeener and P.N. Sen: "Theory for the first-order vibrational spectra of disordered solids", Phys. Rev. B 17 (1978), p. 1928-1933.

[142] D. Brandon, W.D. Kaplan: Microstructural Characterization of Materials, 2nd Edition (John Wiley & Sons Ltd, 2008).

[143] H. Fujiwara: Spectroscopy Ellipsometry Principles and Applications (John Wiley & Sons Ltd, 2007).

[144] H.G. Tompkins: A User's Guide to Ellipsometry (Academic Press, San Diego, CA, 1993).

[145] K. Chida, F. Hanawa, M. Nakahara: "Fabrication of OH-free multimode fiber by vapor phase axial deposition", IEEE J. Quantum. Elect. 18 (1982), p. 1883-1889.

[146] M.J. Weber: "Luminescence decay by energy migration and transfer: Observation of diffusion-limited relaxation", Phys. Rev. B 4 (1971), p. 2932-2939.

[147] A. Lin, A. Ryasnyanskiy, J. Toulouse: "Fabrication and characterization of a water-free mid-infrared fluorotellurite glass", Opt. Lett. 36 (2011), p. 740-742.

[148] H. Zhan, Z. Zhou, J. He, A. Lin: "Intense 2.7 μm emission of Er^{3+}-doped water-free fluorotellurite glasses", Opt. Lett. 37 (2012), p. 3408-3410.

[149] E.F. Chillcce, I.O. Mazali, O.L. Alves, L.C. Barbosa: "Optical and physical properties of Er^{3+}-doped oxy-fluoride tellurite glasses", Opt. Mater. 33 (2011), p. 389-396.

[150] D.L. Sidebottom, M.A. Hruschka, B.G. Potter, R.K. Brow: "Structure and optical properties of rare earth-doped zinc oxhalyde tellurite glasses", J. Non-Cryst. Solids 222 (1997), p. 282-289.

[151] V. Nazabal, S. Todoroki, A. Nukui, T. Matsumoto, S. Suehara, T. Hondo, T. Araki, S. Inoue, C. Rivero, T. Cardinal: "Oxyfluoride tellurite glasses doped with erbium: thermal analysis, structural organization and spectral properties", J. Non-Cryst. Solids 325 (2003), p. 85-102.

[152] H. Bürger, K. Kneipp, H. Hobert, W. Vogel: "Glass formation, properties and structure of glasses in the TeO_2-ZnO system", J. Non-Cryst. Solids 151 (1992), p. 134-142.

[153] A. Jha, S. Shen, and M. Naftaly: "Structural origin of spectral broadening of 1.5-μm emission in Er^{3+}-doped tellurite glasses", Phys. Rev. B 62 (2000), p. 6215-6227.

[154] A. Nukui, T. Taniguchi, M. Miyata: "In situ high-temperature X-ray observation of structural changes of tellurite glasses with p-block oxides; ZnO-TeO_2 glasses", J. Non-Cryst Solids 293-295 (2001), p. 255-260.

[155] C. Duverger, M. Bouazaoui, S. Turrell: "Raman spectroscopic investigations of the effect of the doping metal on the structure of binary tellurium-oxide glasses", J. Non-Cryst. Solids 220 (1997), p. 169-177.

[156] M. Mazzuca, J. Portier, B. Tanguy, F Romain, A. Fadli, S. Turrell: "Raman Scattering in Tellurium-Metal Oxyde Glasses", J. Mol. Struct. 349 (1995), p. 413-416.

[157] T. Sekiya, N. Mochida, A. Ohtsuka: "Raman spectra of $MOTeO_2$ (M = Mg, Sr, Ba and Zn) glasses", J. Non-Cryst. Solids 168 (1994), p. 106-114.

[158] V. Kozhukharov, H. Bürger, S. Neov, B. Sidzhimov: "Atomic arrangement of a zinc-tellurite glass", Polyhedron 5 (1986), p. 771-777.

[159] P.A. Thomas: "The crystal structure and absolute optical chirality of paratellurite, α-TeO_2", J. Phys. C: Solid State Phys. 21 (1988), p. 4611-4627.

[160] K. Hanke: "Die Kristallstruktur von $Zn_2Te_3O_8$" Naturwissenschaften 53 (1966), p. 273.

[161] Y. Himei, A. Osaka, T. Nanba, Y. Miura: "Coordination change of Te atoms in binary tellurite glasses", J. Non-Cryst. Solids 177 (1994), p. 164-169.

[162] B.O. Mysen, W. Larry, W. Finger, O. Virgo and F.A. Seifert: "Curve-fitting of Raman spectra of silicate glasses", Am. Miner. 67 (1982), p. 686-695.

[163] H. Bürger, W. Vogel, V. Kozhukharov: "IR transmission and properties of glasses in the TeO_2–[R_nO_m, R_nX_m, $R_n(SO_4)_m$, $R_n(PO_3)_m$ and B_2O_3] systems", Infrared Phys. 25 (1985), p. 395-409.

[164] S.F. León-Luis, U.R. Rodríguez-Mendoza, E. Lalla, V. Lavín: "Temperature sensor based on the Er^{3+} green upconverted emission in a fluorotellurite glass", Sens. & Actuat. B 158 (2011), p. 208-213.

[165] F. Lahoz, C. Pérez-Rodríguez, S.E. Hernández, I.R. Martín, V. Lavín, U.R. Rodríguez-Mendoza: "Upconversion mechanisms in rare-earth doped glasses to improve the efficiency of silicon solar cells", Solar En. Mat. & Solar Cells 95 (2011), p. 1671-1677.

[166] J.Y. Allain, M. Monerie, H. Poignant: "Tunable green upconversion erbium fibre laser", Electron. Lett. 28 (1992), p. 111-113.

[167] A. Miguel, R. Morea, J. Gonzalo, M.A. Arriandiaga, J. Fernandez, R. Balda: "Near-infrared emission and upconversion in Er^{3+}-doped TeO_2-ZnO-ZnF_2 glasses", J. Lumin. 140 (2013), p. 38-44.

[168] R. Rolli, K. Gatterer, M. Wachtler, M. Bettinelli, A. Speghini, D. Ajò: "Optical spectroscopy of lanthanide ions in ZnO–TeO_2 glasses", Spectrochim. Acta A 57 (2001), p. 2009-2017.

[169] D.K. Sardar, J.B. Gruber, B. Zandi, J.A. Hutchinson, C. Ward Trussell: "Judd-Ofelt analysis of the Er^{3+} ($4f^{11}$) absorption intensities in phosphate glass: Er^{3+}, Yb^{3+}", J. Appl. Phys. 93 (2003), p. 2041-2046.

[170] C.K. Jørgensen, R. Reisfeld: "Judd-Ofelt parameters and chemical bonding", J. Less-Common Met. 93 (1983), p. 107-112.

[171] A.A. Kaminskii: Crystalline Lasers: Physical Process and Operating Schemes, (Boca Raton, FL: CRC, 1996).

[172] A. Miguel, J. Azkargorta, R. Morea, I. Iparraguirre, J. Gonzalo, J. Fernandez, R. Balda: "Spectral study of the stimulated emission of Nd^{3+} in fluorotellurite bulk glass", Opt. Express 21 (2013), p. 9298-9307.

[173] M.J. Weber, J. D. Myers, D. H. Blackburn: "Optical properties of Nd^{3+} in tellurite and phosphotellurite glasses", J. Appl. Phys. 52 (1981), p. 2944-2949.

[174] T. Sasikala, L.R. Moorthy, K. Pavani, T. Chengaiah: "Spectroscopic properties of Er^{3+} and Ce^{3+} co-doped tellurite glasses", J. Alloys Com. 542 (2012), p. 271-275.

[175] N. Jaba, H. Ben Mansour, A. Kanoun, A. Brenier, B. Champagnon: "Spectral broadening and luminescence quenching of 1.53 μm emission in Er^{3+}-doped zinc tellurite glass", J. Lumin. 129 (2009), p. 270-276.

[176] M. Mattarelli, M. Montagna, L. Zampedri, A. Chiasera, M. Ferrari, G.C. Righini, L.M. Fortes, M.C. Gonçalves, L.F. Santos, R.M. Almeida: "Self-absorption and radiation trapping in Er^{3+}-doped TeO_2-based glasses", Europhys. Lett. 71 (2005), p. 394-399.

[177] F. Auzel, G. Baldacchini, L. Laversenne, G. Boulon, "Radiation trapping and self-quenching analysis in Yb^{3+}, Er^{3+}, and Ho^{3+} doped Y_2O_3", Opt. Mater. 24 (2003), p. 103-109.

[178] I. Jlassi, H. Elhouichet, S. Hraiech, M. Ferid: "Effect of heat treatment on the structural and optical properties of tellurite glasses doped erbium", J. Lumin. 132 (2012), p. 832-840.

[179] U.R. Rodríguez-Mendoza, E.A. Lalla, J.M. Caceres, F. Rivera-Lopez, S.F. Leon-Luís, V. Lavín, "Optical characterization, 1.5 μm emission and IR-to-visible energy upconversion in Er^{3+}-doped fluorotellurite glasses", J. Lumin. 131 (2011), p. 1239-1248.

[180] T. Xu, X. Zhang, G. Li, S. Dai, Q. Nie, X. Shen, X. Zhang: "Spectroscopic properties and thermal stability of Er^{3+}-doped TeO_2-B_2O_3-Nb_2O_5-ZnO glass for potential WDM amplifier", Spectrochim. Acta Part A 67 (2007), p. 559-563.

[181] G.C. Righini, S. Pelli, M. Brenci, M. Ferrari, C. Duverger, M. Montagna, R. Dall'Igna: "Active optical waveguides based on Er- and Er/Yb-doped silicate glasses", J. Non-Cryst. Solids 284 (2001), p. 223-229.

[182] S.H. Xu, Z.M. Yang, T. Liu, W.N. Zhang, Z.M. Feng, Q.Y. Zhang, Z.H. Jiang: "An efficient compact 300 mW narrow-linewidth single frequency fiber laser at 1.5 μm", Opt. Express 18 (2010), p. 1249-1254.

[183] L. Huang, A. Jha, S. Shen, X. Liu: "Broadband emission in Er^{3+}-Tm^{3+} codoped tellurite fibre", Opt. Express 12 (2004), p. 2429-2434.

[184] Y. Xu, D. Chen, W. Wang, Q. Zhang, H. Zeng, C. Shen, G. Chen: "Broadband near-infrared emission in Er^{3+}–Tm^{3+} codoped chalcohalide glasses", Opt. Lett. 33 (2008), p. 2293-2295.

[185] R. Balda, J. Fernandez, J.M. Fernandez-Navarro: "Study of broadband near-infrared emission in Tm^{3+}-Er^{3+} codoped TeO_2-WO_3-PbO glasses", Opt. Express, 17 (2009), p. 8781-8788.

[186] A. Miguel, M.A. Arriandiaga, R. Morea, J. Fernandez, J. Gonzalo, R. Balda: "Down- and up-conversion emissions in Er^{3+}-Yb^{3+} codoped TeO_2-ZnO-ZnF_2 glasses", J. Lumin. 158 (2015), p. 142-148.

[187] H. Desirena, E. De la Rosa, A. Shulzgen, S. Shabet, N. Peyghambarian: "Er^{3+} and Yb^{3+} concentration effect in the spectroscopic properties and energy transfer in Yb^{3+}/Er^{3+} codoped tellurite glasses", J. Phys. D: Appl. Phys. 41 (2008), 095102 (7pp).

[188] Q.Y. Zhang, Z.M. Feng, Z.M. Yang, Z.H. Jiang: "Energy transfer and infrared-to-visible upconversion luminescence of Er^{3+}/Yb^{3+}-codoped halide modified tellurite glasses", J. Quant. Spectrosc. Radiat. Transf. 98 (2006), p. 167-179.

[189] V.P. Gapontsev, S.M. Matitsin, A.A. Isineev, V.B. Kravchenko: "Erbium glass lasers and their applications", Opt. Laser Technol. 14 (1982), p. 189-196.

[190] R.S. Quimby, M.G. Drexhage, M.J. Suscavage: "Efficient frequency upconversion via energy-transfer in fluoride glasses", Electron. Lett. 23 (1987), p. 32-34.

[191] A. Miguel, M.A. Arriandiaga, R. Morea, J. Fernandez, J. Gonzalo, R. Balda: "Effect of Tm^{3+} codoping on the near-infrared and upconversion emissions of Er^{3+} in TeO_2-ZnO-ZnF_2 glasses", J. Lumin. 154 (2014), p. 136-141.

[192] X. Xu, Y. Zhou, S. Zheng, D. Yin, X. Wang: "Luminescence properties and energy transfer mechanism of Er^{3+}/Tm^{3+} co-doped tellurite glasses", J. Alloy Compd. 556 (2013), p. 221-227.

[193] M. Sroda, I. Waclawska, L. Stoch, M. Reben: "DTA/DSC Study of Nanocrystallization in Oxyfluoride Glasses", J. Therm. Anal. Calorim. 77 (2004), p. 193-200.

[194] R. Wurth, M.J. Pascual, G.C. Mather, A. Pablos-Martin, F. Munoz, A. Duran, G. Cuello, C. Rüssel: "Crystallization Mechanism of a Multi Component Lithium Aluminosilicate Glass", Mater. Chem. Phys. 134 (2012), p. 1001-1006.

[195] J.M. Rojo, P. Herrero, J. Sanz, B. Tanguy, J. Portier, J.M. Réau: "Relationship between microstructure and ionic conduction properties in oxyfluoride tellurite glass-ceramics", J. Non-Cryst. Solids 146 (1992), p. 50-56.

[196] C. Yu, J. Zhang, L. Wen, Z. Jiang: "New transparent Er^{3+}-doped oxyfluoride tellurite glass ceramic with improved near infrared and up-conversion fluorescence properties", Mater. Lett. 61 (2007), p. 3644-3646.

[197] Z.X. Hou, Z.L. Xue, S.H. Wang: "Synthesis and spectroscopic properties of Er^{3+}-doped CaF_2 nanocrystals in transparent oxyfluoride tellurite glass-ceramics", J. Alloys Compd. 514 (2012), p. 109-112.

[198] C. Joshi, R.N. Rai, S.B. Rai: "Structural, thermal, and optical properties of Er^{3+}/Yb^{3+} co-doped oxyhalide tellurite glasses, glass-ceramics and ceramics", J. Quant. Spectrosc. Ra. 113 (2012), p. 397-404.

[199] H.E. Kissinger: "Reaction kinetics in differential thermal analysis", Anal. Chem. 29 (1957), p. 1702-1706.

[200] S.M. Sidel, F.A. Santos, V.O. Gordo, E. Idalgo, A.A. Monteiro, J.C.S. Moraes, K. Yukimitu: "Avrami exponent of crystallization in tellurite glasses", J. Therm. Anal. Calorim. 106 (2011), p. 613-618.

[201] J. Massera, J. Remond, J. Musgraves, M.J. Davis, S. Misture, L. Petit, K. Richardson: "Nucleation and growth behavior of glasses in the TeO_2-Bi_2O_3-ZnO glass system", J. Non-Cryst. Solids 356 (2010), p. 2947-2955.

[202] A. Marotta, A. Buri, F. Branda: "Nucleation in glass and differential thermal analysis", J. Mater. Sci. 16 (1981), p. 341-344.

[203] C.S. Ray, K.S. Ranasinghe, D.E. Day: "Determining crystal growth rate-type of curves in glasses by differential thermal analysis", Solid State Sci. 3 (2001), p. 727-732.

[204] P.A. Tick, N.F. Borrelli, I.M. Reaney: "The relationship between structure and transparency in glass-ceramic materials", Opt. Mater. 15 (2000), p. 81-91.

[205] G. Gao, S. Reibstein, M. Peng, L. Wondraczek: "Tunable dual-mode photoluminescence from nanocrystalline Eu-doped Li_2ZnSiO_4 glass ceramic phosphors", J. Mater. Chem. 21 (2011), p. 3156-3161.

[206] http://www.fiz-karlsruhe.de/icsd_home.html

[207] O. Lindqvist, Acta Chem. Scand. 22 (1968), p. 997-982.

[208] K. Hanke, Naturwissenschaften 53 (1966), p. 273.

[209] P.C. Becker, G.M. Williams, R.E. Russo, N. Edelstein, J.A. Koningstein, L.A. Boatner, M.M. Abraham: "Resonance electronic Raman scattering in erbium phosphate crystals", Opt. Lett. 11 (1986), p. 282-284.

[210] V. Prathibha, S. Karthika, J. Cyriac, C. Sudarasanakumar, N.V. Unnikrishnan: "Synthesis of pure anatase TiO_2 nanocrystals in SiO_2 host and the determination of crystal planes by ImageJ", Mater. Lett. 65 (2011), p. 664-666.

[211] M.D. Abramoff, P.J. Magelhaes, S.J. Ram: "Image processing with ImageJ", Biophotonics International 11 (2004), p. 36-42.

[212] Powder Diffraction File, Card no. 32-0361, Database Edition. Swathmore, PA, USA: Joint Committee on Powder Diffraction Standards (ICDD); 2003.

[213] A. Miguel, R. Morea, M.A. Arriandiaga, M. Hernandez, F.J. Ferrer, C. Domingo, J.M. Fernandez-Navarro, J. Gonzalo, J. Fernandez, R. Balda: "Structural, optical, and spectroscopic properties of Er^{3+}-doped TeO_2–ZnO–ZnF_2 glass-ceramics", J. Eur. Ceram. Soc. 34 (2014), p. 3959-3968.

[214] R. Reisfeld, G. Katz, N. Spector, C.K. Jørgensen, C. Jacoboni, R. De Pape: "Optical transition probabilities of Er^{3+} in fluoride glasses", J. Solid State Chem. 41 (1982), p. 253-261.

[215] F. Goutaland, P. Jander, W.S. Brocklesby, G. Dai: "Crystallisation effects on rare earth dopants in oxyfluoride glass ceramics", Opt. Mater. 22 (2003), p. 383-390.

[216] G. Dantelle, M. Mortier, G. Patriarche, D. Vivien: "Er^{3+} doped PbF_2: Comparison between nanocrystals in glass-ceramics and bulk single crystals", J. Solid State Chem. 179 (2006), p. 1995-2003.

[217] P.G. Kik, A. Polman: "Erbium doped optical waveguide amplifiers on silicon", MRS Bull. 23 (1998), p. 48-54.

[218] J.M. Ruano, V. Benoit, J.S. Aitchison, J.M. Cooper: "Flame Hydrolysis Deposition of Glass on Silicon for the Integration of Optical and Microfluidic Devices", Anal. Chem. 72 (2000), p. 1093-1097.

[219] S. Shen, W.H. Chow, D.P. Steenson, A. Jha: "Fabrication of Er^{3+} doped oxyfluoride-silicate glass film by pulsed laser deposition for planar amplifier", J. Non-Cryst. Solids 355 (2009), p. 1893-1896.

[220] M. Irannejad, G. Jose, P. Steenson, A. Jha: "Enhancement in optical and microstructure properties of Er^{3+}-doped phospho-tellurite glass thin film", Opt. Mater. 34 (2012), p. 1272-1276.

[221] D. Munoz-Martin, J. Gonzalo, J.M. Fernandez-Navarro, J. Siegel, C.N. Afonso: "Influence of surface effects on the performance of lead–niobium–germanate optical waveguides", Appl. Surf. Sci. 254 (2007), p. 1111-1114.

[222] J. Gonzalo, C.N. Afonso, J. Perrière: "The role of film re-emission and gas scattering processes on the stoichiometry of laser deposited films", Appl. Phys. Lett. 67 (1995), p. 1325-1327.

[223] J.C.S. Kools: "Monte Carlo simulations of the transport of laser-ablated atoms in a diluted gas", J. Appl. Phys. 74 (1993), p. 6401-6406.

[224] Z. Zhao, G. Jose, P. Steenson, N. Bamiedakis, R.V. Penty, I.H. White, A. Jha, "Tellurite glass thin films on silica and polymer using UV (193 nm) pulsed laser ablation", J. Phys. D: Appl. Phys. 44 (2011), Article number: 095501.

[225] D. Munoz-Martin, J.M. Fernandez-Navarro, J. Gonzalo, G. Jose, A. Jha, J.L.G. Fierro, C. Domingo, J. Garcia-Lopez, "Structural and optical properties of tellurite thin film glasses deposited by pulsed laser deposition", Thin Solid Films 520 (2011), p. 131-137.

[226] M. Irannejad, G. Jose, A. Jha, D. P. Steenson: "A parametric study of Er^{3+}-ions doped Phospho-tellurite glass thin films by pulsed laser deposition", Opt. Mater. 33 (2010), p. 215-219.

[227] A.P. Caricato, A. Fazzi, A. Jha, A. Kar, G. Leggieri, A. Luches, M. Martino, F. Romano, S. Shen, M. Taghizadeh, R. Thomson, T. Tunno: "Er-doped oxyfluoride silicate thin films prepared by pulsed laser deposition", Opt. Mater. 29 (2007), p. 1166-1170.

List of publications and communications[1]

Journal publications:

7- *Er^{3+}-doped fluorotellurite thin film glasses with improved photoluminescence emission at 1.53 μm*
R. Morea, A. Miguel, T.T. Fernandez, B. Maté, F.J. Ferrer, C. Maffiotte, J. Fernandez, R. Balda, J. Gonzalo
Submitted to Journal of Luminescence

6- *Down- and up-conversion emissions in Er^{3+}–Yb^{3+} codoped TeO_2–ZnO–ZnF_2 glasses*
A. Miguel, M.A. Arriandiaga, **R. Morea**, J. Fernandez, J. Gonzalo, R. Balda
Journal of Luminescence 02/2015; **158**: 142-148
DOI:10.1016/j.jlumin.2014.09.052

5- *Structural, optical, and spectroscopic properties of Er^{3+}-doped TeO_2–ZnO–ZnF_2 glass-ceramics*
A. Miguel*, **R. Morea***, M.A. Arriandiaga, M. Hernandez, F.J. Ferrer, C. Domingo, J.M. Fernandez-Navarro, J. Gonzalo, J. Fernandez, R. Balda (*equal contribution)
Journal of the European Ceramic Society 12/2014; **34**(15): 3959-3968
DOI:10.1016/j.jeurceramsoc.2014.05.001

4- *Effect of Tm^{3+} codoping on the near-infrared and upconversion emissions of Er^{3+} in TeO_2–ZnO–ZnF_2 glasses*
A. Miguel, M.A. Arriandiaga, **R. Morea**, J. Fernandez, J. Gonzalo, R. Balda
Journal of Luminescence 10/2014; **154**: 136-141
DOI:10.1016/j.jlumin.2014.04.020

3- *Spectroscopic properties of Er^{3+}-doped fluorotellurite glasses*
A. Miguel, M. Al-Saleh, J. Azkargorta, **R. Morea**, J. Gonzalo, M. A. Arriandiaga, J. Fernandez, R. Balda
Optical Materials 09/2013; **35**(11): 2039-2044
DOI:10.1016/j.optmat.2012.09.022

2- *Near-infrared emission and upconversion in Er^{3+}-doped TeO_2-ZnO-ZnF_2 glasses*
A. Miguel, **R. Morea**, J. Gonzalo, M. A. Arriandiaga, J. Fernandez, R. Balda
Journal of Luminescence 08/2013; **140**: 38-44
DOI:10.1016/j.jlumin.2013.02.059

1- *Spectral study of the stimulated emission of Nd^{3+} in fluorotellurite bulk glass*
A. Miguel, J. Azkargorta, **R. Morea**, I. Iparraguirre, J. Gonzalo, J. Fernandez, R. Balda
Optics Express 04/2013; **21**(8): 9298-9307
DOI:10.1364/OE.21.009298

[1] Directly related to the thesis

Conference proceedings:

4- *Down- and up-conversion emissions in Er-doped transparent fluorotellurite glass-ceramics*
A. Miguel, **R. Morea**, J. Gonzalo, J. Fernandez, R. Balda
Proc. SPIE 9359, Optical Components and Materials XII, 93590X (16 March 2015)
DOI: 10.1117/12.2075584

3- *Active mid-IR emissions from rare-earth doped tellurite glass ceramics for bio applications*
R. Morea, T.T. Fernandez, A. Miguel, R. Balda, J. Solís, M. Hernandez, J. Gonzalo, J.M. Ulloa, J. Fernandez
16th International Conference on Transparent Optical Networks, ICTON 2014; Graz; Austria; 6 July 2014 through 10 July 2014; Article number 6876434

2- *2.18 μm Mid IR emission from highly transparent Er^{3+} doped tellurite glass ceramic for bio applications*
R. Morea, T.T. Fernandez, A. Miguel, M. Hernandez, J.M. Ulloa, J.M. Fernandez, R. Balda, J. Solis, J. Gonzalo
CLEO: Science and Innovations, CLEO_SI 2014; San Jose, CA; United States; 8 June 2014 through 13 June 2014; Code 106736

1- *Photoluminescence emission in Er-activated good quality fluorotellurite thin film glasses*
R. Morea, A. Miguel, T.T. Fernandez, J. Fernandez, R. Balda, J. Gonzalo
The European Conference on Lasers and Electro-Optics, CLEO_Europe 2013; Munich; Germany; 12 May 2013 through 16 May 2013; Code 104365

Communications to conferences:

9- SPIE Photonics West, San Francisco CA (USA), February 2015
Down- and up-conversion emissions in Er-doped transparent fluorotellurite glass-ceramics
A. Miguel, **R. Morea**, J. Gonzalo, J. Fernandez, R. Balda
Invited talk

8- ICTON 2014, Graz (Austria), July 2014
Active mid-IR emissions from rare-earth doped tellurite glass ceramics for bio applications
R. Morea, T.T. Fernandez, A. Miguel, R. Balda, J. Solís, M. Hernandez, J. Gonzalo, J.M. Ulloa, J. Fernandez
Invited talk

7- CLEO, San Jose CA (USA), June 2014
2.18 μm Mid IR emission from highly transparent Er^{3+} doped tellurite glass ceramic for bio applications
R. Morea, T.T. Fernandez, A. Miguel, M. Hernandez, J.M. Ulloa, J.M. Fernandez, R. Balda, J. Solis, J. Gonzalo
Conference poster

6- PRE '14, San Sebastian (Spain), May 2014
Er^{3+}-doped fluorotellurite thin film glasses for optical gain at 1.5 μm
R. Morea, A. Miguel, T.T. Fernandez, J. Gonzalo, J. Fernandez, R. Balda
Conference talk

5- E-MRS Spring meeting, Strasbourg (France), May 2013
Improved photoluminescence emission in Er-doped oxyfluorotellurite thin films
R. Morea, A. Miguel, T.T. Fernandez, J. Gonzalo, J. Fernandez, R. Balda
Conference talk

4- CLEO/Europe-IQEC 2013, Munich (Germany), May 2013
Photoluminescence emission in Er-activated good quality fluorotellurite thin film glasses
R. Morea, A. Miguel, T.T. Fernandez, J. Fernandez, R. Balda, J. Gonzalo
Conference poster

3- X RNO, Zaragoza (Spain), September 2012
Estructura y propiedades ópticas de vidrios de fluoroteluritos dopados con Er para aplicaciones fotónicas
R. Morea, M. Hernandez, A. Miguel, F. J. Ferrer, J. Gonzalo, C. Domingo, J. Garcia-Lopez, J. Fernandez, R. Balda
Conference talk

2- GOMD 2012, St. Louis MO (USA), May 2012
Thermal stability and optical properties of rare earth doped oxyfluoride tellurite glasses
R. Morea, A. Miguel, J. Gonzalo, J.M. Fernandez-Navarro, J. Fernandez, R. Balda
Conference poster

1- PRE '12, Kyoto (Japan), March 2012
Spectroscopic properties of Er^{3+}-doped fluorotellurite glasses
A. Miguel, M. Al-Saleh, J. Azkargorta, J. Gonzalo, **R. Morea**, J. Fernandez, R. Balda
Conference poster